APPLICATIONS OF ULTRALONG RAMAN FIBRE LASERS IN PHOTONICS

MERCEDES ALCON CAMAS

Doctor of Philosophy

ASTON UNIVERSITY

February 2011

Aston University

Applications of ultralong Raman fibre lasers in photonics

Mercedes Alcon Camas
Doctor of Philosophy

February 2011

Summary

This thesis presents a numerical and experimental investigation on applications of ultralong Raman fibre lasers in optical communications, supercontinuum generation and soliton transmission. The research work is divided in four main sections.

The first involves the numerical investigation of URFL intra-cavity power and the relative intensity noise transfer evolution along the transmission span. The performance of the URFL is compared with amplification systems of similar complexity. In the case of intra-cavity power evolution, URFL is compared with a first order Raman amplification system. For the RIN transfer investigation, URFL is compared with a bi-directional dual wavelength pumping system. The RIN transfer function is investigated for several cavity design parameters such as span length, pump distribution and FBG reflectivity.

The following section deals with experimental results of URFL cavities. The enhancement of the available spectral bandwidth in the C-band and its spectral flatness are investigated for single and multi-FBGs cavity system. Further work regarding extended URFL cavity in combination with Rayleigh scattering as random distributed feedback produced a laser cavity with dual wavelength outputs independent to each other.

The last two sections relate to URFL application in supercontinuum (SC) generation and soliton transmission. URFL becomes an enhancement structure for SC generation. This thesis shows successful experimental results of SC generation using conventional single mode optical fibre and pumped with a continuous wave source.

The last section is dedicated to soliton transmission and the study of soliton propagation dynamics. The experimental results of exact soliton transmission over multiple soliton periods using conventional single mode fibre are shown in this thesis. The effect of the input signal, pump distribution, span length and FBGs reflectivity on the soliton propagation dynamics is investigated experimentally and numerically.

Keywords: Nonlinear optics, Raman amplification, soliton transmission, supercontinuum generation, relative intensity noise

A mi madre y mi padre

Acknowledgements

This research has been possible thanks to the encouragement and support of many people involved at different stages, both directly and indirectly, through my study towards a PhD degree in the Photonics Research Group at Aston University.

First of all, my great appreciation is towards my supervisors, Dr. Paul Harper and Dr. Juan Diego Ania-Castañón, for their continuous support, expertise, guidance and valuable discussion through this research work. Their patience and encouragement was invaluable.

I would like to thank my collaborators and co-authors of my papers, especially to Dr. Atalla El-Taher, Hua Wang and Dr. Jim Harrison for their time and work effort at my time as student in Aston University and to Dr. Sonia Martín López, Dr. Pedro Corredera Guillén and Dr. Miguel González Herráez for their collaboration and support on my work as student at the Institute of Applied Physics from the CSIC in Madrid. Last but not least, I would like to acknowledge the rest of co-authors of my papers Prof. Ian Bennion, Prof. Sergey Turitsyn, Prof. Luc Thévenaz, Dr. Sergey Babin, Félix Rodríguez Barrios, Lee Barker, Dr. Ana Carrasco Sanz and Dr. Vasilis Karalekas.

During my time as a research student, I found inestimable the support of all the personal, colleagues and friends from the Photonics Research Group at Aston University, the Optics Institute and the Institute of Applied Physics, both from the CSIC. They created a wonderful research environment, which made working on this project enjoyable and very interesting. I own much gratitude to their willingness to help, their friendly company and constructive discussions through lunch and coffee times.

I would like to dedicate my special thanks to my family and friends who has continuously supported my research and life in the UK.

Contents

List of Tables

List of Figures

Abbreviations

AOM	acoustic optic modulator
ASE	amplified spontaneous emission
CW	continuous wave
DDG	digital delay generator
DRS	double Rayleigh scattering
DSF	dispersion shifted fibre
EDFA	Erbium doped fibre amplifier
FBG	fibre Bragg grating
FUT	fibre under test
FWHM	full width half maximum
FWM	four wave mixing
GVD	group velocity dispersión
HN-DSF	highly nonlinear dispersion-shifted fibre
HNLF	highly nonlinear fibre
LEAF	large effective area fibre
MI	modulation instability
MLFL	mode locked fibre laser
MOD	modulator
MPI	multipath interference
NLSE	nonlinear Schrödinger equation
ODE	ordinary differential equation
OPA	optical parametric amplifier
OPC	optical phase conjugation
OSA	optical spectrum analiser
OSNR	optical signal to noise ratio
OTDR	optical time domain reflectometer
PCF	photonic crystal fibre
PD	photodetector
PPG	pulse pattern generator
RFL	Raman fibre laser
RIN	relative intensity to noise

RS	Rayleigh scattering
SC	Supercontinuum
SHG-FROG	second harmonic generation frequency resolved optical gating
SMF	single mode fibre
SNR	signal to noise ratio
SOA	semiconductor optical amplifier
SPM	self-phase modulation.
SRS	stimulated Raman scattering
TOD	third order dispersion
TW	TrueWave
URFL	ultra long Raman fibre lasers
WDM	wavelength division multiplexing
XPM	cross-phase modulation

Chapter 1

Introduction

1.1 Motivation

In our daily life we make use of telecommunications in many areas; from credit card payments to broadcasting news or as culture expression from any side of the world, just to name a few examples. This reliance of our society on information technology for most aspects of our daily life has made telecommunications, including all integrated service network, the motorway to globalisation and an intrinsic part of the logistics to operate in our current society.

The advance in technology has accelerated the changes in our society which poses itself a stress on increasing data traffic; this is translated into the demand of ultra high speed transmission links. Ultra high speed transmission links are achieved by increasing the operating rate and the availability of spectral bandwidth. This type of systems requires long links with very low losses. Increasing the number of repeaters spacing has the effect of reducing cost and at the same time increasing the speed of the network and the affordability to the general public. A lossless link will increase the operating rate as the signal to noise ratio is kept, maintaining the quality of the signal, without the need of lumped amplifiers and undesirable nonlinear effects produced by high intensity signals.

The era of optical communications can be set as starting in the 1960's with the invention of lasers [1] and the work developed by Charles K. Kao, who has won the Nobel price [2] for groundbreaking achievements concerning the transmission of light in fibres for optical communication, and through his work in the 1960´s indicated that the fundamental limitation for glass light attenuation was below 20 dB/km [3]. These discoveries sparked a revolution in the telecommunication industry as a new industry of considerable commercial importance.

In the early years of this technology, the signal propagating in an optical fibre suffered a great deal of fibre loss, which exceeded 1000dB/km. The loss was due to a presence of impurities in the fibre material. In 1966, it was proposed that the glass light attenuation could be minimised, making possible its use for transmission medium [3]. The revolution of optical fibre began in 1970 when Corning demonstrated a silica fibre exhibiting 20dB/km loss [4]. Currently, most modern optical fibres have a typical loss of approximately 0.2dB/km around 1.55μm.

At present, in modern optical transmission systems, Erbium doped fibre amplifiers (EDFAs) [5][6] are widely deployed as lumped amplification systems to compensate for the losses. However, the EDFA itself introduces optical noise due to amplified spontaneous emission (ASE), which was not present in systems employing electronic repeaters. Therefore, a lightwave system deploying EDFAs must operate at relatively high power in order to stop the signal from being buried by the ASE noise. Such a high power enhances the significance of nonlinear effects that become a major problem in high speed long distance systems [7][8][9][10].

The availability of high power sources at the beginning of this millennium has renewed the interest in distributed Raman amplification and fuelled the research towards achieving quasi-lossless transmission systems [11][12][13][14][15][16][17][18][19]. Typically, these attempts have relied either on the loss management of the fibres involved in transmission [12][13][14], or on the use of higher order amplification schemes [17][18], in which multiple cascading pumps at different wavelengths are used to distribute uniformly the amplification of the signal through the line. An alternative approach was proposed by Ania-Castañon in 2004 [15] that combined the simplicity of first order bi-directional pumping with a performance previously achievable only with higher order pumping schemes. The suggested approach was to transform the whole transmission span into an ultralong laser cavity, and to generate secondary pumps inside the cavity directly from the amplified spontaneous emission (ASE) noise present. This technique has been proven and applied successfully in several research work publications [16][19][20][21][22].

The main advantages of the URFL system over the EDFA systems are a lower power variation across the bandwidth range and an extended gain spectral bandwidth. Furthermore, the applications of URFL are not limited to optical communications [19][23][24], but it has found application in other areas such as medium which allow optical solitons investigation [22][25][26] as a laser source in supercontinuum generation [27] or as long length sensing media [28].

1.2 Thesis overview

The work presented in this thesis reflects the renewed research interest in Raman amplification, in particular in ultralong Raman fibre lasers (URFL). The objective of this work was to explore the applications of ultralong Raman fibre lasers in photonics. As part of this research the bi-directional second order pumping scheme used in conventional optical fibres as part of URFL was investigated and optimised. A combination of experimental and numerical results is presented targeting a reduction of optical power excursion and relative intensity noise (RIN) for different cavity design parameters, and an enhancement of the available bandwidth for optical communications. Two examples of URFL applications in photonics are supercontinuum generation (SC) and soliton transmission. The main achievements are an enhancement of the flatness of the SC optical spectra and the first experimental demonstration of soliton transmission over several soliton periods, in both cases, using conventional optical fibres. Although each topic merits its own research, here our research is limited to a few aspects where URFL are used as a source or transmission media. The application of URFL is been successful in areas other than SC generation and soliton transmission, although for coherence further work will not be included here.

This first chapter draws a context for developing this work, including the motivation behind that instigated the research work in ultralong Raman fibre lasers.

Chapter 2 provides the mathematical foundations of nonlinear fibre optics. Basic concepts of optical fibre characterisation are described before heading into the optical fibre nonlinearities and the development of optical wave propagation within the context of optical fibre communications. The effects of group velocity dispersion (GVD), self-phase modulation (SPM), four wave mixing (FWM) and Raman scattering are briefly introduced. The objective is to provide a mathematical and conceptual insight into nonlinear fibre optics which will allow a better understanding of the results presented in later chapters.

Most of the numerical results of this thesis are presented in Chapter 3, which is dedicated to the relative intensity noise (RIN) of URFL. The development of the optical power evolution and the RIN along the propagating fibre are described by the URFL model presented in this chapter. Numerical results are presented targeting a reduction of the relative intensity noise (RIN) for different cavity design parameters such as cavity length, pump distribution and fibre Bragg reflectivity.

Chapter 4 follows the investigation and optimisation of URFL presenting experimental results regarding the enhancement of the available spectrum bandwidth for optical communications whilst keeping the spectrum flatness. Further experimental results, related to pump depletion and its effect on the spectrum flatness are also presented. The effect of

Rayleigh scattering providing feedback is reviewed for longer cavity systems. An interesting result is a laser cavity with two different output wavelengths.

Chapter 5 deals with supercontinuum (SC) generation from a continuous wave pump. An insight on the mechanism providing SC generation in conventional fibres used in optical communications such as TrueWave (TW) and single mode fibre (SMF) is reviewed. Experimental examples in anomalous and normal dispersion are provided. URFL is applied successfully to SC improving the efficiency of broadband spectrum generated.

Chapter 6 involves the study of optical soliton transmission, and the investigation of its stability and dynamics as it propagates in optical fibres. Successful experimental results are provided of the first order true soliton transmission. Further results of higher order solitons are also included. The soliton stability and propagation dynamics are investigated for different URFL cavity parameters such as cavity length, pump distribution and fibre Bragg reflectivity.

Finally, the summary and conclusions of this thesis are presented in Chapter 7.

Chapter 2

Nonlinear fibre optics

2.1 Introduction

The objective of this chapter is to provide the foundations to investigate ultralong Raman fibre lasers and their applications in photonics, in particular optical communication, supercontinuum generation and soliton transmission. A brief description of important aspects of nonlinear optics, involving mathematical foundation and basic concepts, all of them applied to optical fibres as wave guiding material, are introduced in this chapter. The mathematical description towards the nonlinear Schrödinger (NLS) equation as wave propagation in optical fibre is provided for a more clear understanding of the physical origin of the various nonlinear phenomena mentioned in this thesis. It's not the objective of this work to present an exhaustive and precise mathematical approach to the derivation of the wave propagation in optical fibres for high intensity optical signals. A more thorough mathematical description of the NLS equation can be found in the literature [29][30][31][32][33][34].

Some of the nonlinear processes mentioned in this thesis, such as supercontinuum generation or signal amplification, are the result of combined nonlinear effects. Group velocity dispersion (GVD), self-phases modulation (SPM), cross-phase modulation (XPM), four wave mixing (FWM), modulation instability (MI) and Raman scattering are the list, although not exhaustive, of the main concepts introduced in this chapter as general background. These and other concepts such optical solitons or soliton fission will be explained in later chapters as required.

An initial introduction to optical fibres and their characteristics such as number of guided modes or the optical loss introduces this chapter, giving the context of the optical guiding material used through this work.

2.2 Optical fibres

Optical fibre is one of the main media used to transmit information within the telecommunication context, but also, it has become one of the most versatile and flexible medium to propagate, generate, guide and deliver lightwaves signals in other fields, with applications on the industrial, medical and scientific sectors.

One of the most basic types of optical fibres, as defined in the general literature, [31][32][33][34][35][36], is called step index fibre. It consists of a cylindrical glass core enclosed by a cladding layer. The cladding layer can be also externally protected by a surrounding jacket layer.

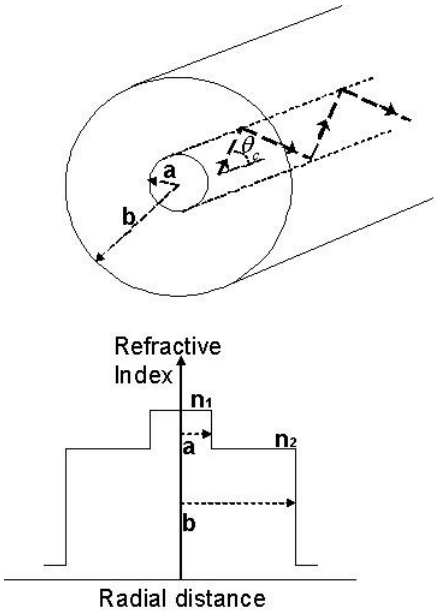

Figure 2.2.1: Step Index Fibre.

The core index n_1, with radius **a**, has a slightly higher value than the cladding index n_2, with radius **b**. The difference between refractive indexes allows guiding of the light along the length of the optical fibre core by the principle of internal reflection.

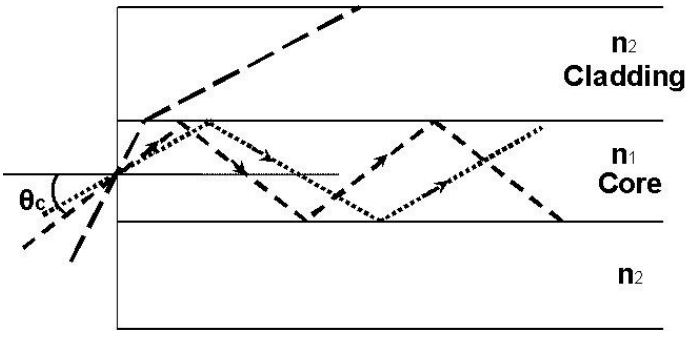

Figure 2.2.2: Propagation angle.

Only light rays with propagation angles equal or lower than the critical angle, θ_c, will be guided and transmitted along the length of the fibre.

$$\theta_c = \arcsin\left(\frac{n_2}{n_1}\right). \qquad \textbf{2.2.1}$$

There are also other types of optical fibres, where the core index decreases gradually, with parabolic shape instead of a single step. Those are called graded index fibre [37]. More recent types of fibres are those called holey fibres or photonic crystals, where the cross-section of the fibre contains microstructures specially designed to produce structural changes and affect particular parameters and properties of the fibre [38][39].

Although the optical fibres are built generally with silica glass, SiO_2, doping from other materials can be introduced in the core and/or the cladding to change its refractive index. There are two main parameters to characterise an optical fibre, the relative core-cladding index difference, given by [33]

$$\Delta = \left(n_1 - n_2\right)\Big/ n_1 \ , \qquad \textbf{2.2.2}$$

and the dimensionless V number that indicates the number of modes supported by a fibre and it's defined as [33]

$$V = \frac{2\pi a}{\lambda_0} NA \, , \qquad \textbf{2.2.3}$$

where a is the core radius and λ_0 is the wavelength of the light. The numerical aperture, NA, is given by

$$NA = \left(n_1^2 - n_2^2\right)^{1/2} \approx n_1\sqrt{2\Delta} \, . \qquad \textbf{2.2.4}$$

The V number can express the number of modes, M, guided along a multimode fibre when V is large [33]. Each mode corresponds to an individual electromagnetic field distribution of the light ray across the fibre.

$$M \approx \frac{V^2}{2} . \qquad \textbf{2.2.5}$$

This means that an optical fibre is single mode for

$$V \leq 2.405 . \qquad \textbf{2.2.6}$$

In practice, the core radius for single mode fibre in the 1.5μm region discussed in this thesis, is less than 10μm. The core radius for multimode fibre is typically 25μm. The

cladding radius has a standard value of 62.5μm for both single mode and multimode fibres [31]. The refractive index lies between the values 1.45 and 1.55 [40].

The loss in an optical fibre is a relevant parameter since it limits the maximum transmission length of an optical signal along the fibre without any type of amplification. It can be quantified by measuring the optical power launched, P_0, in a fibre of length L and the transmitted optical power at the end of the fibre, P(L). The relation can be expressed as

$$P(L) = P_0 e^{(-\alpha L)}, \qquad \textbf{2.2.7}$$

where α is the attenuation constant. It is customary to express the attenuation constant in units of dB/km

$$\alpha_{dB} = \frac{10}{L} \log\left[\frac{P_0}{P(L)}\right]. \qquad \textbf{2.2.8}$$

Therefore a drop in optical power of 20% and 50% correspond to 1dB and 3dB respectively. And 0.2dB/km loss corresponds to a transmission of more than 95.5% per kilometre of the launched optical power. The attenuation of the fibre is wavelength and material dependent. The two main intrinsic factors contributing to the fibre loss are Rayleigh scattering and material absorption.

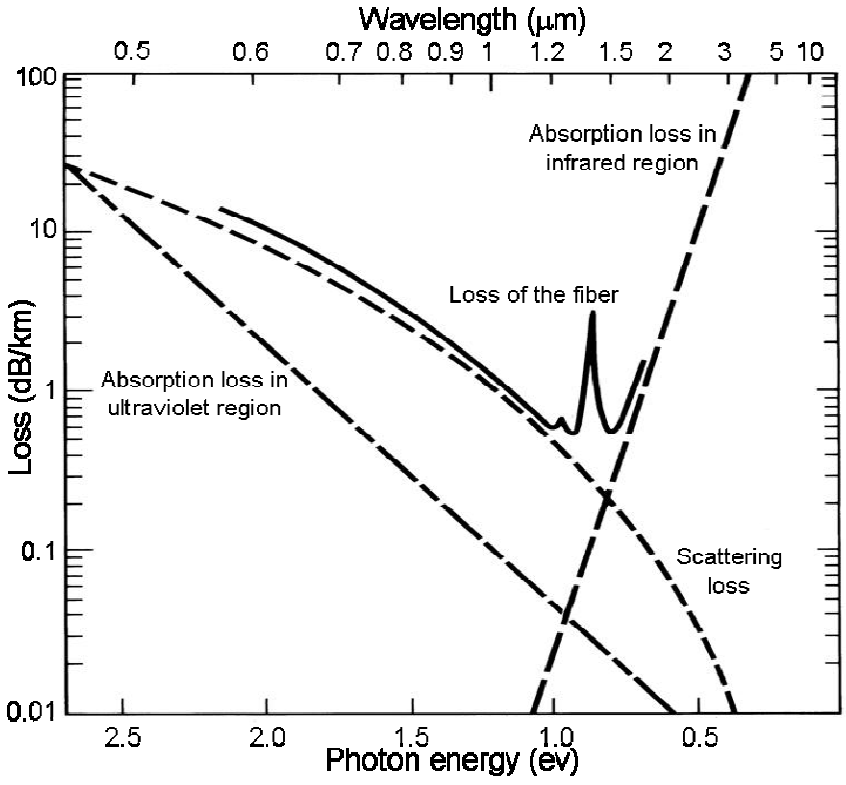

Figure 2.2.3: Absorption and scattering losses in fibre [33].

Silica is an amorphous material and therefore suffers from structural disorder. The outcome is random fluctuations of the refractive index through the material that will act as scattering centres. These local fluctuations scatter light in all directions and hence result in intrinsic fibre loss. This scattering is known as Rayleigh scattering and its contribution is proportional to λ^{-4} [33][41], thus the Rayleigh scattering loss dominates at short wavelengths.

Silica glass absorbs in the ultraviolet and far-infrared regions. The absorption in the ultraviolet region is due to electronic and molecular transitions, while lattice transitions are responsible for the absorption in the far-infrared beyond 2μm. The absorption peaks on the 0.5 to 2μm window are due to the OH^- impurities in the fibre. Special care is taken during the fibre fabrication process to ensure very low levels of OH^- impurities [42].

The different types of absorptions and Rayleigh scattering are shown on Figure 2.2.3. A typical loss value for single mode silica fibre at 1.55μm is 0.2dB/km, with a major contribution from the Rayleigh scattering. However research to develop specific fibres with very low loss among other properties [43][44] is currently active. Other external factors contributing to the loss of the fibre are bends, splices and, in general, any connection between fibres. The loss contribution from material absorption, scattering loss and the absorption of OH^- impurities leave three main working windows where the attenuation is lower. These three windows, around 850nm, 1300nm and 1550nm respectively, are the primary wavelengths for telecommunication transmission.

Optical signals outside the telecommunication windows are expected to experience a severe drop in power when using optical fibre as transmission medium. However the losses can be manageable when using relatively short lengths of fibre to deliver the optical signal locally. Another fact is that the bandwidth or wavelength range of the telecommunication windows is limited by the absorption peaks and the material absorption on the far-infrared region.

2.3 Fibre nonlinearities

As the launch power into the fibre increases, the signal intensity increases and the nonlinear effects in optical fibres become more significant. Nonlinear effects can arise from the nonlinear electric polarisation of bound electrons in silica. The intense light interacts with the dielectric medium, whose response results in the change of the refractive index with the light intensity.

The origin of the nonlinear response can be understood by considering the influence of incident light over the medium properties. The induced polarisation **P**, in function of the spatial coordinates **r** and time t, from the electric dipoles in the electric field **E** is

$$\boldsymbol{P}(\boldsymbol{r},t)=\varepsilon_0\left[\boldsymbol{\chi}^{(1)}\cdot\boldsymbol{E}+\boldsymbol{\chi}^{(2)}:\boldsymbol{EE}+\boldsymbol{\chi}^{(3)}\vdots\boldsymbol{EEE}+....\right], \qquad \textbf{2.3.1}$$

where ε_0 is the vacuum permittivity and $\boldsymbol{\chi}^{(j)}$, (j=1,2,3,..) is the jth order susceptibility tensor. The first order nonlinear susceptibility tensor, $\boldsymbol{\chi}^{(1)}$, corresponds to the linear part of the polarisation. The second order nonlinear effects, related to $\boldsymbol{\chi}^{(2)}$, vanish in fused silica as SiO_2 is a centrosymmetric molecule. The lowest order nonlinear effect in optical fibre originates from the third order susceptibility, $\boldsymbol{\chi}^{(3)}$, which is responsible for third harmonic generation, four wave mixing and nonlinear refraction. As the two first effects require phase matching condition, most of the nonlinear effects are originated from nonlinear refraction.

The refractive index in a fibre is intensity dependent as result of the third order susceptibility contribution [31][32].

$$\tilde{n}(\omega,|\boldsymbol{E}|^2)=n(\omega)+n_2|\boldsymbol{E}|^2, \qquad \textbf{2.3.2}$$

where $n(\omega)$ is the linear part, its value is well approximated by the Sellmeier equation [45], which takes into account the resonance frequencies, ω, of the fused silica,

$$n^2(\omega)=1+\sum_{j=1}^{m}\frac{B_j\omega_j^2}{\omega_j^2-C_j}, \qquad \textbf{2.3.3}$$

with B_i and C_i as the Sellmeier coefficients. And n_2 is the nonlinear refractive index coefficient or optical Kerr coefficient. For simplification, the optical fibres are considered isotropic, uniform in all directions. Therefore the relation between **P** and **E** is independent of the direction of the vector **E.** The susceptibility tensors can be reduced to a scalar quantity and the optical Kerr coefficient expressed as

$$n_2=\frac{3}{8n}\chi^{(3)}. \qquad \textbf{2.3.4}$$

The optical Kerr effect is a self-induced effect in which the phase velocity of the wave depends on the wave's own intensity. The optical Kerr effect condition can be expressed by the following relation,

$$\Delta n(\omega,|\boldsymbol{E}|^2)=n_2|\boldsymbol{E}|^2. \qquad \textbf{2.3.5}$$

The optical Kerr effect causes self-modulation and self-focusing of the optical field. It manifests itself as a self-induced phase and frequency-shift of a pulse of light as it travels through a medium. Also, this self induced refractive index variation is responsible for the nonlinear optical effect of modulation instability, an interaction between high intensity signal and background noise that breaks up a continuous wave signal in a stream of pulses.

The optical Kerr effect together with anomalous dispersion can induce soliton formation, as it will be illustrated in a later chapter. The value of the Kerr coefficient, n_2, is very small in most of the materials and for silica fibre is of the order of $2.3\text{x}10^{-16}\text{cm}^2\text{W}^{-1}$. It's wavelength dependent and sensitive to polarisation.

The intensity dependence of the refractive index leads to self-phase modulation (SPM) and cross-phase modulation (XPS). Self-phase modulation refers to the self-induced phase shift experienced by an optical field during its propagation in optical fibres. Among other things, SPM is responsible for spectral broadening of ultrashort pulses. The change in phase on the optical field is defined as

$$\Delta\phi = \tilde{n}k_0 L = \left(n + n_2 |E|^2\right)\frac{2\pi}{\lambda_0}L \ , \qquad \textbf{2.3.6}$$

where L is the fibre length. The intensity dependent nonlinear phase shift due to SPM is

$$\Delta\phi_{NL} = n_2 \frac{2\pi}{\lambda_0} L|E|^2. \qquad \textbf{2.3.7}$$

Cross-phase modulation refers to the nonlinear shift of an optical field induced by another field having a different wavelength, direction or state of polarisation. Among other things, XPM is responsible for asymmetric spectral broadening of co-propagating optical pulses. If two optical fields at frequencies ω_1 and ω_2 , polarized along the x axis, propagate simultaneously inside the fibre and the total electric field **E** given by

$$\boldsymbol{E} = \frac{1}{2}\boldsymbol{x}\left[E_1 \exp\left(-i\omega_1 t\right) + E_2 \exp\left(-i\omega_2 t\right) + c.c.\right], \qquad \textbf{2.3.8}$$

where c.c. stands for complex conjugate. Then, the nonlinear phase shift for the field at ω_1 is given by

$$\Delta\phi_{NL} = n_2 \frac{2\pi}{\lambda_0} L\left(|E_1|^2 + 2|E_2|^2\right), \qquad \textbf{2.3.9}$$

where the terms $|E_1|^2$ and $2|E_2|^2$ correspond to SPM and XPM respectively. These two nonlinear effects are mentioned in a later chapter dedicated to supercontinuum generation. In particular, the effect of self-phase modulation, crucial to soliton formation, will be expanded later in this chapter.

2.4 Wave propagation in optical fibres

To analyse the impact of the nonlinear phenomena in optical fibres, one needs to understand how a light wave propagates in an optical fibre. The objective of this section is to show that is possible to derive the nonlinear Schrödinger equation that governs the dynamics of signal propagation in the optical fibres. The details of the derivation of the nonlinear Schrödinger equation can be found elsewhere [31][32][36][46][47]. Here, we provide the main relations and concepts leading towards the derivation of the nonlinear Schrödinger equation for our particular case, a signal propagation in conventional optical fibres.

Initially we will consider propagation in a linear dispersive media and then we will include the nonlinear components. We shall start by applying the well known Maxwell's equations to a medium free of charges such as an optical fibre

$$\nabla \times \mathbf{E} = -\frac{\partial \mathbf{B}}{\partial t}, \tag{2.4.1}$$

$$\nabla \times \mathbf{H} = \frac{\partial \mathbf{D}}{\partial t}, \tag{2.4.2}$$

$$\nabla \cdot \mathbf{D} = 0, \tag{2.4.3}$$

$$\nabla \cdot \mathbf{B} = 0, \tag{2.4.4}$$

where $\mathbf{D} = \varepsilon_0 \mathbf{E} + \mathbf{P}$ and $\mathbf{B} = \mu_0 \mathbf{H} + \mathbf{M}$, and **D**, **E**, **B** and **H** represent the electric flux density, electric field intensity, magnetic flux density and magnetic field intensity respectively. **P** and **M** are the induced electric and magnetic polarization. The vacuum permittivity, ε_0, and the free space permeability , μ_0, are related to the speed of light in vacuum, c, by the relation $c^2 = 1/\varepsilon_0\mu_0$. **M**=0 for nonmagnetic media such as optical fibres. To establish a wave equation we apply the curl operator at both sides of Equation 2.4.1 with the corresponding substitutions, obtaining

$$\nabla \times \nabla \times \mathbf{E} = -\varepsilon_0 \mu_0 \frac{\partial^2 \mathbf{E}}{\partial t^2} - \mu_0 \frac{\partial^2 \mathbf{P}}{\partial t^2}, \tag{2.4.5}$$

where $\boldsymbol{P}(\boldsymbol{r},t) = \boldsymbol{P}_L(\boldsymbol{r},t) + \boldsymbol{P}_{NL}(\boldsymbol{r},t)$. In a homogeneous medium with local medium response to external excitation, the relation $\nabla \cdot \mathbf{D} = 0$ implies that $\nabla \cdot \boldsymbol{E} = 0$ as well and considering the vector identity $\nabla \times \nabla \times \mathbf{E} = \nabla(\nabla \cdot \mathbf{E}) - \nabla^2 \mathbf{E}$, the nonlinear wave equation can be expressed by

$$\nabla^2 \mathbf{E}(\boldsymbol{r},t) = \varepsilon_0 \mu_0 \frac{\partial^2 \mathbf{E}(\boldsymbol{r},t)}{\partial t^2} + \mu_0 \frac{\partial^2 \mathbf{P}_L(\boldsymbol{r},t)}{\partial t^2} + \mu_0 \frac{\partial^2 \mathbf{P}_{NL}(\boldsymbol{r},t)}{\partial t^2}. \qquad \textbf{2.4.6}$$

It describes the nonlinear propagation of light in a dielectric and homogeneous medium.

2.4.1 Linear dispersive propagation

The complexity of Equation 2.4.6 requires several simplifying approximations. Initially we will head towards a more simplified model of the wave propagation corresponding to the linear propagation of an optical field in a dispersive and homogeneous medium. As the nonlinear effects are relatively weak in silica optical fibres, a major simplification is the treatment of the nonlinear polarization as a small perturbation to the induced polarization, $|\boldsymbol{P}_{NL}| << |\boldsymbol{P}_L|$. Therefore we can consider $\boldsymbol{P}_{NL} = 0$ and the wave Equation 2.4.6 can be expressed as

$$\nabla^2 \mathbf{E}(\boldsymbol{r},t) = \varepsilon_0 \mu_0 \frac{\partial^2 \mathbf{E}(\boldsymbol{r},t)}{\partial t^2} + \mu_0 \frac{\partial^2 \mathbf{P}_L(\boldsymbol{r},t)}{\partial t^2}, \qquad \textbf{2.4.7}$$

where

$$\mathbf{P}_L(\boldsymbol{r},t) = \varepsilon_0 \int_{-\infty}^{t} \chi^{(1)}(t-t') \cdot \boldsymbol{E}(\boldsymbol{r},t') dt'. \qquad \textbf{2.4.8}$$

As Equation 2.4.7 is linear in **E** and the permittivity, ε, is a function of frequency, ω, it is simpler to work in the Fourier domain, thus

$$\nabla^2 \tilde{\mathbf{E}}(\boldsymbol{r},\omega) + \varepsilon(\omega) \frac{\omega^2}{c^2} \tilde{\mathbf{E}}(\boldsymbol{r},\omega) = 0, \qquad \textbf{2.4.9}$$

where $\tilde{\mathbf{E}}(\boldsymbol{r},\omega)$ is the Fourier transform of $\mathbf{E}(\boldsymbol{r},t)$ defined by

$$\tilde{\mathbf{E}}(\boldsymbol{r},\omega) = \frac{1}{2\pi} \int_{-\infty}^{\infty} \boldsymbol{E}(\boldsymbol{r},t) \exp(i\omega t) dt, \qquad \textbf{2.4.10}$$

and the frequency dependent dielectric constant is defined as $\varepsilon(\omega) = 1 + \tilde{\chi}^{(1)}(\omega)$, where $\tilde{\chi}^{(1)}(\omega)$ is the Fourier transform of $\chi^{(1)}(t)$. The frequency dependent dielectric constant can

be related to the refractive index, $n(\omega)$, and the absorption coefficient, $\alpha(\omega)$ by the definition $\varepsilon = (n + i\alpha c/2\omega)^2$.

Therefore,

$$n(\omega) = 1 + \frac{1}{2}\mathrm{Re}\left[\tilde{\chi}^{(1)}(\omega)\right], \qquad \textbf{2.4.11}$$

$$\alpha(\omega) = \frac{\omega}{nc}\mathrm{Im}\left[\tilde{\chi}^{(1)}(\omega)\right], \qquad \textbf{2.4.12}$$

where Re and Im stands for real and imaginary parts respectively. Hence the wave equation for a linear and non-dispersive media such as optical fibres can be expressed as

$$\nabla^2\tilde{\mathbf{E}}(\boldsymbol{r},\omega) + n^2(\omega)\frac{\omega^2}{c^2}\tilde{\mathbf{E}}(\boldsymbol{r},\omega) = 0. \qquad \textbf{2.4.13}$$

It's convenient to define the propagation constant k for a dispersive medium as

$$k(\omega) = n(\omega)\omega/c = (\omega/c)\sqrt{\varepsilon(\omega)} = k_0\sqrt{1+\tilde{\chi}^{(1)}(\omega)}, \qquad \textbf{2.4.14}$$

where $k_0 = \omega/c$ is the wave number in vacuum and we can obtain the Helmholtz equation for the electric field

$$\nabla^2\tilde{\mathbf{E}}(\boldsymbol{r},\omega) + k^2(\omega)\tilde{\mathbf{E}}(\boldsymbol{r},\omega) = 0. \qquad \textbf{2.4.15}$$

The above equation may be solved under a proper set of boundary conditions for a full description of the wave solutions in the optical fibre.

2.4.2 Nonlinear propagation

The starting point to study nonlinear effects in the optical field propagation in fibres is the wave equation

$$\nabla^2\mathbf{E}(\boldsymbol{r},t) = \varepsilon_0\mu_0\frac{\partial^2\mathbf{E}(\boldsymbol{r},t)}{\partial t^2} + \mu_0\frac{\partial^2\mathbf{P}_L(\boldsymbol{r},t)}{\partial t^2} + \mu_0\frac{\partial^2\mathbf{P}_{NL}(\boldsymbol{r},t)}{\partial t^2}, \qquad \textbf{2.4.16}$$

where the linear and nonlinear part of the induced polarisation are related to the electric field by

$$\boldsymbol{P}_L(\boldsymbol{r},t) = \varepsilon_0\int_{-\infty}^{t}\chi^{(1)}(t-t')\cdot\boldsymbol{E}(\boldsymbol{r},t')dt', \qquad \textbf{2.4.17}$$

$$\boldsymbol{P}_{NL}(\boldsymbol{r},t)=\varepsilon_0\int_{-\infty}^{t}\chi^{(3)}\left(t-t',t-t'',t-t'''\right):\boldsymbol{E}(\boldsymbol{r},t')\boldsymbol{E}(\boldsymbol{r},t'')\boldsymbol{E}(\boldsymbol{r},t''')dt'dt''dt''',$$

2.4.18

We need to make the following simplifying assumptions:

As the nonlinear effects are relatively weak in silica optical fibres, the nonlinear polarization $\boldsymbol{P}_{NL}$ can be treated as a small perturbation to the linear induced polarization $\boldsymbol{P}_L$. Also the optical field is assumed to maintain its polarization along the fibre length so that a scalar approach is valid. And finally, the optical field is assumed quasi-monochromatic, i.e. the signal spectrum centred at ω_0 is assumed to have a spectral width $\Delta\omega$ such as $\Delta\omega \ll \omega_0$. This last assumption is valid for pulses as short as 0.1ps.

For the slow varying envelope approximation adopted here, the electric field can be written in the form

$$\boldsymbol{E}(\boldsymbol{r},t)=\frac{1}{2}\boldsymbol{x}\left[E(\boldsymbol{r},t)\exp\left(-i\omega_0 t\right)+c.c.\right], \qquad \textbf{2.4.19}$$

where x is the polarisation vector and $E(\boldsymbol{r},t)$ is a slow varying function of time. The induced polarisation components can be expressed in similar manner,

$$\boldsymbol{P}_L(\boldsymbol{r},t)=\frac{1}{2}\boldsymbol{x}\left[P_L(\boldsymbol{r},t)\exp\left(-i\omega_0 t\right)+c.c.\right], \qquad \textbf{2.4.20}$$

$$\boldsymbol{P}_{NL}(\boldsymbol{r},t)=\frac{1}{2}\boldsymbol{x}\left[P_{NL}(\boldsymbol{r},t)\exp\left(-i\omega_0 t\right)+c.c.\right]. \qquad \textbf{2.4.21}$$

The intensity dependence nonlinear effects can be included by assuming the following form for the third order susceptibility [48]

$$\chi^{(3)}\left(t-t',t-t'',t-t'''\right)=\chi^{(3)}R\left(t-t'\right)\delta\left(t-t''\right)\delta\left(t-t'''\right), \qquad \textbf{2.4.22}$$

where R(t) is the nonlinear response function normalised. The interaction of the light with the vibrational modes of silica, through the delay-function $R\left(t-t'\right)$, which are responsible for Raman scattering, can be included in the description. The time domain third order susceptibility, $\chi^{(3)}\left(t-t',t-t'',t-t'''\right)$, can be approximated by a product of three delta functions if only the electronic response of the material is wanted, since it is almost instantaneous, in which case one speaks of a Kerr nonlinearity. Using a slowly varying

optical field approximation and taking in account the above assumption we can obtain a simple relation for the nonlinear polarisation density as function of the electric field

$$\boldsymbol{P}_{NL}(\boldsymbol{r},t)=\varepsilon_0\varepsilon_{NL}\boldsymbol{E}(\boldsymbol{r},t)\exp(-j\omega_0 t)\,, \qquad \textbf{2.4.23}$$

where ε_{NL} is the nonelectric permittivity and is given by

$$\varepsilon_{NL}=\frac{3}{4}\chi^{(3)}\left|\boldsymbol{E}(\boldsymbol{r},t)\right|^2, \qquad \textbf{2.4.24}$$

and the wave equation in the nonlinear regime takes the form:

$$\nabla^2\mathbf{E}(\boldsymbol{r},t)-\varepsilon_0\mu_0\frac{\partial^2\mathbf{E}(\boldsymbol{r},t)}{\partial t^2}-\mu_0\frac{\partial^2\mathbf{P}_L(\boldsymbol{r},t)}{\partial t^2}=\mu_0\varepsilon_0\frac{\partial^2}{\partial t^2}\left[\varepsilon_{NL}\left(\left|\boldsymbol{E}(\boldsymbol{r},t)\right|\right)\boldsymbol{E}(\boldsymbol{r},t)\exp(-j\omega_0 t)\right]. \qquad \textbf{2.4.25}$$

Under the assumption of the slow varying envelope approximation, ε_{NL}, can be considered as a constant as the envelope of the electric field satisfy

$$\frac{\partial^2\mathbf{E}(\boldsymbol{r},t)}{\partial t^2}\approx 0\,. \qquad \textbf{2.4.26}$$

Therefore, the second-order time derivative of the nonlinear polarisation density is reduced to

$$\frac{\partial^2\mathbf{P}_{NL}(\boldsymbol{r},t)}{\partial t^2}=-\omega_0^2\varepsilon_0\varepsilon_{NL}\boldsymbol{E}(\boldsymbol{r},t)\exp(-j\omega_0 t)\,. \qquad \textbf{2.4.27}$$

Since ε_{NL} is treated as a constant, the Fourier transform of $\mathbf{P}_{NL}$ becomes

$$\widetilde{\boldsymbol{P}}_{NL}(\boldsymbol{r},\omega-\omega_0)=\varepsilon_0\varepsilon_{NL}\widetilde{\boldsymbol{E}}(\boldsymbol{r},\omega-\omega_0)\,, \qquad \textbf{2.4.28}$$

where

$$\widetilde{\mathbf{E}}(\boldsymbol{r},\omega-\omega_0)=\int_{-\infty}^{\infty}\boldsymbol{E}(\boldsymbol{r},t)\exp(-i\omega_0 t)\exp(i\omega t)dt\,. \qquad \textbf{2.4.29}$$

We can obtain the Helmholtz equation in the form

$$\nabla^2\widetilde{\mathbf{E}}(\boldsymbol{r},\omega-\omega_0)+\tilde{k}^2(\omega)\widetilde{\mathbf{E}}(\boldsymbol{r},\omega-\omega_0)=0\,, \qquad \textbf{2.4.30}$$

where the wave number is defined as

$$\tilde{k}(\omega)=\omega_0\sqrt{\mu_0\varepsilon_0\tilde{\varepsilon}(\omega)}=k_0\sqrt{\tilde{\varepsilon}(\omega)}\,. \qquad \textbf{2.4.31}$$

And the electric permittivity $\tilde{\varepsilon}(\omega)$ in the spectral domain for the nonlinear propagation of a slow varying electric field is defined as

$$\tilde{\varepsilon}(\omega)=\varepsilon(\omega)+\varepsilon_{NL}\,. \qquad \textbf{2.4.32}$$

With the linear and nonlinear components given by

$$\varepsilon(\omega) = \left(1 + \tilde{\chi}(\omega)\right), \quad \textbf{2.4.33}$$

$$\varepsilon_{NL} = \frac{3}{4}\chi^{(3)}\left|\boldsymbol{E}(\boldsymbol{r},t)\right|^2. \quad \textbf{2.4.34}$$

2.4.3 The nonlinear Schrödinger equation

The starting point for the derivation of the nonlinear Schrödinger (NLS) equation is the Helmholtz form of the wave equation as shown in previous sections. The most common method to solve the Helmholtz equation is the method of separation of variable whilst still assuming a slowly varying envelope approximation [31]. As the transmission medium is a fibre, the solution is usually represented as a combination of a function describing the mode field distribution in the fibre cross section and a function that is the slow varying wave envelope. Depending on the boundary conditions and the assumptions, we can obtain the following extended NLS equation for the signal evolution inside a fibre, where higher order nonlinear terms are included:

$$\frac{\partial Q}{\partial z} = -\frac{\alpha}{2} - i\frac{\beta_2}{2}\frac{\partial^2 Q}{\partial T^2} + \frac{\beta_3}{6}\frac{\partial^3 Q}{\partial T^3} + i\gamma|Q|^2 Q - \frac{\gamma}{\omega_0}\frac{\partial}{\partial T}\left(|Q|^2 Q\right) - i\gamma T_R Q\frac{\partial|Q|^2}{\partial T}, \quad \textbf{2.4.35}$$

where $T = t - z/v_g$ is a frame of reference moving with the pulse at the group velocity v_g at the centre wavelength. And Q is the slowly varying envelope of the electric field. z is the propagation distance. α is the fibre loss coefficient in km^{-1}. β_2 is the second order propagation constant in $ps^2\ km^{-1}$. β_3 is the third order propagation constant in $ps^3\ km^{-1}$. γ is the nonlinear coefficient $\gamma = 2\pi n_2/\lambda_0 A_{eff}$. n_2 is the nonlinear index coefficient. A_{eff} is the effective core area of fibre. λ_0 is the centre wavelength. ω_0 is the centre angular frequency and T_R is the slope of Raman gain.

The term related to β_2 refers to the chromatic dispersion, with the group velocity dispersion (GVD) proportional to β_2. Further explanation of the GVD will be given in the section. The term of β_3 relates to higher-order dispersion. It's important for ultra short pulses less than 100fs. The term $i\gamma|Q|^2 Q$ relates to simultaneous fibre nonlinearities. The other two terms left on the right hand side are delayed nonlinear response. The term

$(\gamma/\omega_0)\left(\partial\left(|Q|^2 Q\right)/\partial T\right)$ relates to self-steepening and the term $i\gamma T_R Q\left(\partial|Q|^2/\partial T\right)$ relates to self-frequency shift. The self-steepening has the effect of changing the shape of light pulses as they propagates in the fibre. The velocity of the peak pulse, group velocity, is reduced leading to an increasing slope of the trailing part of the pulse. And self-frequency shift result in an overall spectral shift towards longer wavelengths of the optical pulse.

The Equation 2.4.35 can be simplified assuming optical pulses of width $T_0 >$ 1ps with the carrier wavelength not too close to zero dispersion wavelength. Then, the parameters $1/(\omega_0 T_0)$, T_R / T_0 and the contribution of the third order dispersion become that small that can be neglected.

$$\frac{\partial Q}{\partial z} = -\frac{\alpha}{2} - i\frac{\beta_2}{2}\frac{\partial^2 Q}{\partial T^2} + i\gamma|Q|^2 Q . \qquad \textbf{2.4.36}$$

The above equation, with dispersive terms only up to the second order, is called the NLS equation in the special case of lossless medium ($\alpha \approx 0$), as it resembles the Schrödinger equation with a nonlinear potential term. Optical solitons are well known stationary solution of the Equation 2.4.36 for a lossless waveguide. Further work regarding optical solitons will be discussed in a later chapter. The NLS equation is the simplest mathematical model to describe nonlinear and dispersive propagation of optical pulses in optical fibres in the slow varying envelope approximation.

2.5 Effects in optical communications

There are effects with origin in the optical fibre loss, dispersion and the nonlinearity that are relevant in optical communications and they can affect the optical signal transmission by either limiting, modifying or enhancing some properties of the optical signal. The most important effects related to the understanding of this thesis are reviewed, introducing concepts such as group velocity dispersion (GVD), self phase modulation (SPM) or modulation instability (MI) as example. The idea is to gain enough background knowledge to understand the work presented here. A more extensive and detailed explanation of these effects can be found in the literature review [31][49][50][51][52]

2.5.1 Dispersion

Chromatic dispersion originates from finite spectral linewidth of optical sources. The different spectral components will propagate at different velocities, causing the pulse to

broaden. It results from the frequency dependence of the material refractive index and waveguide structure of the optical fibre.

The refractive index of the material is approximated by the Sellmeier equation, which can be expressed as

$$n^2(\lambda) = 1 + \frac{B_1\lambda^2}{\lambda^2 - C_1} + \frac{B_2\lambda^2}{\lambda^2 - C_2} + \frac{B_3\lambda^2}{\lambda^2 - C_3}. \qquad \textbf{2.5.1}$$

The values of the Sellmeier coefficients for fused silica, B_i and C_i, quoted for λ in micrometers are given in Table 2.5.1.

Table 2.5.1: Sellmeier coefficients for fused silica [54].

B1	B2	B3	C1	C2	C3
0.696166	0.407943	0.897479	0.004679	0.013512	97.934

The refractive index, n, and the group index, n_g, as function of the wavelength are plotted in Figure 2.5.1. The refractive index takes value around 1.45 at 1μm, varying less than one percent at either side of the wavelength spectrum and with decreasing value at longer wavelengths.

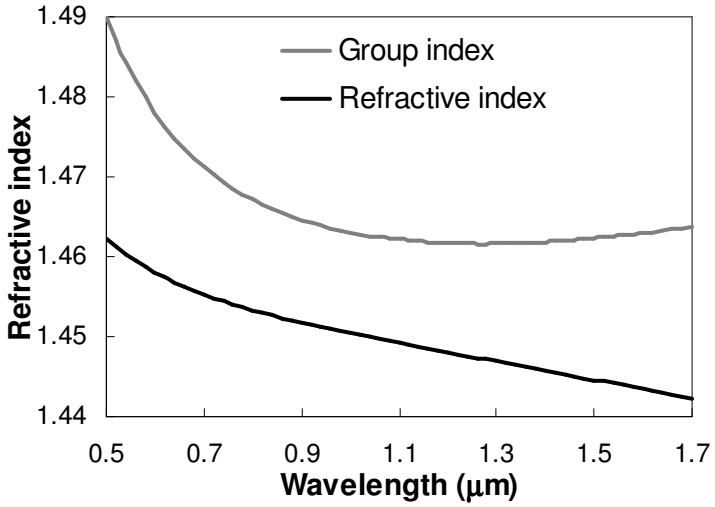

Figure 2.5.1: Refractive index n and group index n_g as function of wavelength for silica optical fibres [31]

The group index, n_g, can be calculated as

$$n_g = n - \lambda\frac{dn}{d\lambda}. \qquad \textbf{2.5.2}$$

The refractive index is related to the propagation constant $\beta(\omega)$ through the relation

$$n(\omega) = \frac{\beta(\omega)}{k_0} = \beta(\omega)\frac{c}{\omega_0}. \qquad \textbf{2.5.3}$$

The dependence of the refractive index on the spectral components results in the variation of the propagation constant β as function of frequency. To gain a better

understanding, it is customary to account for the effect of dispersion by expanding the propagation constant in Taylor series around the central frequency ω_0.

$$\beta(\omega) = \beta_0 + \beta_1(\omega-\omega_0) + \frac{1}{2}\beta_2(\omega-\omega_0)^2 + \frac{1}{6}\beta_3(\omega-\omega_0)^3 + \ldots, \qquad \textbf{2.5.4}$$

$$\text{where } \beta_j = \left[\frac{d^j\beta(\omega)}{d\omega^j}\right]_{\omega=\omega_0} \text{ (j=1,2,3,…).} \qquad \textbf{2.5.5}$$

Every coefficient β_j relates to the refractive index $n(\omega)$ satisfying the following relations:

$$\beta_0 = \frac{2\pi}{\lambda_0}, \qquad \textbf{2.5.6}$$

$$\beta_1 = \frac{1}{c}\left(n + \omega\frac{dn}{d\omega}\right) = \frac{n_g}{c} = \frac{1}{v_g}, \qquad \textbf{2.5.7}$$

$$\beta_2 = \frac{1}{c}\left(2\frac{dn}{d\omega} + \omega\frac{d^2n}{d\omega^2}\right) \simeq \frac{\omega}{c}\frac{d^2n}{d\omega^2} \simeq \frac{\lambda^3}{2\pi c^2}\frac{d^2n}{d\lambda^2}, \qquad \textbf{2.5.8}$$

where n_g is the group refractive index as defined by Equation 2.5.2, v_g is the group velocity and c is the speed of light. Each Taylor component is interpreted as follows. The first component, β_0, is the propagation constant describing the phase velocity of the optical pulse. The second term relates to the group velocity of the pulse envelope, with the first order coefficient, β_1, representing the inverse of the group velocity, v_g. The third term is responsible for the pulse broadening with the second order coefficient, β_2, representing the dispersion of the group velocity and therefore called Group Velocity Dispersion (GVD) parameter. The third order dispersion (TOD) parameter, β_3, relates to the dispersion slope. In most practical cases, this last higher order dispersion term is negligible and most of the contribution of the dispersion induced pulse broadening is due to the GVD term, proportional to β_2. The TOD parameter becomes significant only when $\beta_2 \approx 0$ or for ultrashort pulses, i.e. pulse width lower than 1ps. The dispersion parameter, D with units in ps/nm/km, is commonly used in optical fibre engineering and relates to β_2, expressed in units ps^2/Km, as

$$D = \frac{d\beta_1}{d\lambda} = -\frac{2\pi c}{\lambda^2}\beta_2. \qquad \textbf{2.5.9}$$

Figure 2.5.2 shows the variation of the dispersion parameter, D, versus wavelength for several commercial optical fibres available in our laboratory during the research period when this work was carried out. The single mode fibre SMF-28 and LEAF, meaning large effective area fibre, are commercially available from Corning. TrueWave (TW) is a fibre available from Lucent. The dispersion shifted fibre (DSF) is a type of single mode fibre tailored to shift the zero dispersion wavelength from 1300nm to 1550nm. The total dispersion is a combination of the material dispersion, fused silica in our case, and the waveguide dispersion which depends on fibre design characteristics such as refractive index, cross-section profile.

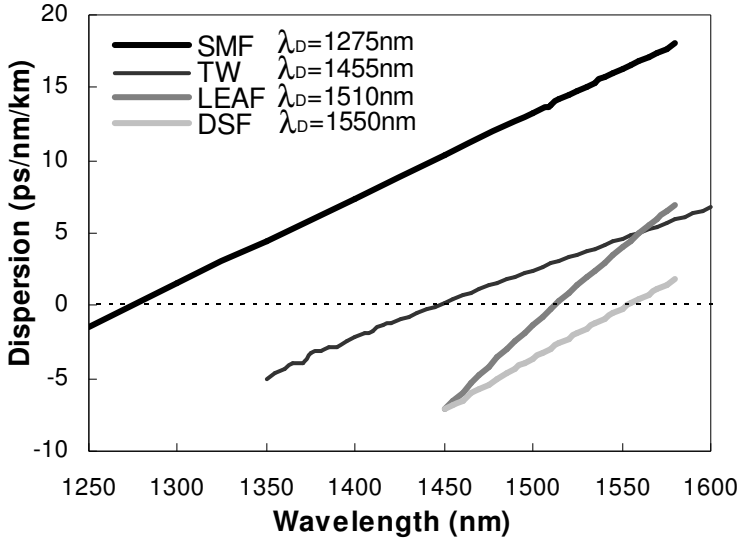

Figure 2.5.2: Dispersion parameter D versus wavelength for several commercial optical fibres [55].

The wavelength at which D=0, denoted as the zero-dispersion wavelength λ_D, separates the dispersion in two regions. The region where D is negative (β_2>0) is designated as normal dispersion region. In this region the lower frequencies (red components) of an optical pulse travels faster than the higher frequencies (blue components). The region for D positive (β_2<0) is called anomalous dispersion regime. In the anomalous dispersion regime the higher frequencies (blue components) travels faster than the lower frequencies (red components).

The effect of GVD on optical pulses causes the different spectral components of the optical pulse to propagate at different velocities. In absence of nonlinearities, the GVD changes the phases of each spectral component of the pulse by an amount that depends on both the frequency and the propagation distance. The result is a linear chirp across the pulse that will affect the pulse spectrum, eventually inducing a temporal pulse broadening. It's

convenient to introduce the dispersion length, L_D, as defined in most of the literature [31][32][33][34][35]. The dispersion length L_D provides the length scale over which dispersive effect become important for pulse evolution.

$$L_D = \tau_0^2 / |\beta_2|, \qquad \textbf{2.5.10}$$

where τ_0 is the pulse width, which relates to its full width at half maximum (FWHM). For propagation lengths comparable or longer than the dispersion length, the dispersion dominant regime is important and the GVD will have a severe impact on the pulse propagation.

2.5.2 Self phase modulation

Self phase modulation (SPM) is a nonlinear process with origins in the optical Kerr effect and which produces a time varying phase of the light pulse as it propagates along the fibre. As already mentioned previously by Equation 2.3.2, the refractive index is dependent on the optical intensity. That relation can be rewritten as a function of the optical power per effective area.

$$\tilde{n}(\omega, | P) = n(\omega) + n_2 \frac{P(t)}{A_{eff}}, \qquad \textbf{2.5.11}$$

where $n(\omega)$ is the ordinary refractive index, n_2 is the nonlinear refractive index coefficient, A_{eff} is the effective core area of the fibre, and P is the power of the optical signal. The relation expressed in Equation 2.5.11 indicates the phenomenon that converts power fluctuations into phase fluctuations in the same optical wave, which is commonly called self phase modulation. The change in phase on the optical field after travelling a total length L is defined as

$$\Delta\phi(t) = \tilde{n} k_0 L = \left(n + n_2 \frac{P(t)}{A_{eff}} \right) \frac{2\pi}{\lambda_0} L. \qquad \textbf{2.5.12}$$

The intensity dependent nonlinear phase shift due to SPM, shown previously by in Equation 2.3.7, can be expressed as a function of the optical power as

$$\Delta\phi_{NL}(t) = n_2 \frac{2\pi}{\lambda_0} \frac{L}{A_{eff}} P(t). \qquad \textbf{2.5.13}$$

The previous relation indicates that the optical signal power modifies its own phase with the optical phase being proportional to the fibre length, and the phase shift varies with time for the optical pulse signal. If we want to take into account the absorption of the medium, we can replace the fibre length L by an effective length L_{eff} [56]

$$L_{eff} = \int_0^L le^{-\alpha l} dl = \left[1 - \exp(1 - \alpha L)\right] / \alpha . \qquad \textbf{2.5.14}$$

In the absence of fibre losses α, the fibre loss coefficient, is equal to zero and $L_{eff} = L$. Otherwise the value of the effective length, L_{eff}, is smaller than L. And the phase shift induced by SPM takes the form

$$\Delta\phi_{NL}(t) = n_2 \frac{2\pi}{\lambda_0} \frac{L}{A_{eff}} P(t) = \gamma L_{eff} P(t), \qquad \textbf{2.5.15}$$

where γ is the nonlinear coefficient defined as

$$\gamma = \frac{2\pi n_2}{\lambda_0 A_{eff}}. \qquad \textbf{2.5.16}$$

The instantaneous frequency of the wave, defined as the variation of the phase with time, at the output of the fibre will be

$$\omega(t) = \frac{\partial\phi(t)}{\partial t} = \frac{2\pi}{\lambda_0} \frac{\partial\Delta n}{\partial t} L_{eff} - \omega_0 . \qquad \textbf{2.5.17}$$

From Equation 2.5.15 and Equation 2.5.17, it can be deduced that the wave undergoes an additional frequency shift and, subsequently, a frequency shift respect to the optical frequency ω_0 due to the Kerr effect. The frequency shift is proportional to the optical power and it is responsible for spectral broadening.

$$\delta\omega(t) = -\frac{\partial\Delta\phi}{\partial t} = -\gamma L_{eff} \frac{\partial P(t)}{\partial t}. \qquad \textbf{2.5.18}$$

When a pulse undergoes SPM, its leading edge (∂P(t)/∂t > 0) is downshifted in frequency while its trailing edge (∂P(t)/∂t < 0) is up shifted. The frequency of the optical signal undergoes a frequency shift from its initial value. This effect is known as frequency chirping, in which different parts of the pulse undergo different phase change [33]. Since this effect depends heavily on the signal intensity, SPM has more effect on high intensity signal pulses. Initially, for unchirped pulses, SPM only introduces a distortion in the pulse spectrum, whereas the pulse shape remains undistorted. However, this is not the case when

GVD becomes important, because the SPM induces a nonlinear chirp across the pulse that GVD will translate it into a pulse broadening or compression.

In the normal dispersion regime, the edges of frequencies which experienced higher shifts tend to move away from the centre of the pulse. The edges of frequencies which red spectrum components have a higher velocity than the blue spectrum components, and thus the front of the pulse moves faster than the back, therefore the pulse undergoes a temporal broadening (i.e. spectral compression). In the anomalous dispersion regime, the rising part propagates more slowly than the falling part and the pulse undergoes temporal compression (i.e. spectral broadening). This produces higher refractive index at the peak of the pulse when compared to the edges of the pulse. There is a special case in the anomalous dispersion regime where the interplay between SPM and GVD will support a stationary pulse, called a soliton, which can propagate undistorted over long distance [57]. Experimental examples of soliton propagation in optical fibre [21][26] will be presented in this thesis in a later chapter.

2.5.3 Cross phase modulation

The origin of cross phase modulation (XPM) is similar to SPM, the material refractive index is dependent on the optical field intensity that travels along the medium. However in this case, two or more optical waves are co-propagating inside the fibre and they interact with each other through their nonlinearities, so the refractive index experienced by each optical wave is not only dependent on its intensity but also dependent on the intensity of the other co-propagating waves, as shown by Equation 2.3.9. The general expression for the total nonlinear phase shift in the optical wave induced by SPM and XPM can be expressed as

$$\Delta\phi_{NL} = \gamma L_{eff}\left(P_j + 2\sum_{m\neq j} P_m\right), \qquad \textbf{2.5.19}$$

where P_j and P_m correspond to the optical power for the optical wave j, and the co-propagating waves m, with $m \neq j$. The factor 2 indicates that XPM is twice as effective as SPM for the same amount of optical power. Cross phase modulation can be a limiting effect in optical communication when using wavelength division multiplexing (WDM) to combine multiple channels into one single fibre. Among other things, XPM is responsible for asymmetric spectral broadening of co-propagating optical pulses.

2.5.4 Four wave mixing

Four wave mixing (FWM) is a nonlinear process with origin in the third order nonlinear susceptibility $\chi^{(3)}$ through the optical Kerr effect. Generally speaking FWM in optical fibre occurs when the interaction between three waves give rise to a forth wave in the signal with different centre of frequency to the others. The relation among the frequencies is described by the frequency-matching condition for FWM [36].

$$\omega_1 + \omega_2 = \omega_3 + \omega_4 . \qquad \textbf{2.5.20}$$

Assuming that k_1, k_2 and k_3 are the wavevectors of the optical waves with centre of frequency ω_1, ω_2 and ω_3 respectively, the corresponding wavevector for the optical wave ω_4 is k_4 such as

$$k_1 + k_2 = k_3 + k_4 . \qquad \textbf{2.5.21}$$

The above equation describes the phase matching condition. Equations, 2.5.20 and 2.5.21 represent conservation of energy and momentum respectively. In the partially degenerative case where two of the waves have the same frequency, $\omega_3 = \omega_4 \equiv \omega_0$, the frequencies are related by

$$\omega_1 + \omega_2 = 2\omega_0 . \qquad \textbf{2.5.22}$$

The frequencies ω_1 and ω_2 are symmetrically located respect the central frequency ω_0 like the sidebands of an amplitude modulated sine wave in the case of modulation instability effect, or the Stokes and anti-Stokes frequencies in Raman scattering [36].

In the practical side, the effect of FWM in optical fibre communications can be seriously damaging, limiting in particular the capacity of wavelength-division multiplexing (WDM) systems, where multiple optical wavelengths are spaced at equal intervals or channel spacing. The interference FWM causes in WDM systems is known as interchannel crosstalk. The effects of FWM are pronounced with decreased channel spacing of wavelengths and at high signal power levels. High chromatic dispersion decreases FWM effects, as the signals lose coherence. FWM can be mitigated by using uneven channel spacing or fibre that increases dispersion.

2.5.5 Modulation instability

Modulation instability (MI) is a nonlinear phenomenon that has been observed nearly simultaneously and with independence in different areas of physics [58], such as convection, water waves, plasma physics and nonlinear optics, just to name a few. The effect of modulation instability can be explained as the interaction between a strong continuous wave at frequency ω and small sidebands $\omega \pm \Omega$. It is a particular case of four wave interaction, two waves at ω creates the sidebands at $\omega \pm \Omega$ (Stokes and anti-Stokes). In the case of optical fibre the steady state of the optical wave becomes unstable as the result of the interplay between anomalous group velocity dispersion and self phase modulation. The MI is enhanced by the interaction of the optical signal with the optical noise background, which provides seeding perturbations over a broad range of frequencies. The sidebands are exponentially amplified with distance by four-wave mixing and they act as a pump to higher order Stokes and anti-Stokes components. This process of exponential amplification of subsequent sidebands leads to the generation of many equally spaced spectral components, which interference originates a pulse train [59].

Modulation instability in optical fibres was first predicted by Hasegawa and Brinkman in 1980 [60] and experimentally demonstrated by Tai and Hasegawa in 1986 [59]. MI manifests itself as the break up of CW radiation into a train of ultrashort pulses. In fact, since MI is described by the same conditions of existence as the stationary pulses called solitons [59][61][62], it is at the origin of higher order soliton formation under high intensity CW light pumping. MI is a fundamental process leading to supercontinuum generation from CW pump source.

The instability is strongly dependent on the frequency of the perturbation. At certain frequencies, a perturbation will have little effect, whilst at other frequencies, a perturbation will grow exponentially. Random perturbations will generally contain a broad range of frequency components, and so will cause the generation of spectral sidebands which reflect the underlying gain spectrum.

2.5.6 Raman scattering

Spontaneous Raman scattering is a nonlinear inelastic scattering effect discovered by C.V. Raman and K.S. Krishnan in 1928 [63], through which radiation propagating through a given medium gets converted to a different frequency, with the corresponding energy difference being provided or stored in the medium's molecules in the form of vibrational energy. The generated frequency shift is called the Stokes shift, if the radiation is converted

to a lower frequency, or anti-Stokes shift, if the radiation is converted to a higher frequency. The frequency shift and the shape of the gain curve are determined by the vibrational modes of the medium, and are completely characteristic of the material. The most commonly observed occurrence of the Raman effect in optical fibres, and the one we are interested in, is the Stokes shift towards lower frequencies.

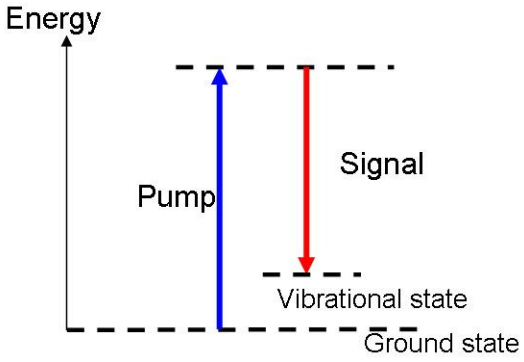

Figure 2.5.3: Energy diagram for Raman scattering

The scattering cross-section for the spontaneous Raman effect is very small. The scattering cross section per unit volume for Raman Stokes is of the order of $10^{-7}cm^{-1}$ [18][53]. In amorphous materials, Raman scattering of light occurs over a large range of frequencies because these materials present a broad vibrational spectrum. The Raman gain spectrum of silica fibre is relatively broad, ~40THz, as it's an amorphous material [64]. The peak of its frequency shift is about 13.2THz. So if a pump wave is set at 1455nm, the signal generated will be at 1550nm approximately.

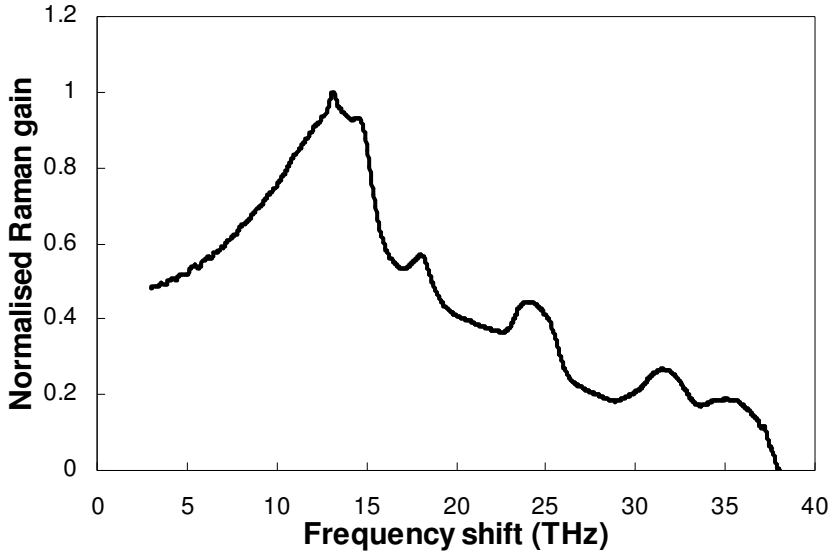

Figure 2.5.4: Experimental Raman gain spectrum for 41km SMF silica fibre

Raman scattering can be efficiently stimulated by excitation of the optical photons. This process is called stimulated Raman scattering (SRS) and it was first discovered by Woodbury and Ng in 1962 [65]. A signal photon enters a nonlinear optical medium together with a pump photon of high frequency. The signal photon stimulates the emission of a second clone signal photon, which is obtained by Stokes shifting the pump photon so that its frequency precisely matches that of the input signal photon. The energy excess of the pump photon is transferred to the vibrational modes of the medium. Compared with spontaneous Raman emission, 10% or more of the incident power can be converted into Stokes components by SRS [32].

The frequency shift and the Raman gain provided by SRS will depend on the material characteristics. Mathematically can be deduced taking in account that the third order nonlinear coefficient $\chi^{(3)}$ is in general a complex value, $\chi^{(3)} = \chi_R^{(3)} + j\chi_I^{(3)}$. Therefore, the intensity dependent self-phase modulation described by Equation 2.5.13 is also complex, as the nonlinear refractive index can be expressed as $n_2 = \left(3\eta_0 / \varepsilon_0 n^2\right)\chi^{(3)}$. The propagation phase factor, $\exp(-j\phi)$, is a combination of phase shift, $\Delta\phi$, given by [36]

$$\Delta\phi = \frac{6\pi\eta_0}{\varepsilon_0}\frac{\chi_R^{(3)}}{n^2}\frac{L}{\lambda_0 A_{eff}}P, \qquad \textbf{2.5.23}$$

and gain $\exp(g_R L/2)$, with the Raman gain coefficient proportional to the optical power and given by

$$g_R = \frac{12\pi\eta_0}{\varepsilon_0}\frac{\chi_I^{(3)}}{n^2}\frac{1}{\lambda_0 A_{eff}}P, \qquad \textbf{2.5.24}$$

with ε_0 as the permittivity of the medium and η_0 the efficiency of the Raman scattering interaction. The Raman gain coefficient, $g_R(\Omega)$, is an important parameter when characterizing Raman amplifiers [53] and it relates to the intensity of the signal generated along the length of fibre, taken as axis z, with the following relation:

$$\frac{dI_s}{dz} = g_R(\Omega) I_p I_s, \qquad \textbf{2.5.25}$$

where Ω represent the Raman shift. I_p and I_s are the intensities of the primary pump and the signal generated at the corresponding frequency shift, so called first Stokes. As the primary pump power increases, the first Stokes wave increases. Once the first Stokes reach a Raman gain threshold value it will behave as a secondary pump transferring energy at the

same frequency shift as previously. This second signal generated, twice shifted to longer wavelengths, is called the second Stokes when referring to the primary pump.

The importance of SRS is underlined as this mechanism can arise in any optical fibre and Raman amplification can occur at any frequency, ranging from 0.3 to 2μm [18] depending on the pump wavelength. An important implication is the access to wavelengths where previously was unachievable through other means. Raman scattering has many applications not only in the optical communication area; such as optical amplification, but also in other areas; as spectroscopic tool for identifying the molecular characteristics of a material or as key process in the generation of supercontinuum light sources

2.6 Conclusion

The foundation of optical fibres and nonlinear optics within the context of optical communications has been reviewed in this chapter. Basic concepts regarding the characterisation of optical fibres, such as refractive index and optical attenuation, are presented before heading into the review of optical fibre nonlinearities. The induced polarisation by high optical intensities and the third order susceptibility are in the origin of the fibre nonlinearities description.

The description of the wave propagation in optical fibres is limited initially for the linear dispersive case and then expanded to include the nonlinear term, presenting finally the nonlinear Schrödinger equation which governs the optical pulse propagation dynamics. Understanding the general or expanded nonlinear Schrödinger equation and the implication of its terms is fundamental. This relation can quantify and analyse the influence of the fibre characteristics and the initial optical signal used over the resulting propagation dynamics. Some important effects, with great impact in optical communications, are discussed briefly in this chapter.

Fibre losses have the effect of decreasing exponentially the amplitude of the signal along with propagation length. Chromatic dispersion, different spectral components travelling at different velocities, results in the broadening of the optical pulse, which can be quantify though the group velocity dispersion (GVD) term.

The refractive index dependence on the optical intensity leads towards the Kerr effect and self-phase modulation, a phase shift dependent on the intensity of the optical signal. The result is the pulse spectral broadening in both normal and anomalous dispersion regimes. In normal dispersion regimes it produces a frequency modulation of the incident field and subsequent spectral broadening. The major impact of self-phase modulation is the temporal

compression of the optical pulse. In anomalous dispersion regimes it initiates modulational instability amplification of quasi-CW fields which leads to the formation of a train of optical pulses from the interplay between the high intensity CW optical field itself and the noise background, generating optical solitons. Modulations instability is a particular case of four wave mixing, where two waves at a central frequency creates two sidebands with a frequency shifted from the central one. Four waves mixing can limit the optical communication capacity through the crosstalk, by generating a fourth frequency from the interaction of three channels with different frequencies. The main effect of Raman scattering is the frequency shift of input signal to lower frequencies. This effect was briefly introduced in this chapter and it will be expanded latter on as required in the thesis.

Chapter 3

Ultralong Raman fibre lasers

3.1 Introduction

Ultralong Raman fibre lasers (URFLs) are based in the distributed nature of Raman amplifiers, improving the optical signal-to-noise ratio along the transmission compared with other lumped amplification systems. The degradation of the signal after amplification can be quantified through the noise figure F_N, defined as the ratio of the signal-to-noise ratio before and after amplification.

$$F_N = (SNR)_{in} / (SNR)_{out}, \qquad \textbf{3.1.1}$$

where the signal-to-noise ratio (SNR) of a signal is defined as the ratio of its square-mean to its variance. Hence, the SNR of a signal with mean value $\overline{P}$ is $SNR = \overline{P}^2 / \sigma_P^2$.

Below it's shown a typical bi-directional pumped diagram of an optical communication system employing Raman amplification.

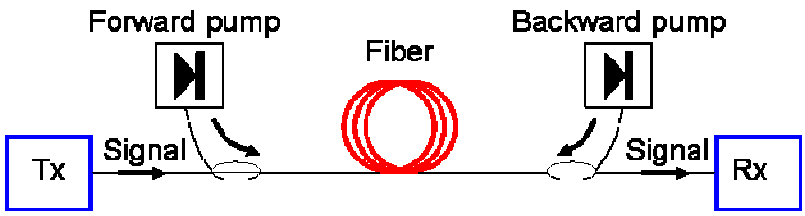

Figure 3.1.1: Raman amplification diagram

The evolution of the pump, P_P, and the signal power, P_S, along the axis of the fibre, z, for Raman amplification can be described using the following equations [53]:

$$\pm\frac{dP_P}{dz} = -\frac{\nu_P}{\nu_S} g_R P_P P_S - \alpha_P P_P, \quad \textbf{3.1.1}$$

$$\frac{dP_S}{dz} = g_R P_P P_S - \alpha_S P_S. \quad \textbf{3.1.2}$$

The initial sign (+) and (-) from Equation 3.1.1 represent the forward and backward propagation from the laser pumps. Where ν_P and ν_S are the frequencies of the pump and the signal, α_P and α_S are the attenuation coefficients and g_R the Raman gain coefficient normalized with respect to the effective area of the fibre.

Ultralong Raman fibre lasers (URFLs) make use of the simplified structure from the basic first order Raman amplification system as shown in Figure 3.1.1 but with improved performance as it will be shown later. URFLs display a series of advantages over other amplification solutions, particularly when minimum power variation along the span transmission is required, included reduced amplification of spontaneous emission noise (ASE) and virtual transparency in a wide range of frequencies. These advantages can nevertheless see themselves offset by the relative intensity noise (RIN) transfer from the pumps to the amplified signal. A numerical investigation of URFL provides a descriptive insight of the full potential of URFL for variations of their cavity design features. Solving numerically the relations that define the power and relative intensity noise evolution allow us a first approximation to the URFL optimum parameters depending on the required application.

This chapter presents two main results. On the one hand, the equations describing the intra-cavity power evolution of the URFL and some numerical simulation results that show the advantages of the URFL scheme over other amplifier structures. On the other hand, the theoretical and numerical description of the relative intensity noise transfer from the pump to the signal for the URFL.

The equations describing the evolution of the RIN transfer from the pump to the signal are presented in this chapter, together with the numerical simulation results showing the effect of different cavity design parameters on the RIN transfer value.

The theoretical and mathematical components of this chapter are based on previous work developed by J-D. Ania-Castañon[15]. The numerical simulation and analysis of the results are generated by the author of this thesis.

3.2 Ultralong Raman fibre laser

The basic scheme for an ultralong Raman fibre laser involves a conventional optical fibre span of several kilometres length confined between a high reflectivity pair of fibre Bragg gratings (FBGs) with central wavelength around the Raman shift for the optical fibre, about 13.2THz. The system is bi-directionally pumped through wavelength division multiplexing (WDM) integrated into the system after the FBGs. The transmitted signal is introduced as the input and measured as the output as shown on Figure 3.2.1. The wavelength of the pump is such that the transmitted signal is about the second Stokes of the pump.

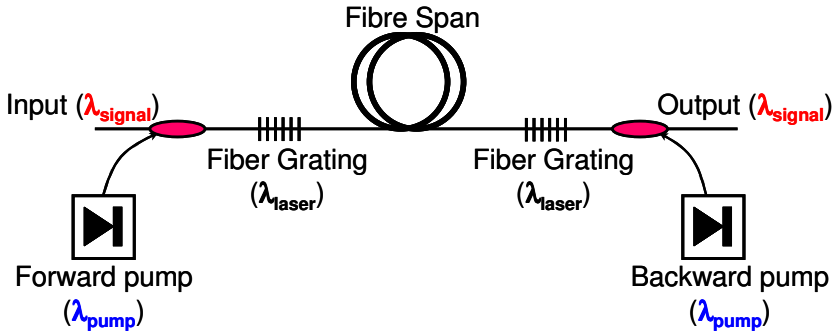

Figure 3.2.1: Basic ultralong Raman fibre laser scheme.

As the pump power introduced into the system is increased, the first Stokes shifted wave is generated within the optical fibre. The wavelength range of the first Stokes generated is around the centre wavelength of the pair of FBGs set at each end of the fibre span. Therefore a laser cavity at the same wavelength the FBGs is built, using them as reflectors. If the pump power keeps increasing, then the first Stokes is confined within the pair of FBGs, it increases and at some point it will generate a second Stokes, behaving as a secondary pump. The range of wavelengths of the second Stokes wave is around the transmitted signal. By using the appropriate pump ratio it is possible to generate enough power at the second Stokes to compensate for the optical fibre losses and measure the same signal level at the output as the input.

As an example, the intra-cavity power profile corresponding to the case of quasi-lossless transmission for 100km span length is shown on Figure 3.2.2. The input signal is 1mW (0dBm) and the URFL is set with FBGs at 90% reflectivity. The pump ratio for the primary pump sources is symmetric, 50% forward and 50% backward pump power. The initial power required from each pump source is 0.8W. And their power profile decreases exponentially along the length of the fibre. The intra-cavity power profile for the forward and backward first Stokes is symmetric. The first Stokes initially increases as the power of the primary pump drops and transfers energy to the first Stokes once in the fibre, reaching to a maximum. Then the power profile of the first Stokes drops as it goes along the length of the

fibre span towards a minimum value. At some point closer to the entrance of the other primary pump, the power profile of the first Stokes increases up to the same initial level. The power profile variation of the signal is minimum, with a value of 2.72dB, for the case of 100km and 90% FBGs reflectivity. Furthermore, the output power of the signal is the same as the input signal.

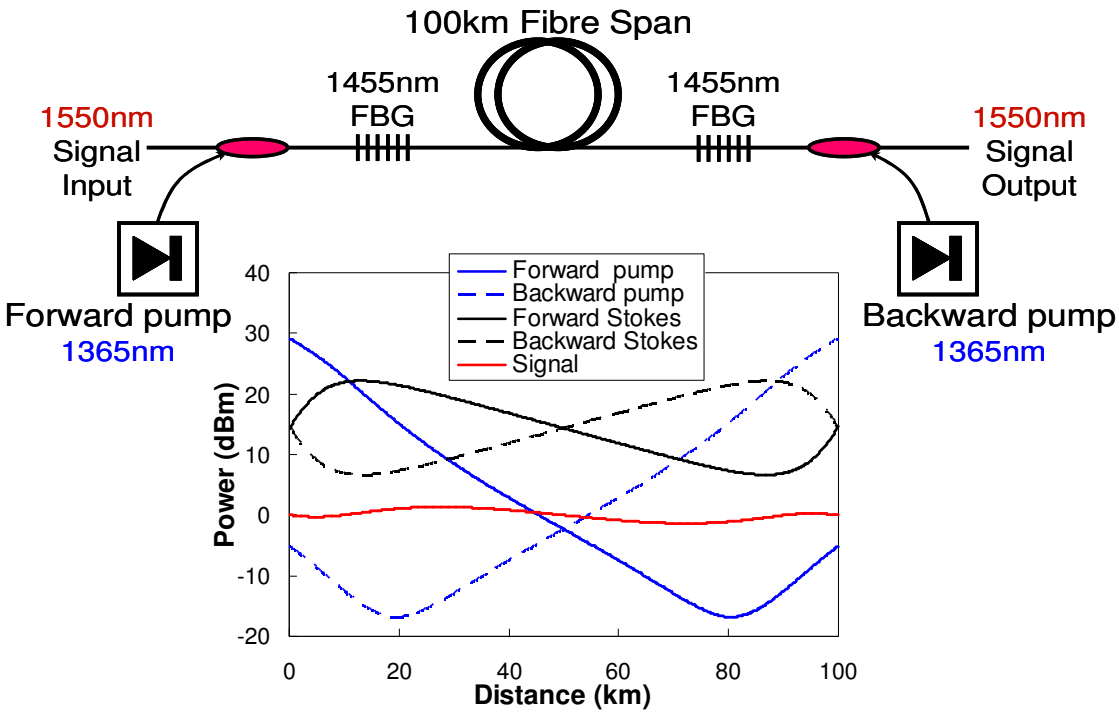

Figure 3.2.2: Simulated intra-cavity power distribution for URFL.

The case just described here is optimized for zero-lossless propagation or minimum power variation along the length of the transmission span, where the whole system and power provided by the primary pumps is symmetric to achieve the appropriate transmission conditions. URFLs can be used also as amplifiers; in such case, the power provided by the primary pumps should be higher than the power required to compensate the fibre losses.

3.2.1 Basic equations for power evolution

The ordinary differential equations that describe mathematically the average power evolution of the different spectral components along the length of the fibre for the basic URFL system are shown below. These relations take into account all the important effects, including pump depletion, amplified spontaneous emission (ASE) and double Rayleigh scattering (DRS) noise. The amplified spontaneous emission (ASE) noise is a result of spontaneous emission photons getting amplified in the same direction as the signal. Double Rayleigh scattering (DRS) can be understood by considering that some signal photons get scattered backwards

by the Rayleigh scattering process. The scattered photon will get amplified by the pump and may be scattered back again into the signal direction resulting in multipath interference (MPI). A more extensive description of the average power performance for the URFL system can be found in the references [15][47].

$$\frac{dP_{P1}^{\pm}}{dz} = \mp\alpha_1 P_{P1}^{\pm} \mp g_1 \frac{\nu_1}{\nu_2} P_{P1}^{\pm}\left(P_{P2}^{+} + P_{P2}^{-} + 4h\nu_2\Delta\nu_2\left(1+\frac{1}{e^{h(\nu_1-\nu_2)/K_BT}-1}\right)\right) \pm \varepsilon_1 P_{P1}^{\mp}, \quad \textbf{3.2.1}$$

$$\frac{dP_{P2}^{\pm}}{dz} = \mp\alpha_2 P_{P2}^{\pm} \pm g_1\left(P_{P2}^{\pm} + 2h\nu_2\Delta\nu_2\left(1+\frac{1}{e^{h(\nu_1-\nu_2)/K_BT}-1}\right)\right)\left(P_{P1}^{+} + P_{P1}^{-}\right)$$

$$\mp g_2 \frac{\nu_2}{\nu_S} P_{P2}^{\pm}\left(P_S + N_S^{+} + N_S^{-} + 4h\nu_S\Delta\nu_S\left(1+\frac{1}{e^{h(\nu_2-\nu_S)/K_BT}-1}\right)\right) \pm \varepsilon_2 P_{P2}^{\mp}, \quad \textbf{3.2.2}$$

$$\frac{dP_S}{dz} = -\alpha_S P_S + g_2 P_S\left(P_{P2}^{+} + P_{P2}^{-}\right), \quad \textbf{3.2.3}$$

$$\frac{dN_S^{+}}{dz} = -\alpha_S N_S^{+} + g_2\left(N_S^{+} + 2h\nu_2\Delta\nu_2\left(1+\frac{1}{e^{h(\nu_2-\nu_S)/K_BT}-1}\right)\right)\left(P_{P2}^{+} + P_{P2}^{-}\right) + \varepsilon_S N_S^{-}, \quad \textbf{3.2.4}$$

$$\frac{dN_S^{-}}{dz} = \alpha_S N_S^{-} - g_2\left(N_S^{-} + 2h\nu_2\Delta\nu_S\left(1+\frac{1}{e^{h(\nu_2-\nu_S)/K_BT}-1}\right)\right)\left(P_{P2}^{+} + P_{P2}^{-}\right) - \varepsilon_S\left(P_S + N_S^{+}\right). \quad \textbf{3.2.5}$$

The (+) and (-) superscripts represent forward and backward propagation respectively, the 1, 2, and S subscripts identify the primary pump, secondary pump and signal respectively, P_{Pi} are the pump powers, P_S are the signal powers and N_S are the noise powers at the frequency of the signal, the ν_i are the corresponding frequencies of the pumps and signal, the $\Delta\nu_i$ represent the effective bandwidths of the secondary pump and the signal (limited, in the case of the secondary pump, by the bandwidth of the fibre Bragg gratings), the g_i are the corresponding Raman gain coefficients (divided by the effective area) for each of the Raman transitions, the α_i are the fibre attenuations at each respective frequency, *h* is Plank's constant, K_B is Boltzmann's constant, *T* is the absolute temperature of the fibre and the ε_i are the double Rayleigh scattering coefficients of the fibre at each particular frequency. The boundary conditions associated to the above equations are the followings:

$$P_{P1}^{+}(0) = P_{10}^{+}; P_{P1}^{-}(L) = P_{10}^{-}; P_{P2}^{+}(0) = R_1 P_{P2}^{-}(0); P_{P2}^{-}(L) = R_2 P_{P2}^{+}(L); N_S^{+}(0) = N_0; N_S^{-}(L) = 0; P_S(0) = P_{IN}, \quad \textbf{3.2.6}$$

where L is the length of the fibre span and R_1 and R_2 are the reflectivity of the fibre Bragg gratings at the beginning (span length value 0) and the end (span length L) of the transmission span. The fibre parameters used in the simulations correspond to those of conventional SMF optical fibre. Their values are summarized in Table 3.2.1.

Table 3.2.1: Fibre parameters used in the simulation.

Wavelength (nm)	g ($W^{-1} km^{-1}$)	α (dB/km)	ε (km^{-1})
1365	0.51	0.33	$1.0x10^{-5}$
1455	0.36	0.26	$6.0x10^{-5}$
1550	-	0.20	$4.3x10^{-5}$

The evolution of the primary pump, secondary pump and signals along the fibre is obtained by solving numerically Equations 3.2.1-3.2.5 with the corresponding boundary conditions, Equation 3.2.6. The integration is done considering room temperature (25°C) and typical values for the various SMF parameters (detailed in Table 3.2.1). The pumps are assumed to be depolarized, so the gain coefficients that appear on the table correspond to this case (i.e., have been multiplied by a factor 1/2). Otherwise, if the Raman pumps were not depolarized, as the Raman gain is polarization dependent, the gain coefficients used in the simulation work would be a fluctuating value between those ones indicated in the Table 3.2.1 and twice its value. The full-width half-maximum (FWHM) reflection bandwidth of the fibre gratings is assumed to be 0.5nm.

The previous Equations, 3.2.1-3.2.5, describe in particular a second order bi-directional Raman fibre amplifier. The relations describing higher order amplification systems could be derived in a similar manner, although further boundary conditions will be required and the solution will be more complex.

3.2.2 Numerical results for first and higher order amplifier

In this section we try to compare the power evolution of first order Raman amplifier Figure 3.2.3(b) and URFL scheme Figure 3.2.3(a) as a second order amplifier system. URFL has a similarly simple structure to that of first order amplifiers but is capable of providing a reduced power excursion performance equivalent to that of second order amplifiers as it will be shown later on. This superior performance is provided by the embedded FBGs that create

a laser cavity in the fibre span at the Stokes wavelength of the primary pumps, allowing the generation of a robust and power-self-adjustable secondary pump.

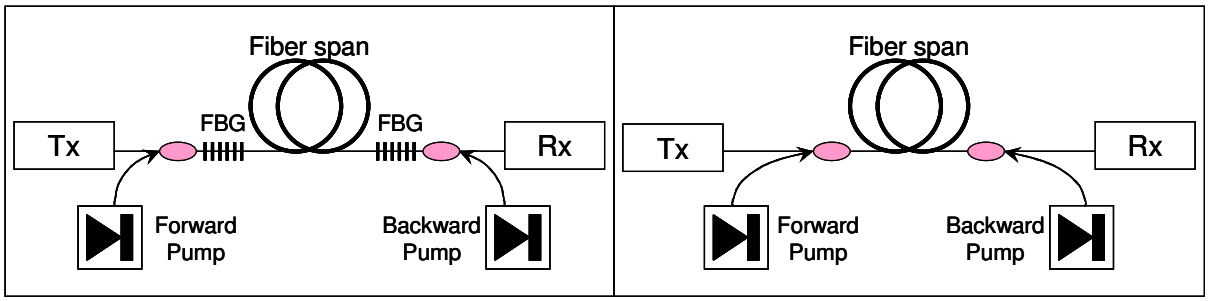

Figure 3.2.3: a) Second order (URFL) and b) first order Raman amplifiers systems

Forward pump is defined as the Raman pump travelling in the same direction as the transmitted signal and backward pump as the Raman pump travelling in the opposite direction to the signal. If we design the above two systems for a transmitted signal with central wavelength at 1550nm, then the Raman pumps will be set at 1365nm for the URFL, Figure 3.2.3(a), and at 1455nm for the first order Raman amplifier, Figure 3.2.3(b).

Below, Figure 3.2.4, is the power variation of the signal along the length of the transmission span for the first and the second order Raman amplification systems described on the above figures, using forward, backward and symmetric pumping schemes.

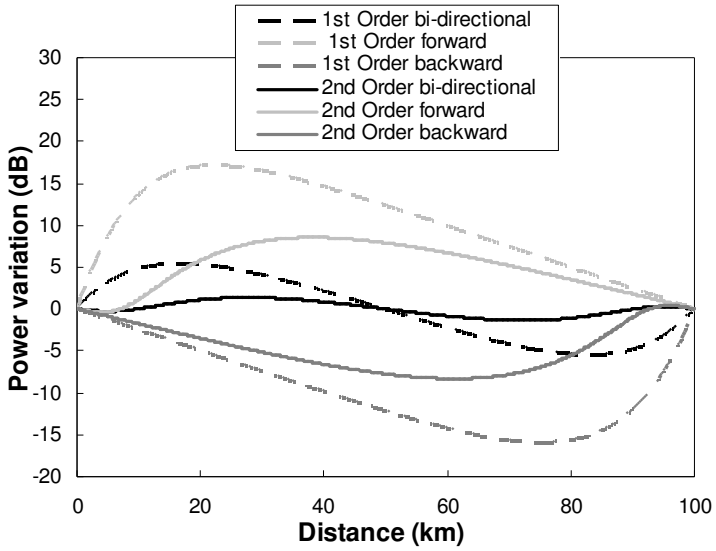

Figure 3.2.4: Power distribution for 100km span length

As reference, the typical power loss for conventional optical fibre is 0.2dB/km, therefore a signal transmitted in a fibre span of 100km without any type of amplification will have a power drop of 20dB. When using first order symmetric Raman amplification (black dotted line from Figure 3.2.4), the power variation along the length of the span can be reduced to approximately 11dB. This power variation can be reduced to less than 3dB for the case of

second order symmetric bi-directional pumping with FBGs at 90% reflectivity (black line Figure 3.2.4). The details of the maximum power variation for all the cases numerically simulated and plotted in Figure 3.2.4 are given in Table 3.2.2.

Table 3.2.2: Maximum power variation corresponding to plots from Figure 3.2.1

Amplifier scheme	Power variation (dB)
1st Order forward	17.19
1st Order backward	15.95
1st Order bi-directional	10.95
2nd Order forward	8.95
2nd Order backward	8.71
2nd Order bi-directional	2.72

In general, the power variation for the forward pumping tends to be greater than the backward pumping case, as the signal power initially increase, having a greater impact on the pump depletion. Therefore the total intra-cavity power variation tends to be greater in the case of forward pumping, except for those cases in which the signal power is much smaller than that of the pumps, so its effect on pump depletion can be considered negligible.

The benefits of an URFL scheme over a first order Raman amplifier are obvious when looking at the power variation for any span length. Figure 3.2.5(a) shows the power variation up to 120km span length for first order Raman amplifier scheme and URFL with FBGs at 90% reflectivity. Both systems use symmetric bi-directional pumping.

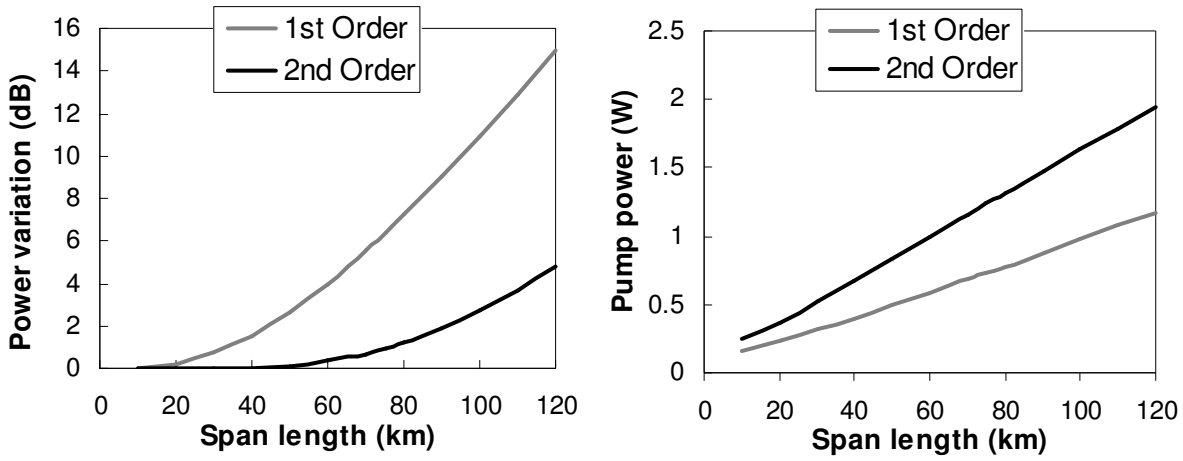

Figure 3.2.5: a) Power variation and b) pump power required with span length for 1st and 2nd order amplifier scheme.

A maximum intra-cavity power variation of 1dB is achieved for just over 30km in the case of the first order Raman amplifier, while with the URFL we can achieve similar performance for twice the length; just over 75km span length. Meanwhile, the power required for a first order Raman amplifier of 75km span is 0.73W, while the power required

for the scheme of 75km URFL with FBGs at 90% reflectivity is just over 0.5W more, with a total of 1.24W, still easily achievable with commercial pump units. Basically the benefits on power variation for an URFL system generally outweight the higher pump power requirements for a similar system length.

3.3 Relative intensity noise transfer

Among the challenges of distributed Raman amplification, an important one is relative intensity noise (RIN) [66][67][68][69] transfer. This is a pump-to-signal noise transfer with origin in the intensity fluctuations of the pump laser source. Any fluctuation of the pump power will produce a variation in signal gain, and thus be imprinted in the signal, creating an additional source of noise that, in some situations and with a low-quality pump source, can be as damaging a noise source as amplified spontaneous emission (ASE) itself.

To gain a better understanding of the RIN limiting effect on the Raman amplification system, we need to improve our understanding of RIN in high-order Raman amplifying systems and investigate its behaviour for different cavity design parameters. Consider a laser pump source with an output power defined as $P(t)$, with a constant average power part, P_0, and a power component fluctuating in time, $\Delta P(t)$, as described by Equation 3.3.1.

$$P(t) = P_0 + \Delta P(t). \qquad \textbf{3.3.1}$$

The ratio between the fluctuating component of the power and the average power is defined as $\delta P(t)$. Generally, the RIN can be understood as the ratio of the amplitude noise to the average power (see Equation. 3.3.2). In most of the bibliography, the RIN is defined mathematically as the square value of $\delta P(t)$, (see Equation 3.3.3). That is the way it will be defined throughout this work, in agreement with the scientific community.

$$\delta P(t) = \frac{\Delta P(t)}{P_0}, \qquad \textbf{3.3.2}$$

$$RIN = \left\langle \delta P^2(t) \right\rangle. \qquad \textbf{3.3.3}$$

The average power values can be calculated from the previous power evolution Equations, 3.2.1-3.2.5, with the corresponding boundary conditions, Equation 3.2.6. The amplitude noise will be calculated using the basic equations for the RIN transfer evolution that will be presented on the next section. Most of the work published regarding RIN transfer

so far relates to the RIN transfer for first order Raman fibre amplifiers [66][68][69][70][71]. The RIN transfer is from the pump to the first Stokes and is defined as Equation 3.3.4.

$$H_{1stOrder}(\omega) = \left| \frac{RIN^{+}_{1stStokes}(\omega)}{RIN^{+}_{pump}(\omega)} \right|, \quad \textbf{3.3.4}$$

$$H_{2ndOrder}(\omega) = \left| \frac{RIN_{S}(\omega)}{RIN^{+}_{pump}(\omega)} \right|. \quad \textbf{3.3.5}$$

In our case, we will present some numerical results for a second order Raman fibre amplifier. Therefore, the RIN transfer is from the pump to the signal, as defined in Equation 3.3.5, with the signal wavelength within the range of the second Stokes of the pump.

3.3.1 Basic equations for RIN transfer evolution

In this section we introduce a numerical model for the RIN transfer in higher order distributed Raman amplifiers, in particular but not exclusively for ultralong Raman fibre lasers. This numerical model allows us to investigate the effect of features design, such as span length, pump distribution and fibre Bragg gratings (FBGs) reflectivity, on the RIN transfer performance of the system. The presented 2nd-order model for RIN transfer is a generalization of previously developed descriptions [66][67][68], with the inclusion of some neglected effects that can have an important impact in RIN transfer in the case of ultralong lasers, such as Rayleigh backscattering. The model includes a set of five partial differential equations describing the RIN propagation from the primary pump and first Stokes or secondary pump in both directions forward and backward plus the RIN from the signal described only in the forward direction.

The system is treated as a multipoint boundary value problem for ordinary differential equations. The complete system of nonlinear ordinary differential equations (ODEs) can be expanded into its real and imaginary parts and solved through a number of methods. The method used as preference in obtaining most of the results of this chapter is a finite element method with spline collocation at Gaussian points, but other approaches such as Runge-Kutta methods with shooting and/or relaxation algorithms can be used.

The following set of ordinary differential Equations 3.3.6 - 3.3.8 describing mathematically the evolution of the RIN along the span for a second order Raman amplification system, require to be used in conjunction with the set of Equations 3.2.1-3.2.5, in order to have the right values of average powers at each point in the fibre span.

$$\frac{dn_1^{\pm}}{dz} + id_1^{\pm}\omega n_1^{\pm} = \mp\alpha_1 n_1^{\pm} \mp g_1 \frac{v_1}{v_2} P_1^{\pm}(n_2^{+} + n_2^{-}) \mp g_1 \frac{v_1}{v_2}(P_2^{+} + P_2^{-}) n_1^{\pm} \pm \varepsilon_1 n_1^{\mp}, \quad \textbf{3.3.6}$$

$$\frac{dn_2^{\pm}}{dz} + id_2^{\pm}\omega n_2^{\pm} = \mp\alpha_2 n_2^{\pm} \pm g_1 P_2^{\pm}(n_1^{+} + n_1^{-}) \pm g_1 n_2^{\pm}(P_1^{+} + P_1^{-}) \mp g_2 \frac{v_2}{v_S} P_2^{\pm} n_S \mp g_2 \frac{v_2}{v_S} n_2^{\pm} P_S \pm \varepsilon_2 n_2^{\mp},$$

3.3.7

$$\frac{dn_S}{dz} = -\alpha_S n_S + g_2 P_S\,(n_2^{+} + n_2^{-}) + g_2 n_S (P_2^{+} + P_2^{-}) + \varepsilon_S n_S^{-}, \quad \textbf{3.3.8}$$

where the n_i represent the spectral density of amplitude noise, the group velocity for each spectral component is represented by υ_i, the term $d_i^{\pm} = 1/\upsilon_s \pm 1/\upsilon_i$ accounts for the effect of the relative propagation speeds of the different spectral components, z is the length measured along the fibre span, P_i represent the pump and signal powers at the different frequencies (obtained through the solution of the set of ODEs, Equations 3.2.1-3.2.5), with the subscript "1", referring to the primary pump at 1366nm, "2" being the first Stokes at 1455nm, and "s" referring to the signal at 1550nm. The attenuation coefficient, α_i, is in units of km^{-1}. The optical frequency for each spectral component is represented by ν_i. The strength of the coupling between the pumps and the signal are determined by g_i, the Raman gain coefficients for the fibre, which have units of $W^{-1}\,Km^{-1}$. The pump modulation frequency is represented by ω. The signs ± correspond to components propagating in forward (+) or backward (-) direction. Here and through this paper is assumed that the signal propagates in the forward +z direction. ε_i are the Rayleigh backscattering coefficients of the fibre at each particular frequency.

The effect of the cavity design parameters are introduced in the boundary conditions. In the case of an ultralong laser, the two FBGs centered at the Stokes wavelength for the primary pump are located at z=0 and z=L and have reflectivity R_1 and R_2 respectively

$$n_1^{+}(0) = n_{10}; n_1^{-}(0) = n_{20}; n_2^{+}(0) = R_1 n_2^{-}(0); n_2^{-}(L) = R_2 n_2^{+}(L); n_S(0) = 0\,. \quad \textbf{3.3.9}$$

Although the two sets of Equations 3.2.1 - 3.2.5, and 3.3.6 - 3.3.8 describe a second order Raman amplification system, in principle, there is no limit for applying similar mathematical approach to higher order Raman amplification systems. Further boundary conditions will be required, making the solution of the system substantially more complex.

3.3.2 RIN transfer numerical results

In order to describe our numerical model, we focus on the study of two particular Raman-amplified systems based on standard single-mode fibre (SMF). They are schematically described in Figure 3.3.1. The first system corresponds to an SMF-based bi-directionally pumped URFL. It involves a conventional standard optical fibre confined between a pair of fibre Bragg grating (FBG) reflectors with a central wavelength of 1455nm, corresponding to the first Raman Stokes of the pump source. Reflectivity will be considered a variable in our study, as well as the length of the fibre span, which ranges from 1 to 100km. The pump power at 1366nm is coupled into the system through WDMs. The wavelength of the transmitted signal is at 1550nm, corresponds to the second Stokes of the pump source.

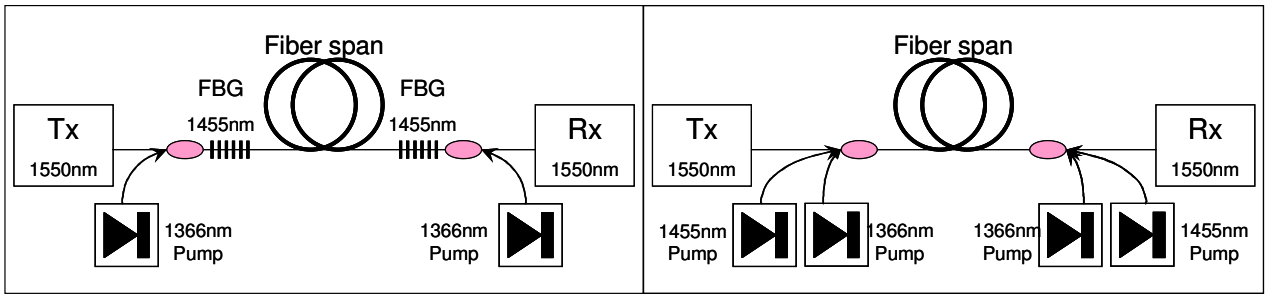

Figure 3.3.1: Schematic description of the studied bi-directional pumped Raman amplifier systems. (a) Ultralong Raman fibre laser. (b) Equivalent power distribution system with dual pumping scheme.

As the pump power injected at 1366nm overcomes the threshold for the fibre cavity, a first Stokes component around 1455nm is generated and trapped between the grating reflectors. This component will behave as a second pump source, providing a wide Raman gain bandwidth to the transmitted signal, located around the second Stokes wavelength of 1550nm. This structure provides quasi-lossless transmission around 1550nm for an optimally adjusted pump power [15][16][21][72].

The second distributed Raman amplifier system involves a conventional standard optical fibre, ranging from 1 to 100km similarly to the first system, but no reflectors at all, hence no laser cavity. The optical fibre is bi-directionally pumped with pumps at 1366nm and 1455nm. The power from both pump sources are coupled into the system through WDMs. The transmitted signal is again at 1550nm, corresponding to the second Stokes of the 1366nm pumps and the first Stokes of the 1455nm pumps.

In order to ensure a fair comparison between the performance of both systems, we operate the second one as follows. We increase the pump power at 1366nm to the same level as we would have done for the first system for an identical span length and signal power.

Then, we calculate the initial power at 1455nm at each end of the fibre span for our first system and use exactly the same 1455nm power value for the pumps of our second system. This allows us to generate an equivalent amplifier system to the first one with exactly the same power distribution for 1366nm, 1455nm and the signal 1550nm, but using an extra bi-directional pump source at 1455nm instead of using FBGs. Hence, average power distributions inside the two amplifiers are identical, which will make it possible to perform a direct comparison of their respective RIN transfer performances. Any difference on the RIN transfer values between these two systems is expected to come from the impact of generating the secondary pump in the ultralong laser cavity instead of using a dual wavelength pumping scheme. Therefore we can quantify how the pump-noise transfer, with origin in the intensity fluctuation of the laser source due to spontaneous emission, evolves and it is magnified when using a laser cavity as amplifier.

To describe fully both systems it's required the ordinary differential equations that describe mathematically our model. On the one side we have a set of ODEs describing the average power evolution of pumps, signal and propagation noise along the length of the fibre for a second order Raman amplifier (with their respective boundary conditions set in accordance to the rules mentioned above to make the comparison fair), Equations 3.2.1-3.2.5. On the other hand, the evolution of the spectral density of amplitude noise in a second-order amplification scheme can be described through a second set of ODEs, given by Equations 3.3.6 to 3.3.8.

The cavity design parameters are introduced in the boundary conditions. The FBGs are located at z=0 and z=L and have reflectivities R_1 and R_2 respectively. Each of the two schemes is described by a different set of boundary conditions:

For scheme 1 (URFL):

$$P_{P1}^{+}(0)=P_{10}^{+};P_{P1}^{-}(L)=P_{10}^{-};P_{P2}^{+}(0)=R_1P_{P2}^{-}(0);P_{P2}^{-}(L)=R_2P_{P2}^{+}(L);N_S^{+}(0)=N_0;N_S^{-}(L)=0;P_S(0)=P_{IN}$$
$$n_1^{+}(0)=n_{10};n_1^{-}(0)=n_{20};n_2^{+}(0)=R_1n_2^{-}(0);n_2^{-}(L)=R_2n_2^{+}(L);n_S(0)=0. \quad \textbf{3.3.10}$$

For scheme 2 (dual-wavelength pumping):

$$P_{P1}^{+}(0)=P_{10}^{+};P_{P1}^{-}(L)=P_{10}^{-};P_{P2}^{+}(0)=P_{20}^{+};P_{P2}^{-}(L)=P_{20}^{-};N_S^{+}(0)=N_0;N_S^{-}(L)=0;P_S(0)=P_{IN}$$
$$n_1^{+}(0)=n_{10}^{+};n_1^{-}(0)=n_{10}^{-};n_2^{+}(0)=n_{20}^{+};n_2^{-}(L)=n_{20}^{-};n_S(0)=0. \quad \textbf{3.3.11}$$

The complete system of equations can be expanded into its real and imaginary parts and solved through a number of methods. Here we have used a finite element method with spline collocation at Gaussian points. Simulation parameters are summarized on Table 3.3.1.

Table 3.3.1: Fibre parameters used in the simulation

Wavelength (nm)	g ($W^{-1}km^{-1}$)	α (dB/km)	ε (km^{-1})	d^+ (s/m)	d^- (s/m)
1366	0.51	0.33	$1.0x10^{-4}$	$2.8x10^{-9}$	$1.0x10^{-5}$
1455	0.36	0.26	$6.0x10^{-5}$	$1.35x10^{-9}$	$1.0x10^{-5}$
1550	-	0.20	$4.3x10^{-5}$	-	-

Unless otherwise stated, all the calculations for the numerical simulation work shown on this chapter are subject to the zero-loss condition; that is, total pump powers are automatically adjusted to obtain identical output signal power to the input one, regardless of span length, pump power distribution or any other parameter of the amplifier system.

3.3.2.1 Span length

The numerical results for the RIN transfer value for different span lengths are graphically represented below. Figure 3.3.2(a) the ultralong laser cavity with 90% reflectivity FBGs and Figure 3.3.2(b) the dual pumping scheme with no FBGs. The value of transmitted signal is 1mW in both cases, ensuring low pump depletion. The final obtained transfer function is independent of the initial RIN of the laser pumps, as long as this is set to be identical for the different sources. The span length ranges from 1 to 100km. The only variable parameter is the length of the fibre span; otherwise the forward-backward pump ratio distribution is symmetric and the zero-loss condition is applied.

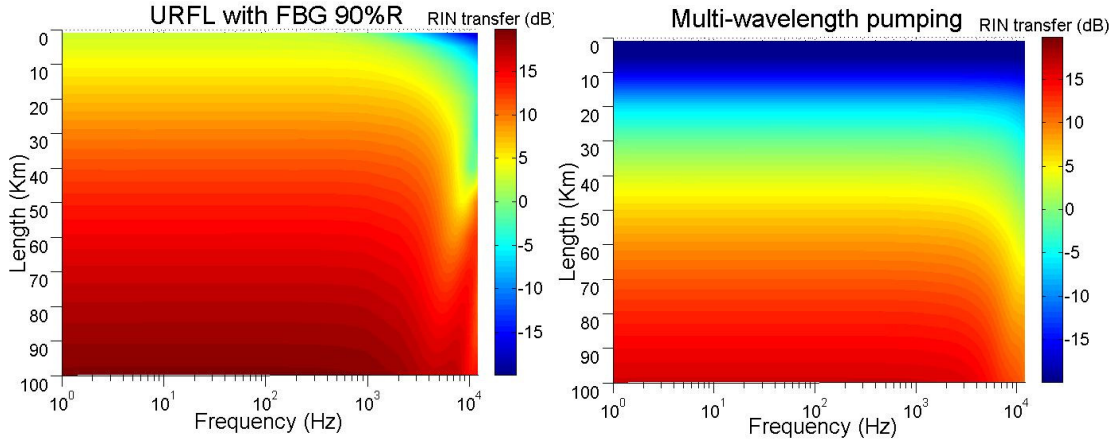

Figure 3.3.2: RIN transfer value at several span lengths for a) laser cavity with 90% FBGs and b) fibre span dual pumping scheme without reflectors

As a general trend, the maximum RIN transfer value increases with length regardless of whether the Raman amplifier is a laser cavity, Figure 3.3.2(a), or a simple fibre span without reflectors, Figure 3.3.2(b). The maximum RIN value at 75km, for the cases of laser cavity with FBGs at 90% reflectivity and fibre span without reflectors, are 17dB and 12.25dB

respectively (i.e. RIN transfer is 4.75dB higher in the ultralong cavity). A penalty in terms of maximum value of the RIN transfer for the ultralong laser cavity in comparison with the dual pumping scheme without reflectors is observed in all cases. The differences between the performances of both schemes, though, are reduced with increasing span length.

A major distinction between both systems is the decline of the RIN transfer value at higher modulation frequencies. Whilst in the case of the dual pumping scheme without reflectors the RIN transfer drops gradually with increasing modulation frequency, in the case of the laser cavity the RIN transfer value shows a fluctuating behaviour towards lower values, especially for the longer span lengths.

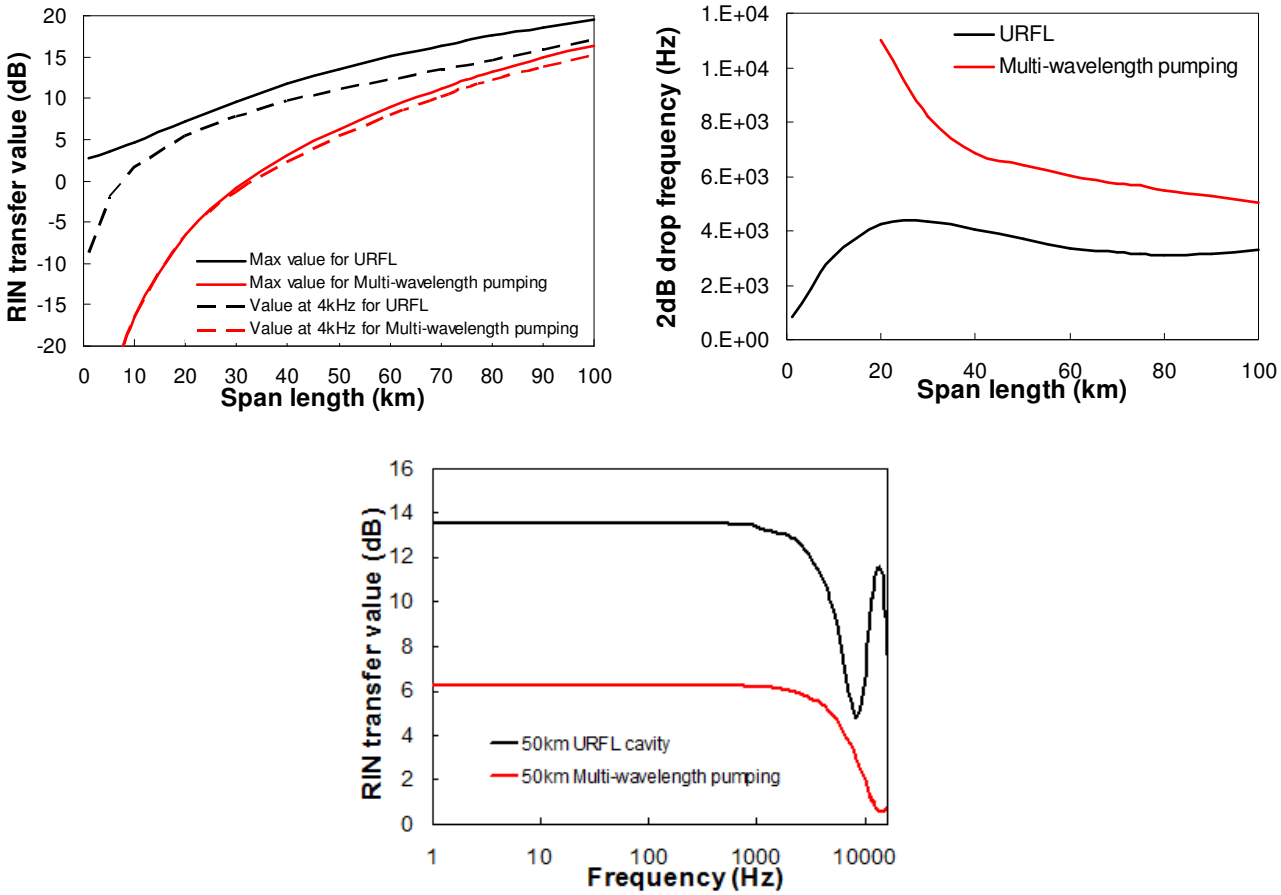

Figure 3.3.3: a) RIN transfer value versus span length and b) 2dB drop frequency versus span length c) RIN transfer value versus frequency, for the two considered scheme.

A direct comparison of the RIN transfer value between both systems is graphically presented in Figure 3.3.3(a) for two particular cases, the RIN transfer value at its maximum (lowest modulation frequency) and at 4kHz. The RIN transfer value in both systems converges for longer span lengths. Also the cut-off value of the RIN transfer at 4kHz is lower in the case of dual pumping scheme than the ultralong cavity. Furthermore, as Figure 3.3.3(b) shows, the cut-off frequency (taken here as the frequency at which the RIN transfer has dropped 2dB below its maximum value for the particular configuration) is lower for the

laser cavity case than for the fibre span without reflectors, given the same fibre length and power conditions. As in the case of a standard amplifier, the cut-off frequency is dependent on dispersion (through pump walk-off) fibre loss, and shows a strong dependence on span lengths mainly for short spans below 40km in the case of standard fibre [66]. The faster oscillating behaviour and lower cut-off frequency in the case of the ultralong cavity are illustrated on Figure 3.3.3(c).

The unusual behaviour of the oscillations in the cavity compared to the case of a standard second-order amplification scheme can be attributed to a combination of the presence of peaks corresponding to the cavity round-trip and the fact that oscillations in the backward-propagating components are reinforced due to the boundary conditions set by the FBG reflectors, which feed them back into the cavity.

3.3.2.2 Pump distribution

The effect of the pump distribution is shown on Figure 3.3.4 for the cases of (a) laser cavity with 90% reflectivity FBGs and (b) dual pumping scheme without reflector. The value of transmitted signal is the same as previously, 1mW. The span length is fixed at 75km. The pump ratio is calculated as the forward pump divided by the total amount of pump (forward and backward).

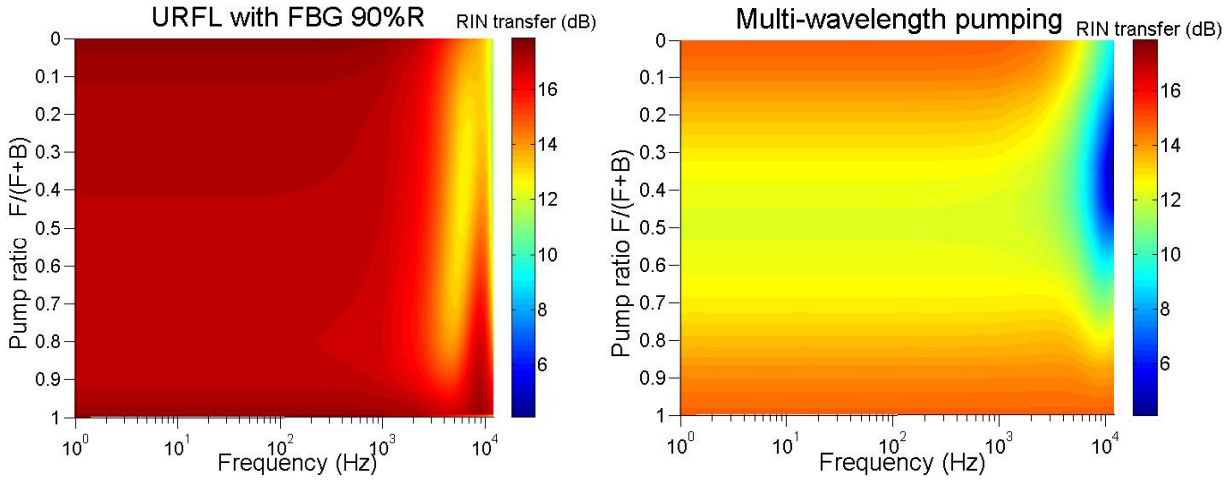

Figure 3.3.4: RIN transfer value for pumping distribution in the case of a) 75km laser cavity with 90% reflectors and b) 75km fibre span without reflectors.

The pump power split has a clear impact on the RIN transfer value. For the case of a laser cavity, shown in Figure 3.3.4(a) and Figure 3.3.5 the optimum pump split for the lowest RIN transfer value at lower frequencies is 80% forward - 20% backward with a RIN transfer function value of 16.83dB. Using any pump power split other than 80% forward and

20% backward will increase the RIN transfer value. The RIN transfer value for the laser cavity case may vary up to 0.9dBs over the 16.83dB value for any other configuration other than 80% forward and 20% backward. Symmetric pumping is, on the other hand, the best option for the case of the dual-wavelength pumping scheme without reflectors, as shown in Figure 3.3.4(b) and Figure 3.3.5, with a RIN transfer value of 12.25dB. In this case, though, the RIN transfer function is much more sensitive to deviations from the optimal case, and can go up to 2.6dB higher if we move away from the symmetrical configuration.

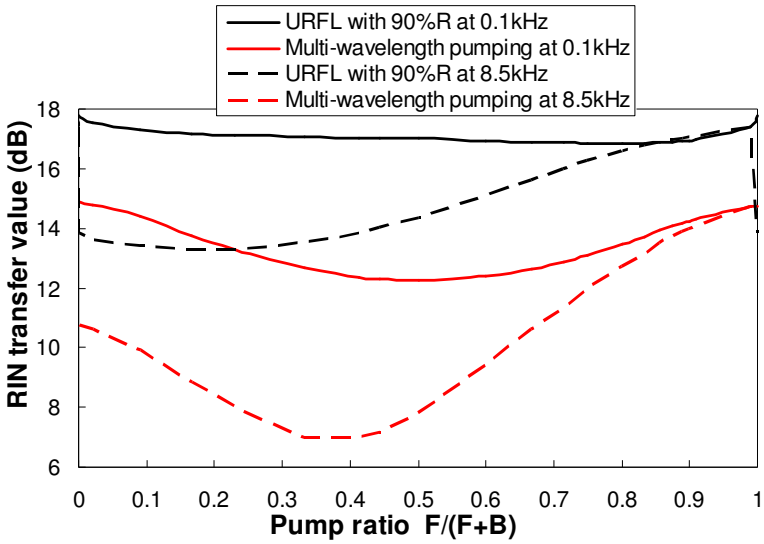

Figure 3.3.5: RIN transfer value versus pump ratio. Subset results from Figure 3.3.4(a) and (b).

The RIN transfer value drops continuously for higher modulation frequencies in all the cases where the major pump contribution is from the backward pump (pump ratio close to zero), whereas forward pumping leads to oscillations in the RIN transfer at higher frequencies, especially in the case of a laser cavity, increasing as well the 2dB drop frequency for the case of dual pumping without reflectors. As before, such drop appears at lower frequencies in the case of a laser cavity than the dual pumping scheme without reflectors. As well, the oscillations of the RIN transfer function are stronger for the case of laser cavity. The behaviour of the URFL cavity case for a pump ratio closed to 1 in Figure 3.3.5 illustrates the effect of the RIN transfer value oscillation at two particular frequencies, 0.1kHz and 8.5kHz.

We have assumed for all this work the transmitted signal travelling in the forward direction. Therefore the only reasonable explanation to this RIN transfer modulation effect at longer frequencies, as observed in Figure 3.3.4(a), could be related to the interaction between the forward pumping and the transmitted signal as they travel on the same direction.

3.3.2.3 FBG reflectivity

Grating reflectivity also plays an important role on the transfer of RIN. Figure 3.3.6 shows the RIN transfer values in a 75km ultralong laser cavity as grating reflectivity is varied from 0.1% to 100%. For all those cases the amplified system model used is the laser cavity described in Figure 3.3.1(a) where the pump power at 1455nm is provided by lasing the cavity with FBGs at that centre of wavelength. As previously, these results were calculated using 1mW forward transmitted signal.

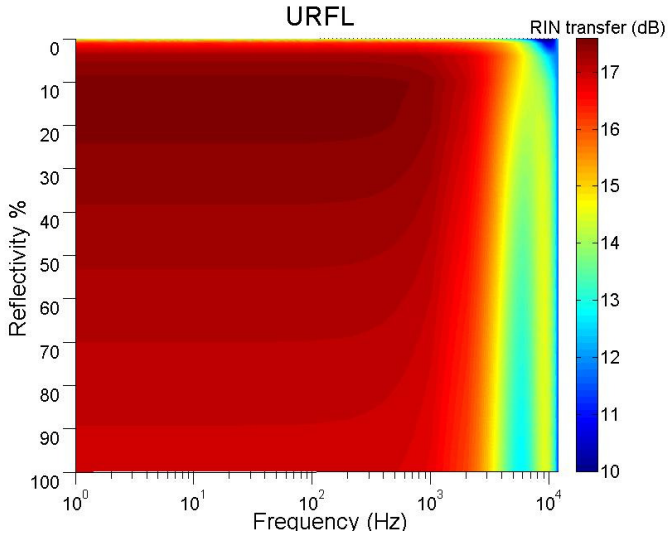

Figure 3.3.6: RIN transfer value vs. reflectivity and frequency for a 75km laser cavity.

As observed in the previous results, the 2dB drop frequency is lower for higher reflectivies. A subset of the results shown on Figure 3.3.6 is plotted on Figure 3.3.7(a). So far, the RIN transfer value was higher for the case of a laser cavity with 90% reflectivity than dual pumping scheme without reflectors. From the figure we can observe that at low frequencies, the maximum value of the RIN transfer is set at 15% reflectivity. At higher modulation frequencies, such as 6kHz, the worst case moves to lower FBGs reflectivity, 5%. The fact that cavities with relatively low reflectivity show worse RIN transfer performance than higher reflectivity may have interesting implications, for example, in areas such as that of random feedback ultralong Raman fibre lasers [73].

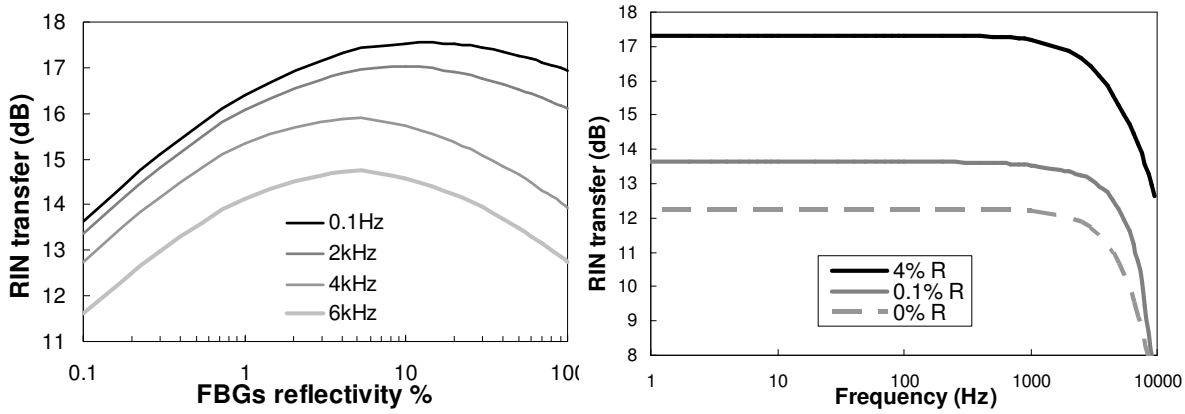

Figure 3.3.7: a)RIN transfer value versus FBG reflectivity and b) RIN transfer value versus frequency for a laser cavity and dual pumping scheme, both with 75km span length.

The numerical calculations for the laser cavity are done down to 0.1% reflectivity and the calculations for dual pumping scheme without reflectors are done with 0% reflectivity (see Figure 3.3.7(b) for a graphic comparison of those results), in practice, those reflectivity values are not realistic. For instance the typical reflectance of the glass at the air/glass interface is 4%. Maximum care should be provided in order to minimize any unwanted reflectivity in an experimental system.

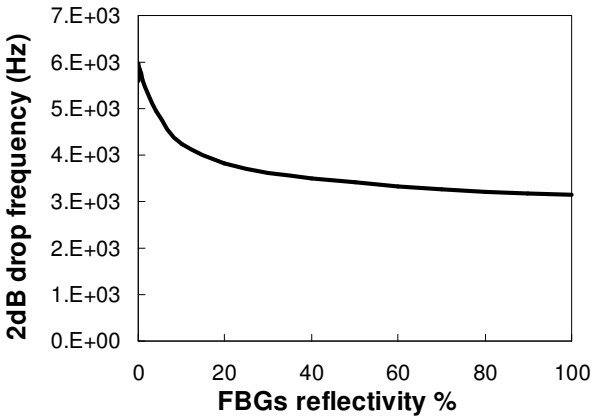

Figure 3.3.8: 2dB drop frequency versus FBG reflectivity for a 75km laser cavity

Furthermore, we observe in Figure 3.3.8 that the 2dB drop is displaced to higher frequencies for the case of low FBGs reflectivity. As the FBG's reflectivity increases the 2dB drop frequency decreases, showing a faster reduction of the RIN transfer value at low frequencies.

3.4 Conclusion

This chapter is focused in the numerical investigation of the intracavity power evolution performance and the RIN transfer evolution in second-order distributed Raman amplifiers, with special attention to ultralong Raman fibre lasers (URFLs).

URFLs are distributed amplifier systems with a similar simple structure to that of first order Raman amplifiers but capable of providing a reduced power performance equivalent to that of a second order Raman amplifier. This improved performance between the first order amplifier scheme and the URFL requires extra pump power. Although the range of powers are still easily achievable with commercial pumps and the benefits on power variation for a URFL system generally outweigh the higher pump power requirements for a similar system length.

Ultralong Raman fibre lasers (URFLs) display a series of advantages over other amplification solutions, particularly when minimum power variation along the span transmission is required, included reduced amplification of spontaneous emission noise (ASE) and virtual transparency in a wide range of frequencies. These advantages can nevertheless see themselves offset by the relative intensity noise (RIN) transfer from the pumps to the amplified signal.

A numerical study of RIN transfer in second-order distributed Raman amplifiers, with special attention to ultralong Raman fibre lasers was presented in this chapter. The new numerical model developed allows us to achieve a better understanding of how the design parameters of an ultralong laser cavity affect the RIN transfer performance of the system.

As expected, span length has a major impact on RIN transfer, increasing the RIN transfer value for longer lengths regardless of the second-order configuration studied, but interestingly, the maximum RIN transfer value reached at low modulation frequencies asymptotically converges towards a common value for long lengths for the different configurations studied. URFLs display a performance penalty in comparison to standard multiwavelength-pumped second-order amplifiers, but also a rather different response to system parameter variation, being in general more robust to pump asymmetries as observed from Figure 3.3.5. The maximum RIN transfer value in URFLs is not linked to the highest FBG reflectivity, but in fact, happens at relative low reflectivity of 15%. Pump split is also a key parameter which affects the maximum value of the RIN transfer function in different degrees depending on whether we are using a laser cavity or a dual-wavelength pumping scheme without reflectors. In addition, it is also related to the oscillating behaviour of the RIN transfer function at higher frequencies, which becomes more obvious as the relative contribution of forward pumping increases.

Finally, we have observed that the cut-off frequency for the RIN transfer function, taken as the frequency at which the RIN transfer has dropped 2dB below its maximum value for the particular configuration, is reduced not only with increasing span length, but also with increasing FBG reflectivity. In addition, cavities with relative low reflectivity show worse RIN transfer performance than higher reflectivity ones, which might have interesting implications in the future design and implementation of low-reflectivity systems making use of random distributed feedback.

Chapter 4

Experimental investigation on URFL

4.1 Introduction

The relevance of Raman amplification within the scientific community in the last decade can be confirmed by the number of publications reported in the subject. The average of publications per year, related to Raman amplification, in last decade is over 10 times greater that in the 1990´s. Furthermore, the number of publications related to Raman amplification has become greater to those reported on Erbium doped fibre amplifiers (EDFAs) since 2002, as shown in Figure 4.1.1. The source of the data regarding the number of scientific publications is a well known engine search covering both topics [74].

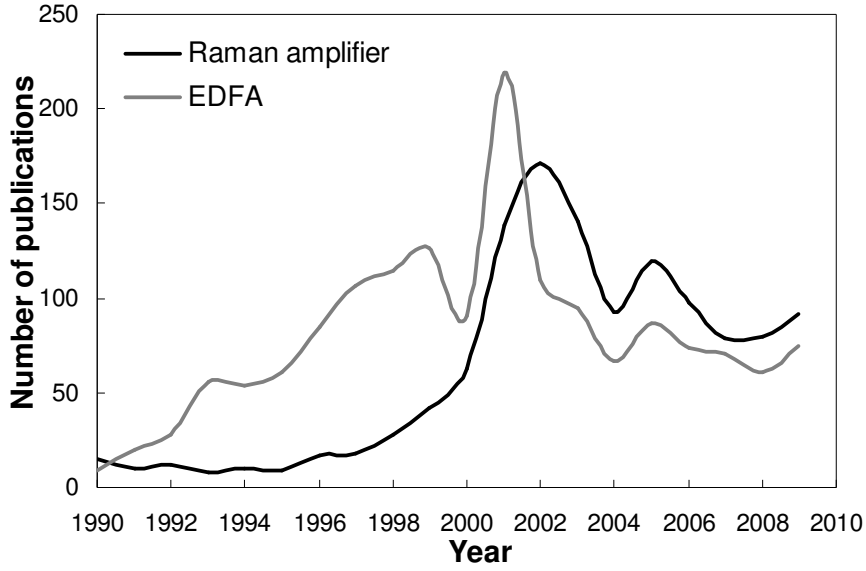

Figure 4.1.1: Number of scientific publications per year

As discussed in the previous chapter, distributed Raman amplification provides certain advantages over other amplification techniques, such as semiconductor optical amplifiers

(SOA) and Erbium doped fibre amplifier (EDFA). The reality is that EDFA systems are deployed extensively in most of the networks environments. The investigation work provided in the last few years by the scientific community support a future shift towards the deployment of other optical amplification techniques or at least combination of EDFA with Raman or SOA, as they can confer more advantages for the specific network environment [75][76].

The main advantages of the URFL system over the EDFA systems are a lower power variation across the bandwidth range and an extended gain spectral bandwidth. Figure 4.1.2 shows a clear comparison of the spectrum profiles around 1550nm for both amplifier systems without using any flattening filter. In the practical side, most of the optical fibre deployed in most of the networks is conventional single mode fibre. URFL can be implemented readily as it uses conventional optical fibre as gain material and transmission link.

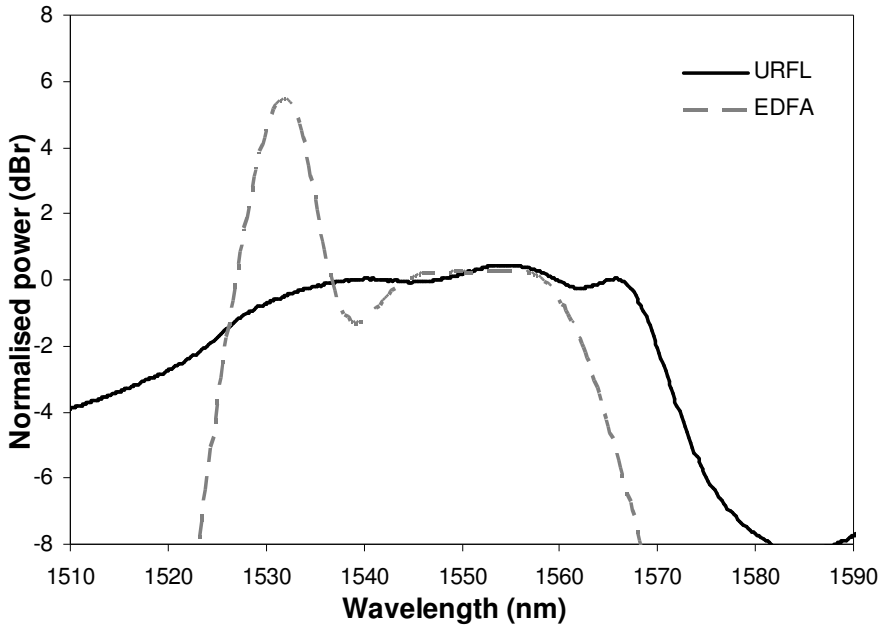

Figure 4.1.2: Experimental spectra for an EDFA and an URFL

The scope of the experimental investigation portrayed in this chapter is to study URFL systems and improve even further its performance. Hence gaining a deep understanding of the restrictions and advantages offered by URFL systems is essential. The work presented here is mainly focused in areas such as the URFL bandwidth enhancement and spectral flatness, the effect of the input signal level in the transmission performance and how URFL systems of longer lengths lead to random laser sources with feedback supported by Rayleigh-scattering. As mentioned in Chapter 2, Rayleigh scattering has its origin in the random fluctuation of the refractive index through the optical fibre. These local fluctuations

scatter light in all directions, acting as small random mirrors. The Rayleigh scattering is proportional to the wavelength, λ^{-4}, in such a way that its contribution dominates at short wavelengths.

4.2 Bandwidth enhancement

Most of the work reported regarding URFL [15][19][21][23][24][72][77][78] operates with a bandwidth of almost 40nm, covering the frequency spectrum from 1528nm to 1568nm within ±0.5dB power variation. That is the case for URFL systems operating with optimised 1366nm Raman pump power, with FBGs centre wavelength set at 1455nm and transmitted signal at 1550nm. A further increase of the covered frequency spectrum with a minimum of power variation across all the range is highly desirable, especially for applications in optical communications [18][23], as it would mean an increase of the transmission system capacity. Therefore, an experimental investigation was carried out with the objective of URFL bandwidth enhancement whilst still retaining the same pumping and cavity structure.

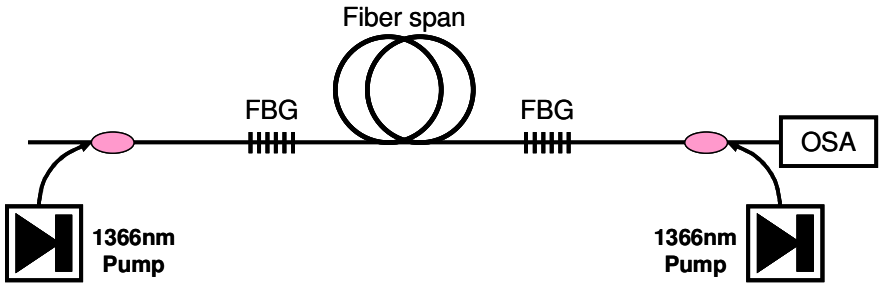

Figure 4.2.1: Schematic diagram of URFL experimental set-up

The scheme of the experimental set-up is shown in Figure 4.2.1. It involves a conventional SMF-28/G.652 optical fibre span, in this case 83km long, confined by one single pair of FBGs with fixed central wavelength. At least ten pairs of FBGs, each pair at different central wavelength, were used in the experiment. The pair of FBGs was swapped by another pair with different central wavelength once the experimental measurements were taken. The set of FBGs pairs used in this experiment had central wavelengths in the range of 1435nm to 1467nm and 3dB bandwidths of approximately 0.5nm. Details of the FBGs are given in Table 4.2.1.

Table 4.2.1: Table with the center wavelength, reflectivity and bandwidth of the FBGs used for this work

Center wavelength (nm)	Reflectivity (%)	Bandwidth (nm)
1467.8	98.5	0.4
1467.6	97.9	0.4
1465.9	97.8	0.5
1465.2	97.3	0.6
1462.9	98.4	0.5
1463.1	98.5	0.4
1460.3	96.8	0.5
1460.4	96.8	0.7
1445.5	97.3	0.5
1445.7	97.3	0.5
1442.7	97.3	0.5
1442.9	97.0	0.9
1440.3	96.5	0.7
1439.9	96.8	0.8
1437.5	99.0	0.5
1437.5	98.9	0.5
1435.3	97.4	0.6
1435.3	97.2	0.7

The system was bi-directionally pumped by Raman fibre laser sources at 1366nm with the pumps being coupled into the fibre through WDMs located at each end of the system outside the laser cavity. The system is therefore essentially a second order Raman pumping scheme but with the gain in the 1550nm region being provided by lasing in the 1455nm region rather than by a multi-wavelength cascading external pump configuration. The output spectra from the system were measured using an optical spectrum analyzer (OSA).

The use of this configuration for transmission applications and the details of how quasi-lossless propagation conditions are achieved can be found in references [24][78]. Here, we will focus on the optimisation of the system to provide a wider spectral gain region around 1550nm without the need of modifying the simple pumping structure of a standard URFL.

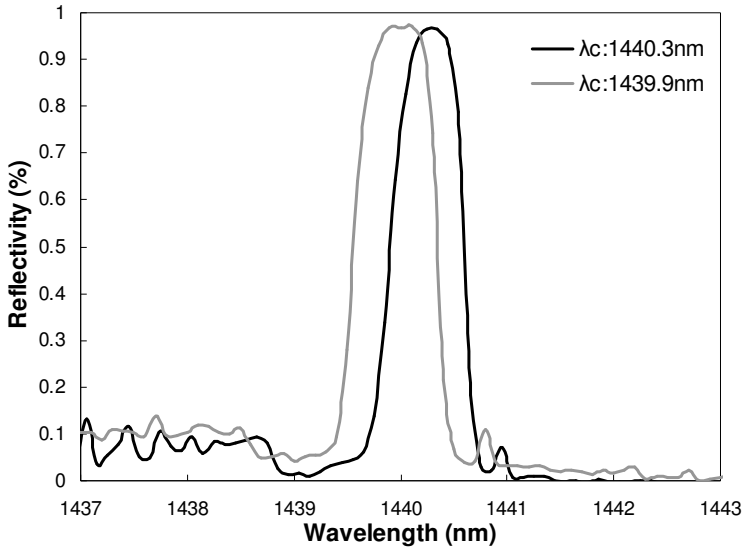

Figure 4.2.2: FBG spectral profile for a pair of FBGs with central wavelength at 1440nm.

As far as possible practically, the FBGs at each end of the cavity had matched reflectivities, bandwidths, and near Gaussian profiles. Figure 4.2.2 shows an example of the pair of FBG spectral profiles with central wavelength at 1440nm.

The FBG grating pair is varied in the experiment for other pairs with central wavelength over the range of 1435nm to 1467nm. The goal is to find the optimal FBG pair which central wavelength value provides the best spectral response. This range of wavelengths was chosen as it corresponds with the high Raman gain region of the first Stokes shift of the 1366nm pump lasers which gives gain in the C-band region (1530nm-1565nm).

Experimental measurements showing the amplifier gain profiles around 1550nm for different cavity grating central wavelengths are shown in Figure 4.2.3. From these results it is clear that there are significant variations in both gain bandwidth and gain flatness as FBG wavelength is changed.

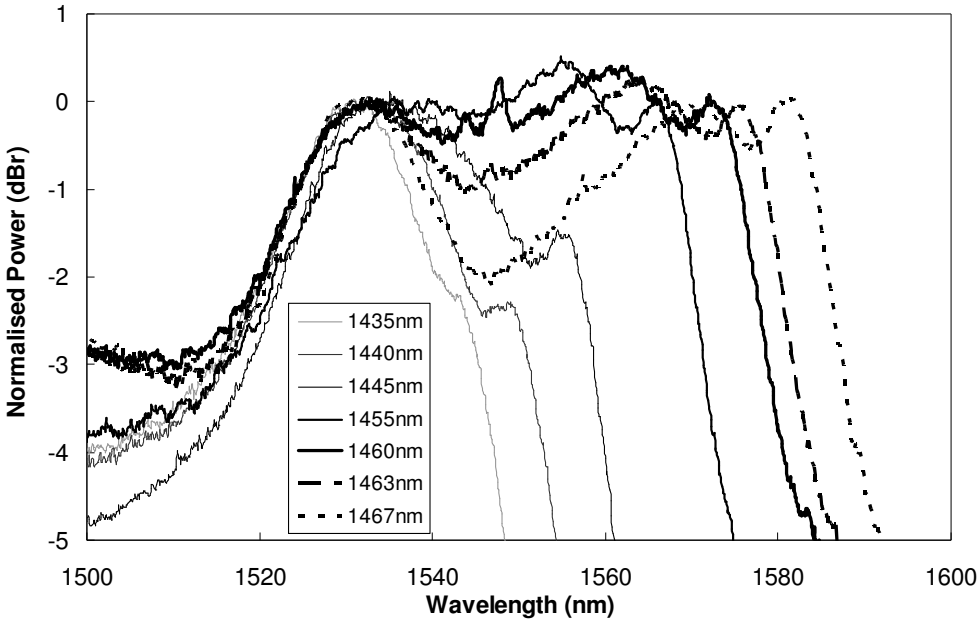

Figure 4.2.3: Output Spectra around 1550nm from URFL systems with a single pair of FBGs at different central wavelengths.

The estimated gain bandwidth is measured taking the peak around 1532nm as power level reference and measuring the bandwidth spectrum that lies within the same range of power levels. For example at 1435nm is only considered the peak at 1532nm and the estimated bandwidth range covers from 1526.5nm to 1535.1nm. For the case of 1467nm, the two reference peaks are at 1532nm at short wavelengths and 1582nm at longer wavelengths. The total estimated bandwidth range is measured at -0.5dB power variation from the reference peaks, in the shorter and longer side of the wavelength range. So for the case of

1467nm the estimated bandwidth range covers from 1526.8nm to 1583.5nm. The estimated bandwidth range as a function of FBG wavelength is plotted in Figure 4.2.4(a). There is a trend towards increased gain bandwidth as the FBG wavelength is increased. This effect can be explained by the fact that the observed gain bandwidth is provided not just by the high-gain region of the 1430-1467nm component, but also, as it was shown previously [19], by the tail of the gain spectrum of the 1366nm pump, which is responsible for the amplification at the lower wavelengths, around 1532nm. By displacing the position of the lasing wavelength slightly off-center from the region of maximum gain and further away from the 1366nm induced peak, we can extend the gain bandwidth of the system in the C-band at the cost of slightly reducing the overall gain flatness.

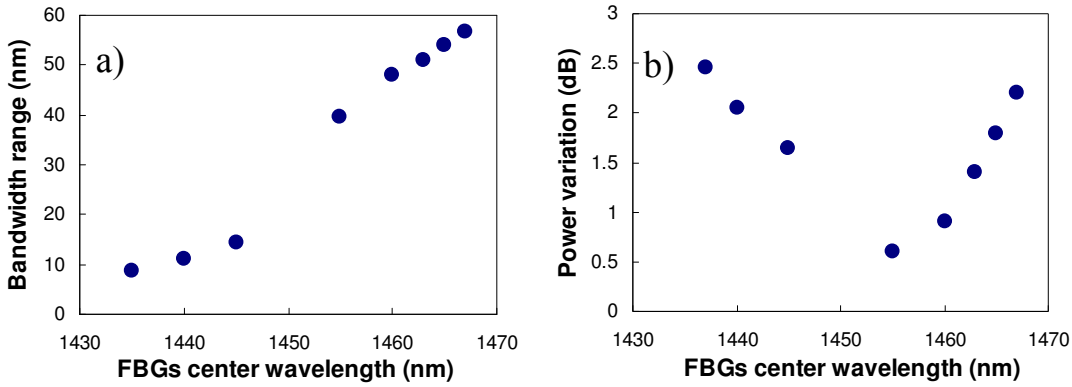

Figure 4.2.4: (a) Estimated bandwidth range and (b) Power variation for URFL systems with FBGs at different center of wavelengths.

Figures 4.2.4(b) show that the power variation or gain flatness across the spectral bandwidth was optimal for 1455nm FBGs. These results gave a ~0.6dB power variation over a ~40nm range covering the entire C band region. The increase in power variations was more pronounced as FBG wavelength was increased from the optimal value, reaching ~1.8dB for 1565nm. So, whilst moving to longer FBGs wavelength would give enhanced spectral coverage, some additional gain flattening would be required in practice to correct for the relatively low gain around 1545nm. FBGs at wavelengths longer than 1468nm were not available for this experiment. However, it is not anticipated that much further improvement to spectral bandwidth would be possible as the FBG wavelength needs to remain within the Raman gain bandwidth of the first Stokes shift of the 1366nm pump lasers.

At FBG wavelengths shorter than 1455nm there is a reduction in both gain bandwidth with the long wavelength end of the C band being compromised. Gain flatness is more difficult to define in this regime as the gain spectrum tends towards a single peak at ~1532nm.

In conclusion, using FBGs at longer centre wavelength can enhance the spectral coverage, up to 57nm when using FBGs at 1467nm. In practice, though, additional gain

flattening would be required to compensate the increase in power variation within the spectral range resulting from such bandwidth extension.

4.3 Spectral flatness

The use of multi-wavelength pump sources in distributed Raman amplification to increase the bandwidth coverage and spectrum flatness is well known [18][79]. It involves adjusting each individual pump in such a manner that the total power provides a flat spectrum covering the desirable bandwidth range. The main disadvantage of this technique relates to the cost of each extra pump source (both the cost of the unit and the increased running cost). Following a similar line of investigation to the previous section, here we try to focus the experimental work in improving the spectrum flatness whilst still keeping the same simple URFL pumping structure. The main changes relate to the FBGs. Instead of using a single pair of FBGs, the URFL system is build with two pairs of FBGs, creating multi-cavities at different centre of wavelengths. This principle is not limited to a maximum number of two FBGs pairs within the cavity, as it could be used with two or more pairs of FBGs. Still, each extra FBGs pair implies extra losses within the system, therefore an increase of the pump power required with the number of FBGs pairs is expected.

The experimental set-up is schematically depicted in Figure 4.3.1. As in the previous section, it uses 83km of conventional G652/SMF-28 optical fibre span, confined by two pairs of FBGs. The specifications for the FBGs used in this experiment are shown in Table 4.2.1, with central wavelengths in the range of 1435nm to 1467nm and 3dB bandwidths of approximately 0.5nm. The system is bi-directionally pumped by Raman fibre laser sources at 1366nm with the pumps being coupled into the fibre through WDMs located at each end of the system outside the laser cavity. The system is a second order Raman pumping scheme with the gain in the 1550nm region being provided by lasing in the 1460nm region rather than by a multi-wavelength external pumping configuration. The output spectra were measured using an optical spectrum analyzer (OSA).

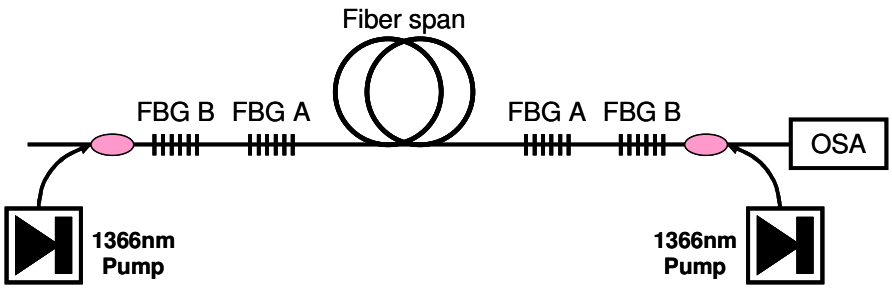

Figure 4.3.1: Schematic diagram of URFL multi-cavity experimental set-up

The first pair of FBGs was chosen to operate with a central wavelength of 1463nm, which gave a broader gain bandwidth range, approximately 51nm (defined as described in the previous section), but higher power variation than the 1455nm FBGs, i.e. 1.4dB power variation within the bandwidth range. A second pair of FBGs at lower wavelength was then added with the intention of providing better gain flatness and specifically to improve the gain in the 1545nm region. The two main parameters for this experiment were the FBGs central wavelength and their reflectivity. Although all the FBGs used in the experiment were within the Raman gain spectrum, their Raman gain coefficient were different, hence the need to balance their contribution through their reflectivity.

The results in Figure 4.3.2 show that adding a pair of grating with central wavelength at 1440nm to the previous pair with central wavelength at 1463nm, improve the power variation across the bandwidth spectrum range 1530nm-1577nm. The power variation along the spectral range could be decreased from 1.4dB (single pair at 1463nm) to 0.7dB (both pairs) without affecting the gain bandwidth. However this is only possible with a considerable increase in the pump power, as the Raman gain at 1440nm is considerably lower than at 1455nm.

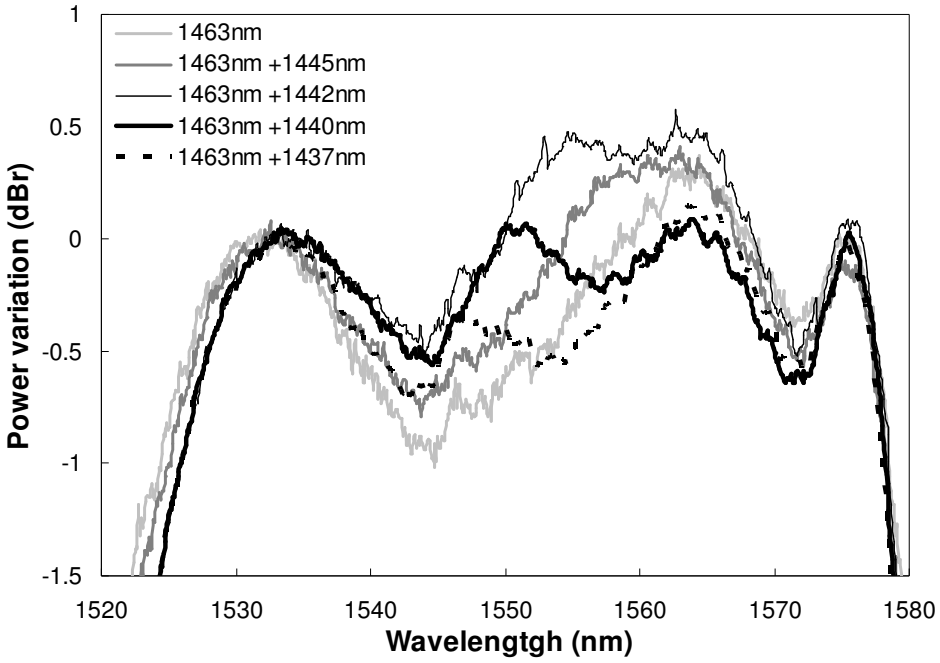

Figure 4.3.2: Spectral profile around 1550nm from URFL systems with combinations of FBG pairs at several central of wavelengths.

The power variation plotted in Figure 4.3.3 is measured similarly to the previous section. The peaks at 1532nm and 1576nm are used as reference of the spectral bandwidth range. The power variation between these two wavelengths is measured from the spectral

profiles and plotted versus the pair of FBGs used for each case. The details of the FBGs used for these results are in Table 4.2.1.

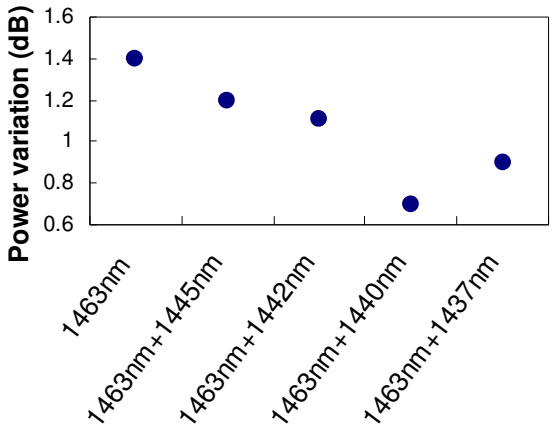

Figure 4.3.3: Power variation from URFL systems with combinations of FBG pairs at several central wavelengths.

Figure 4.3.4 shows how the output spectrum changes with pump power for the optimal (1455nm FBGs) single wavelength system and for the dual wavelength system (1463nm+1440nm). The power variations are measured relative to normalised power for the optimal pump value.

For the single wavelength system the total pump power for minimum power variation was 1300mW. Decreasing pump power led to a reduction in the gain at longer wavelengths, whereas at higher pump powers the spectral peaks at 1555nm and 1566nm became more pronounced.

In the dual wavelength system the total pump power had to be increased to 2265mW for minimum power variation. This is because simultaneous lasing at both 1463nm and 1440nm has to be achieved in the dual wavelength case. The dual wavelength system shows similar trends to the single wavelength system when pump power is increased or decreased in relation to the optimal value.

The required increase in pump power for the dual-wavelength system renders this method impractical for improving gain flatness, unless this improved gain flatness is required during transmission, i.e. for extended spatio-spectral transparency [78]. If the extended bandwidth provided by longer wavelength gratings is required only in terms of overall gain, the use of an external gain flattening filter would be preferable to a 450mw increase for each pump laser. Similarly, the increase on pump power requirement if we were to use longer wavelength gratings makes it impractical to further displace the central wavelength beyond 1463nm, as the Raman gain drops considerably out of the range of 11 to 15.5THz frequency shift from the pump source. Furthermore, it is important to point out that

the right combination of reflectivity between the pairs of FBGs used is critical. If these are not well matched there is a tendency for the resulting spectral profile to be dominated by only one of the FBGs pairs.

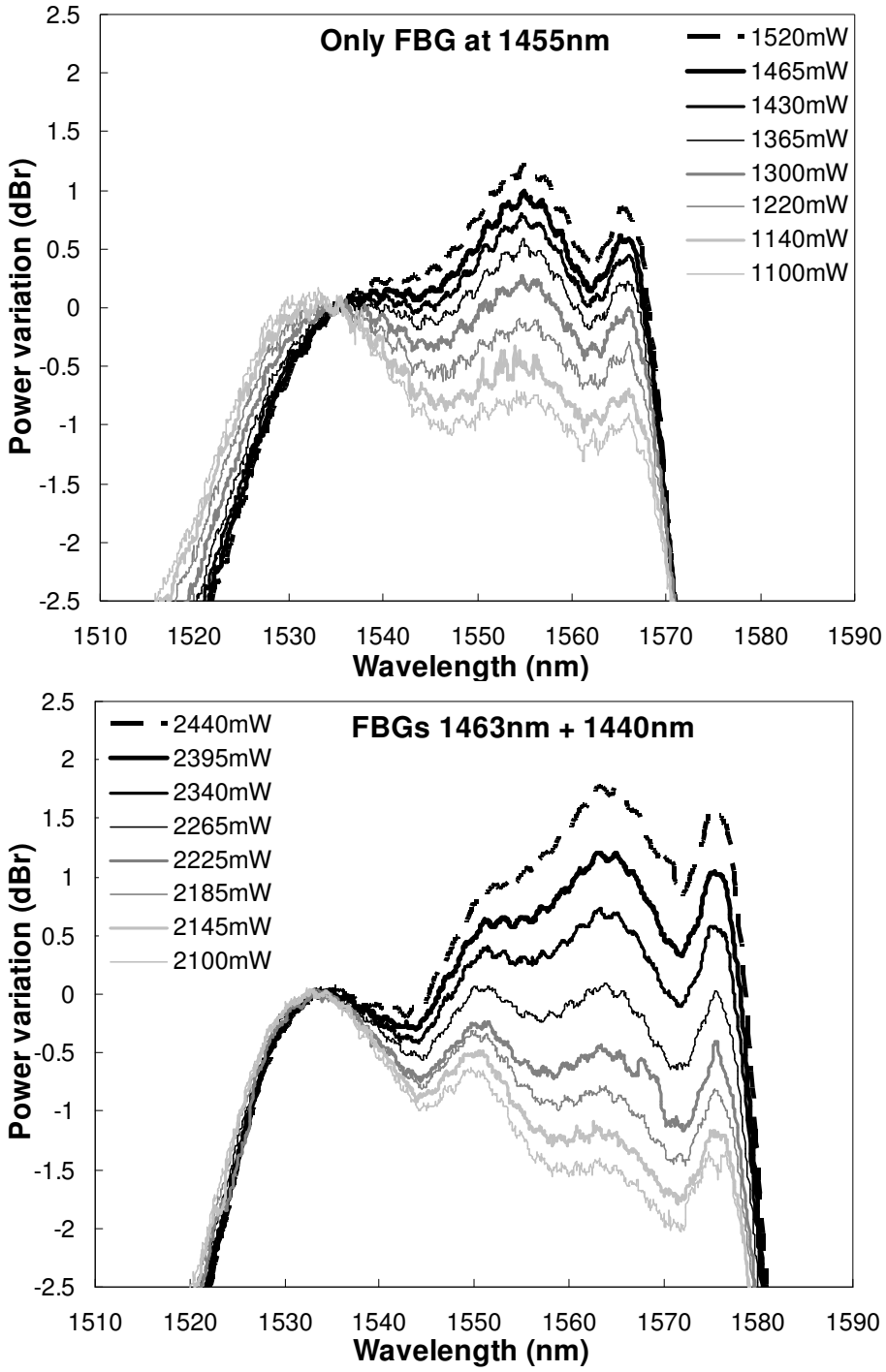

Figure 4.3.4: Spectrum profile variation for increasing pump power for the case of top) single pair of FBGs at 1455nm and bottom) a combination of the FBGs at 1463nm+ 1440nm.

Therefore, the use of multi-cavity within the URFL system provides an extended spectrum bandwidth, approximately 51nm, with a total power variation along the spectrum range of 0.7dB, just 0.1dB greater than the optimum value for a single pair of FBGs at

1455nm. Unfortunately the demand on increasing pump power doesn't make it in most circumstances a practical alternative to the multi-wavelength external pumping scheme.

4.4 Type of fibre

Most of the fibre used in the field with application in optical communications is standard single mode fibre SMF-28/G652, although there are other types of conventional fibre used in much smaller scale and as part of optical modules. Since one application area of URFL is optical communications, the evaluation of these other existing standard fibres under the URFL scheme seemed reasonable. Therefore as part of the experimental investigation on URFLs, the behaviour of several conventional optical fibres were evaluated and compared with the single mode fibre (SMF).

The scheme of the experimental set-up corresponds to this one depicted in Figure 4.2.1, that is the basic URFL scheme. The main fibres used were single mode fibre G652/SMF-28, large effective area fibre (LEAF), TrueWave-RS (TW), and dispersion compensation fibre (DCF). The technical details of these fibres are in Table 4.4.1.

Figure 4.4.1 illustrated the experimental spectrum profile from 1350nm to 1600nm for 46km of TW, 45 km of LEAF and 42km of SMF at pump powers around 1W. The broadening behaviour of TW fibre around the first Stokes peak, 1455nm, is much larger than the one provided by any of the other fibres. The cause of this effect is its zero dispersion being around the first Stokes shift. The first Stokes behaves as a secondary pump and generating the broadening in that region. This effect will have consequences when evaluating the spectral profile around 1550nm, see Figure 4.4.2, in the sense that TW can not provide the desirable spectrum flatness within the same spectral bandwidth as SMF or LEAF. Given a TW with zero dispersion further away from the first Stokes peak, 1455nm in this case, the behaviour of the spectrum profile around 1550nm is likely to be different. Further work regarding TW and its spectral behaviour depending on the relation between the dispersion value and the first Stokes wavelength should be considered.

Table 4.4.1: Fibre details

	SMF	LEAF	DCF	TW
Dispersion at 1550nm (ps/nm-km)	16.3	4.2	-90.9	4.4
Dispersion at 1455nm (ps/nm-km)	10.8	-3.7	-64.5	0.1

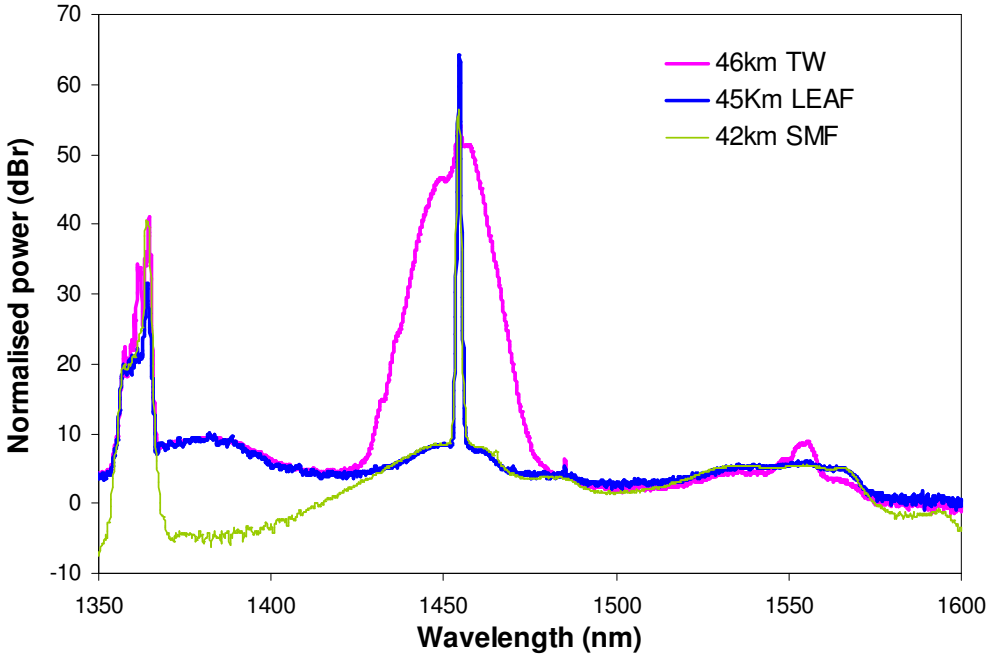

Figure 4.4.1: **URFL Spectrum profile from 1350nm to 1600nm for different type of fibres**

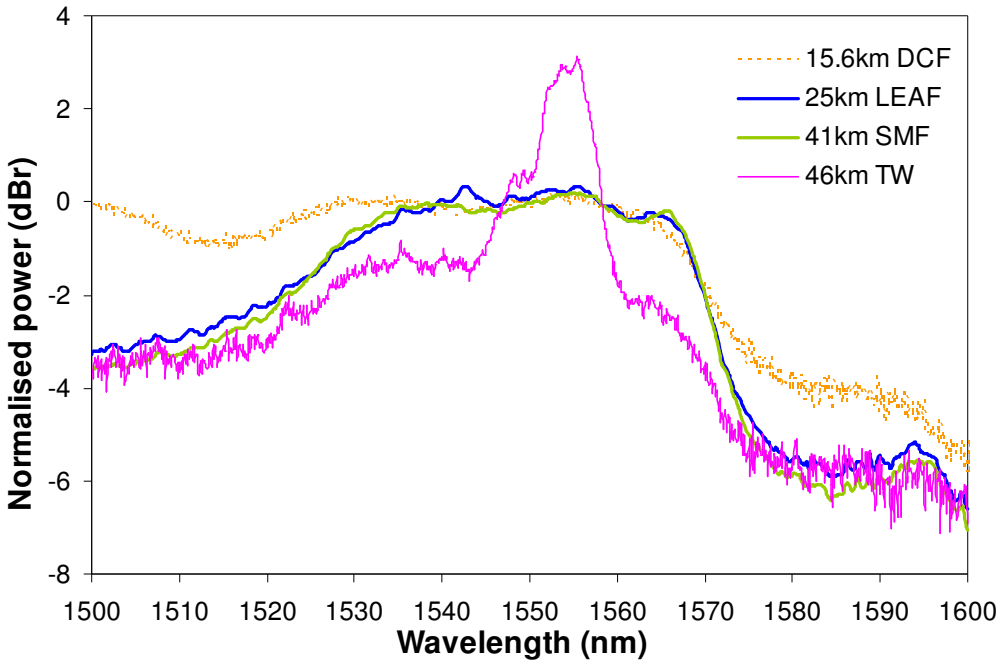

Figure 4.4.2: URFL Spectrum profile around 1550nm for different type of fibres .

A closer look to the behaviour of the optical fibres around the 1550nm region, see Figure 4.4.2, shows that SMF, LEAF and DCF behave in a similar manner covering the bandwidth 1533nm to 1565nm with minimum power variation in that region. Hence DCF seems feasible when its use is intended for virtually lossless transmission or as a distributed amplifier [15][19][21][23][24][77][78][80].

4.5 Pump depletion

The amount of launch input signal can affect the amplifier performance by modifying the transmission spectrum profile level. To explain this phenomenon we have to consider the

Raman scattering effect as a nonlinear two photon process, where the pump power is not only affected by attenuation in the fibre, but in fact the pump and Stokes waves interact with each other following, for the case of second order distributed Raman amplification, the set of coupled equations 3.2.1 to 3.2.5 described in Chapter 3. In the simplest case of a first order system, and in the absence of all losses, it can be deduced that the total number of photons in the pump and Stokes waves remain constant during the process of stimulated Raman scattering as expressed by the following relation.

$$\frac{d}{dz}\left(\frac{P_S}{\nu_S}+\frac{P_P}{\nu_P}\right)=0\,, \qquad \textbf{4.5.1}$$

where P_i represents the pump and signal powers with the optical frequency for each spectral component represented by ν_i.

In practice, as the pump power increases, it reaches a threshold value where the Stokes waves start increasing linearly with pump power. As the Stokes wave reaches a comparable value to the input pump power, this leads to the attenuation of the input pump power. This pump depletion effect can be easily observed by using an external input signal at the same frequency as the Stokes wave. Therefore the amount of Raman pump power required for quasi-lossless transmission will have some dependence not only on the cavity design features but also on the amount of input power transmitted. Only in the case of relative small values of input signal this dependence can be considered negligible.

Here we show some experimental results related to pump depletion. The scheme of the experimental set-up is depicted in Figure 4.5.1. It involves a conventional 83km of single mode fibre confined between a pair of high reflectivity (approximately 95%) FBGs with a central wavelength at 1455nm. The URFL system is pumped at 1366nm through WDM coupled into the system. A set of 13 laser diodes with centre wavelengths ranging between 1534nm to 1557nm were launched as transmission signal into the URFL system and measured by an OSA at the other end of the URFL.

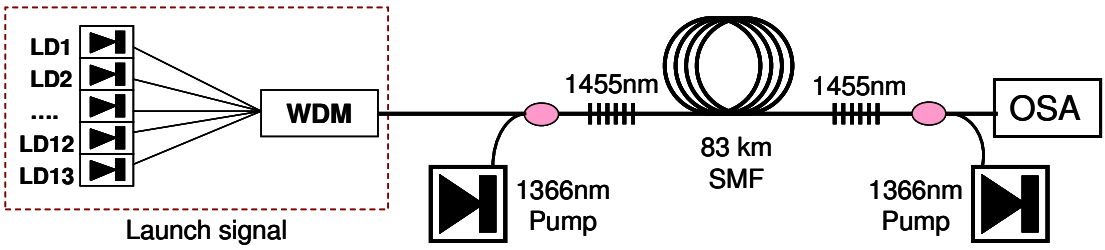

Figure 4.5.1: Experimental set-up for multi-wavelength signal transmission on URFL

Figure 4.5.2 show the experimental traces measured on the OSA for the following cases. The "QL spectrum" plot shows the trace measured by the OSA when using only Raman

pump at 1366nm. The launch signal from the laser diodes is switched off. The pump ratio and the amount of pump power were optimised for quasi-lossless transmission, minimum power variation along the length of the fibre and across the spectral bandwidth, 1528nm to 1568nm. The "Signal over QL" plot shows the effect of the combination of the previous Raman pump power at 1366nm and the launch signal from the laser diodes between 1534nm to 1557nm. The final trace "Launch signal" is the corresponding trace measured by the OSA with the external input signal from the laser diodes switched on and the Raman pump powers switched off. The total signal from the laser diodes was measured in the power meter just before launching it into the URFL, giving a total value of 14.5dBm.

As it can be observed in Figure 4.5.2, launching a considerable amount of signal, 14.5dBm in this case, at the same frequency as the Stokes wave produces pump depletion. This pump depletion relates to the amount of launch signal, as it will be shown in later results, and not to the intrinsic attenuation of the fibre. The pump depletion is not linear along all the bandwidth range, affecting in a greater measure the longer wavelengths range of the Raman gain profile. The effect is similar to a drop in the pump power. For instance, in the experimental case described here, the drop of the spectrum profile at 1566nm is 0.95dB whilst at 1530nm is 0.35dB when launching a signal power of 14.5dBm.

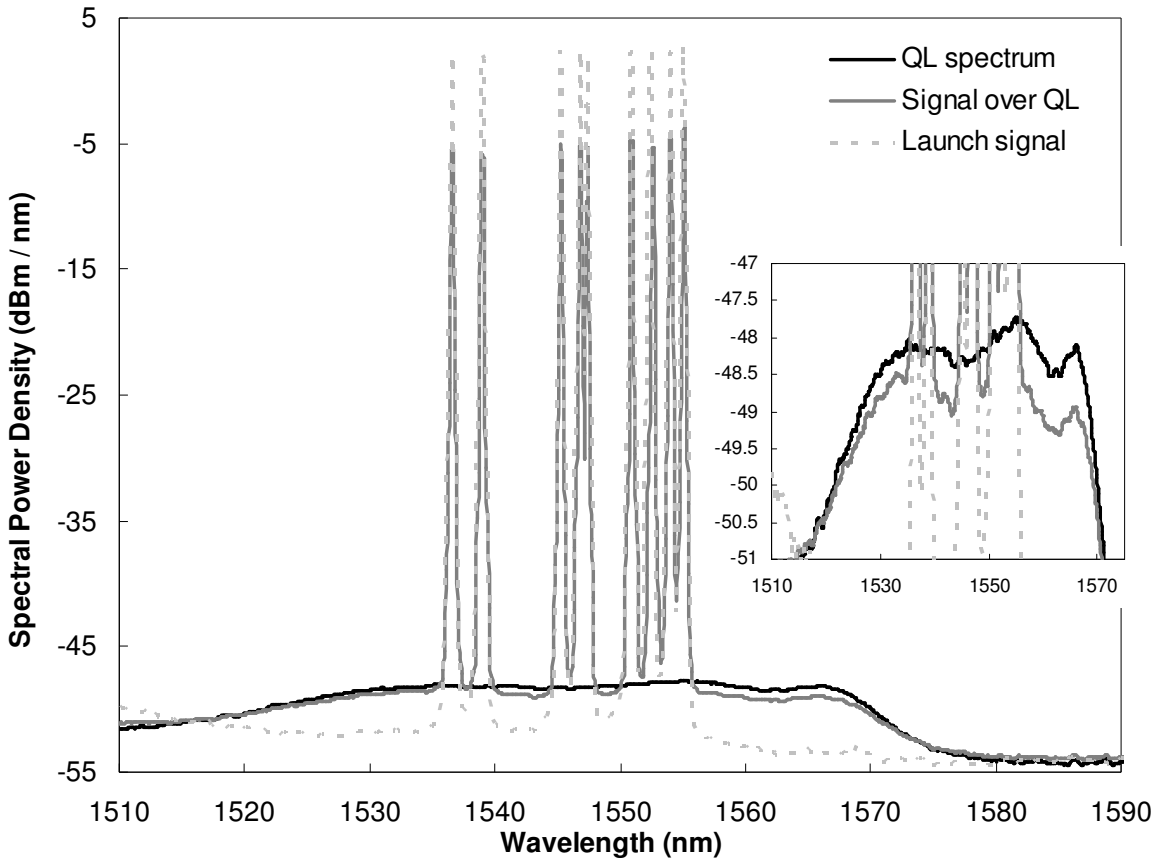

Figure 4.5.2: Spectrum profile for launch signal, URFL profile and transmitted signal

The variation of the spectral power density level with the launch signal at two particular wavelengths, 1556nm and 1530nm, is represented in Figure 4.5.3 through the plotted experimental points. The drop in power was measured by launching through the URFL an increasing number of channels with the laser diodes centre wavelengths ranging between 1534nm to 1557nm and saving the spectrum in the OSA as shown in Figure 4.5.1. The launch power as each channel was switched on was previously measured directly with a power meter.

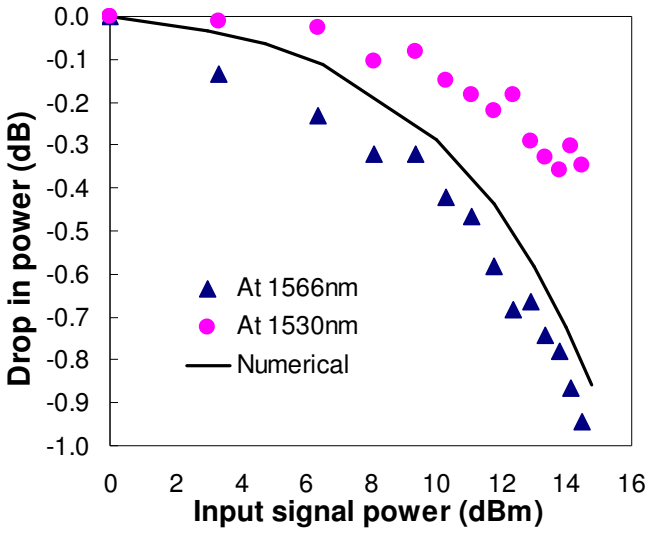

Figure 4.5.3: Experimental and numerical results of power drop with increasing launch signal power.

The black line from Figure 4.5.3 represents the numerical results, from the set of coupled Equations 3.2.1 to 3.2.5 described in Chapter 3, for an URFL system of 80Km SMF and FBGs set at 90% reflectivity. The calculations are optimised for a system with zero-lossless transmission using 1mW input signal. As the launch input signal is increased the pump power requirement for maintaining the same level of zero-lossless transmission is increased. The difference between the required pump power for each increasing launch input signal and the initial one is plotted in the same graph as the previous experimental points.

Although the experimental and numerical results represent slightly different power drops, up to certain extend they are related as the drop of the spectral power density level will relate directly to the drop in pump power. Therefore there is a proportional relation between both values.

The length of fibre span can affect, to a minor degree, the spectral flatness performance of the URFL. As part of the experimental investigation in URFL, spectrum profile traces around the second Stokes 1550nm, were measured for different span lengths.

The experimental set-up is the basic URFL system already described previously, Figure 4.2.1, a fibre span confined between a pair of FBGs and pumped bi-directionally. Several

lengths of conventional single mode fibre were set as fibre spans and their spectrum profile measured using the OSA.

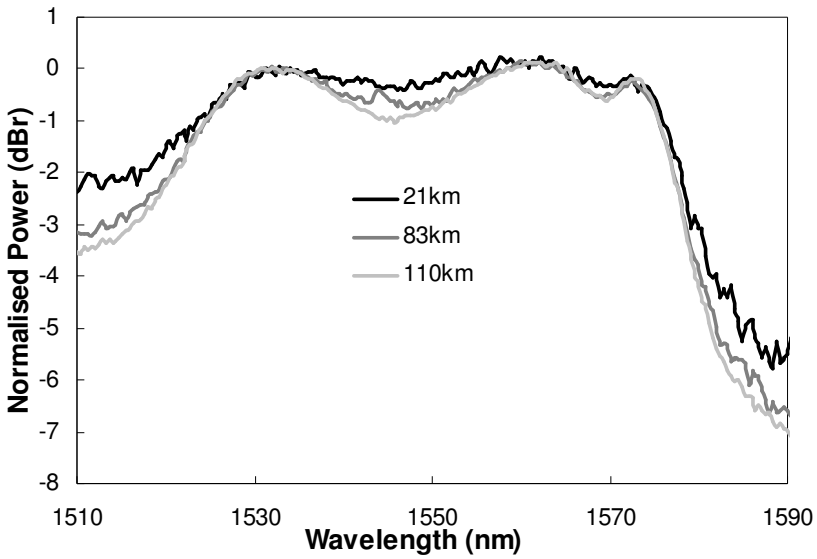

Figure 4.5.4: Spectrum profile for bi-directional 2nd order Raman amplification system with a pair of FBGs at 1460nm at several SMF span lengths

The experimental spectrum profiles for a system with the centre of FBGs set at 1460nm are plotted in the Figure 4.5.4. The bandwidth range between 1528nm to 1575nm approximately seems to be covered for all the span fibres regardless the span length. The main difference among all the lengths has to do with the power variation along the bandwidth spectrum, especially on the region around 1546nm. As the fibre span length increases the power level around this region is reduced, giving an overall increase of the total power variation along the spectral bandwidth.

The lower spectrum profile level around 1546nm can be understood as the effect of the pump depletion in a slightly different way as shown in Figure 4.5.2. Longer fibre spans requires greater Raman pump powers to achieve similar lossless condition, the output power level is equal to the input power level. Also, as the span length increases the overall fibre attenuation is greater. The overall spectrum profile is the result from both contributions, fibre attenuation and Raman gain, which differs at different span lengths

4.6 SRS assisted by Rayleigh-backscattering

So far we have investigated the bandwidth and flatness of the URFL gain spectra. The following investigation relates to extreme cases where Rayleigh scattering can be used as feedback component. Stimulated Raman Scattering is assisted by Rayleigh-backscattering.

Light scattering occurs as a consequence of fluctuations in the optical properties of the medium. The Rayleigh scattering in optical fibres is a result of the inhomogeneous distribution of the molecules during the fabrication process of the fibre. Regardless of the fabrication technique of the optical fibre, this random density distribution will be present in all the fibres. This inelastic scattering effect is one of the major sources of attenuation in optical fibres, with a value of approximately 0.15dB/km for a wavelength of 1500nm [81].

Although most of the scattered light escapes through the cladding, a part of the scattered light, proportional to the wavelength, λ^{-4}, will be coupled into the core mode supported by the single mode fibre structure. The behaviour of this random scattering has the effect of a distributed cavity reflector. The corresponding coefficient of this Rayleigh back scattering effect is quite small. And usually it is considered an extra source of noise to take in consideration in distributed amplifiers. In the case of URFLs it can become an important effect if distributed Raman amplified over long lengths. For instance, the reflections provided by the distributed feedback of Rayleigh backscattering can make possible lasing from an open laser cavity if enough input power is supplied [73].

4.6.1 Rayleigh-scattering and fibre end reflections

The basic material of optical fibres is silica glass, therefore small optical reflections are expected at the interface between glass/air. In the following experiment we wanted to minimise all external reflections, in such a way that the only feedback was provided by Rayleigh backscattering. With this purpose in mind, two experimental systems were build, involving a conventional SMF fibre of 41km long and a pump source coupled to the fibre through a WDM and operating at 1455nm. The pumping scheme is different to the previous experiments. Here the pump is at 1455nm instead of 1366nm. The optical spectrum was monitored using an OSA as indicated in Figure 4.6.1. The only difference between both systems is the fibre termination ends, either flat (left diagram) or angle ends (right diagram).

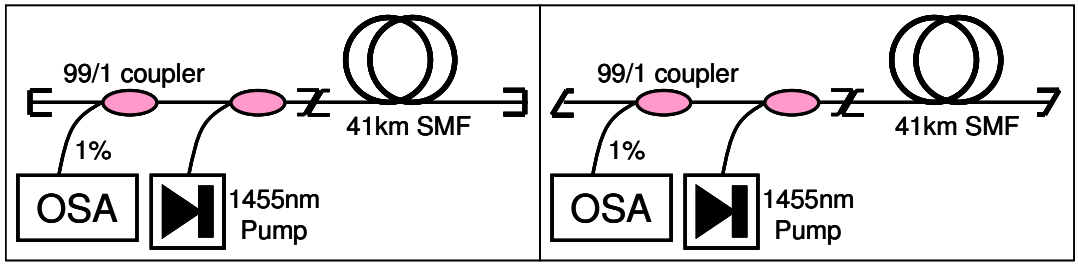

Figure 4.6.1: Experimental set-up for 41km system without any FBGs and endings on (a) flat end and (b) angle end

The experimental optical spectra for both systems was measured at several pump powers, Figure 4.6.2(a1): 1270mW, (a2) (b1): 1450mW, and (a3) (b2) 1735mW. The general behaviour in both cases is similar. The pump power is increased and at certain point a threshold value is reached where noisy pulses in a random and chaotic behaviour are generated. If the pump power is increased further more, then the generated pulse takes a broadband shape of the Raman gain curve of the amplified spontaneous emission superimposed with the random spikes of stochastic pulse generation, Figure 4.6.2(a1) for flat ends and Figure 4.6.2 (b2) for angle ends. Given more input power, a continuous wave regime is reached with strongly suppressed amplitude fluctuations and a stable optical spectrum. The stabilised optical spectrum shows two narrow lines near the Raman gain maximum, see Figure 4.6.2 (a3).

The main difference between both systems is the pump power threshold level where the spiky pulses are generated and the continuous wave regime is reached, 1270mW for the case of flat ends and 1735mW for angle ends. The system with the optical fibre ending in flat seems to carry extra reflections supported by the single mode fibre. Those extra reflections will lower the pump threshold level to achieve the lasing behaviour already described. Angled ends have the effect of minimising the end reflections.

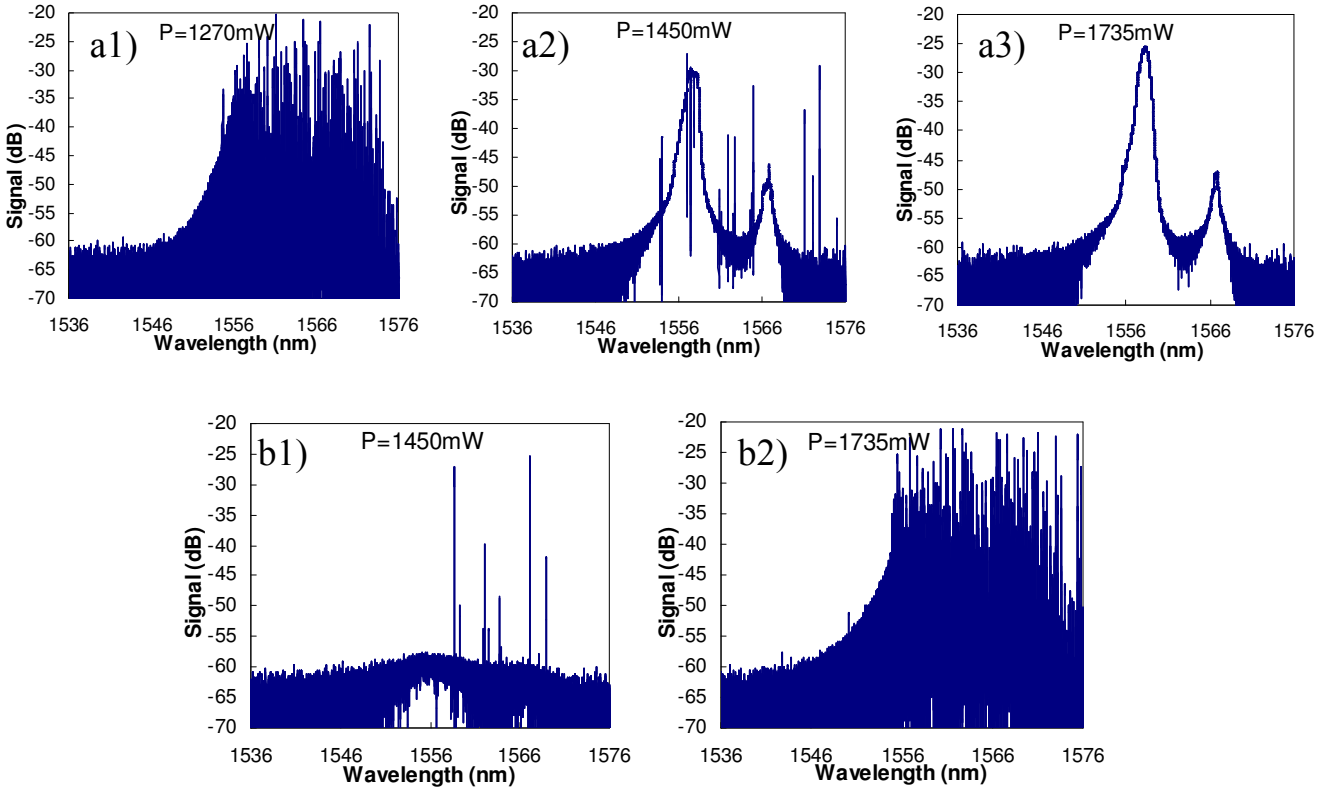

Figure 4.6.2: Output spectrums for the 41km SMF systems at several pump powers.

Similar experimental results were checked with longer lengths, 82km, although bi-directional pumping was used on the experimental set-up instead of only one pump. The

laser behaviour already described was similar to the 41km span length. The main difference was the increase of input pump power to achieve the stabilised lasing regime.

Therefore maximum care should be considered when building system based in Rayleigh scattering effect as extra reflections from the fibre ends may mislead experimental measurements.

4.6.2 Dual wavelength output with Rayleigh-scattering feedback

Lasing in a cavity as long as 270km has been reported [82] in which in addition to typical spectra with mode structure new features have been discovered, namely spectral components generated at wavelengths far from the FBG reflection spectrum with spiky dynamics of the laser output, which appear to be more pronounced near the threshold and at non-symmetric pumping. Moreover, the characteristics of such an asymmetric Raman laser appear almost independent of fibre length in some range, which means that the distributed cavity reflector formed due to the back reflection in the fibre itself, i.e. Rayleigh back scattering (RS) is very significant and strongly influences the characteristics of such a laser. A more detailed study of the RS effects in URFLs proved that the distributed feedback due to the Rayleigh back scattering at propagation of light between FBG reflectors may be comparable with the feedback provided by the FBG itself [83]. Consequently, Raman lasing in the fibre span limited by a lumped FBG reflector at one side only appears possible due to significant reflection from the RS-based "random" distributed mirror at the other side.

In the work presented here we experimentally demonstrate a 200km long dual wavelength Raman laser where feedback is based on the combination of two independent lumped FBG reflectors at slightly different wavelengths and distributed Rayleigh scattering in the same fibre span. It will be shown that the two Raman lasers characteristics are independent from each other and each of them exhibit quite specific temporal behaviour and shapes of optical and RF spectra.

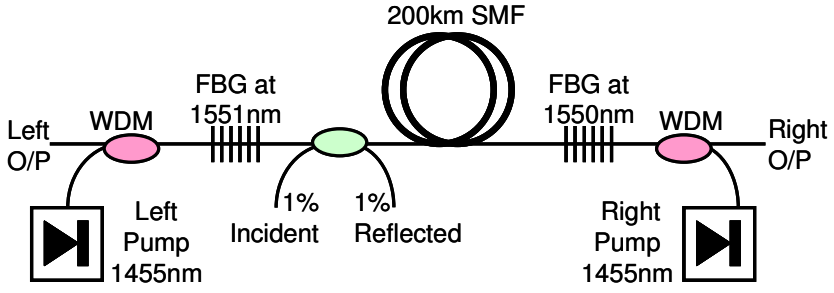

Figure 4.6.3: Schematic description of the experimental set-up

The experimental setup for the studied ultralong Raman laser cavity is schematically illustrated in Figure 4.6.3. We used a configuration with pumping at 1455nm and Raman

lasing at ~1550nm, for which losses are minimal. This offers the possibility of lengthening the URFL cavity, in analogy with the schemes in [82][83]. Two pump lasers were coupled into the fibre span through wavelength division multiplexers (WDM). Two highly reflective FBGs with reflection coefficient R~98% at different central wavelengths are spliced to the fibre span. A FBG with a central Bragg wavelength of 1551nm is spliced to the left end of the span and another FBG with a central Bragg wavelength of 1550nm is spliced to the right end of the span. The width of the reflection profile of the FBGs is less than the 1 nm separation between their Bragg wavelengths. Fibre ends were angle-cleaved to eliminate reflection.

The optical fibre used for the experiment is a 200km long spliced sectioned SMF. To measure the Raman laser characteristics of the waves propagating in opposite directions inside the cavity, a splitter with two 1% ports was inserted near the left FBG. Optical spectra were measured with a high resolution (0.01nm) optical spectrum analyzer (OSA). The radio frequency (RF) spectra characterizing laser intensity fluctuations were also measured using photodiode and electric spectrum analyzer (ESA) with a resolution of ~100Hz and the corresponding time domain intensity behaviour was analyzed by means of an oscilloscope with a 50ps temporal resolution.

In spite of the negligibly small overlapping of the FBGs reflection spectra, the scheme pumped by ~1W power at 1455nm from each side exhibits clear laser properties at both FBG wavelengths, but the output appears to be directional: at the left output end, 1551nm radiation (corresponding to reflection maximum of the left FBG) is dominant whereas at the right end 1550nm radiation provides the main contribution. Besides, the left output power at 1551nm depends only on the injected left pump power (right pump power may be even zero), whereas the right output power at 1550nm depends on the right pump power only, without any significant cross-correlation.

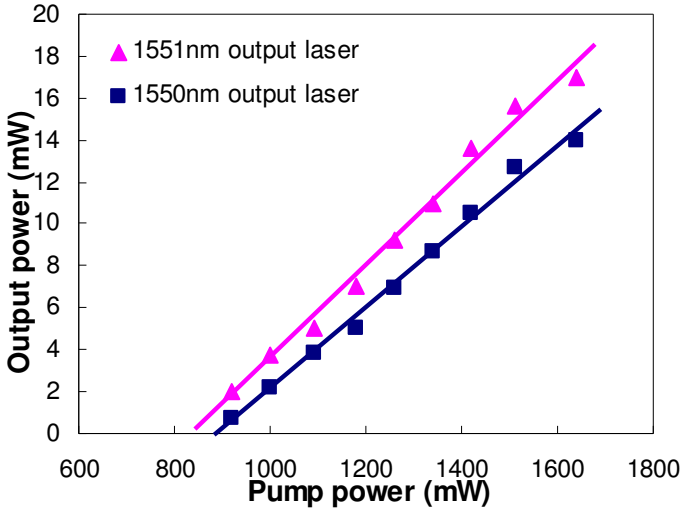

Figure 4.6.4: Laser output power for the dual wavelength output as a function of pump power.

Power curves for each wavelength are shown in Figure 4.6.4 versus the corresponding pump power. They are almost linear and close to each other. The slight difference in thresholds and slopes may be reasoned by different losses of FBGs, WDM couplers and splices at the left and the right parts of the scheme. Therefore, for such a long cavity, most radiation coming from the left-side grating is reflected via Rayleigh backscattering before ever reaching the right side grating, and vice-versa. Hence two independent cavities are created within the same fibre span. Moreover, since most of the Raman gain takes place close to each of the fibre ends, the two cavities can be considered to be independently pumped too, as long as we are near the threshold.

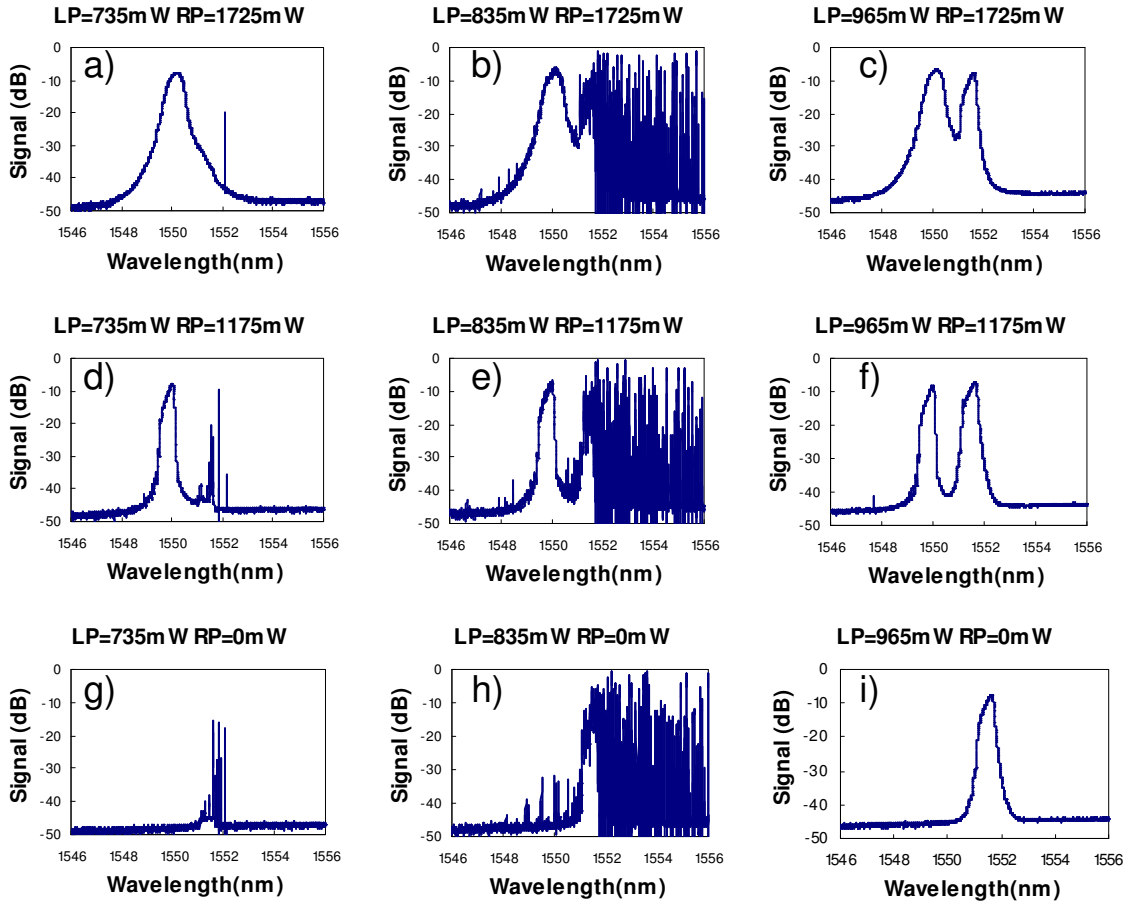

Figure 4.6.5: Experimental spectrum at several left (LP) and right (RP) pump power values measured via the 1% incident output.

In Figure 4.6.5, optical spectra measured inside the cavity via the 1% incident port are shown for different pump powers. The power provided from the right pump (RP) is zero for Figures 4.6.5 (g), (h) and (i) with the left pump (LP) increasing value, corresponding to 735mW, 835mW and 965mW respectively. The power from the left pump is fixed at

735mW for the Figures 4.6.5 (g), (d) and (a) and the power from the right pump increases from 0 to 1175mW and 1725mW respectively. With a single pump (e.g. for the left pump) the spectra behave similarly to those in a single FBG laser [83]: near the threshold (that corresponds to the left pump power of ~735mW) the optical spectrum consists of a narrow peak corresponding to the left FBG reflection spectrum centred at 1551nm and broadband spiky continuum.

At the same time, the measured radio frequency (RF) spectrum shows no sign of mode beating (modes corresponding to a cavity round trip frequency f=c/2Ln would be expected for a closed grating cavity, as seen in [82]. Instead, a single RF peak at ~11GHz is clearly seen (corresponding to the Brillouin scattering Stokes shift), see Figure 4.6.6(b), similar to that on a self-Q-switched laser with RS-Brillouin mirror [80][84]. In the time domain, see Figure 4.6.7(b), stochastic pulses are generated in this regime.

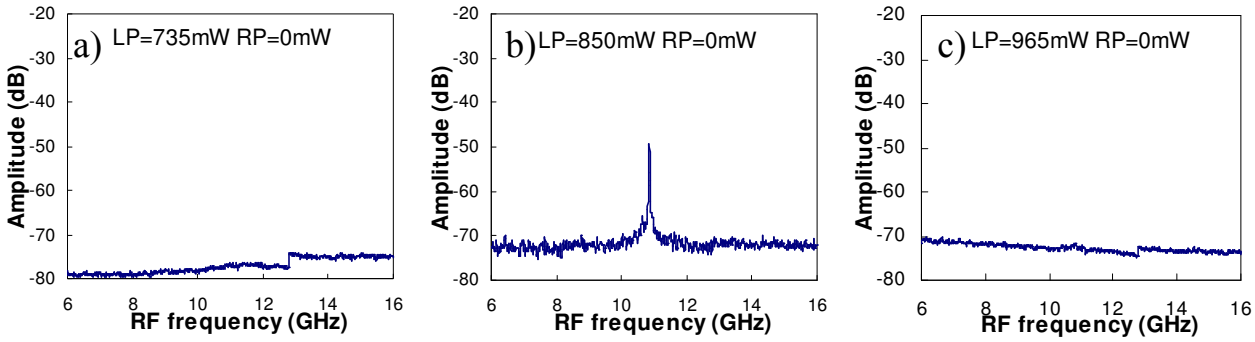

Figure 4.6.6: RF spectra at several left (LP) and right (RP) pump power. a) LP=735mW, RP=0mW, b) LP=850mW, RP=0mW; c) LP=965mW, RP=0mW.

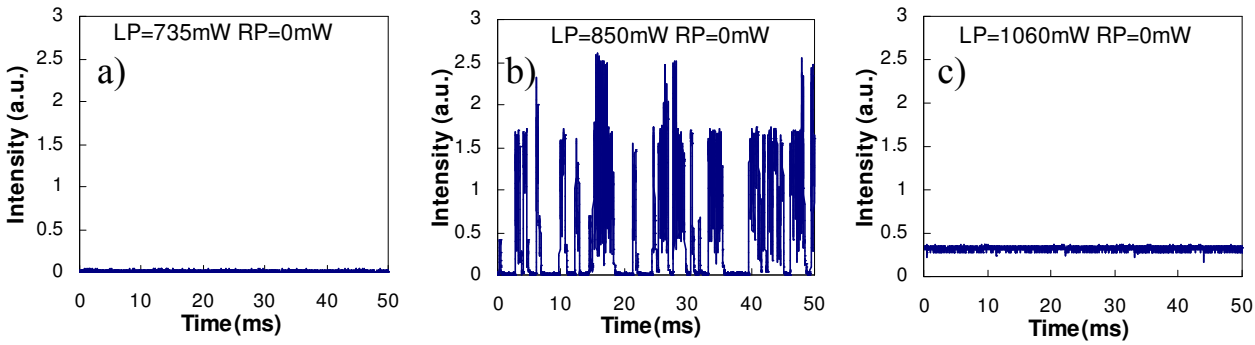

Figure 4.6.7: Time domain behaviour at several left (LP) and right (RP) pump power. a) LP=735mW, RP=0mW, b) LP=835mW, RP=0mW; c) LP=1060mW, RP=0mW.

Well above the threshold, only the peak corresponding to the FBG reflection spectrum is present, while the Brillouin peak in RF spectrum disappears and the operation of

the Raman laser remains quasi-stationary, see Figures 4.6.6(c) and 4.6.7(c). For the right pump only, the corresponding traces are similar but the generation occurs at the right FBG reflection wavelength. Well above threshold, a single wavelength peak at 1550nm is observed. Around the threshold value, the output spectrum will be noisy around the FBG peak (similar as shown previously in Figure 4.6.5(h), the temporal behaviour will be spiky as Figure 4.6.7(b) with a single peak at 11GHz in the RF spectrum, similar to the case of the single left pump. Operating the system with both pumps, although one of then around the threshold level, will add an extra output peak at one of the FBGs whilst the other shows a noisy and spiky behaviour at the threshold (Figure 4.6.5e).

With the two pumps well above the threshold, two separated peaks are present in the optical spectra corresponding to different FBGs reflection at 1550nm and 1551nm, see Figure 4.6.5(c). No peak at 11GHz is observed in the RF spectrum, Figure 4.6.6(c). The intensity is quasi-stationary in the time domain, similarly to the one shown in Figure 4.6.7(c). So, two laser cavities formed by each FBG and RS distributed feedback in the same fibre span operate independently, each of which being similar to the single FBG RS-supported Raman laser described in [83]. Thus, the obtained results clearly prove that a distributed Rayleigh scattering "random" mirror can form a cavity together with each FBG at pumping from this FBG side of the span.

When the distributed Raman gain exceeds the losses in such a distributed cavity, stable laser operation appears possible at the wavelength of corresponding FBG. This laser is "modeless" but its optical spectrum is limited by the FBG reflection curve. When two pumps are applied simultaneously, lasing is possible at two simultaneous wavelengths corresponding to those of both FBGs. These two lasers based on two FBG-RS cavities in a single span are shown to operate independently and stably. Note that this regime does not involve Brillouin scattering leading to self-Q-switched pulse operation [80][84]. Besides, the combined Rayleigh-Brillouin feedback is also utilized for generation of Brillouin-shifted multiple-wavelength combs [85].

We present an experimental demonstration of a 200km long dual wavelength Raman laser based on the Rayleigh scattering utilizing two different fibre Bragg gratings at both side of the same fibre span [86]. The obtained results clearly prove that the two Raman lasers are independent on each other and that a Rayleigh scattering distributed "random" mirror can form a cavity together with a single FBG independent on the other reflector. On the basis of this result, multi-wavelength ultralong fibre lasers with random distributed feedback and multiple gratings at both ends may be developed with the potential for multi-wavelength secondary pump providing extended bandwidth of quasi-lossless transmission. The reported

new laser scheme has a great potential for applications in long-distance communications, as well as in distributed sensor systems based on lasing schemes involving the Rayleigh scattering and reflection from FBGs with different wavelengths [87].

4.7 Conclusion

We have demonstrated that it is possible to provide DWDM-compatible broadband amplification covering the full telecoms C Band using a single pump wavelength Raman amplification technique based on ultralong Raman fibre lasers. Our results show that the gain bandwidth and flatness is dependent of the cavity gratings used: 1455nm FBGs gave 40nm bandwidth which was extended to 57nm using 1467nm FBGs. The increase in bandwidth does however show greater gain variation across the band. Whilst this could be corrected with conventional gain flattening techniques, we have investigated the possibility of using a multi-cavity URFL to improve both gain bandwidth and gain flatness. Our results show that this is possible but requires a large increase in required pump power. The power variation or gain flatness across the spectral bandwidth was optimal for 1455nm FBGs. These results gave a ~0.6dB power variation over a ~40nm range covering the entire C band region. The URFL approach presented here offers a flexible Raman amplification technique requiring only a single pump wavelength. By changing the pump and cavity gratings S or L band amplification would also be possible.

In addition, the brief investigation of TW, DCF and LEAF within the URFL system warns against the use of TW, as its spectra lack the desirable flatness within the same spectral bandwidth as SMF or LEAF. DCF behaves in a similar manner to SMF covering the bandwidth 1533nm to 1565nm with minimum power variation in that region. Hence DCF seems feasible when its use is intended for virtually lossless transmission or in a distributed amplifier.

Furthermore, launching a significant level of input signal power at the same frequency as the Stokes wave produces a pump depletion effect. This pump depletion or pump attenuation is not linear along all the bandwidth range, affecting in a greater measure to longer wavelengths. Consideration of this effect should be taken in account when implementing URFL transmission systems.

The increase of span length within the URFL system does not have any significant impact in the covered transmission bandwidth range. The main difference among all the lengths relates to the power variation along the bandwidth spectrum, especially on the region around 1546nm, for the case of FBGs with centre of wavelength in the region 1455nm. As

the fibre span length increases the power level around this region is reduced, giving an overall increase of the total power variation along the spectral bandwidth.

Finally, we present an experimental demonstration of a 200km long dual wavelength Raman laser based on the Rayleigh scattering utilizing two different fibre Bragg gratings at both side of the same fibre span [86]. The obtained results clearly prove that the two Raman lasers are independent of each other and that a Rayleigh scattering distributed "random" mirror can form a cavity together with a single FBG independent on the other reflector. On the basis of this result, multi-wavelength ultralong fibre lasers with random distributed feedback and multiple gratings at both ends may be developed with the potential for multi-wavelength secondary pump providing extended bandwidth of quasi-lossless transmission. The reported new laser scheme has a great potential for applications in long-distance communications, as well as in distributed sensor systems based on lasing schemes involving the Rayleigh scattering as distributed feedback [83].

Chapter 5

Supercontinuum generation

5.1 Introduction

Supercontinuum (SC) generation is a nonlinear optical process which occurs when a strong single coherent wavelength light source undergoes extreme spectral broadening as it propagates in a nonlinear material generating a strong spectrally continuous output. As the intense light source travels through the medium, it can induce an intensity dependent variation of the refractive index of the medium, which leads to a frequency modulation and as result to an optical spectral broadening and temporal compression. The nonlinear interaction of the pump source and the new spectral components with the medium leads to further complex nonlinear interactions and spectral broadening. The nonlinear processes underlining the SC generation and the resulting optical spectra may differ depending on the initial pump source characteristics and the propagating media.

The origin of SC generation goes back over 40 years ago, with supercontinua generated in bulk glass material and the first intent of understanding nonlinear effects by Alfano [88][89]. The authors explained the SC formation though self phase modulation (SPM) and four wave mixing (FWM). Later on, other researchers in the field contributed to SC generation using other nonlinear materials such as crystal, gasses and optical fibres, with Lin and Stolen in 1976 [90] being one of the first ones to present results in optical fibres. Also explanations other than self phase modulation were offered as the mechanism behind SC generation, as SPM could not explain all the observed optical broadening. Gouveia-Neto in 1988 published a paper describing the formation and propagation of soliton waves from modulation instability [91]. More recently Dudley, Alfano, Gently, Smirnov, Abeeluck [92]-

[98] among many others have contributed to a better understanding of SC formation and the mechanisms underlying an optimum SC generation.

The research and interest in supercontinuum generation is been driving by the advance in new technologies such as the invention of photonics crystal fibres (PCF) in 1996 by Knight [99] and the commercial availability of high power sources at the end of 1990´s. Its characteristics as a high power broadband source has found many interesting applications, not only in the visible spectrum but also in other areas, from optical coherence tomography [100][101] to spectroscopy [102], optical communications [93] or optical frequency metrology [103], just to name a few.

Currently most of the SC generation work developed in the scientific community relates to PCF or microstructured fibres, fibres with channels running along all the length of the fibre. These types of fibres are designed to have high nonlinearity. Therefore the nonlinear effective length is rather small compared with conventional fibre and SC generation can be achieved in shorter lengths, metres or even centimetres when using high peak power pulsed laser sources. The investigations in the field of PCF are quite broad, given the complex structured cross-section of the fibres and the possibility of coupling signal at the same time in several channels with different properties within the same fibre. The research work on SC generation, presented in this thesis, took a different approach. We used conventional telecommunication fibres, which are relatively inexpensive of fabricate compared with PCF and the laser source was continuous wave instead of pulsed. The result is a robust and simple configuration, relative easy to implement

The work presented in this chapter is focused in conventional optical fibre, mainly TrueWave and SMF, operating in anomalous dispersion (D>0) and using a CW laser source. Some cases are also discussed with normal dispersion (D<0). The dispersion coefficient D is defined as

$$D = -\left(2\pi c/\lambda^2\right)\beta_2, \qquad \textbf{5.1.1}$$

where c is the speed of light, λ is the wavelength and β_2 is the second order propagation constant in $ps^2\ km^{-1}$. It refers to the chromatic group velocity dispersion (GVD) or chromatic dispersion, proportional to β_2 as described in Chapter 2.

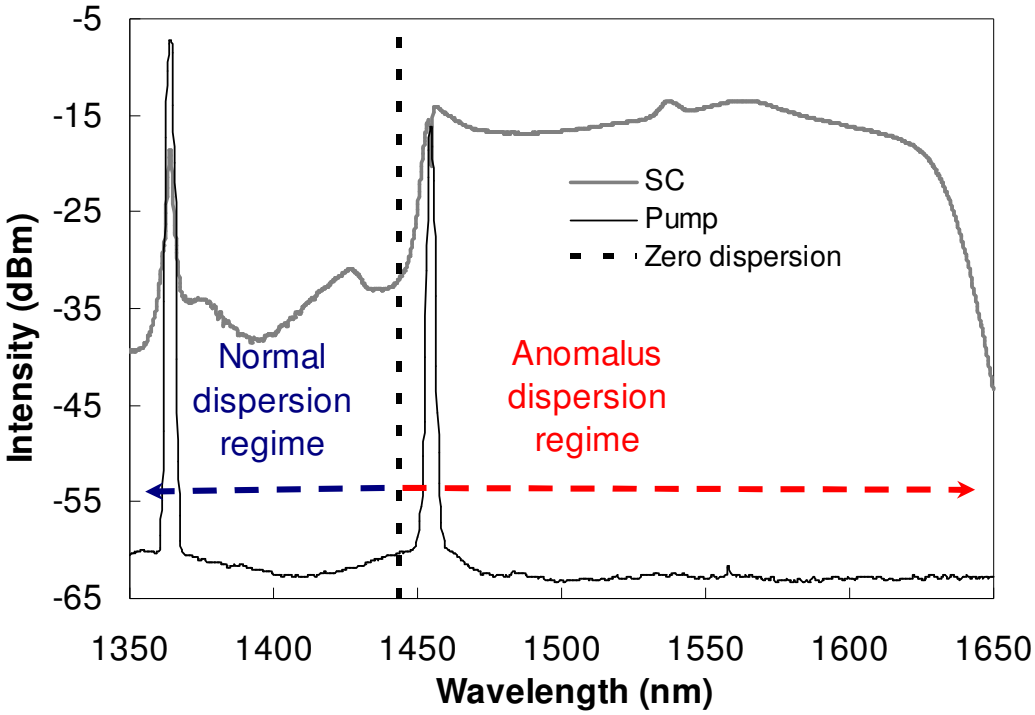

Figure 5.1.1: Experimental optical power spectra of the generated SC from 11km TW fibre using URFL architecture. D $_{1455nm}$~0.47ps/nm/km.

Figure 5.1.1 shows an example of SC generation using URFL cavities where the pump source corresponds to the 1455nm peak and the SC spectra covers the region 1450nm-1620nm. The peak at 1455nm is the first Stokes of the primary pump at 1365nm and it is generated by SRS. The zero dispersion wavelength is plotted by the discontinuous vertical line at ~1443.5nm. The anomalous dispersion regime corresponds to wavelengths greater than the zero dispersion wavelength. The normal dispersion regime is indicated at lower wavelengths than the zero dispersion one.

The SC generation process can be explained as a combination of modulation instability (MI), self phase modulation (SPM), soliton fission, dispersive waves, stimulated Raman scattering (SRS), four-wave mixing (FWM) and cross phase modulation (XPM). As a CW pump is used in the anomalous dispersion regime, the effect the SC generation is originated by modulation instability (MI) which is the modulation of the steady state and it can rise from the interaction of a strong pump signal with the background noise. MI will generate frequency sidebands in the anomalous dispersion regime. The refractive index of the media becomes dependent on the optical intensity and, as described by Chapter 2, the power fluctuation created is converted into phase modulation. SPM induces the break up of the CW Stokes shifted radiation into a train of ultra-short pulses. The combination of SPM nonlinearity and the group velocity dispersion generates higher order soliton formation within a range of spectral frequencies. There are several studies of the soliton propagation

close to zero dispersion wavelength and the dynamics of their stability [104][105]. Although the shape of fundamental solitons are only slightly affected by small perturbation, third order dispersion was found to stimulated the resonant transfer of energy from the soliton to a low amplitude narrow-band dispersive wave background with wavelengths in the normal dispersion regime. Small perturbation of higher order solitons evolution causes solitons breaking up and splitting into lower order or fundamental solitons, releasing excess energy as linear dispersive waves [29][107][108] which are radiated in the normal dispersion region of the fibre. This splitting process from higher order solitons is called generally soliton fission. In absence of perturbation, stationary solitons will propagate without changing their shape, with a balance between SPM and dispersion as it will be shown in a later chapter [21][104][105]. Perturbations to soliton propagation can be induced by numerous causes such as SRS, higher order dispersion or soliton collisions. The supercontinuum generated with continuous wave in anomalous dispersion regime is the result of the nonlinear dynamics of these pulses, generated by soliton fission, and their interplay with effects such as XPM, FWM and SRS which shift their spectral centre to longer wavelength and broaden the overall spectral profile.

The SC generation process in the normal dispersion regime has its origin in the frequency modulation of the strong continuous pump signal by MI resulting in SPM and the subsequent spectral broadening, but without soliton formation. SRS plays a major role with a frequency shift of the generated spectral components to longer wavelengths, as the radiation confinement in the different Stokes waves is greater. The resulting broadening and shifted optical spectra is generated by the interplay of FWM, XPM and SRS. Generally the overall SC spectral profile tends to have a less flatten optical profile as it will be shown in later experimental results.

This chapter does not intend to provide a precise and detailed picture of SC generation as the topic itself is greatly extensive and there is considerable literature review on this topic [31][92][98][106]. The objective is to provide specific examples where URFL are applied effectively. The results presented in this chapter are demonstrated applications of the ultralong Raman fibre laser architecture in photonics, in particular, in providing effective supercontinuum generation without the need of special high nonlinear or photonics crystal fibres.

5.2 Supercontinuum enhancement using URFL cavity

Continuous wave supercontinuum (CW SC) generation in optical fibres has been demonstrated using specifically designed photonic crystal fibre (PCF), highly nonlinear dispersion-shifted fibres (HN-DSFs) or the use of dispersion decreasing fibres [95][96][97]. One of the problems of generating SC is the degradation of the flatness of the output, especially when high pump power is used. The existence of a new breed of Raman lasers with ultralong cavities [72] opens the possibility for a different kind of CW-pumped SC generation architecture, which offers the possibility of improved spectral flatness and SC bandwidth using conventional optical telecommunication fibre.

The objective of the following experimental work is to demonstrate that indeed URFL cavities provide optical spectra advantages in CW pumped SC generation. The experimental setup of the CW pumped SC source is schematically illustrated in Figure 5.2.1. A Raman laser source operating at 1365nm was used to forward pump a cavity delimited by two 1455nm highly reflective fibre Bragg gratings (FBGs). These gratings have a 3dB bandwidth of 1nm, centred at 1455nm and ~98% reflectivity. Pumping above the cavity threshold, we observe lasing of a stable Stokes component at the 1455nm feedback wavelength. The cavity is comprised of 11.3km length of TrueWave fibre. A 1:99 optical coupler was placed before the output FBG to monitor the intracavity SC power and spectrum. The output optical spectrum of the generated SC was monitored using an optical spectrum analyzer (OSA) with a resolution of ~0.07nm.

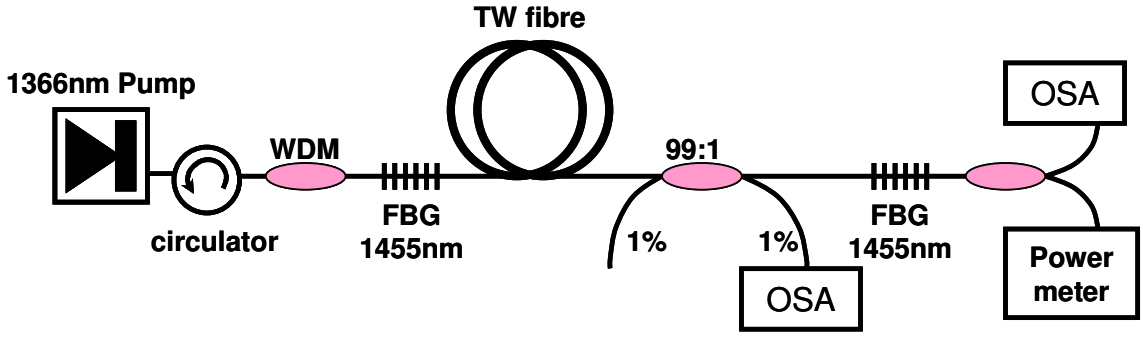

Figure 5.2.1: Schematic depiction of the CW pumped SC ultralong Raman fibre laser.

The zero-dispersion wavelength of the TW fibre is ~1443.5nm, with an average dispersion coefficient at 1455nm of D ~+0.47ps/nm/km. The non-linear coefficient of the TrueWave (TW) fibre is ~1.84$W^{-1}km^{-1}$ at 1550nm. The centre wavelength of our pump laser is 1365nm, and hence lies well within the normal dispersion regime of the fibre. However, if the cavity is pumped above its threshold, lasing of a stable Stokes component centred at

1455nm (the central wavelength of the grating reflectors) is observed. This Stokes component acts effectively as a secondary pump in the spectral region of low anomalous dispersion as shown in Figure 5.2.2, where the discontinuous black vertical line marks the zero dispersion of the fibre.

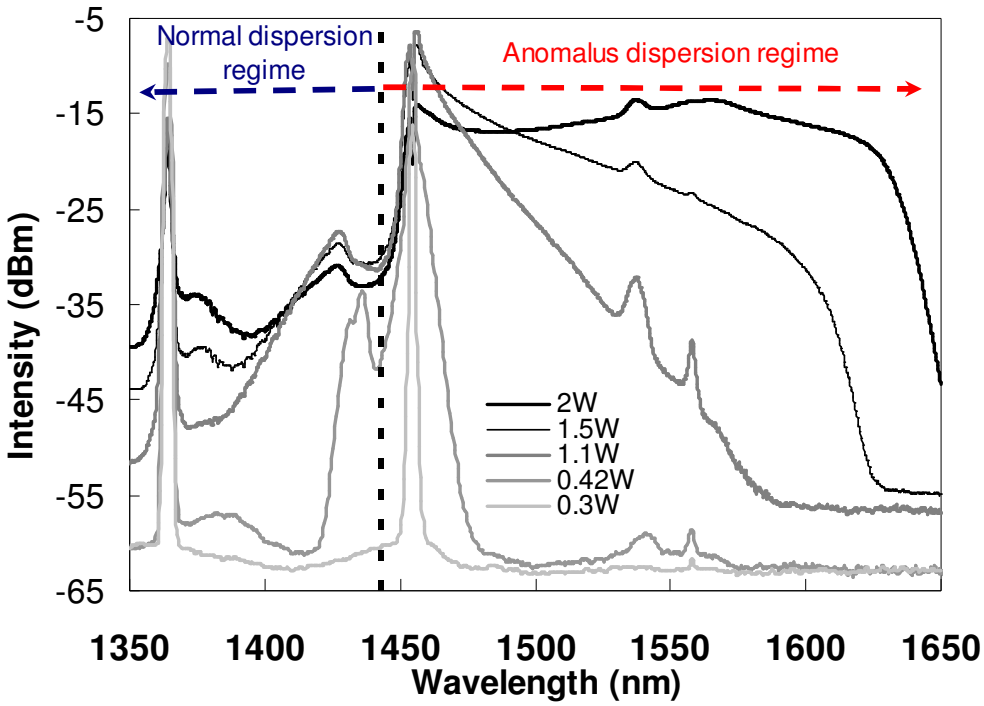

Figure 5.2.2: Experimental optical power spectra of the generated SC from 11km TW fibre using URFL architecture at several input powers. D_{1455nm}~0.47 ps/nm/km.

the primary pump increases, SPM breaks the CW pump in a train of optical pulses. The spectral broadening around 1455nm increases at the same time that soliton fission and the interplay between the different nonlinear processes broaden the optical spectrum. In the presence of small perturbation, the higher order solitons split in fundamental solitons for a range of spectral frequencies. The excess of released energy from these solitons fission can be observed as linear dispersive waves in the normal dispersion regime. This dispersive waves correspond to the sideband around 1430-1435nm. The two peaks around 1540nm and 1560nm are the corresponding SRS from the peaks at 1430nm and 1455nm.

Although the nonlinear process of stimulated Raman scattering is working from the beginning. Its importance varies as the SC is developed and depending on the location of the zero dispersion of the fibre respect to the Stokes centre wavelength.

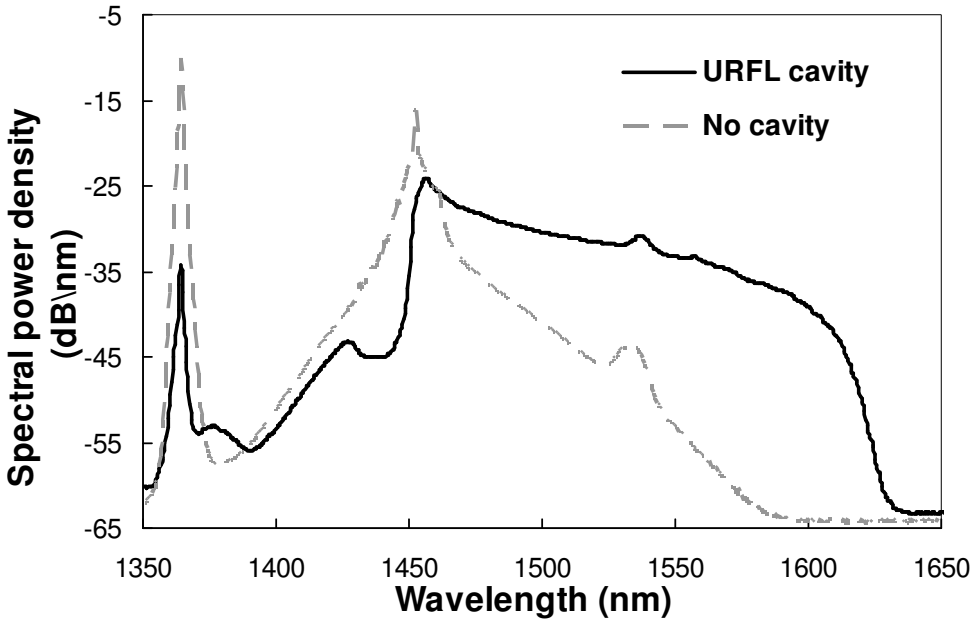

Figure 5.2.3: Optical power spectra of the generated SC from 11km TW and 1.5W input power with and without the Highly Reflecting Gratings

The effect that the use of the cavity has on the generated supercontinuum can be examined by removing the FBG's. Figure 5.2.3 shows two spectra with and without cavity, both spectra corresponding to pump powers of 1.5W. These results show that broadening is significantly enhanced inside the ultralong cavity due to the Stokes wave trapping and more efficient generation of a 1455nm Raman Stokes component, which translates also into an increased SC output power [109].

5.3 Fibre dispersion and Supercontinuum generation

As described by the corresponding literature [95][96][97][110] and observed in the previous section, supercontinuum generation is the result of the combination and interplay of several nonlinear effects. The order and strength of the nonlinear processes involved in SC generation is relevant when trying to achieve a smooth and broaden supercontinua optical spectra. Although it is not feasible to ignore the interplay among the different nonlinear processes involved in SC when investigating each one, we could propitiate up to certain extent a particular nonlinear process over others by choosing carefully the system where the SC is generated and its architecture. Conventional dispersion decreasing fibre [96][110] is an example of a particular arrangement leading towards smoother and broader supercontinuum spectra.

The work published by Abrardi et al. [96] targets the increasing and decreasing dispersion order of the fibres within the anomalous dispersion regime. Here we investigate the effect of using a combination of fibres with low dispersion coefficient on the normal and anomalous dispersion regime and its effect on the supercontinuum spectra generated.

The experimental set-up is shown in Figure 5.3.1. It involves two TrueWave fibre spans of similar lengths and characteristics. One of the TW fibre span is 10.3km long with zero dispersion at 1456.88nm and a dispersion coefficient at 1455nm of D~ -0.19ps/nm/km. The other fibre span is 10.5km long with zero dispersion at 1448.25nm and a dispersion coefficient at 1455nm of D~ 0.23ps/nm/km. Both fibre spans are confined by a pair of high reflectivity (~98%) FBGs with central wavelength at 1455nm and a 3dB bandwidth of 1nm. The system is pumped by a 1366nm laser source and the output is measured by an OSA.

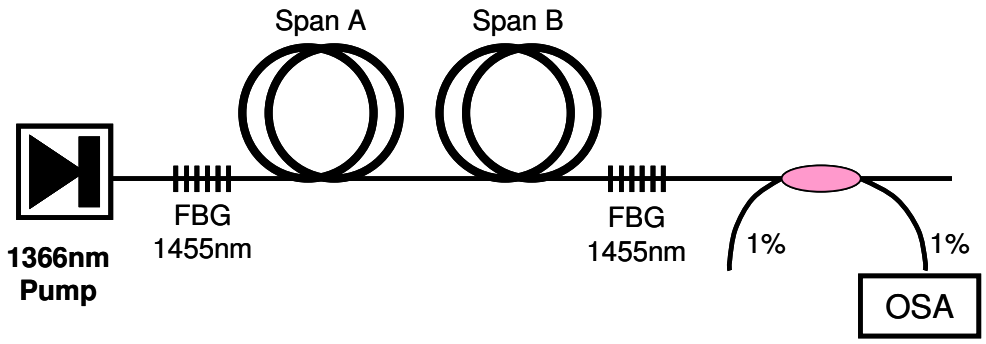

Figure 5.3.1: Schematic depiction of the CW pumped SC ultralong Raman fibre laser.

On the first experiment, the fibres are arranged by increasing dispersion coefficient, i.e. the first fibre (span A on the experimental set-up) is the 10.3km of TW with the dispersion parameter D~ -0.19ps/nm/km and the second fibre (span B on the experimental set-up) is the 10.5km of TW with D~ 0.23ps/nm/km. As the centre of the high reflectivity FBGs is at 1455nm, we use first a fibre in the normal dispersion regime (D~ -0.19ps/nm/km) and them another in the anomalous dispersion regime (D~ 0.23ps/nm/km). The optical spectra at several launch input powers are plotted in Figure 5.3.2. At the lower input power, 1.55W, we can observe as most of the energy is accumulated in the region around a well defined peak at 1455nm. As the input power increases, stimulated Raman scattering (SRS) from the 1455nm component plays a major role on the transfer of energy to longer wavelengths. Evidence of the SRS strength is the dominant peak at 1550nm. A further increase of launch power at 3.1W shifts the optical spectrum towards longer wavelengths but still maintaining a good optical spectra coverage below 1500nm.

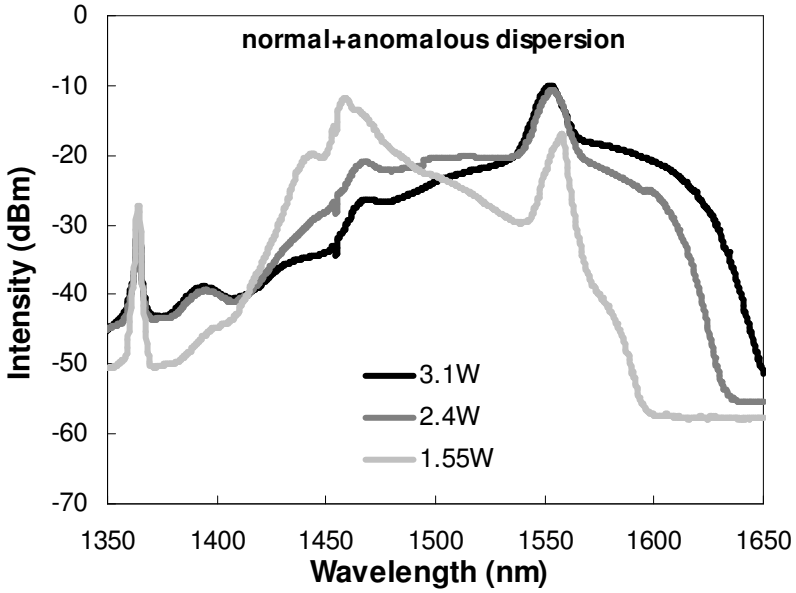

Figure 5.3.2: SC generation for system with normal +anomalous dispersion fibre. Span A: 10.3km TW (D~ -0.19ps/nm/km) and span B: 10.5km TW (D~ 0.23ps/nm/km).

As a second part of the experiment, the order of the fibres was reversed, using first the anomalous dispersion fibre, 10.5km of TW with D~ 0.23ps/nm/km, and then the normal dispersion fibre, 10.3km of TW with D~ -0.19ps/nm/km. The dispersion of the fibres was on decreasing order. The optical spectra at several launch input powers are plotted in Figure 5.3.3.

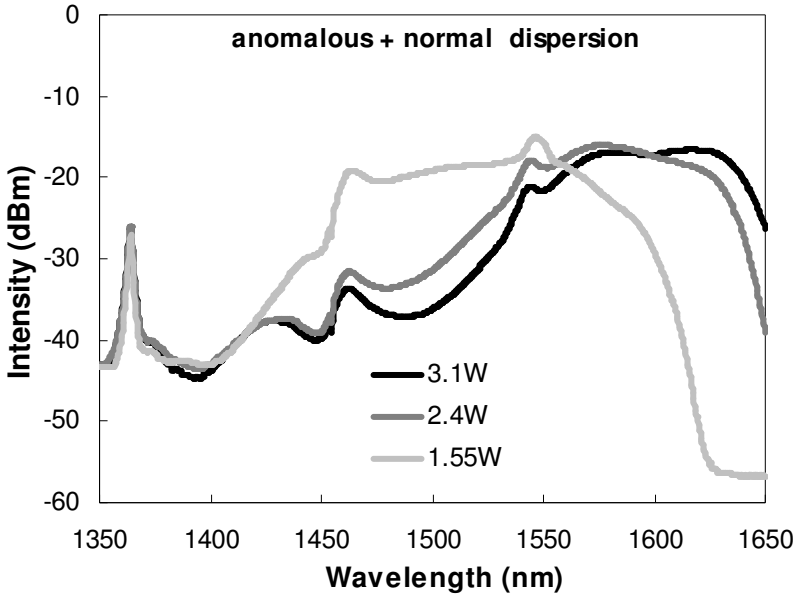

Figure 5.3.3: SC generation for system with anomalous + normal dispersion fibre. Span A: 10.5km TW (D~ 0.23ps/nm/km) and span B: 10.3km TW (D~ -0.19ps/nm/km) .

Although the peak at 1455nm is still observable, its predominance in the overall spectra is lower than the previous case, when using first the fibre with normal dispersion and then anomalous dispersion. At the lowest input power, 1.55W, the energy transfer at longer wavelength is greater than in the previous case. Also, it is worthy to mention the smoother spectra, especially around the 1550nm peak. This means that although SRS is involved in the SC generation, there are other nonlinear effects, such SPM and soliton fission, that distributes the radiation energy in a more uniform profile. A further increase of the launch input power shifts the spectrum to wavelengths longer than 1540nm causing a considerable depletion in the region below 1550nm.

Comparing the optimum spectra of the SC generated by both systems in Figure 5.3.4, we can conclude that the system with anomalous and then normal dispersion fibre provides a SC spectra with smoother optical profile and covering a similar region, 1455nm to 1600nm, at lower input power, 1.55W instead of 2.4W.

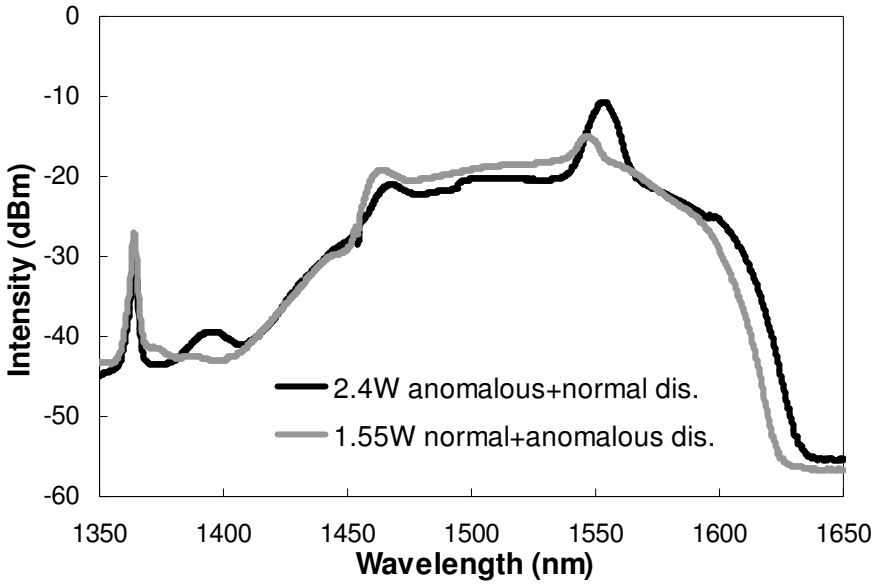

Figure 5.3.4: SC generation comparison for both for system: anomalous + normal dispersion fibre and normal +anomalous dispersion fibre.

The 2.4 W case, with first anomalous and then normal dispersion fibre, has a slightly extended spectral coverage (~10nm) and could be considered the optimum case if the difference on launch power is not considered and the 1550nm peak is filtered out for flattening.

The difference between the spectral power profiles shown in Figures 5.3.3 and 5.3.4, corresponds to the weight given to a particular nonlinear effect by either using first a fibre span either in the normal or anomalous dispersion regime. As observed in Figure 5.3.3, the SRS is prioritised or have a major impact when using first a fibre span in the normal dispersion regime. Therefore, the peak at 1550nm is accentuated. Figure 5.3.4 shows a

reduced peak at 1550nm and a considerable increase of shorter frequencies. This is the result of using first a fibre span in the anomalous regime, therefore giving a major prominence to soliton fission.

5.4 Anomalous and normal regimes

Continuous wave supercontinuum generation (CW SC) has been intensively studied in recent years [92][93][97][111][112][113][114][115]. As the previous section corroborate, these studies have shown that dispersion plays a key role in the spectral broadening process; when pumping in the anomalous dispersion region, modulation instability (MI) seeds the generation of the SC which leads to soliton formation followed by a large red-shift due to intra-pulse Raman scattering. However, solitons cannot be formed in the normal dispersion region and the mechanism of SC generation is completely different in this regime.

The application of ultralong Raman fibre laser to generate efficient broadband CW SC generation has been demonstrated by El-Taher [109], using TrueWave (TW) fibre as gain media. In this work, we use a similar cavity configuration to experimentally study the dependence of SC growth on fibre dispersion for both anomalous and normal dispersion values close to the dispersion zero. We show that with optimisation of the fibre dispersion a high quality supercontinuum can be generated in the anomalous dispersion regime with just a single pump wavelength whereas in the normal dispersion regime dual wavelength pumping can be used to improve the SC spectral characteristics [20].

5.4.1 Dispersion tuning in the anomalous regime

The purpose of the next experiment is to investigate the SC generation spectra for several fibres with low dispersion in the anomalous regime. The experimental set-up is schematically illustrated in Figure 5.4.1. A CW pump laser source operating at 1365nm was used to forward pump a cavity formed by two highly reflective (~98% reflectivity and ~ 1nm bandwidth) fibre Bragg gratings (FBGs) centred at ~1455nm. Pumping above the cavity threshold, we observe lasing of a stable Stokes component centred at 1455nm. Different TW fibres having similar nonlinear and attenuation coefficients but different average chromatic dispersion values, were spliced between the FBGs. Therefore any difference in SC spectra generated is predominantly attributed to the different dispersion values of the fibres used.

The TW fibres used had low anomalous dispersion at the 1455nm Stokes wavelength. The generated SC spectra were measured via a 99:1 splitter using a high resolution OSA

(0.01nm resolution). An isolator was placed between the pump laser and the WDM to prevent any damage caused by backward propagating light.

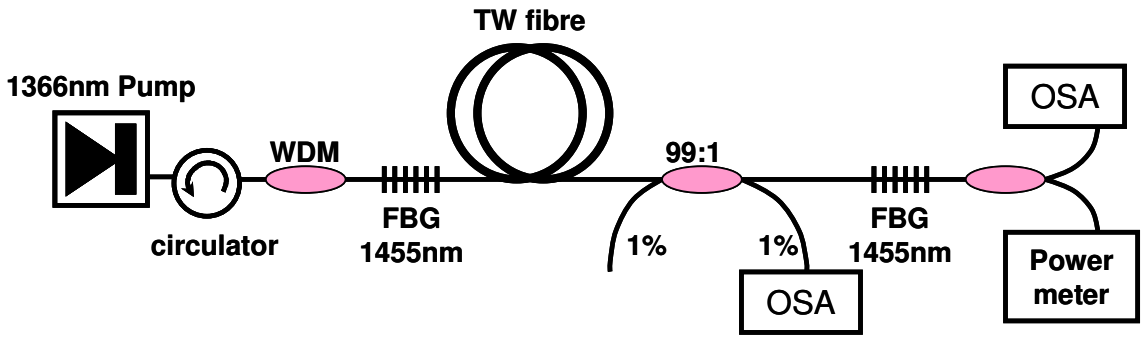

Figure 5.4.1: Schematic depiction of the CW pumped SC ultralong Raman fibre laser

Figure 5.4.2 shows output SC spectra for four different TW fibres, each of which had a different average dispersion value at 1455nm, D ~+0.47ps/nm/km, +0.23ps/nm/km, +0.03ps/nm/km and -0.05ps/nm/km. In this experiment only 1365nm pumping was used and results are shown for three different pump powers, 0.42W, 1.4W and 2W. The first fibre (Figure 5.4.2a) which had the highest anomalous dispersion value of D ~+0.47ps/nm/km at 1455nm, showed significant spectral broadened even at a relatively low pump power of 0.42W. When the input power was increased, MI converts the CW light into a periodic pulse train which leads to soliton fission and a subsequent increase in the SC bandwidth. In this case the SC extends from ~1460nm to ~1650nm showing a power variation of <1dB in the C-band 1550nm region. However, when pumping fibres with lower anomalous dispersion values (see Figure 5.4.2b and c) the nonlinearity from SPM is less pronounced. The generation of higher order solitons, which are split in fundamental solitons and their excess of energy radiated as dispersive waves towards the normal dispersion regime, is reduced. Hence the 1455nm component experiences less broadening.

On the other hand, the 1555nm second Stokes wave is more visible, indicating that at low powers and very low anomalous dispersion, the dominant effect is frequency conversion via double Raman shifting from 1365nm to 1455nm and then to 1555nm. Increasing the pump power causes more broadening of the 1455nm spectral components, generating longer wavelengths in the anomalous dispersion regime. The SPM nonlinearity of those components with the dispersion leads towards the break up of the CW into short pulses as discussed above. As anomalous dispersion is decreased, the confinement of energy around the 1455nm peak is greater. The generated SC bandwidth becomes less smooth and the transfer by SRS to the 1555nm peak becomes more efficient.

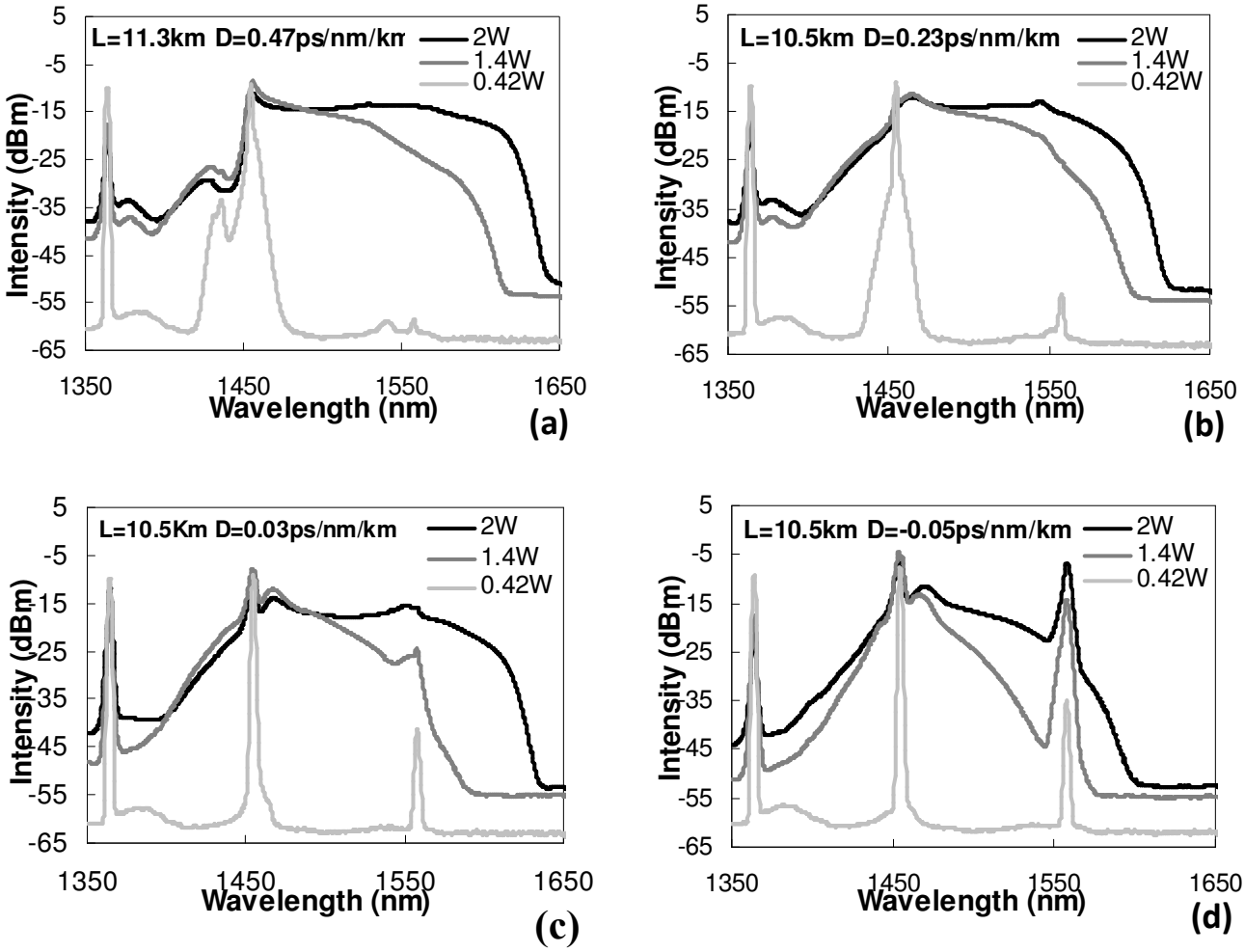

Figure 5.4.2: Output SC spectra for four TW fibres with different dispersion values as 1365nm pump power is varied.

When pumping normal dispersion fibre (see Figure 5.4.2d) soliton formation is not possible and two high peaks appear at 1455 and 1555nm even at low pump powers as the Raman effect dominates. When increasing the primary pump, the broadening around 1455nm, initially by SRS and them by combination of FWM and XFM, eventually may lead to the generation of components in the low anomalous dispersion region which might generate a train of pulses in a later stage. Raman induced frequency shift is the nonlinear process which holds a greater role in the normal dispersion regime, as it takes place to amplify the region between the 1455 and 1555nm peaks. In this case the generated SC has a bandwidth less flat with a very high peak at 1555nm.

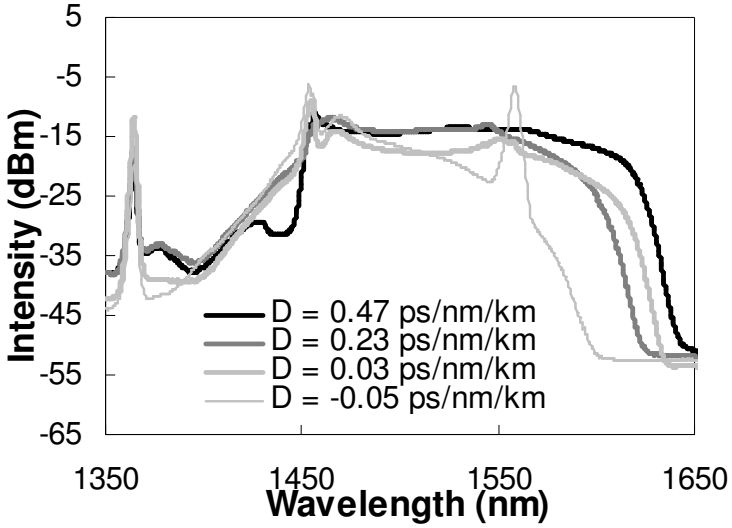

Figure 5.4.3: Comparison of SC spectra for fibres with different dispersions for a 1365nm pump power of 2W.

Figure 5.4.3 shows a direct comparison of the SC spectra between TW fibres with different low dispersion values for a pump power of 2W. The results shown in the above figure are for the fibres equivalent to those in Figure 5.4.2 a, b, c and d. They clearly indicate that the best SC output spectral characteristics, broader wavelength range and smoother spectra, are obtained when using an anomalous dispersion fibre with ~0.47ps/nm/km. This is the case where the nonlinear process of MI and further generation of higher order solitons has initially a greater role than the transfer of energy by SRS from 1455nm to 1550nm.

5.4.2 Dual wavelength pumping in normal regime

In the previous section, the normal dispersion fibre produced a worse SC generation performance than the anomalous dispersion fibres. However an experiment using dual wavelength pumping shows that the SC generation can be significantly improved in the normal regime. For this experiment we use a 17km TW fibre span with a normal dispersion of -0.19ps/nm/km at 1455nm. The experimental set-up is schematically shown in Figure 5.4.4. For this experiment, a secondary seed pump laser operating at a wavelength of 1456nm was coupled into the cavity along with the primary 1365nm pump, using a wavelength division multiplexer (WDM). An isolator was placed between each pump laser and the WDM to prevent any damage caused by backward propagating light. The two highly reflective (~98% reflectivity and ~ 1nm bandwidth) fibre Bragg gratings (FBGs) centred at ~1455nm were the same as previously.

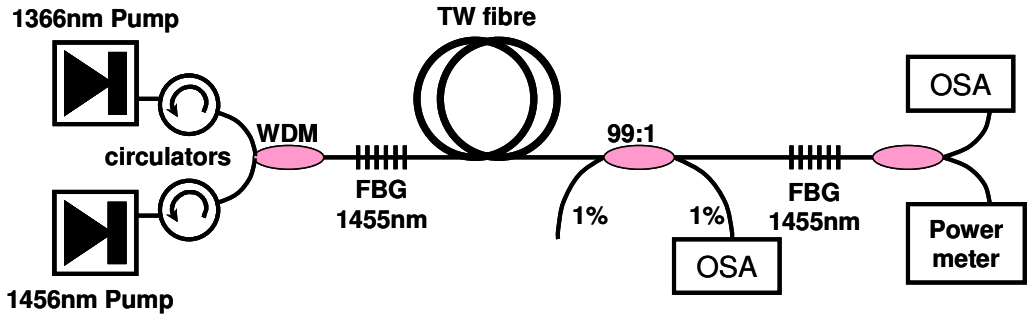

Figure 5.4.4: Schematic depiction of the CW pumped SC ultralong Raman fibre laser

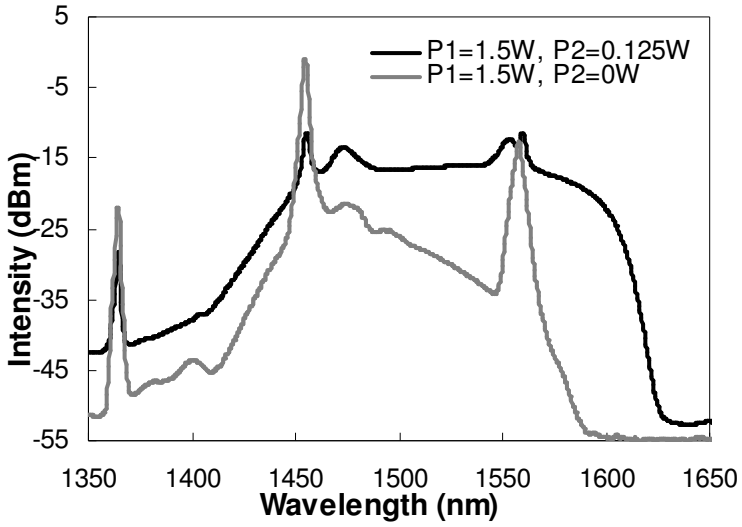

Figure 5.4.5: Comparison between single and dual pumping for a normal dispersion fibre

Figure 5.4.5 shows a comparison of the SC spectra generated using the above configuration with a 17km length of TW fibre with a normal dispersion of -0.19ps/nm/km at the 1455nm Stokes wavelength. With the addition of a secondary seed pump at 1456nm the flatness and bandwidth of the SC spectrum are improved significantly. In this experiment the 1456nm pump power was 0.12W compared with 1.5W for the primary 1365nm pump. As the second Stokes lays in the normal dispersion regime, the absence of broadening due to MI and generation of soliton pulses at different frequencies limits the initial spectrum broadening. The increase of the primary pump power produces a major effect of the SRS, giving priority to the energy transfer to the second and third Stokes, corresponding to 1455nm and 1550nm respectively. Adding a secondary seed pump promotes an earlier energy transfer and broadening around the centre wavelength of this seed by a combination of nonlinear processes such as SRS, SPM, FWM and XPM. As the primary pump increases, part of the broadened spectrum around the secondary seed will be extended to the anomalous

regime. Once in the anomalous regime, the broadening of the spectrum and SC generation will take place as described previously, giving a more uniform output.

Figure 5.4.6 shows a comparison of the dual wavelength pumped normal dispersion and single wavelength pumped anomalous dispersion schemes. Using dual wavelength pumping the normal dispersion fibre generates a similar bandwidth SC to the anomalous fibre. Although the 1555nm peak remains more pronounced for normal dispersion, the efficiency of the SC is improved. The total pump power for the normal dispersion scheme was 1.62W compared to 2W for the anomalous dispersion scheme.

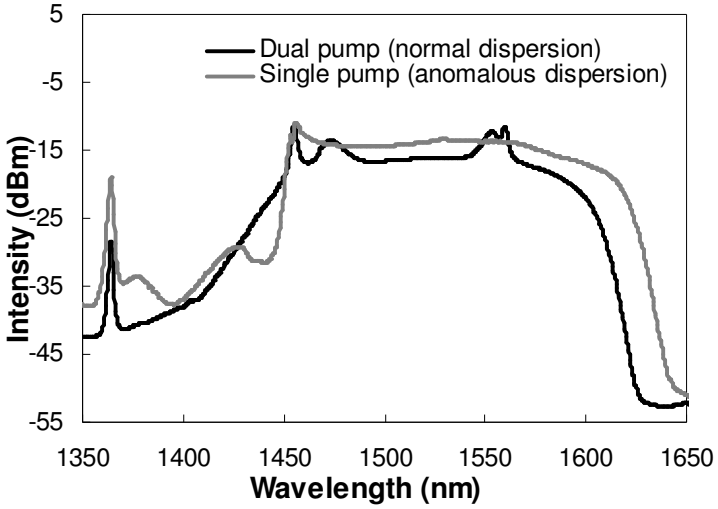

Figure 5.4.6: Comparison of dual and single pump systems.

We have experimentally evaluated supercontinuum generation in ultralong Raman fibre laser for fibre dispersion values in the range +0.47 to -0.19ps/nm/km. Our results show improved performance for higher anomalous dispersion values. In the anomalous dispersion regime high quality SC spectra are generated using only a 1365nm pumping wavelength. We have also shown that when using a normal dispersion fibre significant improvements can be made by using a secondary seed laser at 1456nm. This allows more efficient SC generation with a comparable bandwidth to a single wavelength pumped anomalous dispersion configuration.

5.5 Effect of fibre length in SC generation

Supercontinuun generation results from the combination of several nonlinear effects such as self-phase modulation, stimulated Raman scattering, four-wave mixing and cross-phase modulation. From a practical point of view, the most important parameters for generating supercontinuum in optical fibres are the availability of a high power source, a

fibre with high nonlinear coefficient and a span length such as $\gamma P_0 L$ is greater than 30, according to Agrawal [31]. On the following experimental work, we investigated the effect of the span length on the overall supercontinua spectra generated. Three different lengths of TrueWave fibre with similar fibre characteristics, average dispersion and attenuation coefficient, were measured under the same launch power conditions. The non-linear coefficient of TrueWave (given at 1550nm) is $1.84 W^{-1}$ km^{-1}. The length and fibre dispersion details are shown on the table below.

Table 5.5.1: Details of the TW fibres

Fibre ID	Length (km)	λ_0 (nm)	D_{1455} (ps/nm/km)	D_{1550} (ps/nm/km)
TW - 005144490006	10.4	1451.86	0.03	4.39
TW - 005144490014	25.5	1450.65	0.11	4.44
TW - 990144380006	35.1	1451.26	0.11	4.47

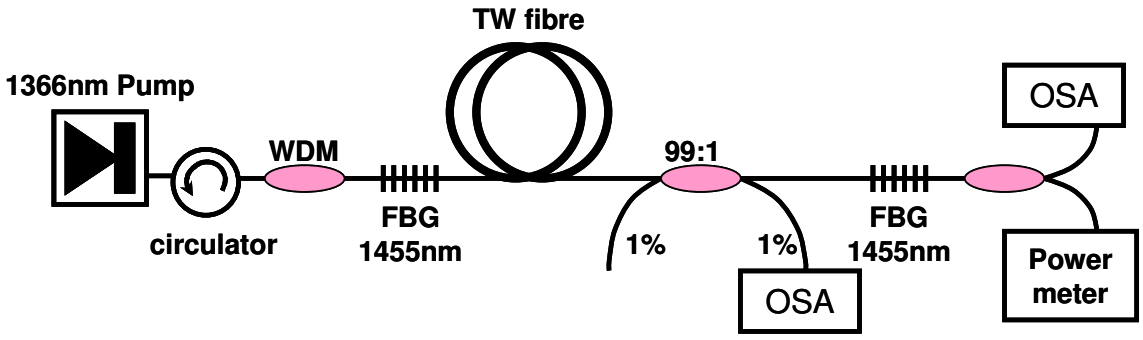

Figure 5.5.1: Schematic depiction of the CW pumped SC ultralong Raman fibre laser

The experimental set-up is as shown in Figure 5.5.1. The system involves a span of TrueWave fibre confined between a pair of high reflectivity (~ 98%) FBGs centred at 1455nm with approximately 1nm bandwidth at 3dB. The system, the fibre span and pair of FBGs, is pumped by a laser source at 1366nm. As we pump 1366nm pump power into the fibre span through the WDM coupled into the system, the pump energy is transferred to the region of 1455nm through stimulated Raman generation. As the FBGs are centred at 1455nm, the confined power behaves as a secondary pump transferring pump energy at longer wavelengths.

The optical spectra for the three span lengths at several input powers are shown on Figure 5.5.2. All the plots correspond to supercontinua generation produced in the anomalous regime, with the value of D at 1455nm slightly positive. The peak at 1550nm is clearly distinguishable, especially at higher input powers, from the rest of the supercontinua spectra, as opposite to the optical spectra from the previous section with the average dispersion coefficient D slightly greater value but still in the anomalous regime. It can be

observed a broadening of the peak at 1455nm with dispersive waves going into the normal dispersion regime for all the fibre length cases. As the peak at 1455nm broaden in the anomalous regime and further energy is transferred at 1550nm through SRS, SPM and soliton formation will eventually occur and the optical spectra at longer wavelengths will be generated through the interplay of the nonlinear soliton dynamics and the other nonlinear effects, XPM, FWM and SRS.

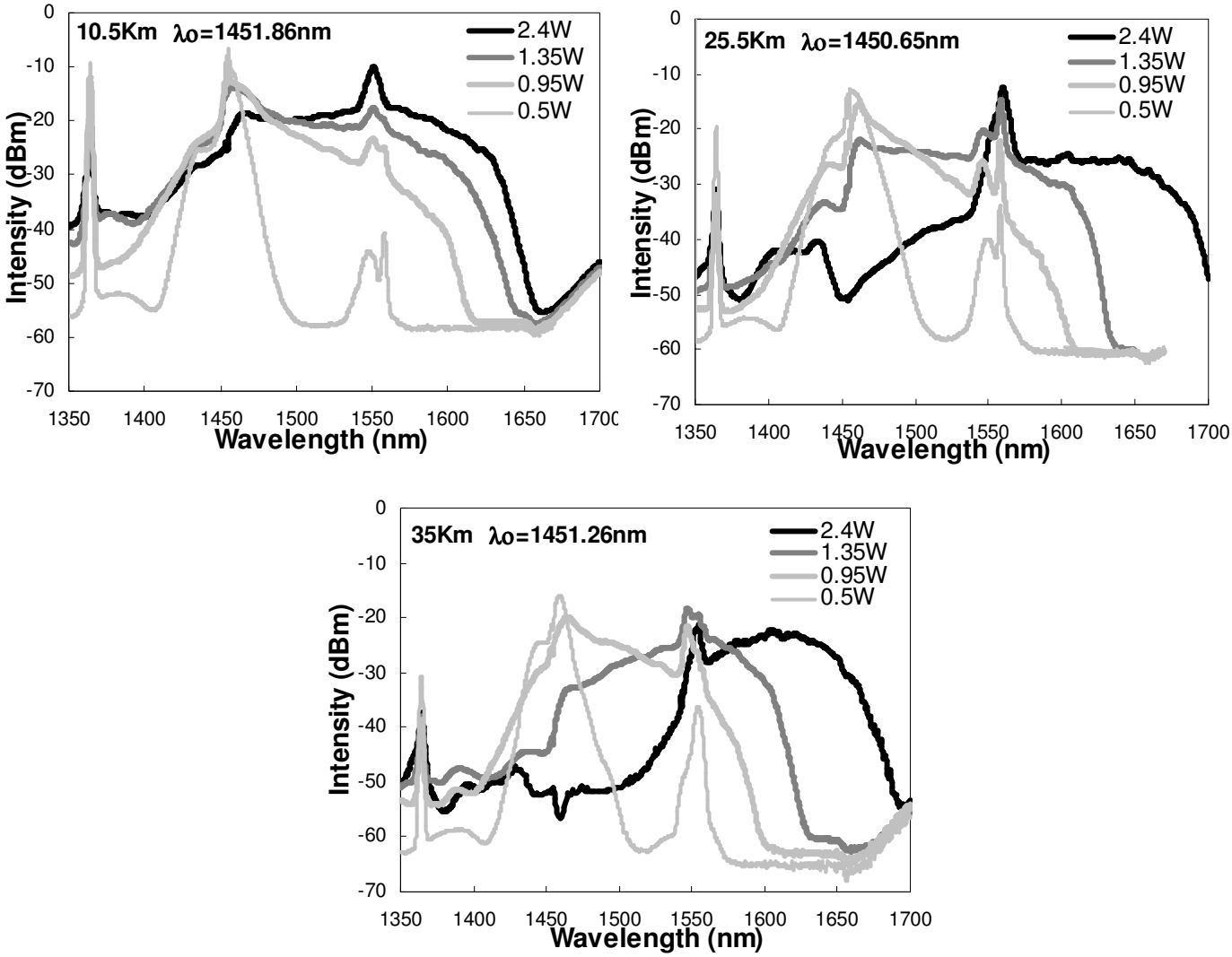

Figure 5.5.2: SC spectra for the different TW span cavity length at different powers, a) 10.5km, b) 25.5km and c) 35km.

For the case of 10.5km span length, it's can be observed the supercontinua spectra self contain around 1550nm, within a range from 1430nm to 1620nm, as the launch input power increases up to 2.4W. The overall optical spectrum picture for the case of 25.5km is a different one. There is an initial peak broadening around 1455nm and further energy transfer at 1550nm combined with spectral broadening between 1455nm to 1610nm. In fact the optical spectrum flatness between 1465nm to 1540nm for an input power slightly lower than 1.35W is optimum. An increase of input power at 2.4W shifts the supercontinua spectra from

the region 1455nm - 1610nm to the region 1550nm - 1685nm. The longest span length used in this experiment, 35km, has similar behaviour as the previous one, 25km, in the sense that a shift of the supercontinua spectra from the region previous to 1550nm to the region after 1550nm can be observed for the range of powers used in this experiment. The main difference comparing the 35km case with the 25.5km one relates to the broadening range of the supercontinua spectra. At 2.4W input power, the supercontinua spectra cover approximately the region 1550nm - 1655nm, approximately 30nm shorter spectral coverage than the case of 25km span. The most likely cause of this reduction on spectral coverage at longer span length is the fibre attenuation.

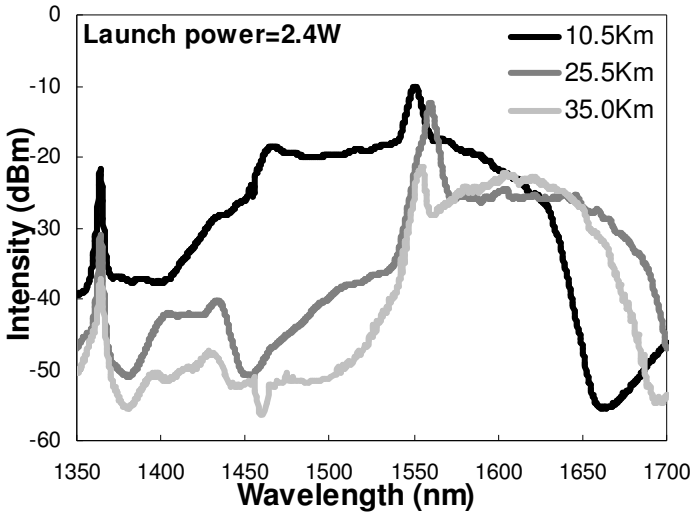

Figure 5.5.3: SC spectra for the three different TW span cavity length at 2.4W launch power

Figure 5.5.3 compares the SC optical spectra for the three span lengths at the same launch input power 2.4W. Increasing cavity length increases the threshold power for the Raman-induced generation of the 1455nm component, delaying its formation, but simultaneously translates into a higher accumulation of nonlinear effects. Raman induced frequency shift (RIFS) grows along the fibre length linearly [29]. On the other side, the SC spectrum is expected to display reduced intensity for longer fibre lengths, due to the additional attenuation.

5.6 SMF and TW hybrid configuration

Highly efficient SC generation has already been demonstrated in ultralong hybrid cavities comprised of TrueWave fibre and highly nonlinear fibre, achieving a flatness of <1dB over 180nm with an output power of 1.15W [20]. Now, in this section, we demonstrate that it is possible to achieve excellent results without the need to resort to specialist highly nonlinear fibre, by carefully combining conventional fibres of different dispersions. Here we generate

CW SC inside a TrueWave and SMF (Standard Single-mode) fibre based ultralong cavity. Different cavity configurations were examined to investigate the effect of adding SMF in the cavity on the efficiency and the flatness of the generated SC.

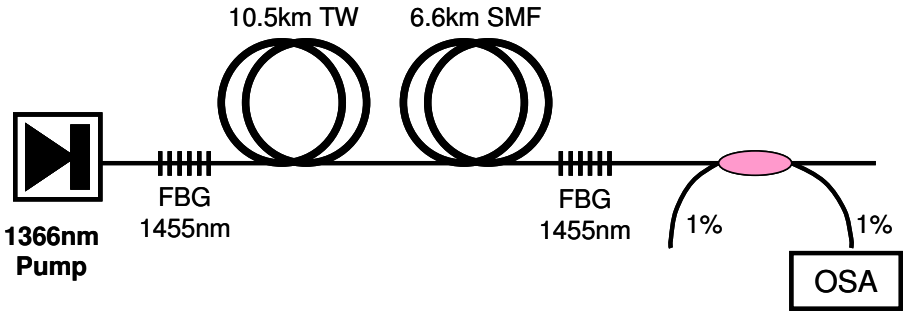

Figure 5.6.1: Experimental set-up of the SC Raman fibre laser

The experimental setup of the SC source is shown in Figure 5.6.1. A Raman pump laser operating at 1365nm was used to forward pump a cavity consisting of two highly reflective (~98% reflectivity) fibre Bragg gratings (FBGs). These gratings have a 3dB bandwidth of 1nm, centred at 1455nm. By using high reflectivity FBGs a very high-Q cavity was formed to efficiently trap the Stokes shifted wavelength and increase the power conversion efficiency. Pumping above the cavity threshold, we observe lasing of a stable Stokes component at 1455nm.

Our fibre cavity consisted of 10.5.km of TrueWave (TW) fibre with a zero-dispersion wavelength of 1451nm, a dispersion slope of 0.046ps/nm^2/km and a non-linear coefficient of ~1.84Wkm^{-1} at 1550nm. The TW fibre was combined with 6.6km of SMF with a zero dispersion wavelength of ~1311nm. A 99:1 coupler was placed at the output FBG to monitor the generated SC power and spectrum. The optical spectrum of the generated SC was monitored using an optical spectrum analyzer with a resolution of ~0.07nm.

The evolution of the generated radiation inside the cavity as the pump power increased is shown in Figure 5.6.2. The zero-dispersion wavelength of the TW fibre is at 1451nm. At low power, our primary 1365nm pump generates a 1st order Stokes component through the process of SRS around the wavelength 1455nm, the broadening is significantly enhanced inside the ultralong cavity due to the Stokes wave trapping and more efficient generation of the 1455nm which enhance the generation of SC. By increasing the pump power, clear signs of higher order soliton formation and the radiation of the dispersive waves towards the normal dispersion regime are observed. The peak around 1435nm corresponds to the dispersive wave spectral components. We also observe the generation of a 2nd order Stokes at 1555nm. By increasing the injected pump radiation inside the cavity, we are able to

generate a supercontinuum spectrum ranging from 1450nm up to >1625nm for input powers up to 2W but for powers higher than this threshold the 1st Stokes wave is depleted and the efficiency of the SC generated spectrum is degraded.

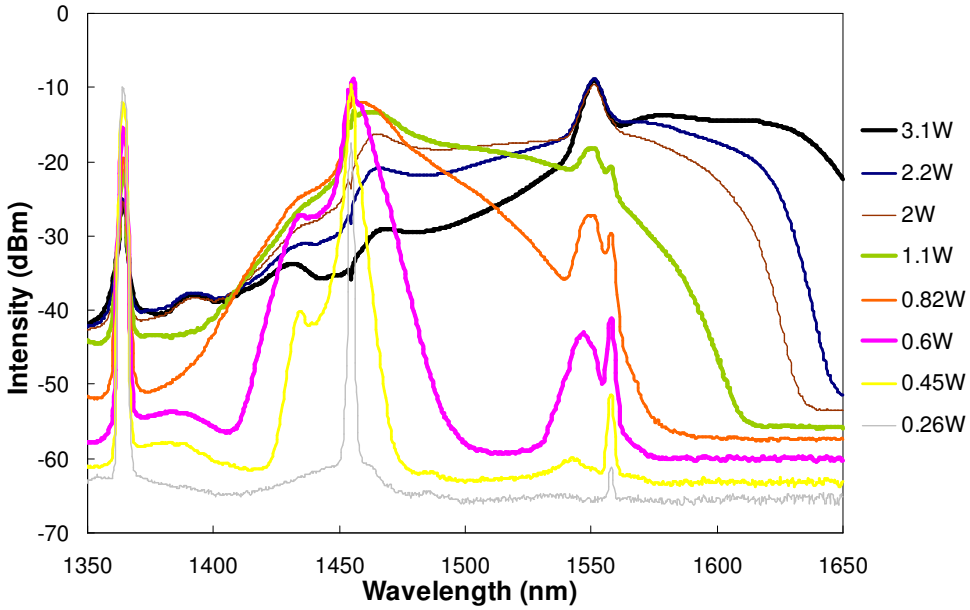

Figure 5.6.2: SC spectrum versus pump power for the configuration shown in Figure 5.6.1.

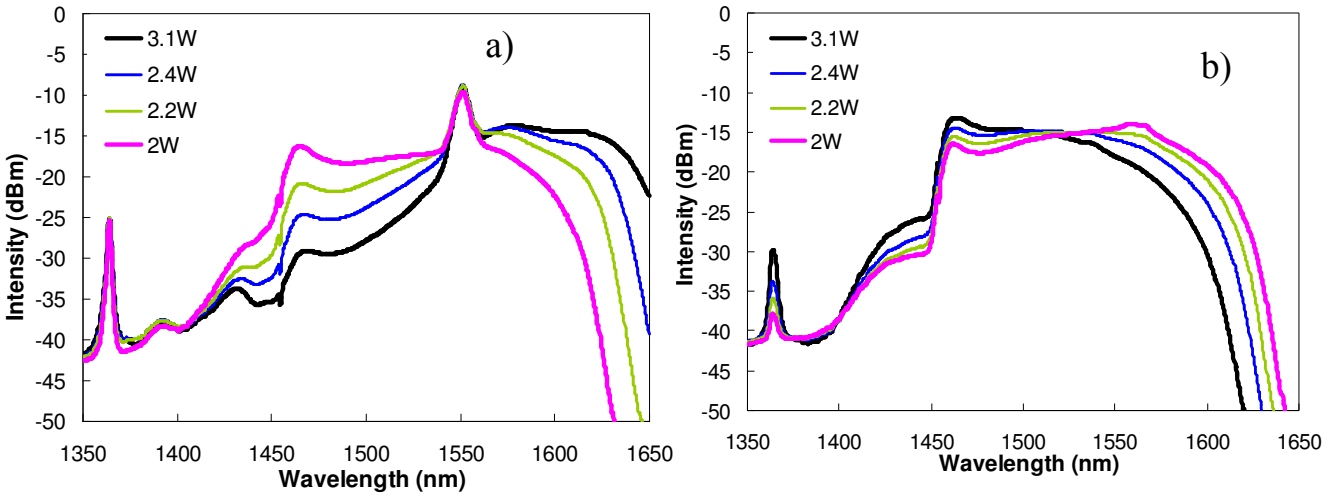

Figure 5.6.3 a) SC spectra for the TW+SMF cavity at different powers, b) SC spectra for the SMF + TW cavity at different powers.

Figure 5.6.3 shows a comparison of SC spectra with the SMF included either before or after the TW fibre. These results show that the efficiency of the SC generation is maximized for a cavity with SMF preceding the TW; by pumping SMF first the strong MI at 1455nm is avoided and the initially dominating effect is a quite efficient frequency conversion via a Raman shift from the 1365nm to 1455nm and then to 1550nm. When the three components are moved to propagate in the TW fibre, the 1455nm component generated in the SMF has broadened, providing a range of spectrums which support a flatter SC with and extended

spectrum (see Figure 5.6.3b). In this case the bandwidth of the SC output covered the S,C & L telecommunication bands. When TW is the first fibre in the cavity the SC spectrum shifts to longer wavelengths generating a flatter region in the L band (1560-1625nm), see Figure 5.6.3a.

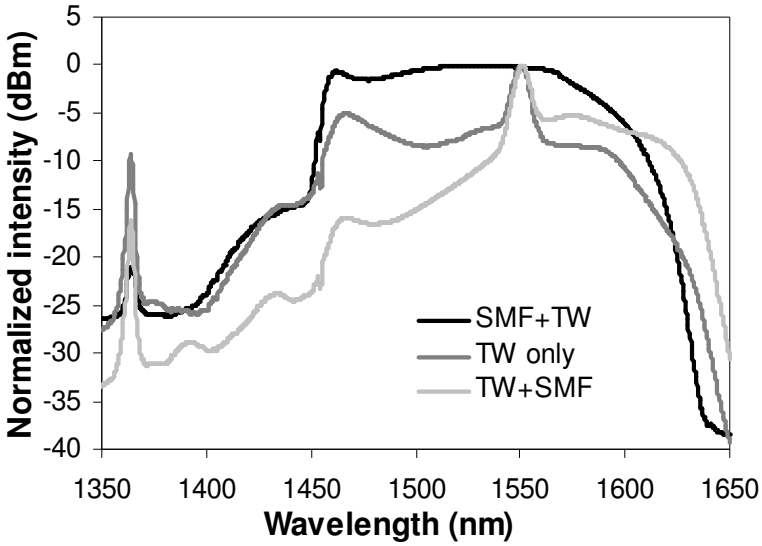

Figure 5.6.4: SC spectra for three different fibre configurations at the same launch power, 2.4W

Figure 5.6.4 shows the spectrum profile comparison for the three system configurations, SMF+TW, TW only and TW+SM, at the same lunch power 2.4W. As it can be observed the configuration with SMF preceding the TW maximize the spectrum flatness profile.

As result, ultralong Raman fibre laser cavity based on only conventional single mode silica fibre (TrueWave and SMF fibres) can be used to generate a flat supercontinuum that spans the S,C & L telecommunication bands. Our results show that for a pump power of 3.1W, the total generated SC had a ~10dB bandwidth of >160 nm. We have demonstrated that including SMF fibre before TW in the ultralong Raman fibre laser cavity dramatically improves the efficiency and the flatness of spectrum, whilst reversing the order of the fibres enhances the L band region.

5.7 Conclusion

Our investigation was focused mainly on CW pumped SC generation using either single fibres or a combination of conventional fibres, TrueWave and SMF, in the normal and anomalous dispersion regime. Within this context, the SC generation process can be explained as a combination of modulation instability (MI), self-phase modulation, soliton fission, stimulated Raman scattering (SRS), four-wave mixing (FWM) and cross phase modulation (XPM).

In the case of pumping in the normal dispersion regime, the dominant effect is stimulated Raman scattering shifting at longer wavelength the pump energy until reaching the anomalous regime. For the special case of zero dispersion, the pump will be broadened by four wave mixing and modulation instability sidebands around the pump. The high pump power will break in high order solitons with the corresponding soliton fission at different frequencies. Pumping in the anomalous regime will add the effect of stimulated Raman scattering to the combination of four wave mixing, modulation instability sidebands and soliton fission, giving the smoothest and best distributed SC optical spectra. Those are the general dynamics formation of the SC generated for the cases presented in this chapter.

As part of using the URFL architecture in SC generation system, we have demonstrated that broadening is significantly enhanced inside the ultralong cavity due to the Stokes wave trapping, which translates also into more efficient SC generation and an increased SC output power.

Through the different experiments pumping in normal and anomalous dispersion, we have concluded that systems with anomalous and then normal dispersion fibre provide SC spectra with smoother optical profile. Therefore dispersion management of the fibre is a key element for supercontinuum generation. SC generation can be also provided in normal regime under special circumstances, allowing a comparable bandwidth to the one provided by anomalous dispersion regime. We have shown that with optimisation of the fibre dispersion a high quality supercontinuum can be generated in the anomalous dispersion regime with just a single pump wavelength whereas in the normal dispersion regime dual wavelength pumping can be used to improve the SC spectral characteristics. The best SC output spectral characteristics, broaden wavelength range and smoother spectra, are obtained when using an anomalous dispersion fibre with slightly higher dispersion values.

Increasing cavity length increases the threshold power for the Raman-induced generation of the 1455nm component, delaying its formation, but simultaneously translates into a higher accumulation of nonlinear effects. Raman induced frequency shift grows along the fibre length linearly. On the other side, the SC spectrum is expected to display reduced intensity for longer fibre lengths, due to the additional attenuation.

An important result is that ultralong Raman fibre laser cavities based on only conventional single mode silica fibre, TrueWave and SMF fibres, can be used to generate a flat supercontinuum that spans the S, C & L telecommunication bands. The result is a SC generated with over 160nm at ~10dB bandwidth [20]. Including SMF fibre before TW in the ultralong Raman fibre laser cavity dramatically improves the efficiency and the flatness of the spectrum, whilst reversing the order of the fibres enhances the L band region.

In overall, we have demonstrated high quality SC generation based in conventional optical fibres, without the need of photonic crystal fibres or special dedicated fibres, by using URFL architecture. The relation between pump wavelength and fibre dispersion predispose a range of nonlinear mechanism to generate the SC and the optical broadband spectra profile expected. This SC broadband source could be optimised and improved by flattening filters if required. SC application where spectral slicing is required and the spectral range can be achieved by combination of single laser diode channels may not be appropriated as it can be cost and power inefficient. The main advantage of URFL architecture is the enhancement of SC generation with a greater output power at optical spectral ranges that may not be easily accessible otherwise.

Chapter 6

Stability and dynamics of soliton transmission

6.1 Introduction

Optical solitons in silica fibre are understood as optical pulses which propagate with constant shape of the temporal intensity profile, maintaining the intensity and phase information, as they travel along the fibre. It is well known that optical solitons exist as theoretical solutions of the classic Nonlinear Schrödinger Equation (NLSE) [30] traditionally used to describe propagation through an optical fibre waveguide and expressed as follows.

$$i\frac{\partial Q}{\partial z}=\frac{\beta_2}{2}\frac{\partial^2 Q}{\partial T^2}-\gamma|Q|^2 Q, \qquad \textbf{6.1.1}$$

where z is the length of the fibre, Q is the slowly varying envelope of the electric field, β_2 is the group velocity dispersion (GVD) parameter and γ is responsible for self-phase modulation (SPM). Distortion free soliton transmission can be achieved, in theory, based on an exact balance between the anomalous chromatic dispersion of the transmission fibre and the Kerr-induced self phase modulation. In practice, the intrinsic loss of the fibre, α, breaks this balance by attenuating the optical signal intensity. Equation 6.1.1 is modified to included the fibre loss as follows

$$i\frac{\partial A}{\partial z}=\frac{\beta_2}{2}\frac{\partial^2 A}{\partial T^2}-\gamma|A|^2 A-\frac{i\alpha}{2}A. \qquad \textbf{6.1.2}$$

Therefore the nonlinearity decrease along the fibre preventing soliton pulses from being used in practical optical transmission systems without some kind of arrangement for optical

amplification to compensate for fibre attenuation during propagation. The resulting optical pulse tends to show a reduced amplitude signal and broadened temporal profile due to chromatic dispersion.

Since the original optical soliton proposition by Hasagawa in 1973 [62] and the experimentally demonstration by Mollenauer in 1980 [104], the study of optical solitons has broaden extensively, involving a wide range of research areas, including basic nonlinear optics [116], laser sources [117], all-optical signal processing, signal regeneration [118] and optical communications [119][120][121][122]. The emphasis of this chapter relates to the capability of URFL cavity to provide distributed Raman gain for soliton pulse propagation along the transmission span, enabling the practical application of Raman technologies in future high-speed optical communication systems [13][53][123][124]. The actual investigation of optical solitons in this thesis is limited to this chapter and with focus on their transmission stability and some aspects of their dynamics as solitons evolve along the fibre span.

Long-distance optical soliton transmission has already been studied in various contexts, both numerically and experimentally [125][126][127][128][129][130]. Erbium-doped fibre amplifiers (EDFAs) have been used as lumped amplifiers to periodically recover transmission losses. The average-soliton solution is achieved when average dispersion balances average nonlinear effects, however, the average soliton principle states that discrete amplifiers must be placed at intervals shorter than the soliton period which is of order 1km for picosecond input pulses [126], which limits transmission bit rate in practice. Dispersion-managed solitons and loss-compensating dispersion solitons are also other approaches to transmit optical solitons [127][129][131]. Utilizing such techniques the dispersion of the special transmission fibre is either periodically changed to generate periodically stable pulses with partial dispersion compensation [127] or changed point by point to follow the fibre loss using loss-compensating dispersion decreasing fibres to match between nonlinearity and dispersion at all points in the fibre [129]. However, exact or true (understood as not loss managed) soliton transmission requires fibre loss to be compensated exactly along the fibre span by some sort of distributed amplification technique. Ideal distributed amplification would be equivalent to inducing artificial lossless transmission conditions in the allowing very short soliton pulses to be transmitted at an ultrahigh bit rate. Distributed Erbium amplification over the whole length of the system span is one possible method, and this approach has been used to propagate femtosecond solitons over 18km in a dispersion-shifted distributed EDFA, where the erbium doped fibre was pumped by a forward and backward pumping configuration to generate uniform gain distribution [128].

A more practical option, however, is the use of Raman amplification. The application of URFL as virtually lossless link is a key element to prove experimentally true soliton transmission. Furthermore URFL cavities can be used to investigate the evolution and dynamics of solitons as they are travelling along the fibre span. The difference of this work in respect to other approaches to soliton investigation is the provision by distributed Raman amplification of a quasi lossless link where the fibre attenuation can be compensate along the length of the fibre without the use of lumped amplification. This approach is the closest so far to the ideal one described by equation 6.1.1, where the two main components are the chromatic dispersion related to β_2 the group velocity dispersion (GVD) parameter and the nonlinearity related to γ, responsible for self-phase modulation (SPM).

This chapter is structured in three main sections. The first one corresponds to the description of two measuring techniques used through this work. Although they are well known techniques and widely published [132][133], it is worthy to include an explanation of their functionality and application to our particular set-up as it will clarify the experimental results. The second part of this chapter shows the experimental results that prove true soliton transmission using conventional optical fibre [21]. Experimental FROG spectrograms for first order and higher order solitons at several distance intervals are presented. Finally, the soliton dynamics are investigated using URFL cavity as transmission media. Especial emphasis is set in the following parameters: span length, pumping ratio, FBGs reflectivity and input pulse.

6.2 Measurement techniques

Obtaining experimental results of soliton transmission required different experimental techniques for fibre and optical pulses characterisation. Here we are explaining two of the most frequent experimental techniques used through this work. Although they are well known techniques [132][133] their application to our particular system may differ slightly from standard measurements.

6.2.1 Optical time domain reflectometer

An optical time domain reflectometer (OTDR) is an optoelectronic instrument used for optical fibre characterisation. The usual technique is to connect the OTDR equipment to the fibre to be tested, send an optical pulse envelope and measure the returned signal from back Rayleigh backscattering and other reflections due to refractive index changes. It can be used

for estimating the fibre length and overall attenuation. The typical plot for a length of standard fibre is a straight line with a decreasing gradient of approximately 0.2dB/km as shown in Figure 6.2.1. The figure shows a typical experimental OTDR trace for 22km of LEAF fibre, where the value of the fibre drops from 28.6dB at 0km down to 24.2dB at 22.4km. The important value is the variation between these two points, as the power level may drop or increase depending on the amount of light scattered back to the OTDR system.

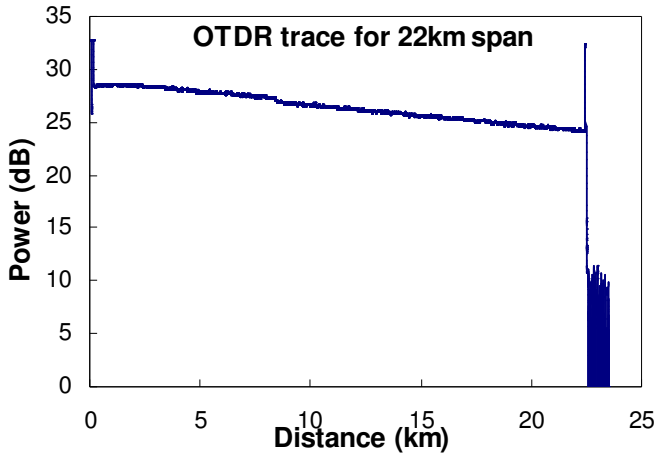

Figure 6.2.1: Typical experimental OTDR trace for 22km span

Using the same principle to measure the power profile of an ultralong Raman fibre laser (URFL) operating as a second order distributed Raman amplification system requires a different set-up, shown in Figure 6.2.2, to the standard one. Also the following set-up gives the flexibility of allowing measurement of the power profile characteristics, attenuation and losses of the fibre at wavelengths other than 1550nm.

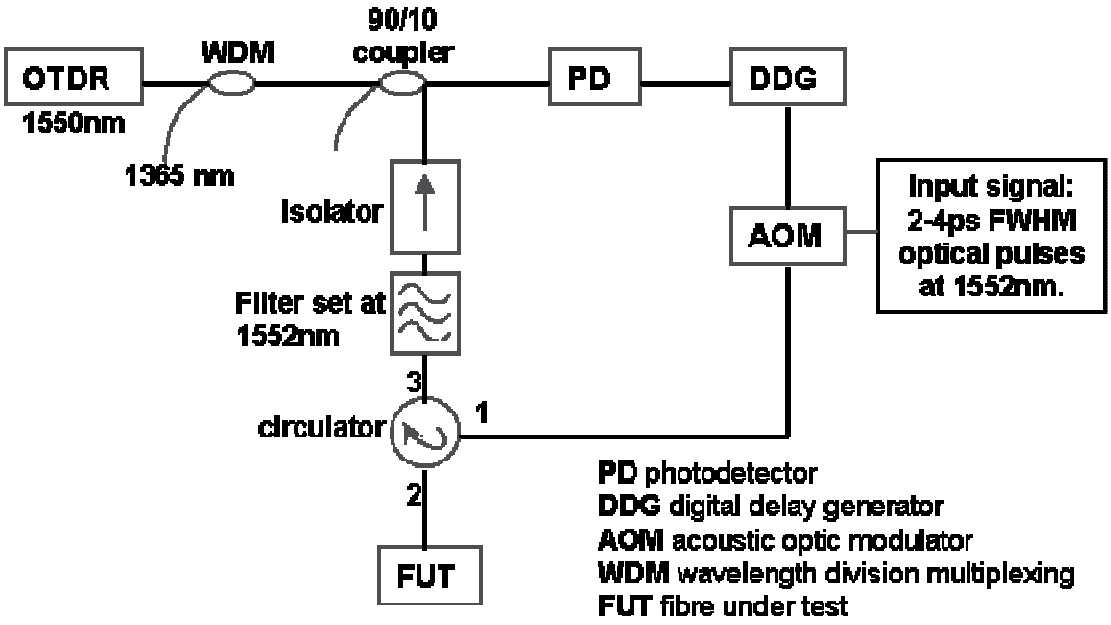

Figure 6.2.2: OTDR experimental set-up

The OTDR instrument is still used to send an optical pulse envelope ranging from 500ns to 4μs. The optical signal is detected by a photodiode that converts the signal from optical to

electrical. The photodiode triggers a digital delay generator (DDG), so that the DDG is triggered synchronously with the OTDR. This digital delay generator amplifies the electrical signal and is connected to an acoustic optic modulator (AOM). The AOM opens and closes, replicating the initial optical envelope signal from the OTDR. From another set-up, we have an optical signal source around 1550nm that will be used as the transmission signal in our URFL cavity system. The pulse width of the signal is approximately 2 to 4 picoseconds. The AOM is used to modulate this optical signal around 1550nm with the same pulse envelope as the OTDR. This signal around 1550nm is sent to our system under test using a circulator. The signal we get back from our system is a combination from the Rayleigh backscattering of 1550nm plus remaining from the 1365nm Raman pumps and the first Stokes at 1455nm. A filter is set-up at the exactly same wavelength as the initial optical signal to reduce as much as possible all the other wavelengths. After the isolator, a 90/10 coupler and a Raman coupler the scattered signal reach the OTDR. The OTDR then records the back scattered signal as normal and display the power profile along the fibre length.

6.2.2 Second harmonic generation frequency resolved optical gating

Second harmonic generation frequency resolved optical gating (SHG FROG) is a characterisation technique for ultrashort optical pulses [133]. It involves splitting the pulse in two different optical paths, t and $t-\tau$, changing the time delay of one of the optical paths by moving one of the mirrors, and recombining them in a nonlinear crystal, that will creates its second harmonic as shown in Figure 6.2.3.

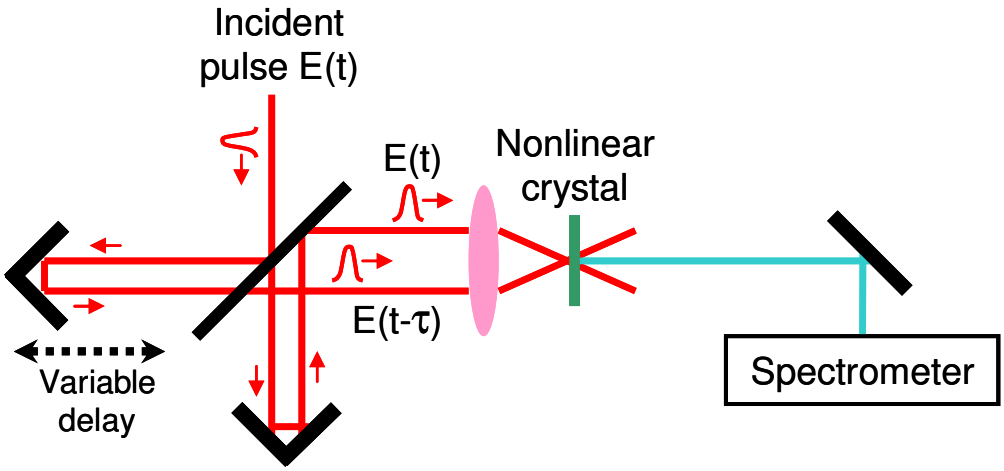

Figure 6.2.3: Schematics for SHG FROG set-up

The main difference with other conventional characterisation techniques is that with the SHG-FROG is possible to recover from the measured spectrogram not only the associated

time dependent intensity but also the phase information. An example of two dimensional time-frequency spectrogram of the laser pulse, known as a FROG trace, is shown in Figure 6.2.4, where is represented simultaneously time (horizontal) and wavelength (vertical) information.

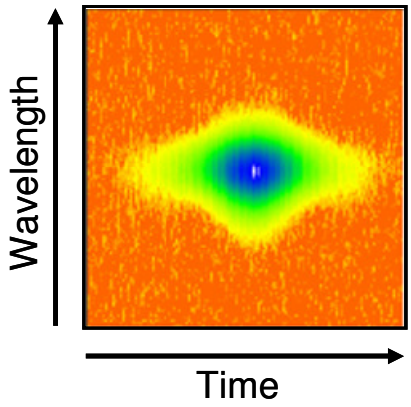

Figure 6.2.4: Experimental FROG spectrogram

Although the time direction is ambiguous with the SHG-FROG, its importance in these measurements is not relevant as the expected spectrograms are symmetric respect the vertical axis passing by the centre.

6.3 Experimental results for true soliton transmission

As previously mentioned, exact optical soliton solutions have many potential applications in optical communications [120][134], laser sources [117] or all-optical signal processing and signal regeneration [118], although they exist only under non-dissipative conditions. Unfortunately, in practical optical transmission systems, the intrinsic fibre loss makes unperturbed soliton transmission over long distances impossible even for low-loss media, as the integrity of the soliton pulse relies on the balance between the power-dependent self phase modulation in the transmission fibre and the constant anomalous chromatic dispersion of the fibre.

To overcome this problem, a number of techniques have been used to obtain approximations to the exact fundamental soliton solution. Average solitons find a balance between nonlinearity and dispersion on average over fibre spans where the loss is periodically compensated by lumped amplifiers [120][126]. Dispersion managed soliton experiments use periodically alternating dispersion values within the transmissions path to obtain periodically stable pulses [135]. Solitons can also be supported in decreasing dispersion fibre engineered to match the decrease in nonlinearity due to loss [129]. These approaches do produce soliton-like pulses with interesting properties and potential

applications but rely on either custom fibre or exact replication of a loss cycle/dispersion unit cell between amplification stages to be successful.

An alternative option is to reduce signal power excursion along the fibre by using distributed Raman amplification. This has been shown to support soliton transmission over long distances in recirculating loop experiments [136]. However to date such demonstrations have been restricted to the case where the fibre spans are shorter than the soliton period due to considerable power variation along the span length.

6.3.1 URFL set-up for soliton stability transmission

The experimental results presented here are the first demonstration of transmission of fundamental solitons over multiple soliton periods in conventional optical fibre with negligible amplitude or phase distortion. To achieve this we use an ultralong Raman fibre laser (URFL) transmission scheme, as shown in Figure 6.3.1, which allows signal propagation over long distances in optical fibre with extremely low power level excursions [15][78].

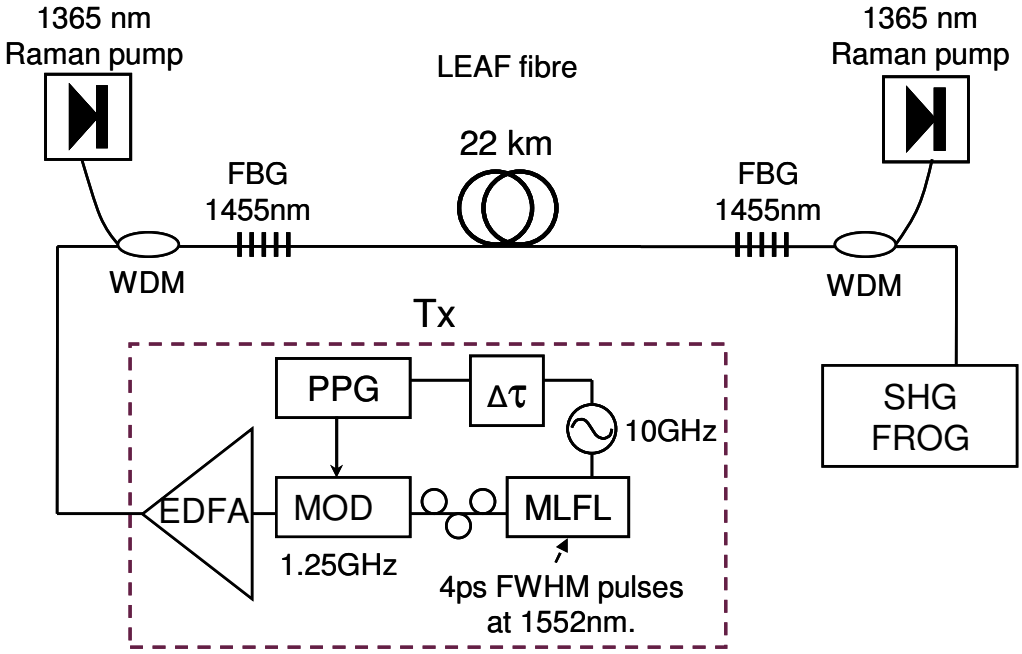

Figure 6.3.1: Experimental set-up for soliton transmission.

When measuring power profiles along the span the OTDR set-up was positioned at either the input or output of the sytem under test. In Figure 6.3.1 this is equivalent to the OTDR set-up replacing either the SHG FROG or the transmitter. The OTDR set-up was as shown in Figure 6.2.2. The optical output pulse from the OTDR is used to generate an electrical trigger pulse used to gate the output of the source laser. The source laser output is then used as the probe input to the system under test, which in this case comprised the fibre

span, FBGs and WDMs. As described in Section 6.2.1 the light scattered backwards through the system was returned to the OTDR for measurement.

Our initial transmission span consisted of 22km of conventional single-mode large effective area Silica fibre with a second-order dispersion parameter, β_2, of -5.8ps^2/km and a nonlinear coefficient, γ, of 1.2W^{-1}km^{-1} at the 1552nm operating wavelength. LEAF fibre is a conventional optical communications fibre with a dispersion coefficient approximately four times lower than single mode fibre (SMF). Therefore the launch power required for soliton transmission is lower than the power required if SMF were used in this experiment. Otherwise LEAF fibre has similar characteristics to SMF. High-reflectivity (99%) fibre Bragg gratings (FBGs) with a full width at half maximum bandwidth of 0.6nm were used to form the cavity. The system was bi-directionally pumped using two 1365nm Raman laser sources. The gratings were designed to give maximum reflectivity at 1455nm (the wavelength of the first Raman Stokes shift of our pumps), hence creating a cavity for radiation at that wavelength. The pump and the pulsed signal at 1552nm were coupled into the transmission system through 1365/1550nm wavelength division multiplexers (WDMs). Using optical time-domain reflectometry (OTDR) it is possible to monitor power excursion at 1550nm, and manually adjust pump power to fully compensate for fibre attenuation [78].

The sech profile signal pulses, with FWHM of approximately 4ps and a soliton period of ~1.4km, were generated by a mode locked fibre laser (MLFL) operating at 1552nm. The 10GHz output pulse train of the fibre laser was modulated down to a repetition rate of 1.25GHz, so that relatively high peak power could be achieved at low average power levels without introducing nonlinear distortion effects from the Erbium doped fibre amplifier (EDFA). The modulation at 1.25GHz was achieved by synchronising the pulse pattern generator (PPG) and the MLFL with some time delay in between. The PPG had a pattern of 10000000 bits and was connected to a lithium niobate Mach-Zehnder amplitude modulator. The modulator (MOD) was set allowing only one every 8 bits to go through by applying a voltage to one of the arms of the modulator. Therefore the operating rate was reduced from 10GHz to 1.25GHz

Note that the focus of this experiment was to prove the transmission of individual fundamental soliton pulses and no form of data encoding was applied. The output signal pulses were characterised using second harmonic generation frequency-resolved optical gating (SHG-FROG) [133], which generate complete spectrograms with simultaneous time (horizontal) and wavelength (vertical) information. The average launch power required for fundamental solitons in the ideal case was calculated to be 6.8dBm. However, in practice the required power was slightly higher, 7.8dBm (pulse energy 4.6pJ and 1120mW peak power),

due to the additional losses within the experimental system (mainly fibre connections). The output of the MLFL was carefully adjusted to obtain a launched pulse intensity profile as close as possible to the typical $sech^2$ of the fundamental soliton.

Similarly, the URFL span was pumped to provide distributed gain as close as possible to ideal transparency. By under pumping or over pumping with respect to this optimal value, it is possible to move from a dispersion-dominated regime to a nonlinearity dominated regime. In the case of under pumping Figure 6.3.2 (iii), the pulse displays temporal broadening due to chromatic dispersion. The resulting output pulse, Figure 6.3.4 (iii) will be temporally broadened with respect to the input pulse. Figure 6.3.3. On the other hand, if the Raman pump power is higher than optimal Figure 6.3.2 (i), the pulse experiences a net gain across the span, and self phase modulation (SPM) dominates, leading to temporal compression. The resulting output pulse, Figure 6.3.4 (i) is clearly temporally shorter than the launch pulse Figure 6.3.3. Optimal pumping, Figure 6.3.2 (ii), turns the cavity into a virtually non dissipative link with minimum power excursion, in which the balance between the dispersion and nonlinearity can be maintained. The output, Figure 6.3.4 (ii), and launched, Figure 6.3.3, pulse spectrograms are similar, therefore its spectral and temporal characteristics are also the same.

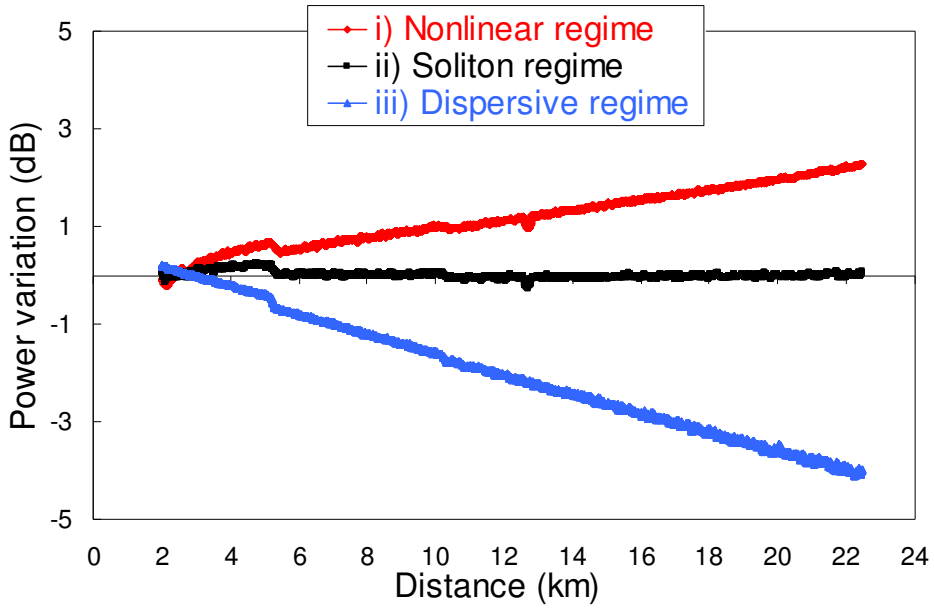

Figure 6.3.2: Power variation profile along a 22km fibre span for the (i) nonlinear regime (SPM dominates), 0.83W Raman power; (ii) soliton regime (virtually non dissipative), 0.56W Raman power; and (iii) dispersive regime (dispersion dominates), 0.29W Raman power.

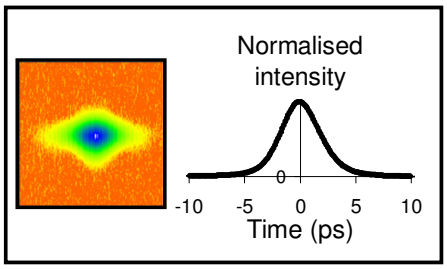

Figure 6.3.3: Spectrogram and temporal intensity profile of the launched pulse.

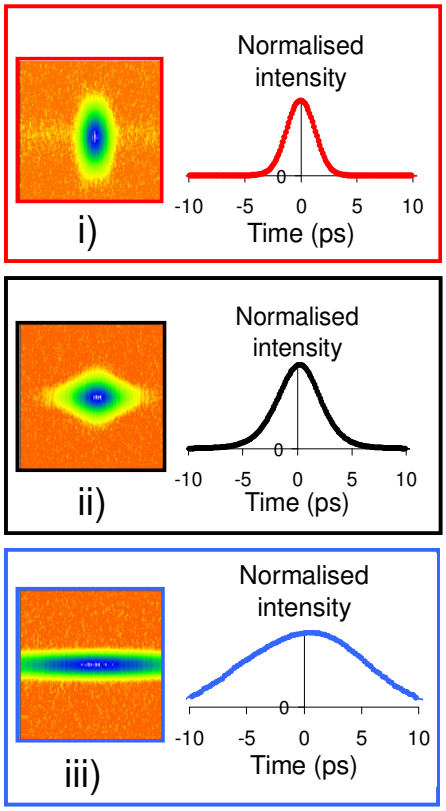

Figure 6.3.4: Spectrogram and temporal intensity profile of the output pulse (i) when SPM dominates, (ii) for the soliton regime, and (iii) when dispersion dominates.

The spectrograms, which display the characteristic $sech^2$ shape of a soliton, together with the effectively null intensity variation across the fibre length observed via OTDR, give a good indication of the dynamics of the fundamental optical soliton, but are not full proof of unperturbed evolution within the fibre span.

6.3.2 First order soliton

In order to experimentally demonstrate that the soliton remains undistorted across the whole length of the fibre, the initial fibre span of 22km (~16 soliton periods) was divided into four different lengths (3km, 2km, 5km and 12km) as schematically depicted in Figure 6.3.5, and spectrograms were taken after each interval and combination order of the different lengths. The four fibre lengths were chosen in such way that was possible to take a measurement every couple of kilometres by setting the span length order in different combinations. A single 1% monitoring coupler, with an insertion loss of 0.4dBm, was moved across the range of available positions in the span to measure at different points in the fibre.

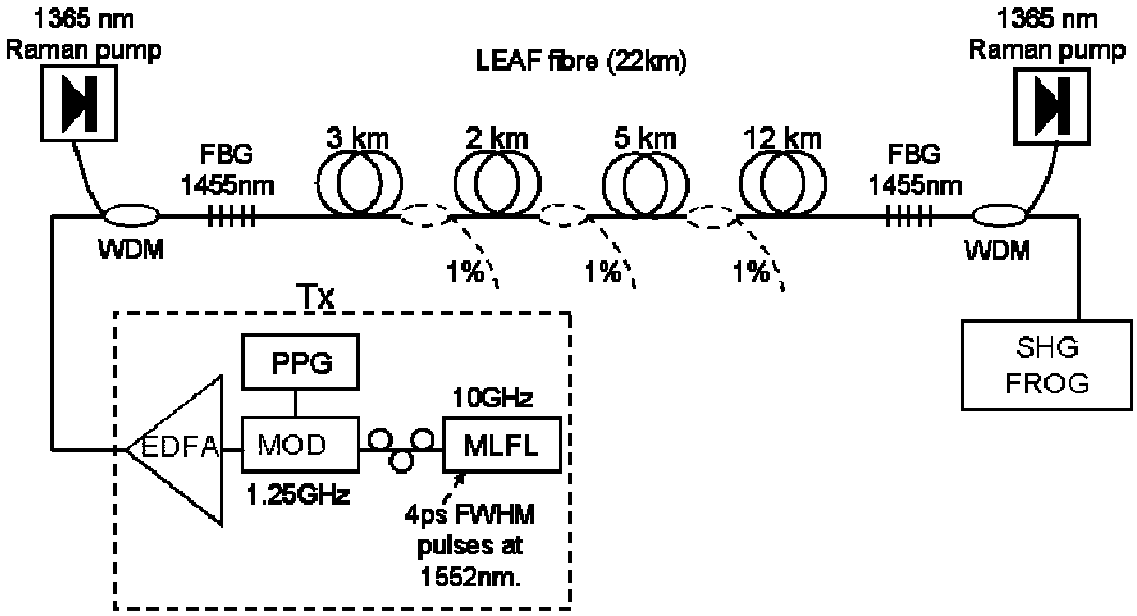

Figure 6.3.5: Experimental set-up for observing the soliton transmission at different positions along the fibre.

Once the FROG spectrogram was taken at one point, the single 1% monitoring coupler was moved to another interval and the rest of the fibre spans spliced to minimised fibre losses. The optical power profile along the fibre span was verified to be as similar as possible with the same value of power excursion for each interval measurement.

The set of spectrograms for first order soliton at a launch power of 7.8dBm is shown in Figure 6.3.6 (top row). SHG-FROG spectrograms were measured on a 33.8ps x 2nm grid with 128 x 128 points (264fs x 0.016nm resolution). As expected, the experimental traces closely resemble each other regardless of their position along the fibre. Therefore it can be said that pulse characteristics remain the same for the whole transmission span. Note that the small variations in pulse duration on the experimental trace are caused by the equally small loss variations due to the repositioning of the output coupler.

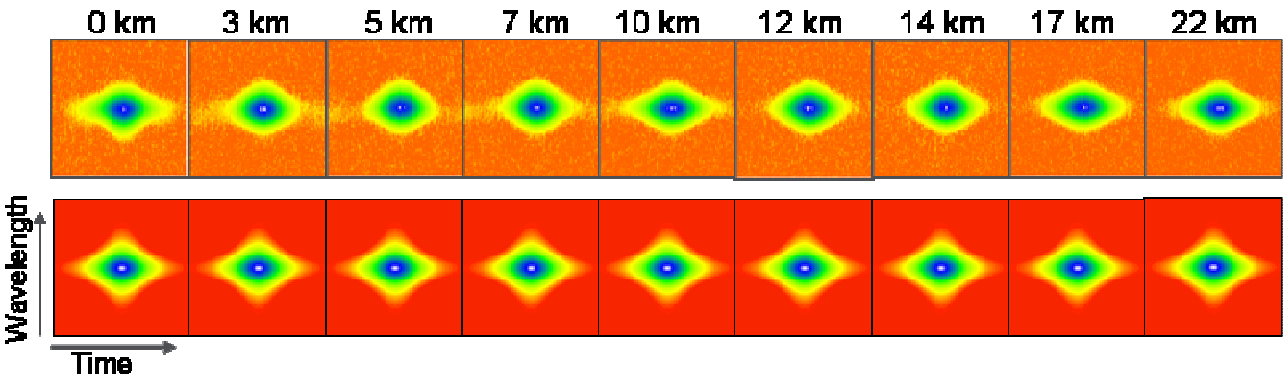

Figure 6.3.6: Set of experimental (top row) and numerical simulation (bottom row) FROG spectrograms at different locations along the fibre span [21].

Otherwise the experimental results are consistent for the whole span, achieving excellent agreement with the numerical simulation results for a fundamental soliton evolution shown on the bottom row of Figure 6.3.6. The pulse duration, recovered from the spectrograms, is represented versus distance in Figure 6.3.7. This is represented as the ratio of the pulse duration period versus the number of soliton periods.

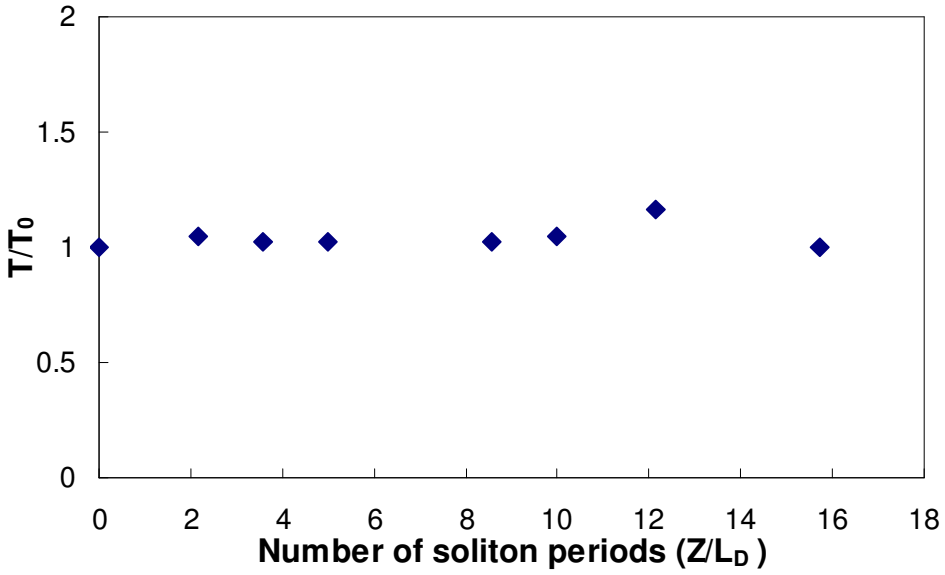

Figure 6.3.7: Experimental results for pulse width versus propagation distance.

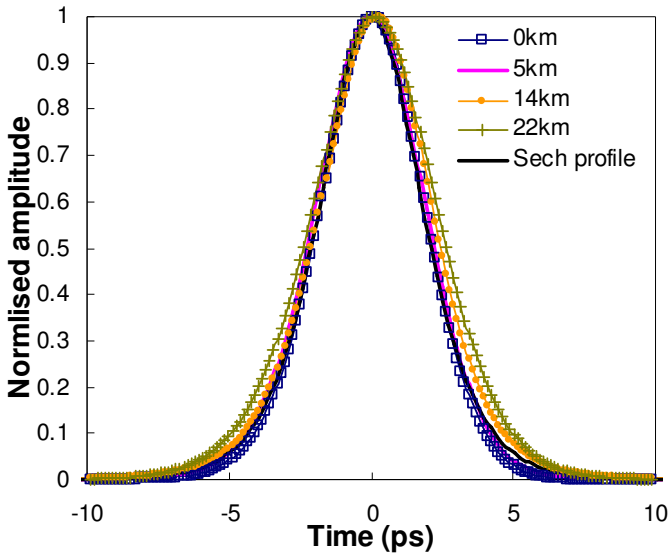

Figure 6.3.8: Amplitude recovery from the experimental FROG spectrograms for the positions 0, 5, 14 and 22km and the theoretical 4ps sech^2 pulse shape.

Figure 6.3.8 show the recovered time from the FROG spectrograms for a few of the previous cases, 0, 5, 14 and 22km. The intensity profiles match among each other and also with the expected $sech^2$ pulse profile for a 4ps FWHM soliton pulse.

Further experimental work was carried out with span lengths of 50 and 72km. The experimental spectrograms for the launch and output pulses are represented in Figure 6.3.9. Given that a pulse with adequate energy and duration can be expected to evolve naturally into a fundamental soliton while propagating through our virtually non-dissipative fibre link, we did not perform an initial optimization of the pulse shape in this case, using instead a 4ps pseudo-Gaussian pulse. As expected, the optical pulse evolved towards the typical soliton shape after some initial stabilisation.

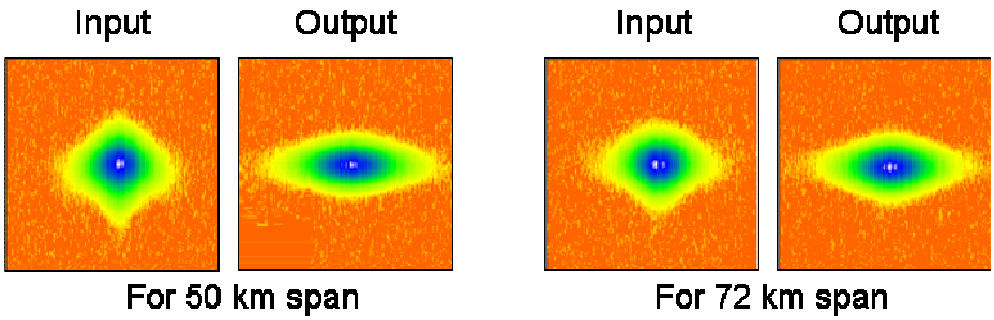

Figure 6.3.9: Measured spectrograms from launch and output pulses at 50km (left) and 72km (right).

Note that the increasing power excursion of longer fibre spans [78] makes pulse measurements more difficult within the fibre span due to the introduction of losses. Therefore, pumping optimization in the transmission span becomes particularly important. In spite of the added difficulties, the spectrograms for the output pulses for the case of 72km are still consistent with a soliton profile, indicating that intensity variations within the span, approximately 1dB, are still small enough not to have introduced a significant perturbation to the pulse dynamics.

In conclusion, long distance transmission of fundamental optical solitons over multiple soliton period without amplitude, temporal or phase variation has been demonstrated. An ultralong Raman fibre laser amplification scheme was used to provide a virtually non dissipative medium that allowed the signal to propagate at a constant power level as required for soliton stability. Pulse dynamics were monitored and verified using SHG-FROG measurements which produce spectrograms which are entirely consistent with those predicted through numerical simulations of fundamental soliton transmission. Our initial experiment shows stability of a 4ps soliton over a 22km span of LEAF fibre a distance equivalent to over 15 soliton periods. This distance was then extended to over 50 soliton periods for a 72km span. These results, obtained using conventional fibre, represent an

important step towards the possible implementation of practical soliton transmission and optical processing systems.

6.3.3 Second order soliton

Once fundamental soliton transmission in conventional optical fibre was experimentally achieved, the following logical step was to investigate higher order soliton and their dynamics within a soliton period. Higher order soliton required peak power energy, P_0, higher than the fundamental soliton, by a factor square to N, with N being the soliton order as shown by the following relation:

$$P_0 = N^2 \left|\beta_2\right| / \gamma\tau_0^2 . \qquad \textbf{6.3.1}$$

N=1 is for fundamental soliton. N=2 is for the second order soliton. With β_2 and γ as the group velocity dispersion and the self-phase modulation parameters. τ^2_0 is the soliton pulse width. The temporal shape of a higher order soliton is not constant, but rather evolves periodically during propagation, returning to the initial optical pulse after the so called soliton period, Z_0. The relation between the soliton period and L_D, the dispersion length is given by Equation 6.3.2, with L_D defined by Equation 6.3.3.

$$Z_0 = \pi / 2.L_D . \qquad \textbf{6.3.2}$$

$$L_D = \tau_0^2 / \left|\beta_2\right| . \qquad \textbf{6.3.3}$$

Second order solitons require four times the power for the fundamental soliton given the same soliton pulse width, as given by Equation 6.3.1. We could increase the pulse width of the optical pulses to reduce the power required but this has the effect of increasing the soliton period, reducing in practice the capacity of optical transmission at higher repetition rates.

Whereas fundamental solitons have a constant shape through propagation, higher order solitons evolve periodically, breathing in and out, as shown in Figure 6.3.10 for the case of a second order soliton. They can break up into fundamental solitons under the influence of various nonlinear effects, such as self-phase modulation, higher order dispersion and Raman scattering. Such solitons break-up or so-called soliton fission are essential in the process of supercontinuum generation in optical fibres as discussed in the previous chapter.

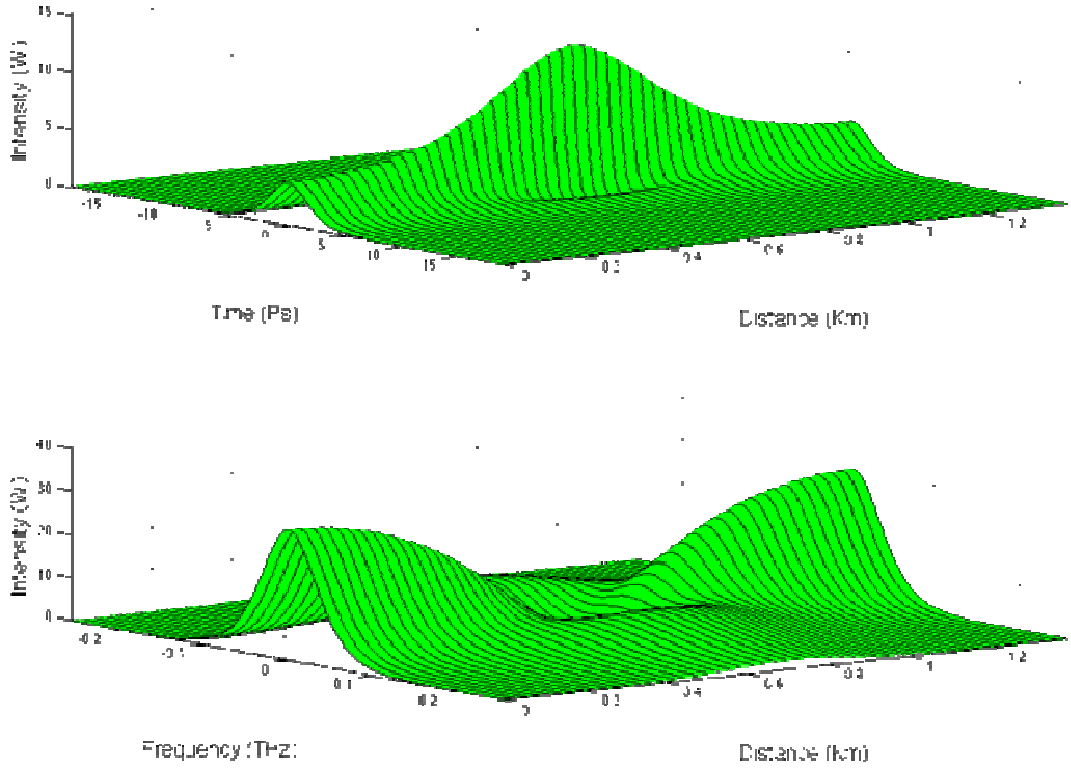

Figure 6.3.10: Simulation for second order soliton evolution within one soliton period by J.D. Ania-Castañon [137].

The objective of our work in this section was to provide distributed Raman gain in the transmission media to make possible practical higher order soliton transmission. Any further investigation on higher order solitons performance was outside of our scope in this work.

The experimental set-up for higher order soliton transmission is depicted Figure 6.3.11. In this case, the optical pulse width was increased to 9ps, so the required launch power for the ideal case of second order soliton transmission was 10dBm instead of 13.4dBm as it would be for 4ps pulse width. This meant that the soliton period was ~7km in this case. Therefore the total length of the conventional LEAF fibre, with second-order dispersion parameter, β_2, of -5.4ps^2/km, was increased to 48km. The fibre was divided in several reels and we were using a four port 1%-99% coupler at different optical fibre positions so we could obtain FROG spectrograms within the soliton period at regular intervals.

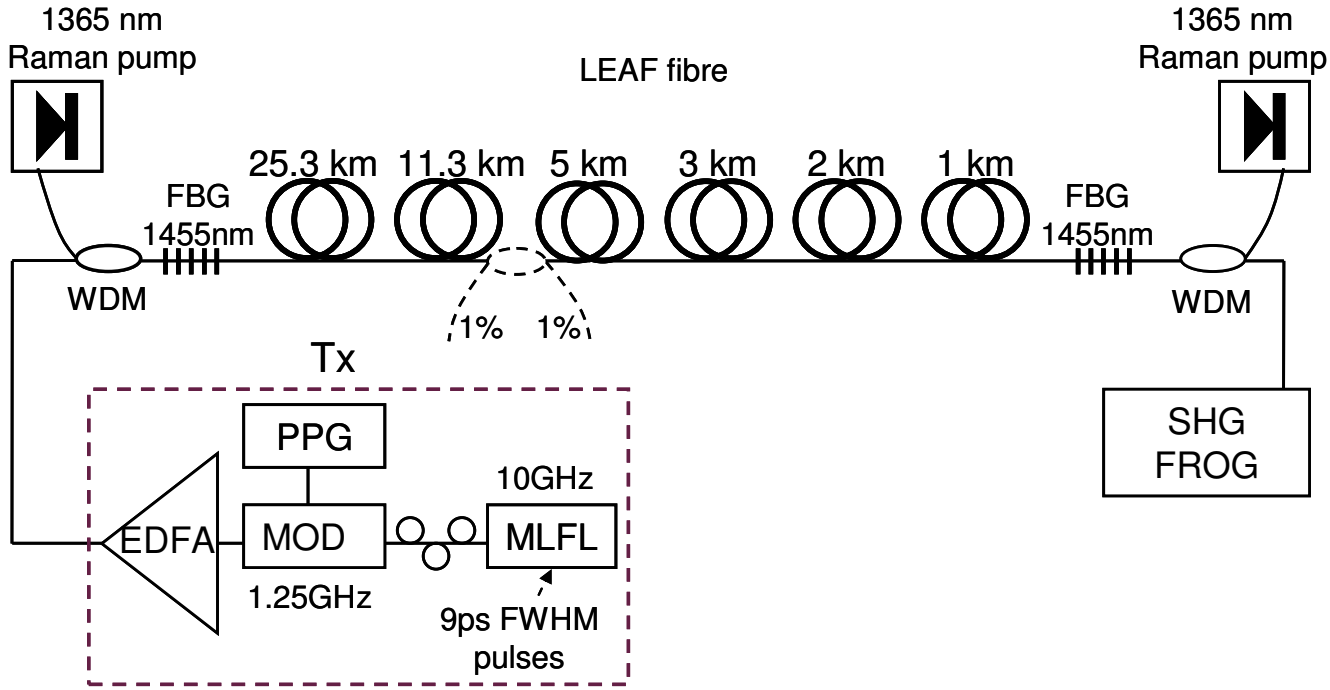

Figure 6.3.11: Experimental set-up for second order soliton transmission.

As in the previous experiment, the power required in practice was expected to be approximately 1dBm higher, to account for fibre losses and dispersive radiation energy as the pulse evolve from the launch pseudo-Gaussian pulse to the soliton sech type. This level of power was in the upper range limit available from our source after optical amplification. Figure 6.3.12 shows experimental spectrograms taken between 0km and 37.6km at several intervals, with some of them less than 1km apart. SHG-FROG spectrograms were measured on a 129.5ps x 2nm grid with 128 x 128 points (1012fs x 0.016nm resolution).

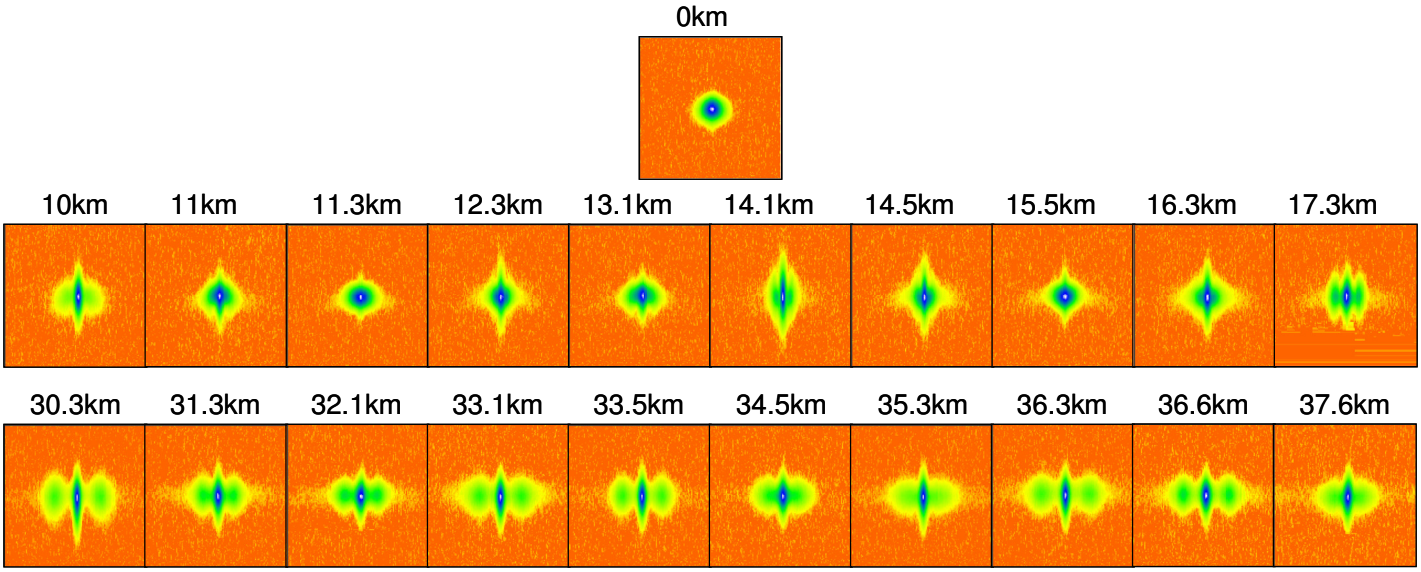

Figure 6.3.12: Set of experimental FROG spectrograms at different location along the fibre for second order soliton transmission.

The top spectrogram from Figure 6.3.12 at 0km corresponds to the launch input pulse of 9ps pulse width. The middle and bottom row trace the output FROG spectrograms obtained for two intervals sets, just over 7km, one from 10km to 17.3km and another from 30.3km to 37.6km. Although the experimental results from Figure 6.3.12 are not all exactly at the same interval difference, it can be observed that there is a sort of breathing of the optical pulse in a periodic way, especially in the interval ranging from 10km to 17.3km. Unfortunately the behaviour is not quite the same in the interval 30.3km to 37.6km. Although there is some periodic pulse evolution, the optical pulse has broadened and the initial shape characteristic cannot be fully recovered. The experimental results were not adequate to demonstrate in a irrefutable manner second order soliton transmission. The equivalent simulation for a second order soliton within the soliton period is shown in Figure 6.3.13.

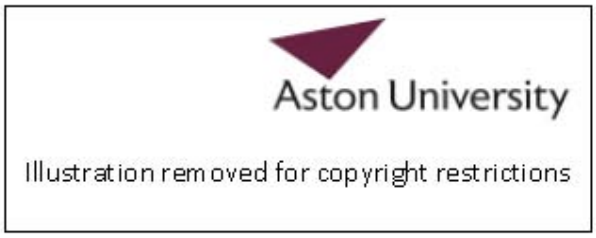

Figure 6.3.13: Set of simulated FROG spectrograms for second order soliton transmission within one soliton period by J.D. Ania-Castañon [137].

The spectrogram from Figure 6.3.12 at 14.1km could be identified as the one expected at half soliton period. The one at 12.3km could be the equivalent to one quarter or three quarter soliton period, and the one at 11.3km or 15.5km could be identified with the beginning or end of the period. Unfortunately and despite all the experimental effort, the results are not conclusive enough to identify without any doubt each spectrogram with a particular stage of the soliton period, showing the expected soliton dynamics over several soliton periods. The two major drawbacks were the power limit available for the launch input signal and the losses involved delivering the signal and within the transmission system. Although the system involved an EDFA amplifier, delivering the signal at the entrance of the transmission span could involve a drop in power of approximately 7-8dB in the best of the cases. Therefore, we could not be sure of delivering in all the cases enough input signal for second order soliton transmission.

6.4 Effect of URFL cavity design on soliton dynamics

It the previous section ultralong Raman fibre laser (URFL) cavities were shown to be virtually lossless transmission links using second order distributed Raman amplification to provide near ideal distributed gain to a soliton signal. The first experimental demonstration of long-distance exact soliton propagation through conventional optical fibre was presented using such a virtually non-dissipative link, paving the way for multiple applications in communications and signal processing. Although both the total signal power excursion and the maximum effective local attenuation in ultralong cavities are extremely low compared with those of conventional transmission schemes, they still show an exponential growth with span length. Furthermore, the effective attenuation profile itself can be affected by high power transmitted signals due to pump depletion. Hence, it is of particular importance to determine the operational limits of these virtually lossless links in terms of both cavity length and nonlinear tolerance to signal characteristics.

To that end, the dynamics and stability of soliton pulses across URFL transmission links is investigated, as well as the dependence of these dynamics on cavity design (length, pump symmetry, FBGs reflectivity) and input pulse characteristics [25]. In this chapter we present a combination of simulation and experimental results regarding the performance of soliton transmission in URFL links for a range of input pulse powers and variation of the following cavity parameters; length, pump symmetry and FBG reflectivity.

The experimental set-up for our soliton transmission link is depicted in Figure 6.4.1. It involves a URFL cavity operating as a second order pumping Raman distributed amplification scheme. The URFL cavity acts as both amplifier and transmission link. Two equal power depolarized primary pumps centred at 1365nm are launched from both extremes of the transmission span and FBG reflectors are positioned at each end of the fibre span, each of them with a full width at half maximum bandwidth of 0.6nm centered at 1455nm, given the characteristic 13.2THz Raman shift of silica fibre of the primary pumps, to form a cavity for the generated laser radiation. Above threshold, when the stimulated Raman scattering (SRS) overcomes the fibre attenuation suffered by the first Stokes, a secondary bi-directional pump at 1455nm is generated that can be used to provide a nearly constant Raman gain around the signal wavelength of 1550nm. Before each FBG a 1365/1550nm wavelength division multiplexer (WDM) was placed at each side to couple the pump and the signal into the transmission span.

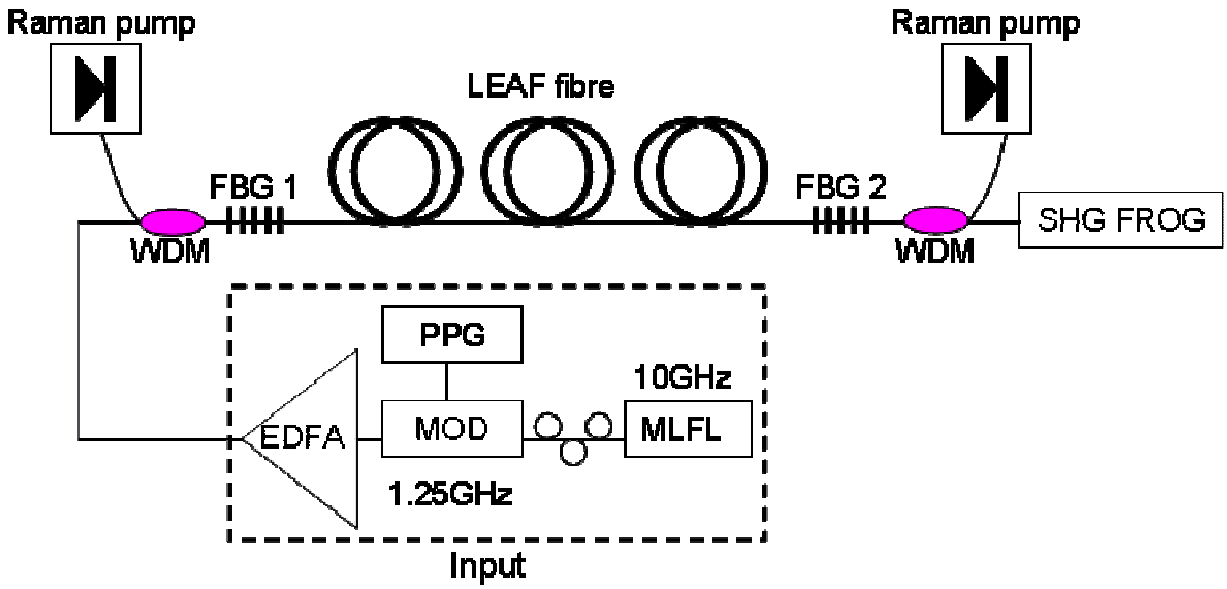

Figure 6.4.1: Experimental set-up for soliton transmission link.

In our experiment the transmission span consisted of conventional single-mode large effective area (LEAF) Silica fibre with a second-order dispersion parameter, β_2, of -5.8ps^2/km and a nonlinear coefficient, γ, of 1.2W^{-1}km^{-1} at 1552nm. The transmitted sech profile optical signal pulses were generated by a mode locked fibre laser (MLFL) operating at 1552nm, with FWHM pulses of approximately 2.8ps. The 10GHz output pulse train of the fibre laser was modulated down to a repetition rate of 1.25GHz, so that relatively high peak power could be achieved at low average power levels without introducing nonlinear distortion effects from the Erbium doped fibre amplifier (EDFA). The output of the MLFL was adjusted practically as much as possible to obtain a launched pulse intensity profile closed to the typical sech^2 of the fundamental soliton.

Power variation profiles along the fibre length were monitored via optical time domain reflectometry OTDR and the launched and output signal pulses were characterised using second harmonic generation frequency-resolved optical gating (SHG-FROG). Both pulse intensity and phase profiles can be recovered from these SHG-FROG traces. The output pulse spectrograms, together with the intensity variation profile observed across the fibre length via OTDR, give a good indication of the dynamics of the fundamental optical soliton.

6.4.1 Input pulse

Higher power signals affect the transmission link performance due to pump depletion, as confirmed by the experimental results from Chapter 4 (experimental investigation of URFL). Our objective in this section is to investigate and quantify the effect of increasing input pulse

powers in the transmission link performance. The results of this investigation will provide us with some operational limits and indicate in the worst case scenario how to improve the nonlinear transmission tolerance.

The average input signal power in most of our experimental work was 10dBm or lower, with input pulses of approximately 2.8ps operating at 1.25GHz. This range of powers were limited by practical reasons, the maximum amplified signal power without inducing nonlinear effects by the EDFA saturation level, and the intrinsic attenuation produced by connectors, splices and fibre when delivering the input signal. As we try to extend soliton transmission to higher rates for high speed transmission, a wider range of input signal powers will be considered when investigating input signal power effect in transmission. The results provided in this section cover a range of input signal powers between 1mW to 100mW (0dBm to 20dBm).

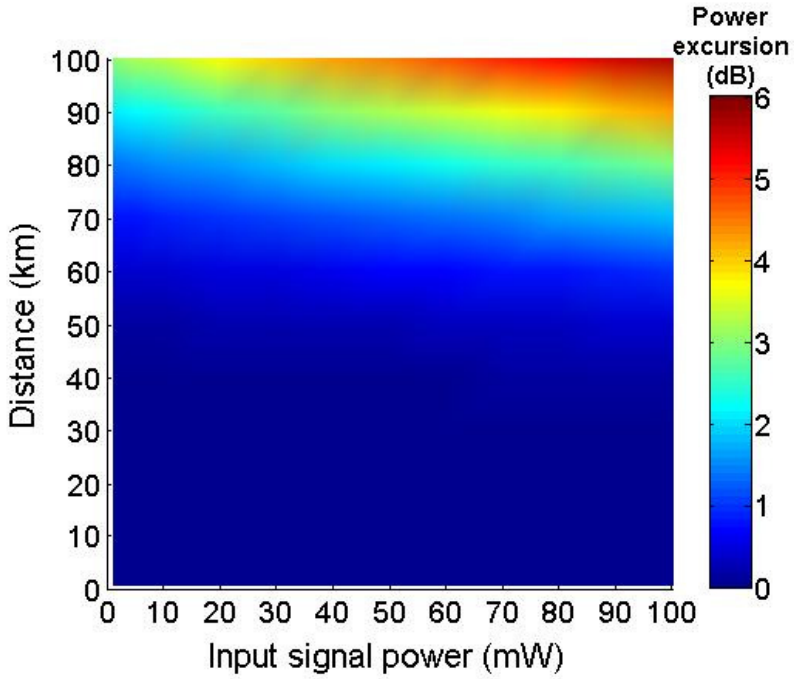

Figure 6.4.2: Numerical results of the power excursion for a range of input powers 1 to 100mW and a range of span lengths, 1 to 100km. The FBGs are 90% reflectivity and the pump ratio is symmetric.

Figure 6.4.2 shows the numerical results of the power variation along the length of the transmission span for a range of span lengths, 1 to 100km, and a range of average input signal powers, 1 to 100mW. The increase of average input signal relates to a higher repetition rate and not an increase of peak powers, as we use similar pulse duration, approximately 2.8ps, through all this work unless otherwise mentioned.

The results were obtained assuming symmetric bi-directional pumping and FBGs with 90% reflectivity. The increase of input signal powers has especially a greater effect in the higher span length region; 75km to 100km. The power excursion along the transmission

span is greater at longer span lengths. As example, Figure 6.4.3 shows the power excursion versus the input signal power for three particular span lengths, 50, 90 and 100km. The power excursion is linearly dependent on the input signal with a greater gradient for longer span lengths. As we can observe from Figure 6.4.2 and 6.4.3, the impact of the increasing input signal seems only significant for longer span lengths, well above 50km. The power excursion for 50km and lower span lengths are below 0.5dB regardless of the input signal level.

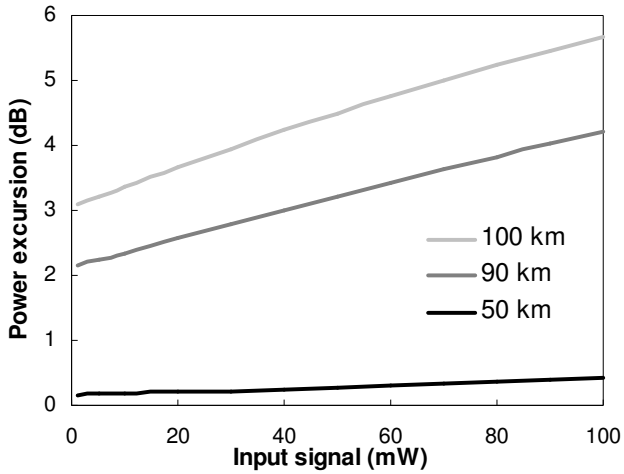

Figure 6.4.3: Numerical results of the power excursion versus input signal power for 50km, 90km and 100km.

From the previous results we can deduce that the greater variation of power excursion between the 1mW to 100mW range of signal investigated is given for the longest span length, 100km. The transmission link performance could be modified by changing the FBGs reflectivity.

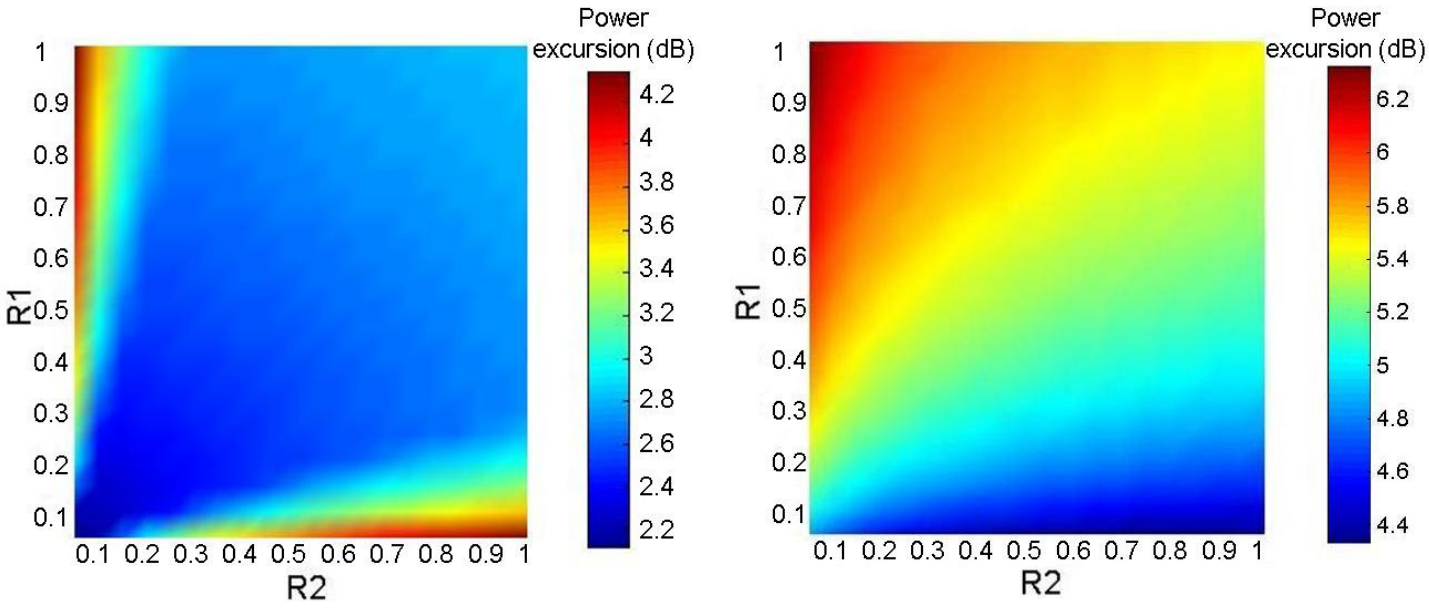

Figure 6.4.4: Maximum power excursion vs. grating reflectivity in a 100km standard fibre URFL for left) 10mW transmitted average power, right) 100mW transmitted average power [137].

For the case of 10mW input signal, Figure 6.4.4 left, the optimum link performance correspond to symmetric FBGs reflectivity with a lower power excursion at lower FBGs reflectivity. The power excursion value drops from over 3dB at 90% reflectivity to less than 2.5dB with FBGs set at 20% reflectivity. For the case of 100mW, Figure 6.4.4 right, the transmission link performance improves its power excursion value by using asymmetric FBGs reflectivity, one FBGs reflectivity (R2) greater than the other (R1). As example, the expected drop in power excursion for both FBGs at 90% corresponds to 5.7dB and it will down to 4.5dB for R2 equal to 90% reflectivity and R1 equal to 15% reflectivity. The previous results confirm the asymmetric behaviour of higher input signal powers as result of pump depletion.

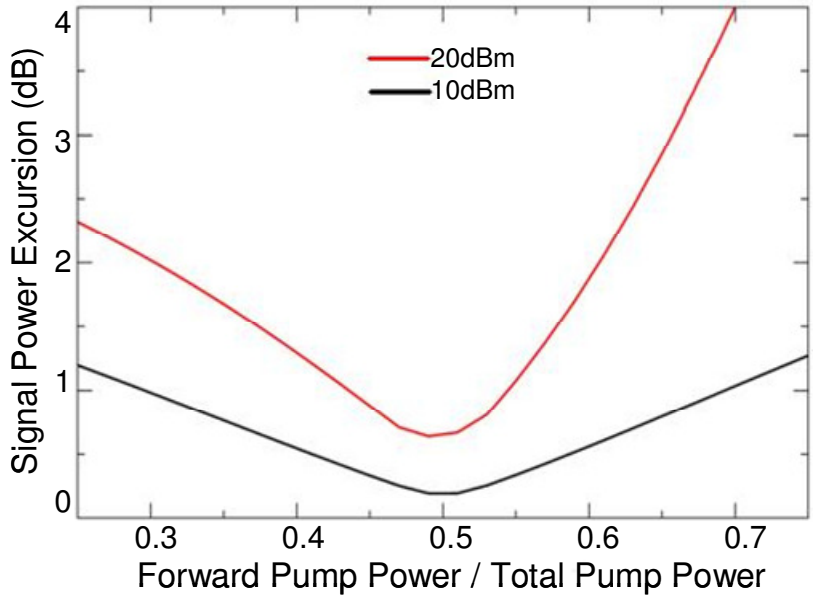

Figure 6.4.5: Numerical simulation of power excursion versus pump ratio for 50km span length at two input signal powers, 10 and 20dBm (10 and 100mW) [137].

Figure 6.4.5 shows how the behaviour of power excursion versus pump ratio may differ for different input signals. The case shown in Figure 6.4.5 corresponds to 50km span length. The pump ratio is defined as the forward pump power divided by the total pump power. The two input signal compared are 10dB and 20dB. Similarly as shown in the Figure 6.4.4, the behaviour when varying a cavity parameter for different input signals is not the same. A greater symmetric behaviour can be observed at low input signals. At higher input signal power, the symmetric relation between the power excursion and the cavity parameters such as FBGs reflectivity and pump ratio is broken. In the particular case of 50km span, the optimum pump ratio for the lowest power excursion is still closed to 50% forward pump and 50% backward pump regardless the input signal. We could say that the impact of pump depletion becomes more obvious, both in the increasing value of power excursion and the

asymmetric behaviour of the system response at higher repetition rates. Still, for all cases considered here, symmetrical pumping offers power excursions below 0.8dB, supporting robust soliton transmission.

6.4.2 Cavity length

One of the key parameters of the URFL cavity as soliton transmission link is the cavity length. As shown by Figure 6.4.2, the cavity length has a major influence in the power excursion performance of the transmission link, drawing the operating limits of URFL as a soliton transmission link. Figure 6.4.6 shows a set of those results. It displays the power excursion versus distance for three input signal values, 0dBm, 10dBm and 20dBm. As we can observe, the power excursion is negligible at lower span lengths, with a maximum value below 0.5dB for a length of 50km span regardless the input signal value. Then the power excursion increase exponentially with a maximum value below 3dB for 80km at 20dBm and increasing to 5.7dB for the case of 100km and 20dBm.

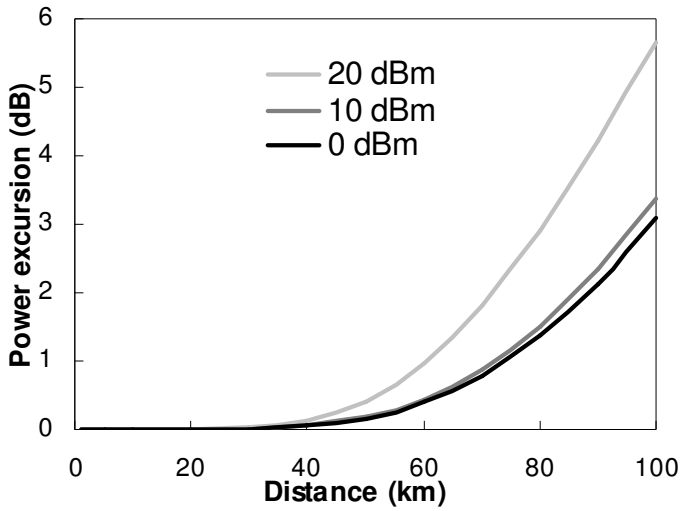

Figure 6.4.6: Numerical simulation of power excursion versus distance for three values of input signal; 0dBm, 10dBm and 20dBm.

From the previous graph we can say that depending on the power excursion tolerances and the value of the input signal required to transmit, we could use longer or shorter span lengths. Most of the experimental work carried out in this thesis was with input pulses in the range of 2ps to 9ps and at repletion rates of 1.25GHz, the input signal power was around 10 dBm or lower. Figure 6.4.7 shows a set of experimental FROG spectrograms at 90km and 100km. Both rows of FROG spectrograms were measured using an URFL cavity with FBGs set at 96% reflectivity and a launch power of approximately 7.3dBm. The pump distribution was symmetric and the losses within the system where minimised by splicing the optical

fibre. The total Raman power required for the case of 90km was 1.2W and the measured power excursion along the fibre span was 2.1dB. The Raman power required for the 100km span was 1.4W and the measured power excursion 3dB.

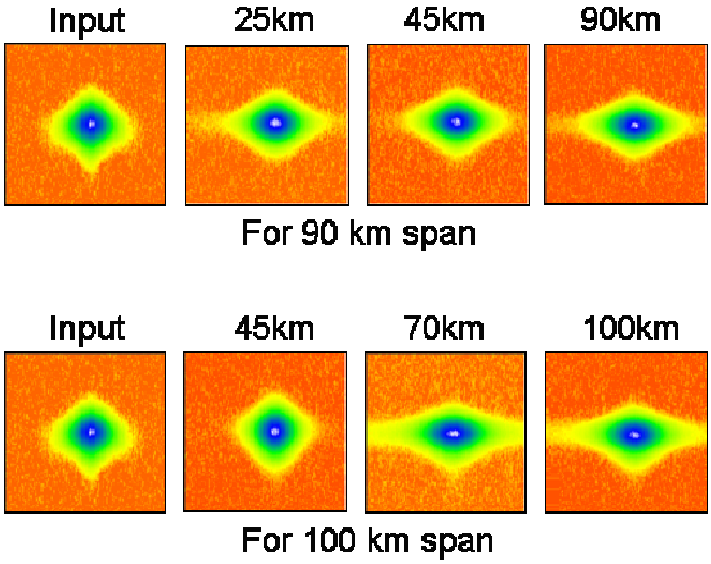

Figure 6.4.7: Experimental FROG spectrograms for 90km span (top row) and 100km span (bottom row) at several distance intervals. FBGs set at 96% reflectivity.

From the previous FROG spectrograms, Figure 6.4.7, we can observe that soliton transmission within the range of input powers and experimental conditions seems within the limits but still feasible for transmission lengths up to 90km. Longer span length with greater power excursion value, degrade the optical pulse, broadening the optical spectrum without being able to recover the initial characteristics of the pulse as shown for the case of 100km span. A way to reduce the power excursion at longer span length is to optimise the system using different FBGs reflectivity. As we saw previously, in Figure 6.4.4 left, for the case of 10mW, the power excursion value can be reduced by using FBGs with lower reflectivity instead of high reflectivities. The power excursion could drop for that particular case by at least 0.5dB. Figure 6.4.8 shows the experimental FROG spectrogram results of the same 100km span system with the main difference that both FBGs are set at 70% reflectivity instead of 96%. The result is an improvement of the output pulse, keeping the same soliton shape and maintaining all the initial characteristics.

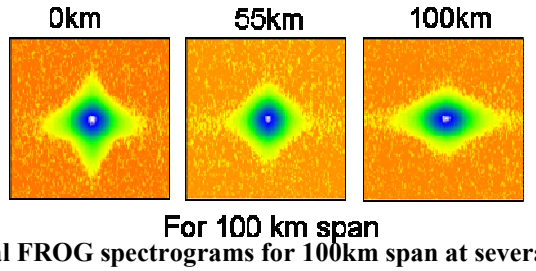

Figure 6.4.8: Experimental FROG spectrograms for 100km span at several distance intervals. FBGs are set at 70%.

The following pair of graphs, Figure 6.4.9, shows how power excursion changes with grating reflectivity and span length. Figure 6.4.9 left side is the case for 50km, and on the right side is the case for 100km. The input signal in both cases is 20dBm. We can observe that for this particular high input average signal, the symmetric behaviour for both FBGs is not accomplished and the optimum value, lower power excursion, tends to be with the FBG 2 at higher value than the reflectivity of FBG 1, with FBG 1 and FBG 2 defined as described in Figure 6.4.1. This can be explained as the higher input signal is transmitted from FBG 1 to FBG 2, therefore higher pump depletion is expected on the side of FBG 1. The main difference between both graphs, left one at 50km and right one at 100km, is the variation in power excursion and how this asymmetric behaviour becomes more obvious not only with increasing average input signal but also with higher span lengths.

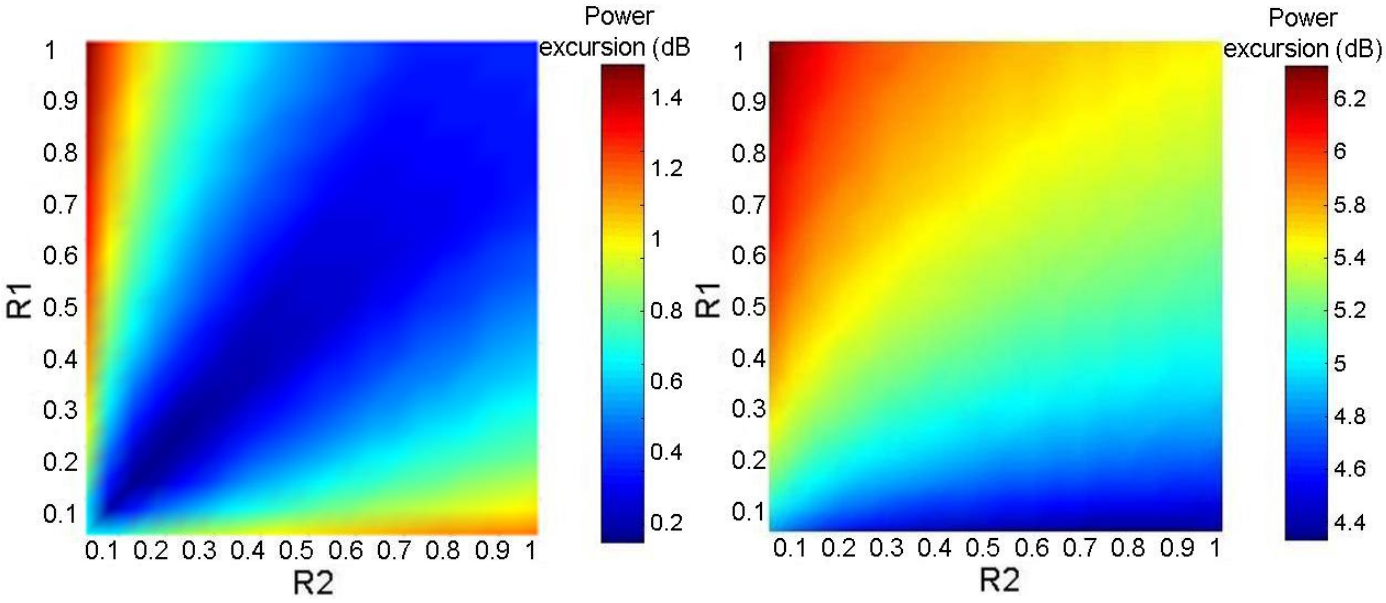

Figure 6.4.9: Maximum power excursion versus grating reflectivity in a left) 50km and right) 100km standard URFL cavity for 20dBm average signal powers [137].

As part of the cavity length investigation, the results on Figure 6.4.10 show the signal power excursion behaviour with pump ratio distribution at several cavity lengths for 10dBm input signal power and FBGs set at 90% reflectivity. As we saw earlier in Figure 6.4.5 the optimum value, lower power excursion, tends to be for symmetric pumping, 50% forward pump power and 50% backward pump power. As the span length increase, the minimum power excursion increases too as shown in Figure 6.4.6. The major effect of increasing the span length relates to an increase of the power excursion. A minor effect of increasing the span length is the non symmetric behaviour of the power excursion with respect to equally bi-directional pumping. This non symmetric behaviour is slightly more obvious at longer lengths, although the non symmetric effect is not that strong as the effect of increasing the input signal as shown by Figure 6.4.5. Also, we can observe a slightly displacement of the

minimum value of power excursion from 50% forward pumping to a slightly lower value with the rest of the power being backward pumped. As already mention, those effects are minimum compared with the effect of increasing the input signal or the cavity length.

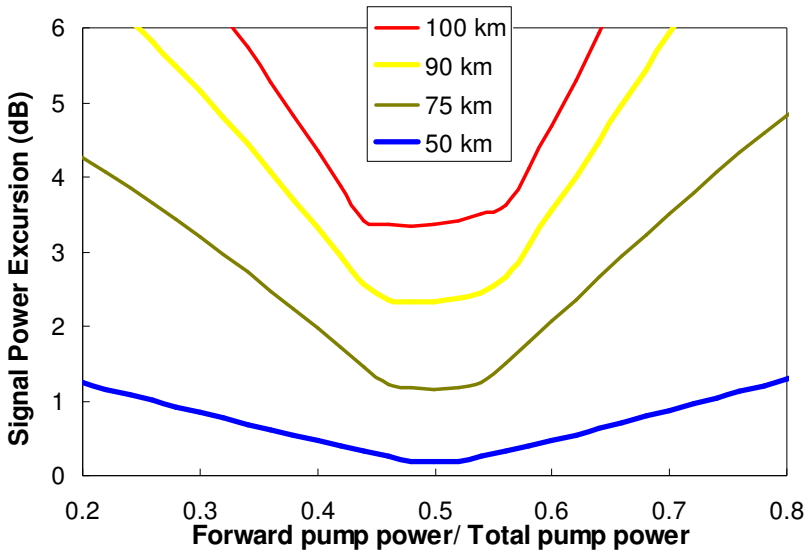

Figure 6.4.10: Numerical simulation of signal power excursion versus pump ratio for 10dBm input signal and 50, 75, 90 and 100km span length.

From the above results we can conclude that cavity length has a major impact on the transmission link performance, drawing operating limits depending on the power excursion tolerances of the transmitted signal. The increase of power excursion given by longer cavity lengths could be offset by changing the FBGs reflectivity, as demonstrated by the results from Figure 6.4.8 at 100km, or using input signals at lower range of values.

6.4.3 Asymmetric pumping

All the work presented in this chapter, including the experimental transmission results, is conditioned to generate an output signal with the same initial input power level unless otherwise stated. This means that the net gain of the system is 0, although it could have local areas of gain and areas of loss, depending on the power distribution along the length of the fibre. Asymmetric pumping relates to the way the distributed Raman gain is generated. Depending on the span length of the system, we could use a mix for forward and backward pumping in different ratios or even use only one pump in the forward or backward direction.

The objective of this work is to confirm experimentally the numerical simulation results and to investigate the effect that asymmetric pumping may have in the transmitted signal, measured by the output signal FROG spectrograms.

The following graph, Figure 6.4.11, shows the numerical simulation (solid line) and experimental results (single points) of the power excursion versus pump ratio for 50km,

75km and 100km. The FBGs reflectivity for the numerical results is 90%. The experimental FBGs are 96% reflectivity. Given the difference of reflectivity and within the experimental conditions, we could say that the experimental results are in good agreement with the numerical results. As expected the power excursion increase with cavity length and for values of pump distribution away from symmetric pumping.

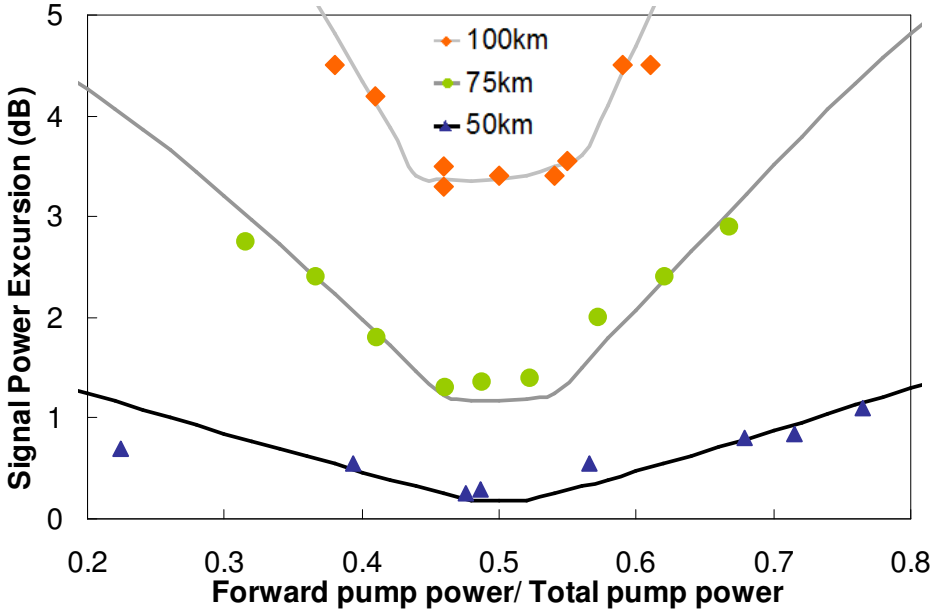

Figure 6.4.11: Experimental (points) and numerical results (line) of the power excursion versus pump ratio for 10dBm input signal and 50km, 75km and 100km span length.

As an example of the experimental power profile distribution along the length of the fibre, we are presenting in Figure 6.4.12, the power profile for the case of 75km and three different pump power ratio, 0.62, 0.49 and 0.32 with a corresponding power excursion of 2.4dB, 1.35dB and 2.75dB respectively.

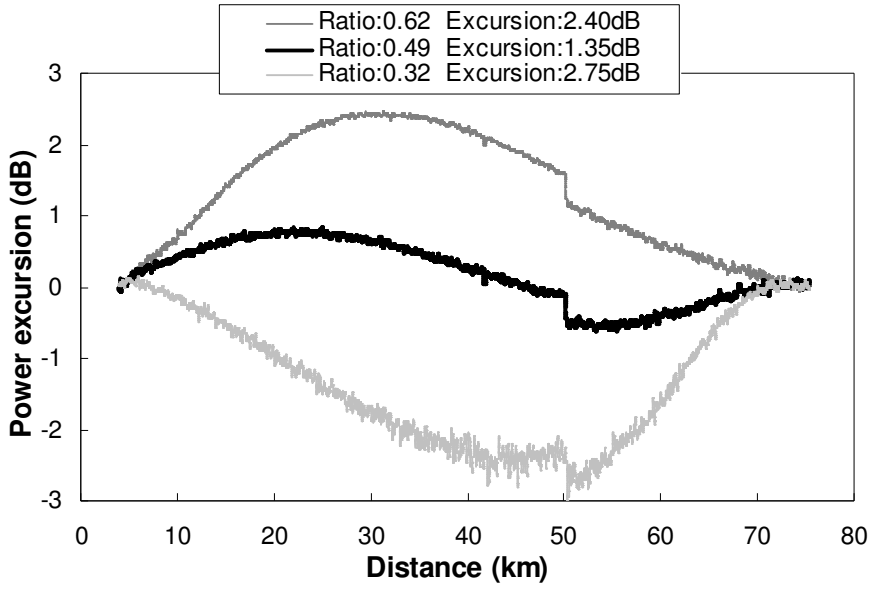

Figure 6.4.12: Experimental power profile for a 75km span length at three different cases of forward pump power/ Total pump power, 0.62, 0.49 and 0.32.

The case of forward pump power/total pump ratio equal to 0.49 represents the symmetric pumping case with a minimum power excursion along the fibre span, in this case 1.35dB. The upper solid line from Figure 6.4.12 shows the case where the forward pump is greater than the backward pump (ratio: 0.62). The power profile along the fibre shows an initial gain profile in the forward direction (from left to right) and then a drop in power reaching the same power value as the initial one. The power excursion is 2.4dB. The lower solid line represents the opposite case. The power profile drops below the initial power level and then increases reaching at the fibre end with the same power value as the initial one. Although the power level at the beginning and the end of the fibre span has the same value in all the cases, the power profile of the fibre along the span is quite different, with most of the fibre span power greater, similar or below the initial soliton power level, depending on the pump ratio. The interesting result is to confirm if the power profile of the transmission span has any effect on the resulting optical spectra of the pulse, even if it reachs the same soliton power, after its propagation through the fibre.

Figure 6.4.13, top row, shows three output FROG spectrograms for 50km span for an average launch power of 9.23dBm and 2.8ps FWHM. The power excursion for the pump ratios of 0, 0.49 and 1 correspond to 1dB, 0.3dB and 1.5dB respectively. The power profile distribution for these three cases will follow similar profile as those shown in Figure 6.4.12 but with lower power excursion. There is not obvious difference between the FROG spectrograms regardless the pump distribution or the power profile along the fibre span in the case of 50km. As we move to 75km span, Figure 6.4.13 middle row, the output FROG spectrograms vary slightly one from each other. The power excursion for the pump ratios of 0.32, 0.49 and 0.62 correspond to 2.75dB, 1.35dB and 2.40dB. Although the power excursion is greater, up to 2.75dB, than in the previous case for 50km, still the difference between the FROG spectrograms are minimum and the typical $sech^2$ of the fundamental soliton shape is recognizable. In these particular experimental results, the output FROG spectrograms for 75km it can be observed a slight energy radiation on the horizontal axes towards the middle of the spectrograms. This energy radiation is generally an indication of the output pulse instability or degradation, shredding energy away as it travels along the fibre. In this particular case, 75km, the optical pulse may be closed to the limits to the typical $sech^2$ soliton shape. This comment is based on the recovery amplitude profiles and other experimental results, where clear soliton pulse shapes were obtained using longer transmission links, i.e 90Km, and similar power excursion values.

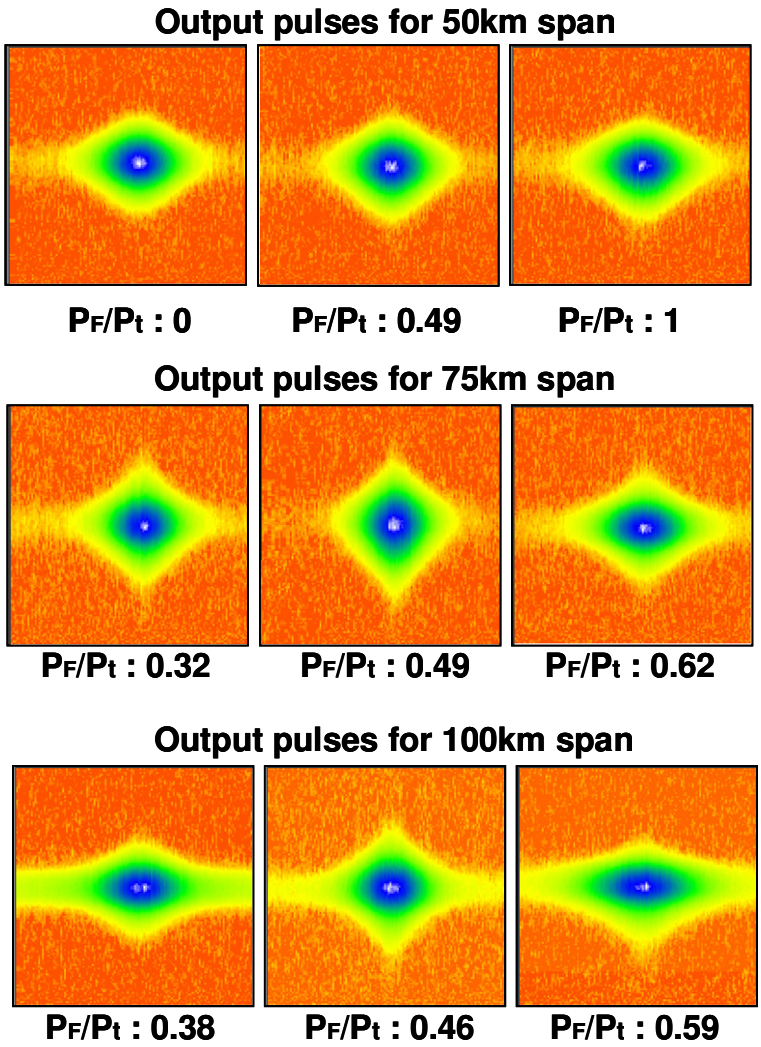

Figure 6.4.13: Experimental output FROG spectrograms for three span lengths: 50km, 75km and 100km at three different pump ratios.

The last set of experimental FROG spectrograms is for the case of 100km. Figure 6.4.13 bottom row shows the FROG spectrograms for three output pulse from an average input pulse at 9.23dBm and 2.75ps FWHM. The power excursion for the pump ratios of 0.38, 0.46 and 0.59 correspond to 4.5dB, 3.3dB and 4.5dB respectively. The experimental FROG spectrograms show a heavy degradation of the output pulse, by temporal broadening the pulse and shredding energy, without completely recovering the soliton shape. As the power excursion on these cases is greater than the two previous one, it seems reasonable to link the degradation effect of transmitted signal to the net amount of power excursion along the span respect the initial values.

6.4.4 FBG reflectivity

The last cavity design parameter investigated in this chapter is the FBGs reflectivity. As previously observed experimentally, by the case of 100km and both FBGs set at 70%, FBGs could redefine the operational limits of soliton transmission links, making feasible the

soliton transmission a longer length at the cost of optimising the FBGs reflectivity. In this section, the transmission link performance is investigated for different FBGs reflectivity. The two cavity lengths proposed for this research are 50km and 100km.

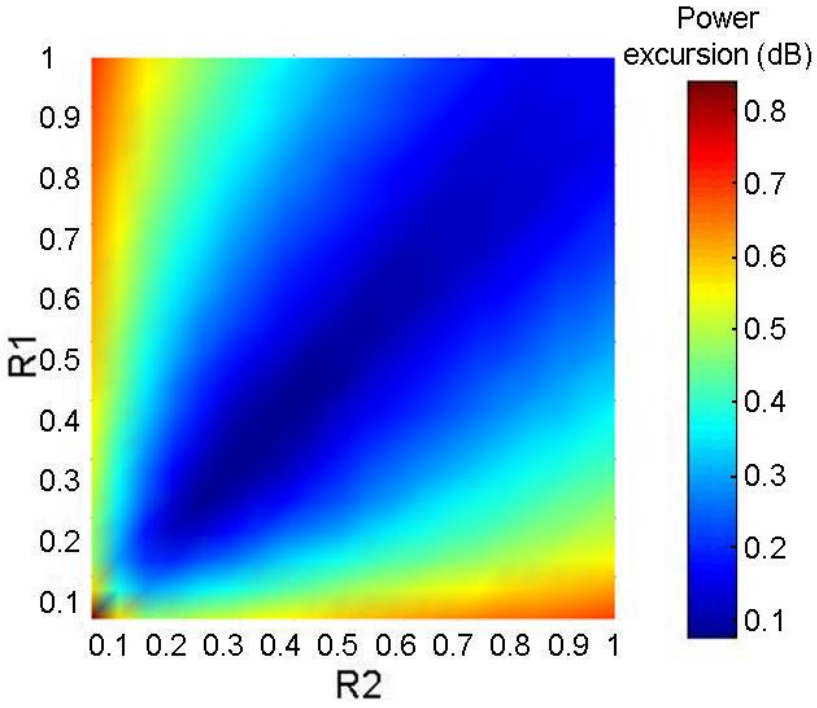

Figure 6.4.14: Maximum power excursion vs. grating reflectivity in a 50km standard fibre URFL for 10dBm transmitted average power [137]

Figure 6.4.14 depicts the power excursion for a 50km URFL cavity, 10dBm input power and a range of FBGs reflectivity, with R1 in the vertical axis and R2 in the horizontal axis. The minimum power excursion, ranging from 0.1 to 0.2dB is achieved for FBGs, R1 and R2, with the same reflectivity value. The maximum power excursion with a value of 0.9dB is obtained when using a single high reflective FBG on one extreme of the cavity and no reflection on the other end. The above results indicates that regardless the reflectivity of the FBGs, the total power excursion along the fibre is below 0.9dB, therefore the soliton transmission is expected to be achieved regardless the conditions.

The experimental FROG spectrograms for 50km are shown in Figure 6.4.15 top row. The average power of the launch input pulse is 9.23dBm with 2.8ps FWHM. The output FROG spectrograms are for the cases with the FBGs, R1 and R2, set at 0%-96%, 96%-96% and 96%-0%. The measured power excursions for these three cases are 0.65dB, 0.3dB and 0.8dB. The output FROG spectrograms are very similar to each other, despite moving drastically away from a symmetric reflectors configuration. The system continues supporting soliton transmission. The increase of power excursion for the cases of single FBG is in agreement with the numerical simulation and below the 0.9dB expected.

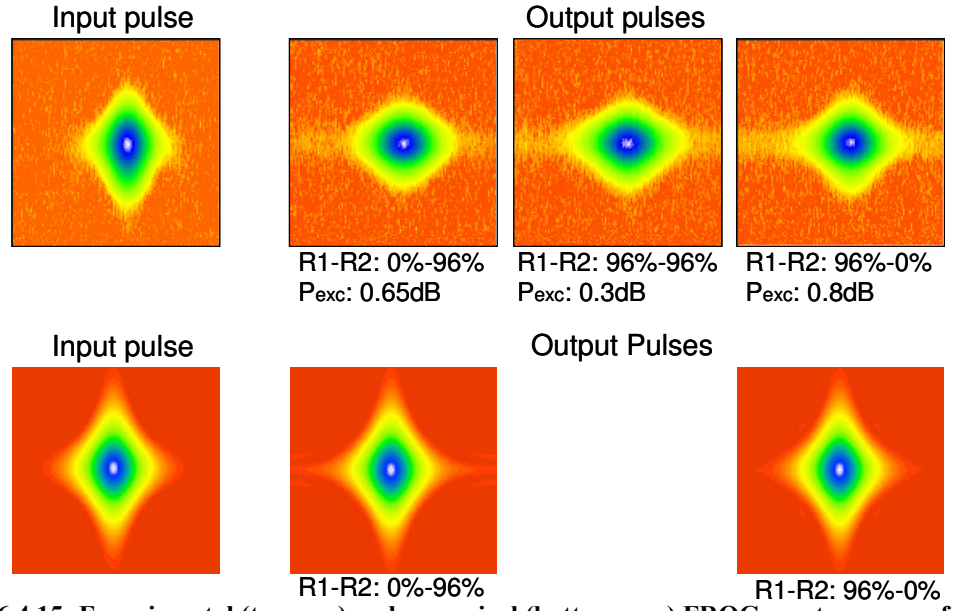

Figure 6.4.15: Experimental (top row) and numerical (bottom row) FROG spectrograms of the input pulse and the output pulses for 50km transmission span at different FBGs reflectivities.

The numerical input and output spectrograms for the cases of and 0%-96% and 96%-0% reflectivity are shown in Figure 6.4.15 bottom row, for which power excursion grows to nearly 0.9dB. In both cases, output spectrograms are very similar to the input ones, although pulse dynamics during propagation are notably different in the two cases. In the 96%-0% case, pulse power remains below the ideal soliton power for the 2.8ps input pulse over the whole span, whereas in the 0%-96% case the opposite occurs, which results in greater distortion and instability during propagation.

The power profile and pulse evolution for 50km is represented in the following three graphs.

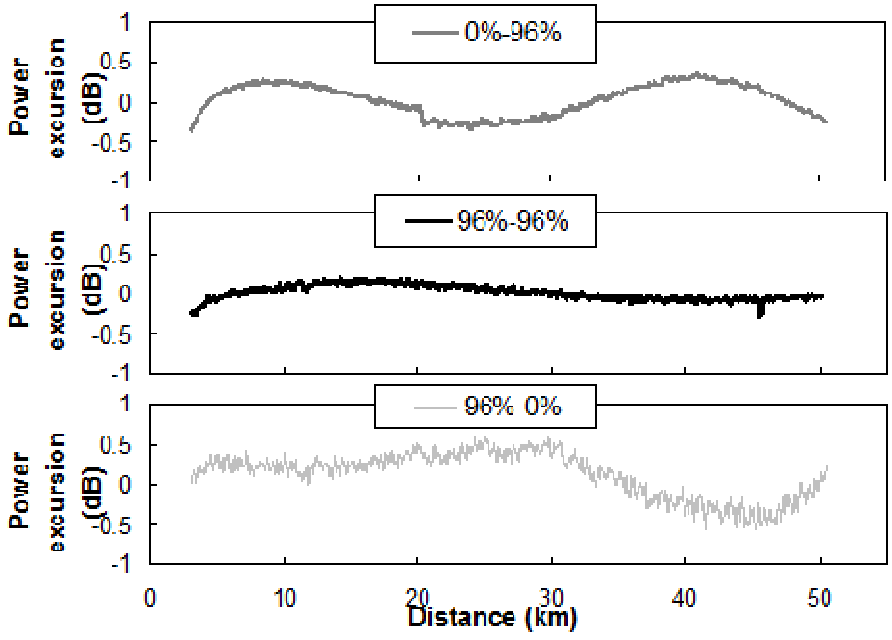

Figure 6.4.16: Experimental power profile along 50km span for the cases R1-R2 as 0%-96%, 96%-96%, 96%-0%.

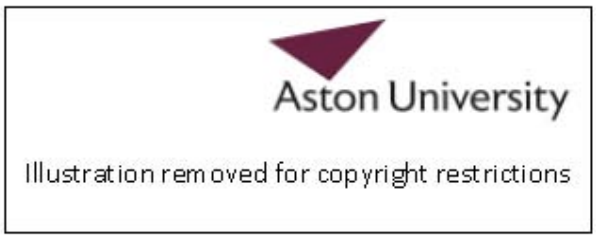

Figure 6.4.17: Numerical pulse evolution of 10dB input power for 50km span and the case of 0%-96% reflectivity by J.D. Ania-Castañon [137].

Figure 6.4.18: Numerical pulse evolution of 10dB input power for 50km span and the case of 96%-0% reflectivity by J.D. Ania-Castañon[137].

Figure 6.4.16 represents the experimental power profile evolution along the fibre span for the three reflectivity cases from Figure 6.4.15. The middle plot, for the case 96%-96% has the lowest power excursion, 0.3dB, with very small variation along the fibre. The top plot, case 0%-96%, has a power profile with an evolution above soliton power for 2.8ps pulse width, showing local gain across the whole fibre. The small discontinuity around 20km is related to a splice within the fibre. This pulse evolution is confirmed by Figure 6.4.17 where shows the frequency and time evolution of the pulse along the transmission span for the same characteristics. The bottom plot from Figure 6.4.15 corresponds to 96%-0% reflectivity. The power profile for this case tends to be below the soliton power for 2.8ps pulse width. The expected pulse evolution for this case is the one shown in Figure 6.4.18. In all the cases, soliton transmission seems quite robust for a 50km span regardless the FBGs reflectivity or the pulse evolution along the transmission span.

Moving to longer span length, Figure 6.4.19 portray the numerical results of the power excursion for 100km URFL cavity with the same input signal, 10dBm, and FBGs conditions as Figure 6.4.14. The power excursion ranges from over 4dB for the case of FBGs with reflectivity high and zero to below 2dB for both FBGs with low reflectivity. For a laser cavity with both FBGs the same value, the expected power excursion range from over 3dB with both FBGs at high reflectivity to below 2.5dB for both FBGs at low reflectivity. The power excursion maintains similar value or even increases if one of the FBGs is set at high reflectivity and the other varies.

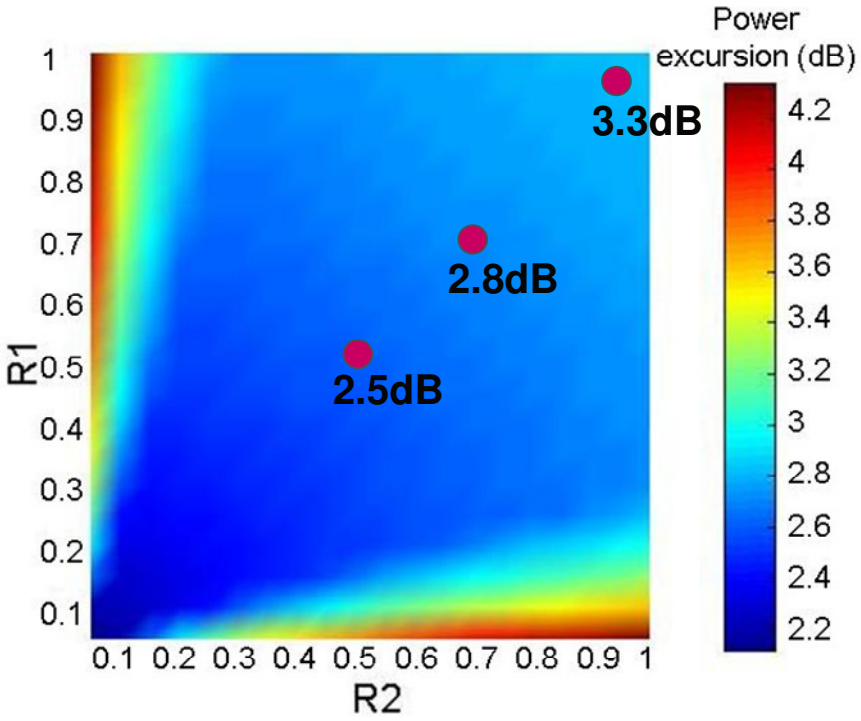

Figure 6.4.19: Experimental power excursion value for 100km span at several FBGs reflectivity over the numerical results. Input signal 10dBm.

The effect of changing the FBG reflectivity in a 100km cavity is similar to a 50km cavity. The main difference relates to a set of power excursion values more extreme for longer cavity lengths.

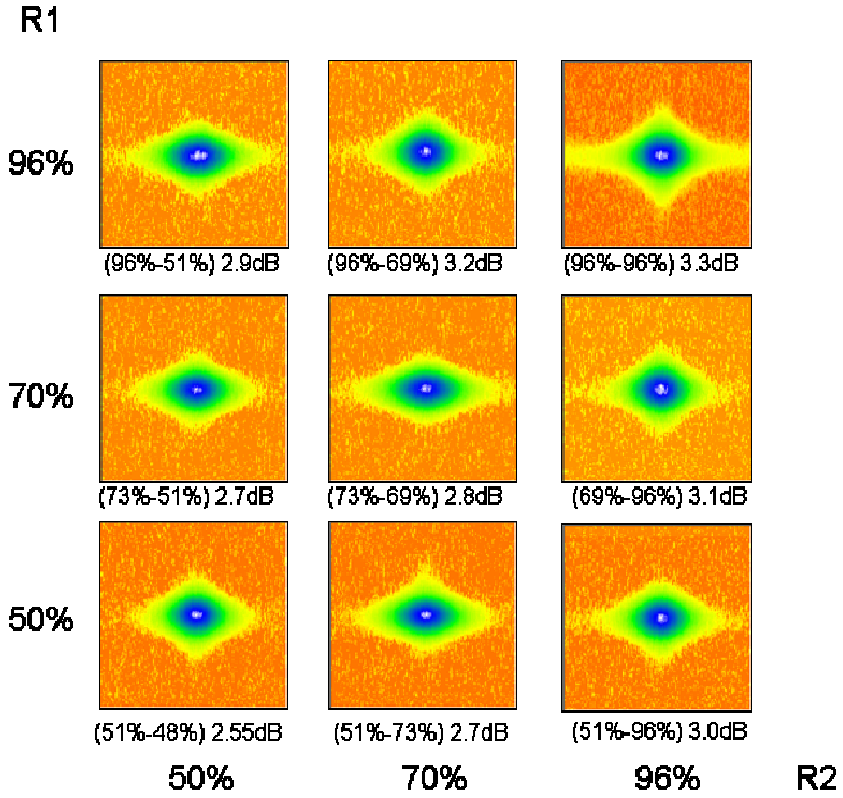

Figure 6.4.20: Experimental FROG spectrograms of the output pulses for 100km transmission span at different FBGs reflectivity with the power excursion indicated in dB.

Figure 6.4.20 illustrates with experimental output FROG spectrograms the change on FBG reflectivity in the laser cavity for a 100km transmission span and an input signal of 8.4dBm with 2.9ps pulse width. The label below each spectrogram corresponds to the FBG reflectivity (R1-R2) and the experimental power excursion measured in dB for each case. The FBGs reflectivity ranges from 96% to approximately 48%. The soliton transmission link performance can be deduced by the output FROG spectrogram and the recovery pulse information from the spectrograms. As we move from 96%-96% reflectivity towards lower reflectivity, the typical soliton shape of the spectrogram seems better defined, with a clear advantage of the case 51%-48% against 96%-96%, as confirmed by Figure 6.4.21. The measured experimental power excursion for the cases 96%-96%, 73%-69% and 51%-48% correspond to 3.3dB, 2.8dB and 2.5dB as plotted over Figure 6.4.19.

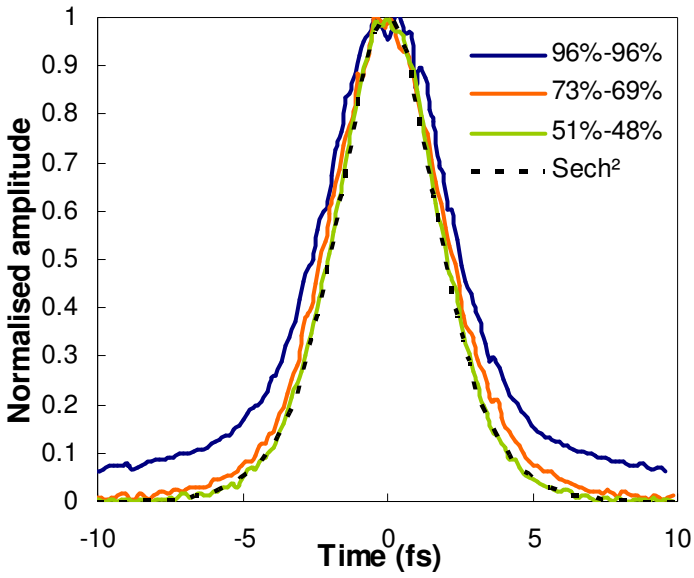

Figure 6.4.21: Amplitude information from the FROG spectrograms with reflectivity 96%-96%, 73%-69% and 51%-48% and the sech^2 shape for a soliton pulse.

The pulse amplitude information from three FROG spectrograms are plotted together in Figure 6.4.21 for comparison with the typical sech^2 shape for a soliton pulse of 4ps FWHM. These three amplitude profile correspond to the FROG spectrograms from Figure 6.4.20 with the same reflectivity. As observed on the FROG spectrogram of Figure 6.4.20, the lowest level of the amplitude profile for the case R1-R2: 96%-96% is maintained above the noise floor without dropping to zero as the other two cases: 73%-69% and 51%-48%. Meanwhile the amplitude profile for the case 51%-48% fits closely to the theoretical sech^2 shape of 4ps soliton pulse width.

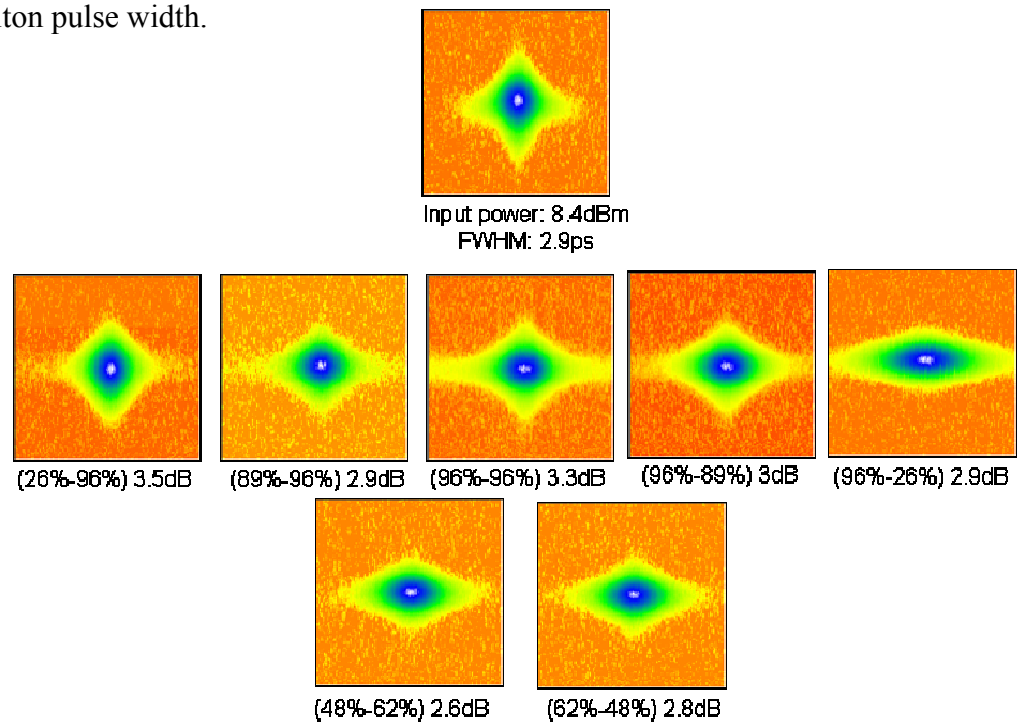

Figure 6.4.22: Experimental FROG spectrograms of the input pulse (top row) and the output pulses for 100km transmission span at different FBGs reflectivity with the power excursion indicated in dB.

Experimental FROG spectrograms for 100km span and 10dBm input signal at other FBGs reflectivity are shown in Figure 6.4.22. The top row corresponds to the input signal with a launch power of 8.4dBm and 2.9ps pulse width. The middle row corresponds to output spectrograms with at least one FBG set at 96% reflectivity. The power excursions in this range are between 2.9dB to 3.5dB. The bottom row corresponds to other output FROG spectrograms, for FBGs with reflectivity below 96%. The power excursion is below 2.8dB.

Experimentally we have seen that for the range of inputs, the soliton stability was fairly robust for transmission spans below 50km. At longer span length soliton transmission is feasible at lower power excursion, giving as indicative upper limit approximately 2.8dB. Changing the power profile along the fibre and taking FROG spectrograms demonstrated that solitons follow similar approach to the power profile by either compressing or broadening depending on a particular area of greater or lower than the soliton power, although the soliton evolution seems tolerant enough to return at the initial characteristics for a smooth power evolution within certain value of power excursion.

6.5 Conclusion

The objective of this work was to prove the feasibility of URFL cavities as soliton transmission links and to experimentally demonstrate agreement with the numerical results. To that end long distance transmission of fundamental optical solitons over multiple soliton periods without amplitude, temporal or phase variation was demonstrated.

A second order ultralong Raman fibre laser amplification scheme was used to provide a virtually non dissipative medium that allowed the signal to propagate at a constant power level as required for soliton stability. The fundamental soliton robustness was confirmed by the power profile measurements along the length of the fibre using the OTDR technique, and the spectrograms obtained at regular intervals using SHG-FROG measurements. The spectrograms are entirely consistent with those predicted through numerical simulations of fundamental soliton transmission and our initial experiment showed stability of a 4ps soliton over a 22km span of LEAF fibre a distance equivalent to over 15 soliton periods. This distance was then extended to over 120 soliton periods for a 2.8ps pulse width over a 90km span.

Furthermore, all this experimental work was obtained using conventional LEAF fibre. LEAF fibre has similar characteristics as SMF with the main difference that its dispersion parameter is four times smaller. Therefore the average input signals for LEAF fibre are

lower than those required for SMF in similar research work. LEAF is typically used in optical communications and it was used in these experiments without the need of using expensive or specifically designed specialist optical fibre. These results represent an important step towards practical implementation of soliton transmission and optical processing in current systems.

Higher order soliton transmission was experimentally and numerically investigated. As second order solitons require four times the power of a fundamental soliton given the same soliton pulse width, we use a longer pulse width to reduce the input power requirements. The main impact of using a longer pulse was an increase of the soliton period, from 1.4km for 4ps pulse to 7km for 9ps pulse. Therefore, the optical fibre span used on this experiment was longer, up to 48km, in order to cover several soliton periods.

Whereas fundamental solitons have a constant shape through propagation, second order solitons varies periodically, breathing in and out, but returning to the original temporal and intensity shape after each soliton period. Some of the experimental FROG spectrograms could be identified with the ones expected from the numerical simulations. Unfortunately and despite all the experimental effort, the results were not sufficiently conclusive to clearly identify each spectrogram with a particular stage of the soliton period, showing the expected soliton dynamics over several soliton periods.

Although both the total signal power excursion and the maximum effective local attenuation in ultralong cavities are extremely low compared with those of conventional transmission schemes, they still show an exponential growth with span length. The effective attenuation profile itself can be affected by high power transmitted signals due to pump depletion. Hence, it is of particular importance to determine the operational limits of these virtually lossless links in terms of both cavity length and nonlinear tolerance to signal characteristics. To that end, we have studied the dynamics and stability of soliton pulses across URFL transmission links for different input pulse powers, as well as the dependence of these dynamics on cavity design, length, pump symmetry, FBGs reflectivity, but without any kind of dispersion profiling or management, using conventional LEAF fibre.

Anticipating soliton transmission at higher rates, a wide range of input signal powers, 1mW to 100mW, was considered when investigating input signal power effect in transmission. At higher input signal power, the symmetric relation between the power excursion and the cavity parameters such as FBGs reflectivity and pump ratio is broken. We could say that the impact of pump depletion becomes more obvious, both in the increasing value of power excursion and the asymmetric behaviour of the system response at higher repetition rates.

From the results presented in this chapter, we can conclude that links of the order of 50km show excellent nonlinear transmission performance, providing a robust and stable optical pulse transmission for a broad range of input signal powers and cavity design parameters. Longer URFL transmission links are affected by a greater power excursion, increasing the attenuation profile along the optical fibre link and reducing the stability for soliton transmission. The approximated gradient of the power excursion with the input signal increases considerably at longer cavity lengths. The nonlinear tolerance can be highly improved at longer lengths by introducing asymmetries in the system design to partially compensate for those caused by pump depletion or reducing the FBGs reflectivity.

In particular we have experimentally demonstrated soliton transmission for 100km by reducing both FBGs from 96% down to 70% or 50%. Similarly, for a 100km link, we have demonstrated numerically that the power excursion can be reduced by up to 2dB by means of managing grating reflectivity. Agreement between theory and experiment is excellent, which allows us to predict system performance in a variety of situations.

Based on the experimental and numerical results, the application of soliton transmission links for submarine systems where the span length required is ~50km seems ideal. This type of cavity length offers high tolerance, allowing practical optimum soliton transmission in a wide range of input signal powers, FBGs reflectivities and pump distribution. Terrestrial soliton transmission links of the order 70-100km are still practical but with reduced tolerances regarding the cavity design and the input signal. The most likely effect could be an upper limit of the transmission rate (the limit of the upper input signal). Practical unrepeated links of over 100km are very unlikely within the current circumstances. If soliton transmission were achieved for over 100km, then it would be done only under very specific cavity parameters such as low FBGs reflectivities, high Raman pump powers and low input signal power. The tolerances of the system would be very tight and unpractical.

Chapter 7

Conclusions

The objective of this thesis is to contribute to the advances of optical communications and nonlinear optics in our society. The research work presented deals mainly but not exclusively with the nonlinear inelastic Raman scattering effect and its efficient application in the ultralong Raman laser scheme. URFLs have become a well defined optical module or optical component itself with multiple applications in photonics. As described through this work and demonstrated by the experimental and numerical results, URFLs have the efficiency of a second order Raman amplification scheme but the simplicity of a first order amplification system. The enhancement of the URFL performance compared with other first order Raman amplification systems is achieved by bi-directional pumping a conventional optical communication single mode fibre confined by a pair of FBGs. Its successful application has been demonstrated not only in optical communications, as amplifier and zero-lossless transmission link, but also in other photonics areas such as laser source, for SC generation, and as nonlinear media tool to investigate optical solitons dynamics. Other applications not included in this thesis are within the area of long distance sensing.

The research motivation for this work comes from the combination of two different areas. On one hand, the technical advances regarding high pump powers makes feasible the use of Raman amplifiers. Their cost and accessibility makes Raman pump much more available than a decade ago. This means that URFLs can become affordable and commercially available. On the other hand, the advance in optical communications and dependence of our society on information technology has created an increasing demand for high speed long distance communications. The application of URFLs to our current optical network can enhance the available spectral bandwidth and improve the signal to noise ratio

performance, meeting the demand for a higher data traffic using conventional optical fibre and without especially dedicated fibre.

The work presented in the two first chapters of this thesis is introductory material. The first one includes the contextual motivation for this work and a general overview of the thesis. Chapter 2 includes most of the mathematical and conceptual foundations related to optical fibres and nonlinear optics. The wave propagation in optical fibres is derived from the Maxwell equations taking in account the fibre nonlinearities. The terms of the general or extended nonlinear Schrödinger equation are explained, indicating the effects of these terms in the optical wave propagation. The different nonlinear processes are briefly reviewed, including SPM, XPM, FWM, SRS and MI. Although URFL makes use of the Raman scattering effect, a good understanding of the other nonlinear effects and their interplay is fundamental for the optimisation and application of URFL in photonics. The interaction and balance between self phase modulation and dispersion plays a major role in soliton transmission. Understanding the broadening effect of self phase modulation in the normal and anomalous dispersion regime is essential for supercontinuum generation.

Most of the numerical and experimental results related to this research work are reproduced in the following four chapters. Chapter 3 and 4 involve a numerical and experimental investigation of several aspects of URFL. Chapter 3 presents numerical simulation results describing the intra-cavity power evolution of the URFL and the investigation of the RIN transfer evolution from the pump to the signal for different cavity design parameters. The main advantages of URFL over other amplification systems are the reduced power excursion over a wider range of spectral frequencies. This implies an improved performance of the signal to noise ratio as the amplified spontaneous emission (ASE) is reduced and the increase of transmission capability due to the extra available spectral range. These advantages can be offset by the relative intensity noise (RIN) from the pump to the signal. The numerical investigation confirms the span length as parameter having a major impact on RIN transfer. URFLs performance shows a RIN transfer value penalty in comparison to standard multiwavelength pumped second order amplifiers. This is translated as a greater requirement for the Raman pumps used in the URFL system, in order to minimise the overall RIN value. Otherwise, URFL performance is generally more robust and tolerant to pump asymmetries and its RIN transfer value drops at earlier modulation frequencies than the case of a multiwavelength pump system.

Two interesting observed results are: the oscillating behaviour of the RIN transfer at higher frequencies and the maximum value of the RIN transfer associated at relative low reflectivities. The oscillating behaviour of the RIN transfer with modulation frequency

becomes more obvious with greater contribution of the forward pumping, which happens to be the same propagation direction of the transmitted signal. Hence it seems reasonable to relate this oscillating behaviour of the RIN transfer to the interplay between the signal and wave components related to the forward pump. The generated noise from this interplay is likely to be enhanced within the cavity. The other interesting result relates to the maximum RIN transfer value associated with relative low FBGs reflectivities, which is 15%. This maximum RIN transfer value shifts towards even lower reflectivities for higher modulation frequencies. This result may have interesting implication in the design of cavities with low reflectivity systems making use of random distributed feedback.

The numerical results of the RIN transfer were obtained assuming single mode fibre, further work could be developed for other types of fibre, with different characteristics to those of SMF.

Also, experimental investigation of the RIN will be required to confirm the obtained results in Chapter 3, specially the enhanced oscillating behaviour of the RIN transfer at longer modulation frequencies and the RIN transfer maximum value for relative low reflectivities. Research on those areas may bring further understanding to the physics behind the RIN transfer value enhancement in URFL cavities and the opportunity to reduce its effect in practical applications.

Chapter 4 deals with the experimental investigation of the results on URFLs. Power variation and spectral bandwidth coverage was investigated for single and multicavity URFL systems. For the case of signal transmission in the C band region and Raman pumps at 1366nm, the optimum pair of FBGs giving the lowest power variation was found at 1455nm. The results gave a 0.6dB power variation over a 40nm range covering the entire C band region. The use of a multicavity URFL extended further the bandwidth coverage, 51nm, whilst keeping the power variation low, 0.7dB. Unfortunately the use of multicavity URFL implies a considerable increase of the pump power, which may not be practical in all applications unless extended spatio-spectral transparency is required.

Another approach, already published, for extending the spectral bandwidth range is the use of several Raman pumps at different wavelengths [18][79]. Although there are advantages in spectral power coverage and, perhaps, total Raman pump power, the increase of complexity of using several pumps will require some feedback control for output power optimisation.

The transferable application of URFLs to spectral ranges other than the C band region, as shown in Chapter 4, is straightforward. It requires laser pumps and FBGs at different

wavelengths but with similar frequency shift relation between them and the transmission region, corresponding to the first and second Stokes of the Raman gain shift.

Another interesting result is the experimental demonstration of a 200km long dual wavelength Raman laser based on the Rayleigh scattering. Each single FBG with different central wavelength form a cavity with the distributed random feedback provided by Rayleigh scattering. The two Raman laser outputs are independent of each other. This random feedback distribution provided by Raman scattering was also demonstrated at shorter span lengths, 41km, and with only one FBG. The scheme of multiwavelength Raman laser with random distributed feedback may have great potential application in long distance communications as well as in distributed sensors. Although some of those applications may be limited by the RIN transfer due to the low reflectivity provided by the random distributed feedback.

The following two chapters provide results demonstrating the application of URFLs in SC generation and soliton propagation dynamics. The URFL is portrayed as an enhancement tool for the SC generation when using a continuous wave pump. The generated spectral broadband is provided using conventional fibre without the need of special or dedicated fibre. Several URFL systems were investigated using conventional fibre in the normal and anomalous dispersion regime, and using single and dual pumping. In principle, the case of single pump in the anomalous dispersion regime is optimum for an enhanced SC with a considerable flatness of the spectrum. Although the flatness of the spectrum may be improved with dual pumping, when using fibre in the normal dispersion regime.

The work presented in this thesis regarding SC generation is limited to a few configurations of URFL cavities with conventional telecommunication fibres and CW laser source. Further research in this area could demonstrate the benefits of using URFLs for SC generation compared to other methods. Other than cost reduction, as the components are readily available, the simplicity of the URFL cavity should bring a greater stability to SC generation. Further work could be developed using special types of fibres and pulsed laser sources whilst keeping a simple structure.

SC generation has its own area of applications as a light source. The broadband spectra may cover regions that otherwise can not be generated by other means. URFL as SC light source may be also applied to optical communications to provide the basic spectrum for a spectral comb. Although its cost efficiency may not be practical, especially when using a very low number of single channels which may be already available by low cost laser diodes.

Chapter 6 portrays URFL as an excellent media tool for investigating optical soliton transmission and its propagation dynamics. Using a URFL as a zero-lossless transmission link allowed the experimental demonstration of exact fundamental soliton transmission over multiple soliton periods in conventional optical fibre. In principle, this work could be extended to higher order solitons, although its experimental demonstration requires extra launch signal to meet the required optical soliton powers. The investigation of soliton propagation dynamics provided the impact performance that URFL cavity design parameters may have in the soliton transmission. As expected, increasing the span length increased the power excursion and therefore limited the length for soliton transmission. An important result is that the limitation of increasing span length may be compensated by a reduction of the FBGs reflectivity. In fact soliton transmission was demonstrated for a 100km link by reducing both FBGs from 96% down to 70% or 50%. Unfortunately, the reduction of FBGs reflectivity implies an increase of the Raman pump power to meet the same level of zero-lossless transmission. In general the performance of URFL cavities of 50km long are very robust and tolerant for soliton transmission regardless of the transmission signal, FBGs reflectivity or the pump distribution. Cavity links up to 70-80km are still practical although the tolerances for soliton transmission are slightly reduced. Longer cavities are more demanding, requiring specific conditions that allow soliton transmission.

The main objective of the research work developed around the stability and dynamics of soliton transmission was to prove that, in fact, undistorted true soliton transmission can be achieved for several soliton periods using URFLs as transmission links. Considering solitons as a practical format for data transmission involves other issues such the increase of the transmission rate and reduction of the channel spacing. Those issues involve an investigation on the effect of soliton interactions. The tolerances for soliton transmission as high speed data rate are expected to be more demanding. Further work using URFLs in a transmission and receiver system can indicate the limits to those tolerances.

In general URFL cavities can be used as tool for basic research in nonlinear optical interactions. Simply speaking, the investigation in soliton transmission can be understood as an investigation of the balance between SPM and GVD.

Other than higher order soliton dynamics and basic nonlinear interactions research, the work described in this thesis could be extended to other research aspects related to URFL and its applications in photonics. For instance the Raman gain is polarisation dependent and URFL are based on the Raman scattering effect. Hence a cavity design with selective polarisation may have potential applications as self-amplitude modulated cavity or other applications where polarisation changes will be translated in other optical effects.

In conclusion, the research work presented in this thesis provides an interesting insight to distributed Raman amplification technology, with particular emphasis in ultralong Raman fibre laser schemes. The numerical and experimental results related to URFL schemes, portray URFLs as a flexible optical module with great potential commercially in a wide range of photonics areas.

Publications

[1] M. Gonzalez-Herraez, S. Martin-Lopez, M. Alcon-Camas, P. Corredera, L. Thévenaz and J.D. Ania-Castañon, *Ultralong range distributed fibre sensing using virtually transparent propagation*, European Conference on Lasers and Electro-Optics and the XIIth European Quantum Electronics Conference 2011: CE 550

[2] J. D. Ania-Castañón, S. Martín-López, M. Alcon-Camas, F. Rodríguez-Barrios, A. Carrasco-Sanz, P. Corredera, L. Thévenaz and M. González-Herráez, *Raman-assisted BOTDA sensors*, IEEE Winter Topicals, Colorado, USA (2011)

[3] M. Alcon-Camas, and J. D. Ania-Castañón, *RIN transfer in 2nd-order distributed amplification with ultralong fiber lasers*, Optics Express, Vol. 18, Issue 23, pp. 23569-23575 (2010)

[4] E. El-Taher, M. Alcon-Camas, S. A. Babin, P. Harper, J-D Ania-Castañón, S. K. Turitsyn, *Dual wavelength, ultralong Raman laser with a Rayleigh scattering feedback*, Optics Letters, Vol. 35, Issue 7, pp. 1100-1102 (2010)

[5] S. Martín-López, M. Alcon-Camas, F. Rodríguez, P. Corredera, J.D Ania-Castañón, L. Thévenaz and M. González-Herráez, *Brillouin optical time-domain analysis assisted by second-order Raman amplification*, Optics Express Vol. 18, Iss. 18, pp. (2010)

[6] M. Alcon-Camas, and J. D. Ania-Castañón, *Relative Intensity Noise transfer in high-order distributed amplification through ultralong fibre cavities*, in Proc. of SPIE Photonics North 2010, Session 14, Niagara Falls, Canada.

[7] M. Alcon-Camas, A.E. El-Taher, J-D. Ania-Castanon, P. Harper, *Gain bandwidth optimisation and enhancement in ultralong Raman fibre laser based amplifiers*, Torino, Italy ECOC 2010

[8] L. Barker, A.E. El-Taher, M. Alcon-Camas, J.D. Ania-Castanon , P. Harper, *Extended bandwidth for long haul DWDM transmission using ultralong Raman fiber lasers*, Torino, Italy ,ECOC 2010

[9] M Alcon-Camas , P. Harper , A. E. El-Taher , H.Wang , V. Karalekas , J. Harrison and J-D. Ania-Castañón, *Long-distance soliton transmission through conventional optical fibre ultralong lasers*, Optics Letters, Vol. 34, Issue 20, pp. 3104-3106 (2009)

[10] F. Rodríguez-Barrios, S. Martín-López, A. Carrasco-Sanz, P. Corredera Guillén, M. Alcon-Camas, J.D. Ania-Castañón, L. Thévenaz and M. González-Herráez, *Experimental study of the impact of pumping configuration in Raman-assisted fiber optic distributed Brillouin sensors*, Optical Fibre Measurement Conference 2009 (OFMC09) Teddington (UK)

[11] P. Harper, L. Barker, A. E. El-Taher, M. Alcon-Camas, J-D Ania-Castañón, S. K. Turitsyn, I. Bennion, *Optical Communications Applications of Ultralong Raman Fiber Lasers*, International Conference on Optical Communications and Networks (ICOCN) 2009

[12] A.E. El-Taher, M. Alcon-Camas, V. Karalekas ,J-D. Ania-Castañón, P. Harper, *Improved Supercontinuum Generation by Dispersion Tuning and Dual Wavelength Pumping*, European Conference on Optical Communication (ECOC) Viena, 2009

[13] J-D Ania-Castañón, M. Alcon-Camas, A. El-Taher, H.Wang, P.Harper, *Soliton dynamics in transmission through ultralong lasers*, CLEO Europe, Munich, 2009

[14] L. Barker , A. E. El-Taher, M. Alcon-Camas, J-D Ania-Castañón , P. Harper, *42.6Gb/s RZ-ASK transmission over 2500km using quasi-lossless transmission spans*, Conference on Lasers and Electro-Optics, CLEO Europe, Munich, 2009

[15] A.E. El-Taher, M. Alcon-Camas, J-D. Ania-Castañón, P. Harper, *Enhanced supercontinuum generation using multi-fibre ultralong Raman cavities*, Conference on *Lasers* and Electro-Optics, IEEE/LEOS, Innsbruck, 2009

[16] P. Harper, A. E. El-Taher, H. Wang, M. Alcon-Camas, V. Karalekas , J-D Ania-Castañón, *True soliton transmission through ultralong laser,* European Conference on Optical Communication (ECOC), Brussels, Belgium, 2008.

Bibliography

[1] T.H. Maiman. Stimulated optical radiation in ruby. Nature 187 (4736): 493-494 (1960).

[2] K.C. Kao. The Nobel Prize in Physics 2009. Nobel Foundation. October 6, 2009. http://nobelprize.org/nobel_prizes/physics/laureates/2009/press.html.

[3] K.C. Kao and G.A. Hockham. Dielectric-fiber surface waveguides for optical frequencies. Proceeding of the IEEE, 133:1151 (1966)

[4] F.P. Kapron, D.B. Keck, and R.D. Maurer. Radiation losses in glass optical waveguides. Applied Physics Letters, 17:423 (1970)

[5] E. Desurvire. Erbium-doped Fiber Ampliers. Principles and Applications, John Wiley & Sons, New York, 2002.

[6] R.J. Mears, L. Reekie, I.M. Jauncey, D.N. Payne, *Low-noise erbium-doped fibre amplifier operating at 1.54μm*, Electronics Letters, vol.23, no.19, pp.1026-1028, (1987)

[7] D.S. Govan, W. Forysiak, N.J. Doran, *40 Gbit/s RZ transmission over more than 2000 km of standard fibre with dispersion management*, IEE Colloquium on High Speed and Long Distance Transmission (Ref. No. 1999/022), pp.3/1-3/6, 1999.

[8] M.I. Hayee, X.Y. Zou, A.E Willner, *Degradations due to both dispersion and SPM/CPM on dispersion-managed WDM long-distance systems*, Optical Fiber Communications, 1996. OFC '96, pp. 78- 79, 25 Feb.-1 March 1996.

[9] M. Matsumoto, *Efficiency and stability of transmission control of long-distance and high-speed WDM transmission using solitons*, Digest of the Advanced Semiconductor Lasers and Applications/Ultraviolet and Blue Lasers and Their Applications/Ultralong Haul DWDM Transmission and Networking/WDM Components, 2001. LEOS Summer Topical Meetings, pp.2, 2001

[10] E. Pincemin, A. Tan, A. Bezard, A. Tonello, S. Wabnitz, J.D Ania-Castañón, and S. Turitsyn, *Robustness of 40 Gb/s ASK modulation formats in the practical system infrastructure*, Optics Express 14, pp. 12049-12062 (2006)

[11] J.C. Bouteiller, K. Brar and C. Headley , *Quasi-constant signal power transmission*, in Proceedings of European Conference on Optical Communications, ECOC 2002, OSA, S3.04, 2002.

[12] T. Okuno, T. Tsuzaki, M. Nishimura, *Novel optical hybrid line configuration for quasi-lossless transmission by distributed Raman amplification*, Photonics Technology Letters, IEEE , vol.13, no.8, pp.806-808, (2001)

[13] M.N. Islam, *Raman Amplifiers for Telecommunications*, Springer-Verlag, 2004.

[14] I.P. Kaminow and T.L. Koch. *Optical fiber telecommunication III*. Academic Press, 1997.

[15] J.D. Ania-Castañón, *Quasi-lossless transmission using second-order Raman amplification and fibre Bragg gratings*, Optics Express 12, pp. 4372-4377 (2004)

[16] V. Karalekas, J.D. Ania-Castañón, P. Harper and S.K. Turitsyn, *Ultra-long Raman fibre laser transmission links*, 11th International Conference on Transparent Optical Networks, 2009. ICTON '09. pp.1-4, June 28 2009-July 2, 2009.

[17] G.P. Agrawal. *Fiber-Optic Communication Systems*. Elsevier Academic Press, 2005.

[18] M.N. Islam, *Raman amplifiers for telecommunications*, IEEE Journal of selected topics in quantum electronics, 8 (3), pp. 548-559 (2002)

[19] T.J. Ellingham, J.D. Ania-Castañón, R. Ibbotson, X. Chen, L. Zhang, S.K. Turitsyn, *Quasi-lossless optical links for broad-band transmission and data processing*, IEEE Photonics Technology Letters. 18, pp. 268-270 (2006)

[20] A.E. El-Taher, M. Alcon-Camas, V. Karalekas, J.D. Ania-Castañón, P. Harper, *Improved supercontinuum generation by dispersion tuning and dual wavelength pumping*, ECOC 2009, 35th European Conference on Optical Communication, pp.1-2, Vienna, 2009.

[21] M. Alcon-Camas, A.E. El-Taher, H. Wang, P. Harper, V. Karalekas, J.A. Harrison, and J.D. Ania-Castañón, *Long-distance soliton transmission through ultralong fiber lasers*, Optics Letters 34, pp. 3104-3106 (2009)

[22] P. Minzioni, P. Harper, V. Pusino, L. Barker, C. Langrock, M.M Fejer, J.D. Ania-Castañón, I. Cristiani, and V. Degiorgio, *Optical phase conjugation for dispersion and nonlinearity compensation in a 1600km, 42 Gb/s quasi-lossless system*. In Nonlinear Optics: Materials, Fundamentals and Applications (NLO). Honolulu, Hawaii (US), 17 July 2009.

[23] L. Barker, A.E. El-Taher, M. Alcon-Camas, J.D. Ania-Castañón, P. Harper, *42.6Gb/s RZ-ASK transmission over 2500km using quasi-lossless transmission spans*, European Conference on Lasers and Electro-Optics 2009 and the European Quantum Electronics Conference. CLEO Europe - EQEC 2009, pp.1, 14-19 June 2009.

[24] L. Barker, A.E. El-Taher, J.D. Ania-Castañón, P. Harper, *Extended bandwidth for long haul DWDM transmission using ultra-long Raman fiber lasers*, 36th European Conference and Exhibition on Optical Communication (ECOC), pp.1-3, 19-23 Sept. 2010.

[25] J.D. Ania-Castañón, M. Alcon-Camas, A. El-Taher, H.Wang, P.Harper. *Soliton dynamics in transmission through ultralong lasers*. European Conference on Lasers and Electro-Optics 2009 and the European Quantum Electronics Conference. CLEO Europe - EQEC 2009.

[26] P. Harper, A.E. El-Taher, H. Wang, M. Alcon-Camas, V. Karalekas , J.D. Ania-Castañón. *True soliton transmission through ultra-long laser*. ECOC 2008, 34th European Conference on Optical Communication, Brussels, Belgium, 2008.

[27] A.E. El-Taher, M. Alcon-Camas., J.D. Ania-Castañón, P. Harper, *Enhanced supercontinuum generation using multi-fibre ultra-long Raman cavities*, IEEE/LEOS Winter Topicals Meeting Series, pp. 203-204, Innsbruck, 2009.

[28] S. Martin-Lopez, M. Alcon-Camas, F. Rodriguez, P. Corredera, J.D. Ania-Castañon, L. Thévenaz, and M. Gonzalez-Herraez, *Brillouin optical time-domain analysis assisted by second-order Raman amplification*, Optics Express, 18, pp. 18769-18778 (2010)

[29] Y. Kodama and A. Hasegawa, *Nonlinear pulse propagation in a monomode dielectric guide*, IEEE Journal of Quantum Electronics, vol. 23, no. 5, pp. 510-524 (1987)

[30] V.E. Zakharov and A.B. Shabbat, *Exact theory of two dimensional self-focusing and one dimensional self-modulation of waves in nonlinear media*, Soviet Physics - JETP 34, pp.62-69 (1972)

[31] G.P. Agrawal, *Nonlinear Fiber Optics*, Fourth Edition, Academic Press, 2007.

[32] R.W. Boyd, *Nonlinear optics*. Academic Press, 2003.

[33] G.E. Keiser, *Optical Fiber Communications*, 3rd edition, McGraw Hill, New York. 2007.

[34] J.M. Senior. *Optical fibre communication: principle and practice*. Prentice Hall, 2007.

[35] J. Hecht. *Understanding fiber optics*. International ed., 4th ed. London: Pearson/Prentice Hall, 2002.

[36] B.E.A. Saleh and M.C. Teich, *Fundamentals of photonics*. Wiley, 2007.

[37] ITU-T study group 15. Transmission media and optical systems characteristics - Optical fibre cables Characteristics of a 50/125µm multimode graded index optical fibre cable for the optical access network. 2007. http://www.itu.int/itu-t/recommendations/rec.aspx?id=9181

[38] J.C. Knight, J. Broeng, T.A. Birks and J. Russell, *Photonic Band Gap Guidance in Optical Fibers*, Science 282, pp. 1476-1478 (1998)

[39] P. Russell. *Photonics crystal fibers*. Science, 299, pp. 358-362 (2003)

[40] Acterna. *Guide to Fiber Optic Measurement*. JDSU, 2001.

[41] R. Olshansky. *Propagation in glass optical waveguides*. Reviews of Modern Physics, 51 (2), 341 (1971)

[42] E.T. Li. *Optical Fiber Communications: Fiber Fabrication*. Academic Press, 1985.

[43] S.M.A. Razzak, Y. Namihira and F. Begum. *Ultra-flattened dispersion photonic crystal fibre*. Electronics Letters 43, 11 pp. 615-617 (2007)

[44] K. Tsujikawa, K. Tajima, M. Ohashi, *Rayleigh scattering reduction method for silica-based optical fiber*, Journal of Lightwave Technology, vol.18, no.11, pp.1528-1532 (2000)

[45] D. Marcuse, *Light Transmission Optics*, Van Nostrand Reinhold, New York, 1982.

[46] L. Abrardi. *Experimental study of new mechanisms for the development of spectrally-controlled supercontinuum sources in optical fibres under continuous-wave dumping*, PhD thesis, Universidad de Alcala, 2008.

[47] N. Kurukitkoson. *Numerical modelling of devices and advanced transmission schemes embracing Raman effect*, PhD thesis, Aston University, 2004.

[48] K.J. Blow and D. Wood, *Theoretical description of transient stimulated Raman scattering in optical fibers*, IEEE J. Quantum Electron., vol. 25, pp. 2665–2673 (1989)

[49] M.N. Islam, L. Mollenauer, R. Stolen, J. Simpson, and H. Shang, *Cross-phase modulation in optical fibers*, Optics Letters. 12, pp. 625-627 (1987)

[50] M. Shtaif, *Analytical description of cross-phase modulation in dispersive optical fibers*, Optics Letters. 23 (15), pp. 1191-1193 (1998)

[51] A. Zheltikov, *Phase-matched four-wave mixing of guided and leaky modes in an optical fiber*, Optics Letters, 33, pp. 839-841 (2008)

[52] J. Thompson and R. Roy, *Multiple four-wave mixing process in an optical fiber*, Optics Letters, 16, 557-559 (1991).

[53] C. Headley and G.P. Agrawal. *Raman Amplification in Fiber Optical Communication Systems*. Elsevier Academic Press, 2005.

[54] Schott technical information document TIE-29, 2007.

[55] Aston University, Photonics Research Group, database from photonics laboratory, 2010.

[56] R.H. Stolen and C. Lin, *Self-phase modulation in silica optical fibers*, Physical Review A, vol. 17, no. 4, pp. 1448–1453 (1978)

[57] L.F. Mollenauer and J.P. Gordon, *Solitons in optical Fibers*, Academic Press, 2006.

[58] V.E. Zakharov and L.A. Ostrovsky, *Modulation instability: The beginning*. Physica D: Nonlinear Phenomena, 238, 5, pp. 540-548 (2009)

[59] K. Tai, A. Tomita, J.L. Jewell and A. Hasegawa, *Generation of subpicosecond solitonlike optical pulses at 0.3 THz repetition rate by induced modulation instability*, Applied Physics Letters, vol. 49, no. 5, pp. 236–238 (1986)

[60] A. Hasegawa and W.F. Brinkman, *Tunable coherent IR and FIR sources utilizing modulational instability*, IEEE Journal of Quantum Electronics, vol. 16, no. 7, pp. 694-697 (1980)

[61] A. Hasegawa, *Generation of a train of soliton pulses by induced modulation instability in optical fibers*, Optics Letters, vol. 9, no. 7, pp. 288-290 (1984)

[62] A. Hasegawa and F. Tappert, *Transmission of stationary nonlinear optical pulses in dispersive dielectric fibers*, Applied Physics Letters, vol. 23, no. 3, pp. 142-144, (1973)

[63] C.V. Raman, *A new radiation*. Indian Journal of Physics, 2, 387 (1928)

[64] R.H. Stolen and E.P. Ippen, *Raman gain in glass optical waveguides*. Applied Physics Lettre, 22 (6), pp. 276-278 (1972)

[65] E.J. Woodbury and W.K. Ng, *Ruby laser operation in the near IR*, Proceedings of the IRE, vol. 50, no. 11, pp. 2367-2367 (1962)

[66] C.R.S. Fludger, V. Handerek and R.J. Mears, *Pump to Signal RIN Transfer in Raman Fiber Amplifiers*, IEEE Journal of Lightwave Technology 19, 1140-1148 (2001).

[67] M.D. Mermelstein, K. Brar and C. Headley, *RIN Transfer Measurement and Modeling in Dual-Order Raman Fiber Amplifiers*, IEEE Journal of Lightwave Technology 21, 1518–1523 (2003)

[68] B. Bristiel, S. Jiang, P. Gallion, E. Pincemin, *New model of noise Figure and RIN transfer in fiber Raman amplifiers*, IEEE Photonics Technology Letters. 18(8), pp.980-982, (2006)

[69] C. Martinelli, L. Lorcy, A. Durécu-Legrand, D. Mongardien, and S. Borne, *Influence of Polarization on Pump-Signal RIN Transfer and Cross-Phase Modulation in Copumped Raman Amplifiers*, IEEE Journal of Lightwave Technology, Vol. 24, Issue 9, pp. 3490- (2006)

[70] V. Kalavally, I. Rukhlenko, M. Premaratne, and T. Win, *Analytical Study of RIN Transfer in Pulse-Pumped Raman Amplifiers*, IEEE Journal of Lightwave Technology 27, pp. 4536-4543 (2009).

[71] M. Krause, S. Cierullies, H. Renner, and E. Brinkmeyer, *Pump-to-Stokes transfer of relative intensity noise in Raman fiber lasers*, Technical Digest in Conference on Lasers and Electro-Optics/International Quantum Electronics Conference and Photonic Applications Systems Technologies, (Optical Society of America, 2004), paper CMD5.

[72] J.D. Ania-Castanon, T. J. Ellingham, R. Ibbotson, X. Chen, L. Zhang and S.K. Turitsyn, *Ultralong Raman fiber lasers as virtually lossless optical media*, Physical Review Letters 96, p. 23902 (2006)

[73] S.K. Turitsyn, S.A. Babin, A.E. El-Taher, P. Harper, D. Churkin, S.I. Kablukov, J.D. Ania-Castanon, V. Karalekas, and E.V. Podivilov, *Random distributed feedback fibre laser*, Nature Photonics, 4, 231 (2010)

[74] IEEE Xplore. http://ieeexplore.ieee.org/Xplore/guesthome.jsp

[75] P. Urquhart, O.G. Lopez, G. Boyen, A. Bruckmann, *Optical Amplifiers for Telecommunications*, IEEE International Symposium on Intelligent Signal Processing, WISP 2007, pp.1-6, 3-5 Oct. 2007.

[76] D.R. Zimmerman, L.H. Spiekman, *Amplifiers for the Masses: EDFA, EDWA and SOA Amplets for Metro and Access Applications*, IEEE Journal of Lightwave Technology, 22 (1), pp. 63-70 (2004)

[77] M. Alcon-Camas, A.E. El-Taher, J.D. Ania-Castañón, P. Harper, *Gain bandwidth optimisation and enhancement in ultra-long Raman fibre laser based amplifiers*, 36th European Conference and Exhibition on Optical Communication (ECOC), pp.1-3, 19-23 Sept. 2010.

[78] J.D. Ania-Castañón, V. Karalekas, P. Harper and S.K. Turitsyn, *Simultaneous Spatial and Spectral Transparency in Ultralong Fiber Lasers*, Physical Review Letters 101 (12), p. 123903 (2008)

[79] S. Namiki, S. Koji, N. Tsukiji, S. Shikii, *Challenges of Raman amplification*, Proceedings of the IEEE, vol. 94, 5, pp 1024-1035 (2006)

[80] G. Ravet, A.A. Fotiadi, M. Blondel and P. Megret, *Passive Q-switching in all-fibre Raman laser with distributed Rayleigh feedback*, Electronics Letters, 40, 528 (2004)

[81] T. Schneider, *Nonlinear Optics in Telecommunications,* Springer-Verlag Berlin Heidelberg, 2004.

[82] S.K. Turitsyn, J.D. Ania-Castanon, S.A. Babin, V. Karalekas, P. Harper, D. Churkin, S.I. Kablukov, A.E. El-Taher, E.V. Podivilov and V.K. Mezentsev, *270-km Ultralong Raman Fiber Laser*, Physical Review Letters, 103, 133901 (2009)

[83] S.A. Babin, A.E. El-Taher, P. Harper, D.V. Churkin, S.I. Kablukov, E.V. Podivilov, and S.K. Turitsyn, *Raman fiber lasers with a random distributed feedback based on Rayleigh scattering*. Physical Review A 82(3): 033828 (2010)

[84] S.V. Chernikov, Y. Zhu, J.R. Taylor and V.P. Gapontsev, *Supercontinuum self-Q-switched ytterbium fiber laser*, Optics Letters. 22, pp. 298-300 (1997)

[85] K. Zamzuri, M.I.M. Ali, B. Ahmad and R. Mohamad, *Brillouin-Raman comb fiber laser with cooperative Rayleigh scattering in a linear cavity*, Optics Letters, Vol. 31, Issue 7, pp. 918-920 (2006)

[86] A.E. El-Taher, M. Alcon-Camas, S.A. Babin, P. Harper, J.D. Ania-Castañón and S.K. Turitsyn, *Dual-wavelength ultralong Raman laser with Rayleigh-scattering feedback*, Optics Letters, Vol. 35, Issue 7, pp. 1100-1102, (2010)

[87] O. Frazão, C. Correia, J.L. Santos, J.M. Baptista, *Raman fiber Bragg-grating laser sensor with cooperative Rayleigh scattering for strain-temperature measurement*, Measurement Science and Technology. 20, 045203 (2009)

[88] R.R. Alfano and S.L. Shapiro, *Emission in the Region 4000 to 7000 Å Via Four-Photon Coupling in Glass*, Physical Review Letters, vol. 24, Issue 11, pp. 584-587 (1970)

[89] R.R. Alfano and S.L. Shapiro, *Observation of Self-Phase Modulation and Small-Scale Filaments in Crystals and Glasses*, Physical Review Letters, vol. 24, Issue 11, pp. 592-594 (1970)

[90] C. Lin and R.H. Stolen, *New nanosecond continuum for excited-state spectroscopy*, Applied Physics Letters, 28, pp. 216–218 (1976)

[91] A.S. Gouveia-Neto, A. Gomes, and J. Taylor, *Femto soliton Raman generation*, IEEE Journal of Quantum Electronics, 24, pp. 332-340 (1988)

[92] J.M. Dudley, G. Genty and S. Coen, *Supercontinuum generation in photonic crystal fiber, Reviews of Modern Physics*, vol. 78, no. 4, pp. 1135-1184 (2006)

[93] S.V. Smirnov, J.D. Ania-Castañón, T.J. Ellingham, S.M. Kobtsev, S. Kukarin and S.K. Turitsyn, *Optical spectral broadening and supercontinuum generation in telecom applications*, Optical Fiber Technology, 12 (2), pp. 122-147 (2006)

[94] A.K. Abeeluck, C. Headley, and C.G. Jørgensen, *High-power supercontinuum generation in highly nonlinear, dispersion-shifted fibers by use of a continuous-wave Raman fiber laser*, Optics Letters, Vol. 29, 18, pp. 2163-2165 (2004)

[95] A.K. Abeeluck and C. Headley, *Continuous-wave pumping in the anomalous- and normal-dispersion regimes of nonlinear fibers for supercontinuum generation*, Optics Letters, Vol. 30, Issue 1, pp. 61-63 (2005)

[96] L. Abrardi, S. Martín-López, A. Carrasco-Sanz, P. Corredera, M.L. Hernanz, and M. González-Herráez, *Optimized All-Fiber Supercontinuum Source at 1.3 μm Generated in a Stepwise Dispersion-Decreasing-Fiber Arrangement*, IEEE Journal of Lightwave Technology, Vol. 25, Issue 8, pp. 2098-2102 (2007)

[97] G. Genty, S. Coen, and J.M. Dudley, *Fiber supercontinuum sources*, The Journal of the Optical Society of America ,B 24, pp. 1771-1785 (2007)

[98] R.R. Alfano, *The Supercontinuum Laser Source: Fundamentals With Updated References*. Springer, 2006.

[99] J.C. Knight, T.A. Birks, P.S. Russell, D.M. Atkin , *All-silica single-mode optical fiber with photonic crystal cladding*, Optics Letters, 21 (19) pp. 1547-1549, (1996)

[100] I. Hartl, X.D. Li, C. Chudoba, R.K. Ghanta, T.H. Ko, J.G. Fujimoto, J.K. Ranka, and R.S. Windeler, *Ultrahigh-resolution optical coherence tomography using*

continuum generation in an air-silica microstructure optical fiber, Optics Letters, Vol. 26, Issue 9, pp. 608-610 (2001)

[101] P. Hsiung, Y. Chen, T.H. Ko, J.G. Fujimoto, C.J.S. de Matos, S.V. Popov, J.R. Taylor and V.P. Gapontsev, *Optical coherence tomography using a continuous-wave, high-power, Raman continuum light source*, Optics Express 12, pp. 5287-5295 (2004)

[102] A.B. Fedotov, A.M. Zheltikov, A.A. Ivanov, M.V. Alfimov, D. Chorvat, V.I. Beloglazov, L.A. Melnikov, N.B. Skibina, A.P. Tarasevitch, D. von der Linde, *Supercontinuum-generating holey fibers as new broadband sources for spectroscopic applications*, Laser Physics 10, pp. 723–726 (2000)

[103] T. Udem, R. Holzwarth, and T.W. Hänsch, *Optical Frequency Metrology*, Nature 416, pp.233-237 (2002)

[104] L.F. Mollenauer, R.H. Stolen, and J.P. Gordon, *Experimental observation of picosecond pulse narrowing and solitons in optical fibers*, Physical Review Letters, vol. 45, no. 13, pp. 1095–1098 (1980)

[105] L.F. Mollenauer, R. H. Stolen, J. P. Gordon, and W. J. Tomlinson, *Extreme picosecond pulse narrowing by means of soliton effect in single-mode optical fibers*, Optics Letters, vol. 8, no. 5, pp. 289–291 (1983)

[106] A.L. Gaeta, *Nonlinear propagation and continuum generation in microstructured optical fibers*, Optics Letters. 27, pp. 924–926 (2002)

[107] P.K.A. Wai, H.H. Chen and Y.C. Lee, *Radiation by "solitons" at the zero group-dispersion wavelength of single-mode optical fibers*, Physical Review Letters, vol. 41, no. 1, pp. 426–439 (1990)

[108] N. Akhmediev and M. Karlsson, *Cherenkov radiation emitted by solitons in optical fibers*, Physical Review A, vol. 51, no. 3, pp. 2602–2607 (1995)

[109] A.E. El-Taher, V. Karalekas, P. Harper, J.D. Ania-Castañón, *High efficiency supercontinuum generation using ultra-long Raman fibre cavities*, ECOC 2008, 34th European Conference on Optical Communication, Mo3B3, Brussels, 2008.

[110] J.N. Kutz, C. Lynga, and B.J. Eggleton, *Enhanced supercontinuum generation through dispersion-management*, Optics Express, vol. 13, no. 11, p. 3989, (2005)

[111] F. Vanholsbeeck, S. Martin-Lopez, M. Gonzalez-Herraez and S. Coen, *The role of pump incoherence in continuous-wave supercontinuum generation*, Optics Express, 13, pp. 6615-6625 (2005)

[112] B. Han and X. Zhang, *Composite broad-band fiber Raman amplifiers using incoherent pumping*. Optics Express, Vol. 13, Issue 16, pp. 6023-6032 (2005)

[113] J.K. Ranka, R.S. Windeler and A.J. Stentz, *Visible continuum generation in air-silica microstructure optical fibers with anomalous dispersion at 800 nm*, Optics Letters. 25, pp. 25-27 (2000)

[114] J.M. Dudley, G. Genty, B. Eggleton, *Optical rogue wave dynamics in supercontinuum generation*, OECC/ACOFT 2008, Joint conference of the Opto-Electronics and Communications Conference and the Australian Conference on Optical Fibre Technology, pp.1-2, Sydney, 2008.

[115] J.M. Dudley, G. Genty, F. Dias, B. Kibler, N. Akhmediev, *The dynamics of a developing CW supercontinuum: Analytical predictions and experiments*, OFC/NFOEC 2010, Conference on Optical Fiber Communication and National Fiber Optic Engineers Conference, pp.1-3, San Diego, CA, 2010.

[116] J.M. Soto-Crespo, N. Akhmediev, C. Mejia-Cortes, and N. Devine, Dissipative *ring solitons with vorticity*, Optics Express, 17, pp. 4236-4250 (2009)

[117] K. Sumimura, T. Ohta and N. Nishizawa, *Quasi-super-continuum generation using ultrahigh-speed wavelength-tunable soliton pulses*, Optics Letters, 33, 24, p.2892-2894 (2008)

[118] E. Desurvire, O. Leclerc, and O. Audouin, *Synchronous in-line regeneration of wavelength-division multiplexed solitons signals in optical fibers*, Optics Letters. 21, pp. 1026-1028 (1996)

[119] A. Hasegawa and Y. Kodama, *Solitons in Optical Communications*. Clarendon Press, 1995.

[120] N.J. Doran and K.J. Blow, *Solitons in optical communications*, IEEE Journal of Quantum Electronics, vol. 19, pp. 1883-1888 (1983)

[121] E. Iannone, F. Matera, A. Mecozzi, and M. Settembre, *Nonlinear Optical Communication Networks*. Wiley, 1998.

[122] S.B. Alleston, P. Harper, I.S. Penketh, I. Bennion, N.J. Doran, A.D. Ellis, *40 Gbit/s soliton transmission over dispersion managed standard fibre links*, IEE Colloquium on High Speed and Long Distance Transmission (Ref. No. 1999/022), pp.2/1-2/4, 1999.

[123] R.H. Stolen and E. P. Ippen, *Raman gain in glass optical waveguides*, Applied Physics Letter, vol. 22, pp. 276-278 (1973)

[124] L.F. Mollenauer, J.P. Gordon and M.N. Islam, *Soliton propagation in long fibers with periodically compensated loss*, IEEE Journal of Quantum Electronics, vol. 22, pp. 157-173 (1986)

[125] H. Kubota and M. Nakazawa, *Long-Distance Optical Soliton Transmission with lumped Amplifier*, IEEE Journal of Quantum Electronics, vol. 26, pp. 692-700 (1990)

[126] K.J. Blow and N.J. Doran, *Average soliton dynamics and the operation of soliton systems with lumped amplifiers*, IEEE Photonics Technology Letters, 3, p.369-371 (1991)

[127] N.J. Smith, F. M. Knox, N. J. Doran, K. J. Blow and I. Bennion, *Enhanced power solitons on optical fibres with periodic dispersion management*. Electronics Letters, vol 32, pp. 54-55 (1996)

[128] M. Nakazawa and K. Kurokawa, *Femtosecond soliton transmission in 18 km long dispersion shifted distributed erbium-doped fibre amplifier*, Electronics Letters, 27, pp. 1369-1371 (1991)

[129] D.J. Richardson, L. Dong, R.P. Chamberlin, A.D. Ellis, T. Widdowson and W.A. Pender, *Periodically amplified system based on loss compensating dispersion decreasing fibre*, Electronics Letters 32, 4 p.373 (1996)

[130] L.F. Mollenauer and K. Smith, *Demonstration of soliton transmission over more than 4000 kmin fiber with loss periodically compensated by Raman gain*, Optics Letters, 13, pp. 675-677 (1988)

[131] J.D. Ania-Castañón, S. K. Turitsyn, A. Tonello, S. Wabnitz, and E. Pincemin, *Multi-level optimization of a fiber transmission system via nonlinearity management*, Optics Express 14, pp. 8065-8071 (2006)

[132] B.L. Danielson, *Optical time-domain reflectometer specifications and performance testing*, Applied Optics. 24, pp. 2313-2322 (1985)

[133] J.M. Dudley, L.P. Barry, P.G. Bollond, J.D. Harvey and R. Leonhardt, *Characterizing Pulse Propagation in Optical Fibers around 1550 nm Using Frequency-Resolved Optical Gating*, Optical Fiber Technology 4, pp. 237-265 (1998)

[134] Hasegawa, *Soliton-based optical communications: an overview*, IEEE Journal of Selected Topics in Quantum Electronics, vol.6, no.6, pp.1161-1172, Nov/Dec 2000.

[135] N.J. Smith, N.J. Doran, W. Forysiak and F. M. Knox, *Soliton transmission using periodic dispersion compensation*, Journal of Lightwave Technology, 15, pp.1808-1822 (1997)

[136] L.F Mollenauer, *Raman amplification and dispersion-managed solitons for all-optical, ultra-long-haul, dense WDM*, in Optical Amplifiers and Their Applications, OSA Technical Digest Series (Optical Society of America), paper OMA2, 2001.

[137] Private email by J.D. Ania-Castañón